

**University of Alberta**

**FAILURE CRITERIA FOR TEARING OF TELESCOPING WRINKLES**

by

**Arman Uddin Ahmed**

A thesis submitted to the Faculty of Graduate Studies and Research  
in partial fulfillment of the requirements for the degree of

Doctor of Philosophy

in

**Structural Engineering**

Department of Civil and Environmental Engineering

©Arman Uddin Ahmed

Spring 2011

Edmonton, Alberta

Permission is hereby granted to the University of Alberta Libraries to reproduce single copies of this thesis and to lend or sell such copies for private, scholarly or scientific research purposes only. Where the thesis is converted to, or otherwise made available in digital form, the University of Alberta will advise potential users of the thesis of these terms.

The author reserves all other publication and other rights in association with the copyright in the thesis and, except as herein before provided, neither the thesis nor any substantial portion thereof may be printed or otherwise reproduced in any material form whatsoever without the author's prior written permission.

**Examining Committee:**

Dr. J.J. Roger Cheng, Civil and Environmental Engineering

Dr. Robert Driver, Civil and Environmental Engineering

Dr. Samer Adeeb, Civil and Environmental Engineering

Dr. Weixing Chen, Chemical and Materials Engineering

Dr. Ben Jar, Mechanical Engineering

Dr. John Tassoulas, Civil, Architectural and Environmental Engineering, The  
University of Texas at Austin

## ABSTRACT

An ever increasing demand to exploit oil and natural gas reserves has significantly increased extraction activities even in the remotest regions of the Arctic and sub-Arctic regions of the Canadian North. Steel pipelines are the most efficient mode for transporting and distributing these resources. These pipelines, particularly buried in cold region, often subjected to extreme geo-environmental conditions, where significant inelastic deformation may occur resulting in localized wrinkles. Under continued deformation, there is a possibility of excessive cross-sectional deformation at wrinkle locations, eventually leading to fracture or damage in the pipe wall jeopardizing pipeline safety and integrity . Prior research indicated that occurrence of fracture in pipe wrinkle is rare under monotonic load-deformation process. However, a recent field fracture was observed within the wrinkle location of an energy pipeline. Similar failure mode was observed in a laboratory specimen at the University of Alberta. Both field and laboratory observations had indicated that the final failure was a “tearing” failure at the fold of the telescopic wrinkles resulting from monotonic application of axial load not aligned with pipe axis.

This research program was designed to study this specific failure mode and to develop design tool for pipeline engineers. This research started with examining the failed field and test specimens. A preliminary investigation was carried out using nonlinear finite element (FE) model to simulate test and field behaviour. Numerical results have indicated that even under monotonic loading, significant strain reversals could occur at the wrinkle fold . Presence of these strain reversals

was proposed as the preliminary failure criterion responsible for this unique failure mechanism.

In next phase, a full-scale ‘pipe-wrinkling’ test program was carried out concurrent to this research to better understand the loading condition responsible for this type of failure. Results of this test program have shown the presence of tearing fracture or rupture in the pipe walls of several of test specimens. A series of FE analyses was then carried out to predict and verify the behaviour of these test specimens. After successful simulation of the test behaviour, further numerical analyses were carried out using tension coupon model developed herein to simulate the material behaviour using the material test data and hence to formulate the limiting conditions in terms of critical strain responsible for the tearing failure.

Based on these numerical results, a double criterion – ‘Strain Reversal’ and ‘Critical Equivalent Plastic Strain Limit’, were proposed to predict tearing fracture of wrinkled pipe under monotonic loading. Results of these numerical analyses have demonstrated that the proposed criteria predict this failure mode with reasonable accuracy. In the final phase of this research, a parametric study was carried out to consider the effect of different parameters on failure modes of wrinkled pipe. Results of this parametric study describe the range of parameters under which the tearing mechanism can/may exhibit.

## ACKNOWLEDGEMENTS

This research project was conducted with the financial assistance from TransCanada Pipelines Ltd. The author would like to thank WestCoast Energy Inc. for providing the NPS10 failed specimen for this research project. The author also acknowledges supports, in the form of awards and scholarships, provided by Faculty of Graduate Studies and Research, University of Alberta, Alberta Ingenuity Fund, Chevron Canada, and Petro-Canada.

The author wishes to express his thanks to his supervisor, Dr. J.J. Roger Cheng for his incessant guidance, assistance and support throughout this project. His active interest in this topic and valuable advice were the source of author's inspirations. The author also thanks to the fellow graduate students and colleagues Dr. Mohammad Behbahanifard, Dr. Jianmin Zhang, Dr. Zoulong Chou, and Mehmet Aydin for their invaluable contributions during this research project.

The encouragement and support from my family especially from my wife, Shaila, and daughter, Anushka provided confidence to the author in conducting the research work successfully. The author also wishes to express his appreciations to his parents, other family members, colleagues and friends for their co-operation and companionship extended to him during the study at University of Alberta.

# TABLE OF CONTENTS

<b>ABSTRACT</b> .....	<b>III</b>
<b>ACKNOWLEDGEMENTS</b> .....	<b>V</b>
<b>LIST OF SYMBOLS AND ABBREVIATIONS</b> .....	<b>XXIV</b>
<b>1. INTRODUCTION</b> .....	<b>1</b>
1.1 Problem Statement .....	1
1.2 Research Objectives, Scope, and Significance.....	3
1.3 Research Approach.....	4
1.4 Organization of Thesis .....	5
<b>2. LITERATURE REVIEW</b> .....	<b>8</b>
2.1 General .....	8
2.2 Geo-Environmental Loading and Pipeline Integrity .....	8
2.3 Consequences of Pipeline Failure Incidents.....	11
2.3.1 Morgan Falls Landfill .....	11
2.3.2 Winchester, Kentucky .....	12
2.3.3 Prince George’s County .....	13
2.4 History of Pipeline Research in Wrinkling .....	13
2.5 Failure Modes of Wrinkled Pipe .....	15
2.5.1 Low Cycle Fatigue .....	16
2.5.2 Accordion Wrinkles .....	17
2.5.3 Telescopic Tearing.....	18
2.6 Ductile Fracture of Steel.....	21
2.7 References .....	33

<b>3. PRELIMINARY INVESTIGATION OF TEARING FAILURE.....</b>	<b>40</b>
3.1 General .....	40
3.2 Previous Experimental Investigation .....	42
3.2.1 Loading Steps.....	43
3.2.2 Test Results .....	44
3.3 Development of the Numerical Model.....	45
3.3.1 Element Selection .....	46
3.3.2 Mesh Sensitivity.....	47
3.3.3 Circumferential Direction.....	48
3.3.4 Longitudinal Direction.....	49
3.3.5 Modeling of End Plates and Collars .....	49
3.3.6 Material Modeling .....	51
3.3.7 Boundary Conditions and Loading Sequence.....	53
3.3.8 Initial Imperfection Model.....	54
3.3.9 Contact Formulation .....	55
3.3.10 A Brief Note on Solution Strategy.....	56
3.4 Verification of the FE Model .....	57
3.5 Discussion of Analytical Results.....	59
3.5.1 Deformed Configuration.....	59
3.5.2 Stress-Strain History .....	60
3.6 Discussion of Failure Phenomena .....	62
3.7 References .....	82

<b>4.</b>	<b>NUMERICAL VERIFICATION OF EXPERIMENTAL RESULTS ....</b>	<b>84</b>
4.1	General .....	84
4.2	Experimental program .....	87
4.2.1	Test Setup.....	88
4.2.2	Instrumentation .....	89
4.3	Loading Procedures.....	90
4.4	Test Results .....	94
4.4.1	Moment-Curvature Relationships.....	94
4.4.2	Wrinkle Location .....	95
4.5	Comments on Strains .....	96
4.5.1	Strain Gauge Strains .....	96
4.5.2	Demec and Calliper Strains.....	97
4.5.3	Final Deformed Configurations and Failure Modes .....	99
4.6	Summary of Experimental Results.....	100
4.7	Numerical Studies .....	101
4.7.1	Description of FE Model .....	102
4.7.2	Boundary Conditions and Loading Sequences .....	103
4.7.3	True Stress-True Plastic Strain Curves .....	104
4.8	Verification of FE Model .....	107
4.8.1	Load-Displacement (P- $\Delta$ ) Response.....	107
4.8.2	Moment-Curvature (M- $\phi$ ) Response.....	110
4.8.3	Comparison of Deformed Shapes .....	112
4.8.4	Comparison of Strain Values .....	115

4.9	Summary of Numerical Results .....	116
4.10	References .....	160
<b>5.</b>	<b>DEVELOPMENT OF FAILURE CRITERIA' .....</b>	<b>163</b>
5.1	General .....	163
5.2	Development of Failure Criteria .....	166
5.2.1	Tension Coupon Tests.....	166
5.2.2	True Stress –True Plastic Strain Curves .....	167
5.2.3	Failure Criterion – Critical Plastic Strain ( $\bar{\epsilon}_c^p$ ) Limit .....	168
5.2.4	Finite Element Models of Tension Test Coupons.....	171
5.3	Application of Failure Criteria— 'Double Criteria'.....	173
5.3.1	Specimen 1 (D12P0A3.4-1).....	176
5.3.2	Specimen 2 (D16P0A5-2).....	178
5.3.3	Specimen 3 (D16P40A7-3).....	180
5.3.4	Specimen 4 (D20P40A3.5-4).....	183
5.3.5	Specimen 5 (D20P0A5-5).....	184
5.3.6	Specimen 6 (D20P80A4-6).....	185
5.4	Discussion and Postulation.....	187
5.4.1	Effect of Loading Condition .....	188
5.4.2	Effect of End Rotation .....	188
5.4.3	Effect of D/t Ratio.....	188
5.4.4	Effect of Operational Condition.....	189
5.5	Summary .....	189
5.6	References .....	232

<b>6.</b>	<b>EFFECTS OF PARAMETERS ON TEARING FAILURE MODE .....</b>	<b>235</b>
6.1	General .....	235
6.2	Simulation of Field Loading .....	236
6.3	Effect of Loading Condition.....	238
6.4	Effect of D/t Ratio .....	240
6.5	Effect of End Rotation.....	242
6.6	Effect of Operational Condition.....	245
6.7	Effect of Material Properties .....	246
6.7.1	Strain-hardening Exponent .....	247
6.7.2	Bauschinger Effect.....	247
6.8	Summary .....	249
6.9	References .....	281
<b>7.</b>	<b>SUMMARY, CONCLUSIONS, AND RECOMMENDATIONS .....</b>	<b>282</b>
7.1	Summary .....	282
7.2	Conclusions .....	285
7.3	Future Research Recommendations .....	287
7.4	References .....	288

## LIST OF TABLES

Table 4.1 Full-scale Test Matrix and Load Values .....	117
Table 4.2. Maximum Curvature and Strain Values .....	118
Table 4.3 Material Properties of Test Specimens from Coupon Tests .....	119
Table 4.4 Assumed Material Properties .....	119
Table 4.5 Comparison of Test and Analytical Results .....	120
Table 5.1 Material Properties of Test Specimens from Coupon Tests .....	191
Table 5.2 Cross-sectional Dimensions of Test Specimens from Coupon Tests ..	192
Table 5.3 Full-scale Test Parameters used in FE Simulations .....	193
Table 6.1 Summary of Parametric study .....	251

## LIST OF FIGURES

Figure 1.1 (a) Accordion type failure under monotonic loading (Das et al. 2002); and (b) fractures under cyclic deformation (Das et al. 2007c).....	7
Figure 1.2 Pipe segment showing tearing fracture at wrinkle location obtained from (a)WestCoast Energy, and (b) Experimental work performed at University of Alberta (Das et al. 2002).....	7
Figure 2.1 Typical Wrinkle Shapes (Das 2003; Aydin 2007) .....	24
Figure 2.2 Schematic views showing different geo-hazards on pipelines buried in cold environments (Murray 1997; Tart Jr. 2007; Martens et al. 2009; Tanaka et al. 2009) .....	26
Figure 2.3 Exposed wrinkle of Norman wells pipeline at Slope 92 (Wilkie et al. 2001) .....	26
Figure 2.4 (a) Wrinkle (buckle) in a 40 inch diameter steel pipe with (b) close-up view of wrinkled pipe showing through-the-wall cracks (NTSB 1999).....	26
Figure 2.5 Rupture of an energy pipe due to presence of dent along with operating pressure fluctuations (NTSB 2001) .....	27
Figure 2.6 (a) Wrinkle or buckle location in the failed pipe, (b) Presence of significant crack at the wrinkle crest (NTSB 2002).....	27
Figure 2.7 Fracture of wrinkled pipe under cyclic axial loading (Das et al. 2007a)	28
Figure 2.8 Non-axisymmetric wrinkles under bending deformation (Das et al. 2008) .....	28

Figure 2.9 Deformed shape after closing of 1 <sup>st</sup> wrinkle under monotonic loading (Zhang et al. 2008a) .....	29
Figure 2.10 Accordion type of failure under monotonic loading (Das et al. 2002)	29
Figure 2.11 Load-displacement response of an NPS12 pipe under monotonic deformation (Das 2003; Zhang and Das 2008a) .....	30
Figure 2.12 Final deformed shapes of the specimens obtained from (a) the WestCoast Energy Inc. and (b) the test (Das et al. 2002) .....	30
Figure 2.13 Schematic of (a) surface-breaking, and (b) buried defects in the pipe wall (Canadian Standards Association (CSA) 2007) .....	31
Figure 2.14 Mechanism of ductile fracture in metal (Khoo 2000) .....	32
Figure 3.1 Accordion type failure under monotonic loading (Das et al. 2002) .....	64
Figure 3.2 Pipe segment showing tearing fracture at wrinkle location obtained from WestCoast Energy (Das et al. 2002) .....	64
Figure 3.3 Schematic view of the test set with sequence of applied axial and transverse load (Das et al. 2002) .....	65
Figure 3.4 Load-displacement response for the test specimen (Das et al. 2002) .....	66
Figure 3.5 Fracture (through-thickness crack) in the wrinkle fold of the pipe specimen (Das et al. 2002) .....	66
Figure 3.6 Schematic View of the developed FE model .....	67
Figure 3.7 Configuration of section points in a homogeneous shell element (Hibbitt, H.D., Karlsson, B.I., and Sorensen, P., 2006) .....	68
Figure 3.8 Effect of mesh refinement in circumferential direction on axial load- displacement response .....	68

Figure 3.9 Effect of mesh refinement in longitudinal direction on axial load-displacement response .....	69
Figure 3.10 Typical geometry and initial boundary condition for the full-pipe model.....	70
Figure 3.11 True stress versus true plastic strain behaviour until failure .....	71
Figure 3.12 Nonlinear kinematic hardening illustrating evolution of yield surface in the stress space.....	72
Figure 3.13 Evolution of back-stress using kinematic hardening model saturating at $c/\gamma$ . .....	72
Figure 3.12 Load versus displacement response of shell structures (Bushnell 1981) .....	73
Figure 3.13 Schematic views of assumed initial imperfection patterns where X-axis represents the longitudinal direction of pipe (Dorey et al. 2006).....	74
Figure 3.14 Imperfections Patterns adopted in the present FE Model.....	75
Figure 3.15 MTS load—displacement relationship obtained from FE Analysis and test result (Das et al. 2002) .....	76
Figure 3.16 Comparison of Deformed shapes of the specimen obtained from (a) the present analytical work, (b) the experiment, and (c) the WestCoast Energy Inc.(Das et al. 2002).....	77
Figure 3.17 Predicted location of self-contact between inner surfaces of pipe wall ( $\eta^+$ is the direction of normal indicating outer surface of the pipe).....	78
Figure 3.18 Predicted progression of deformed configuration for the pipe specimen .....	79

Figure 3.19 Predicted wrinkle formation process on the compression side of the pipe.....	80
Figure 3.20 Longitudinal Stress-Strain relationship at some selected elements....	81
Figure 4.1 Typical Wrinkle Shapes (Das 2003; Aydin 2007) .....	121
Figure 4.2 (a) Accordion type failure under monotonic loading (Das et al. 2002); and (b) fractures under cyclic deformation (Das et al. 2007b). .....	121
Figure 4.3 Final deformed shapes of the specimens obtained from (a) the WestCoast Energy Inc. (Das et al. 2002) , (b) the test (Das et al. 2002), and (c) the numerical work (Ahmed et al. 2010) .....	122
Figure 4.4 Initial deformed configurations of Specimen 2, 3, 4, and 5 .....	123
Figure 4.5 Schematic of test setup .....	124
Figure 4.6 Typical layouts of strain gauges and Demec points .....	125
Figure 4.7 MTS load versus displacement response of Specimen 2 and 3 .....	126
Figure 4.8 MTS load versus displacement response of Specimen 4, 5 and 6.....	127
Figure 4.9 Free body diagram of the moment arm for calculating global and local end moment.....	128
Figure 4.10 Global moment curvature behaviour of Specimen 2 and 3 .....	129
Figure 4.11 Global moment curvature behaviour of Specimen 4, 5 and 6 .....	130
Figure 4.12 Local moment curvature behaviour of Specimen 3 and 5 .....	131
Figure 4.13 Local longitudinal strains versus global curvature for specimens 2, 3, 4 and 6.....	131
Figure 4.14 Local circumferential strains versus global curvature for 16" pipes	132
Figure 4.15 Local circumferential strains versus global curvature for 20" pipes	132

Figure 4.16 Global curvature- global longitudinal compressive strain relationships for specimens 2-5 .....	133
Figure 4.17 Global longitudinal compressive (Demec) strain growth with axial shortening.....	134
Figure 4.18 Global longitudinal compressive (Caliper) strain growth with axial shortening.....	135
Figure 4.19 Comparison of final deformed shapes between (a) Specimen 2 and 5, and (b) Specimen 3 and 6.....	136
Figure 4.20 Cut segment from the compression side of Specimen 2 and 3 .....	137
Figure 4.21 Fracture in the wrinkle fold of (a) the field (Das et al. 2002), and (b) the test specimen (Das et al. 2002); and location of strain reversal in FE model (Ahmed et al. 2010). .....	137
Figure 4.22 Typical geometry and initial boundary condition for full-pipe model.....	138
Figure 4.23 Typical geometry and initial boundary condition for half pipe model.....	139
Figure 4.24 Engineering stress-strain plot of X60 and X65 grade steel obtained from tension coupon test.....	140
Figure 4.25 True stress-true plastic strain behaviour of X-60 and X-65 grade steel (up to 20% strain).....	141
Figure 4.26 True stress-true plastic strain behaviour of X-60 and X-65 grade steel (up to failure) .....	142

Figure 4.27 MTS load—displacement relationship obtained from FE analyses and test results of NPS16 pipes .....	143
Figure 4.28 MTS load—displacement relationship obtained from FE analyses and test results of NPS20 pipes .....	144
Figure 4.29 MTS load—displacement relationship obtained from FE analyses and test results of specimen 5 for different load condition.....	145
Figure 4.30 Global moment—global curvature relationship obtained from FE analyses and test results of NPS16 Pipes .....	146
Figure 4.31 Global moment—global curvature relationship obtained from FE analyses and test results of NPS20 Pipes .....	147
Figure 4.32 Comparison of initial deformed shapes of specimen 2 and 3.....	148
Figure 4.33 Comparison of initial deformed shapes of specimen 4 and 5.....	149
Figure 4.34 Comparison of final deformed shapes of specimen 2 (D16P0A5-2).....	150
Figure 4.35 Comparison of final deformed shapes of specimen 3 (D16P40A7-3).....	151
Figure 4.36 Comparison of final deformed shapes of specimen 4.....	152
Figure 4.37 Comparison of final deformed shapes from FE analyses of specimen 5 with two different internal pressure conditions .....	153
Figure 4.38 Comparison of final deformed shapes of specimen 4.....	154
Figure 4.39 Comparison of final deformed shapes of specimen 6.....	155
Figure 4.40 Comparison of global longitudinal compressive (Caliper) strain —axial shortening response of NPS16 specimens.....	156

Figure 4.41 Comparison of global longitudinal compressive (Caliper) strain —axial shortening response of NPS20 specimens.....	157
Figure 4.42 Comparison of global curvature-longitudinal compressive strain response for NPS16 specimens.....	158
Figure 4.43 Comparison of global curvature-longitudinal compressive strain response for NPS20 specimens.....	159
Figure 5.1 True stress-true plastic strain relationship (up to failure) all the pipe materials used in this research program.....	194
Figure 5.2 Typical engineering (nominal) stress-strain plot obtained from tension coupon test showing a schematic location of critical strain ( $\bar{\epsilon}_c^p$ ).....	195
Figure 5.3 Tension coupon specimen with cross-sectional (schematic) comparison before and after test.....	196
Figure 5.4 FE model of the steel tension bar: (a) a plane view with dimensions in mm; (b) loading and boundary conditions on a ¼ FE model; (c) the FE mesh ...	197
Figure 5.5 Experimentally measured and numerically computed load- displacement ( $P$ - $\Delta$ ) responses of X60 and X65 grade steel coupons.....	198
Figure 5.6 The deformed shapes of 3D FE coupons for X60 grade, and (b) X65 grade without the mesh.....	199
Figure 5.7 The deformed shapes of 3D FE coupons: (a) X60 grade, and (b) X65 grade; obtained at point $E_1$ and $E_2$ on $P$ - $\Delta$ plots.....	200
Figure 5.8 The distribution of the equivalent plastic strain (PEEQ or $\epsilon^p$ ) at (a) point $E_1$ ; and (b) point $C_1$ on $P$ - $\Delta$ response of X60 coupon.....	201

Figure 5.9 The distribution of the equivalent plastic strain (PEEQ or $\varepsilon^p$ ) at (a) point E <sub>2</sub> ; and (b) point C <sub>2</sub> on P- $\Delta$ response of X65 coupon .....	202
Figure 5.10 True stress-true plastic strain relationship of all the pipe materials indicating the location of the critical strain ( $\bar{\varepsilon}_c^p$ ) values.....	203
Figure 5.11 Close-up view of the cut segments from the compression side of specimen 2 (D16P0A5-2) and specimen 3 (D16P40A7-3).....	204
Figure 5.12 Fracture in the wrinkle fold of (a) the field (Das et al. 2002), and (b) the test specimen D12P0A3.4-1 (Das et al. 2002); and location of strain reversal in the FE (full-pipe) model (Ahmed et al. 2010) .....	205
Figure 5.13 Longitudinal stress-strain relationship at some selected elements of specimen 1 (D12P0A3.4-1) .....	206
Figure 5.14 True longitudinal stress-equivalent plastic strain plots of some selected elements for specimen 1 .....	207
Figure 5.15 Contour plots of the equivalent plastic strain (PEEQ or $\varepsilon^p$ ) obtained from outer surface of specimen 1.....	208
Figure 5.16 Close-up view of wrinkled pipe for specimen 2 and 3 .....	209
Figure 5.17 Longitudinal stress-strain relationship at some selected elements of specimen 2 (D16P0A5-2) .....	210
Figure 5.18 True longitudinal stress-equivalent plastic strain plots at some selected elements of specimen 2 .....	211
Figure 5.19 Contour plots of equivalent plastic strain (PEEQ) obtained from outer surface of specimen 2 and 3.....	212

Figure 5.20 Longitudinal stress-strain relationship at some selected elements of specimen 3 (D16P40A7-3) .....	213
Figure 5.21 True longitudinal stress-equivalent plastic strain plots at some selected elements of specimen 3 .....	214
Figure 5.22 Plastic strain growth with displacement history for specimen 2 and 3.....	215
Figure 5.23 Close-up view of wrinkled pipe along with a wrinkle-strip for specimen 4 .....	216
Figure 5.24 Longitudinal stress-strain relationship at some selected elements of specimen 4 (D20P40A3.5-4) .....	217
Figure 5.25 True longitudinal stress-equivalent plastic strain plots at some selected elements of specimen 4 .....	218
Figure 5.26 Contour plots of equivalent plastic strain (PEEQ) obtained from outer surface of specimen 4.....	219
Figure 5.27 Close-up view of wrinkled pipe along with a wrinkle-strip for specimen 5 .....	220
Figure 5.28 Longitudinal stress-strain relationship at some selected elements of specimen5 (D20P0A5-5) .....	221
Figure 5.29 True longitudinal stress-equivalent plastic strain plots at some selected elements of specimen 5 .....	222
Figure 5.30 Contour plots of equivalent plastic strain (PEEQ) obtained from outer surface of specimen 5.....	223

Figure 5.31 Close-up view of wrinkled pipe along with a wrinkle-strip for specimen 6 .....	224
Figure 5.32 Longitudinal stress-strain relationship at some selected elements of specimen5 (D20P0A5-5) .....	225
Figure 5.33 True longitudinal stress-equivalent plastic strain plots at some selected elements of specimen 5 .....	226
Figure 5.34 Contour plots of equivalent plastic strain (PEEQ) obtained from outer surface of specimen 6.....	227
Figure 5.35 Progression of von Mises stress after few increments for specimen 6.....	228
Figure 5.36 Plastic strain growth with displacement history for specimen 1 and 3.....	229
Figure 5.37 Plastic strain growth with displacement history for specimen 3 and 4.....	230
Figure 5.38 Plastic strain growth with displacement history for specimen 4 and 6.....	231
Figure 6.1 Wrinkled pipe under extreme curvature (Sen 2006) .....	252
Figure 6.2 Plastic strain growth with displacement history for specimen 1 and 3.....	253
Figure 6.3 Deformed shape after applying shear load .....	254
Figure 6.4 (a) Final deformed shape and (b) equivalent plastic strain contour of specimen 1 under end moments.....	255
Figure 6.5 Plastic strain growth with or without shear load for specimen 1 .....	256

Figure 6.6 Plastic strain growth with displacement history for specimen 3 and 4.....	257
Figure 6.7 Effect of D/t ratio on initial deformed shape.....	258
Figure 6.8 Effect of D/t ratio on final deformed shape.....	259
Figure 6.9 Initiation of second wrinkle for higher D/t ratio.....	260
Figure 6.10 Effect of D/t ratio on longitudinal stress-strain relationship (i.e. Strain-Reversal) .....	261
Figure 6.11 Effect of D/t ratio on plastic strain growth.....	262
Figure 6.12 Effect of curvature on initial deformed shape .....	263
Figure 6.13 Effect of curvature on final deformed shape .....	264
Figure 6.14 Effect of curvature on stress-strain relationship (i.e. Strain-Reversal) .....	265
Figure 6.15 Plastic strain growth development under increasing curvature .....	266
Figure 6.16 Initiation of second wrinkle under relatively smaller curvature.....	267
Figure 6.17 Plastic strain growth with displacement history for specimen 4 and 6.....	268
Figure 6.18 Effect of internal pressure on initial deformed shape.....	269
Figure 6.19 Effect of internal pressure on final deformed shape.....	270
Figure 6.20 Initiation of second wrinkle under higher internal pressure condition .....	271
Figure 6.21 Effect of internal pressure condition on stress-strain relationship (i.e. Strain-Reversal) .....	272
Figure 6.22 Plastic strain growth development under increasing curvature .....	273

Figure 6.23 True stress-true plastic strain relations with different strain-hardening exponents (i.e. 'n' in Equation 4.13).....	274
Figure 6.24 Effect of 'n' stress-strain relationship (i.e. Strain-Reversal).....	275
Figure 6.25 Plastic strain growth under different strain-hardening exponent .....	276
Figure 6.26 Nonlinear kinematic/Isotropic hardening illustrating evolution of yield surface in the stress space .....	277
Figure 6.27 Evolution of back-stress using Armstrong-Fredrick kinematic hardening model saturating at $c/\gamma$ . .....	277
Figure 6.28 True stress-true plastic strain relations under cyclic and monotonic loading.....	278
Figure 6.29 Bauschinger Effect on strain-reversal behaviour.....	279
Figure 6.30 Effect of different hardening model on plastic strain growth.....	280

## LIST OF SYMBOLS AND ABBREVIATIONS

### *Latin Symbols*

a	Crack width or depth along the thickness of the pipe in Figure 2.13
$A_0$	Initial Cross-section area using mid-section dimension before test
$A_{\text{fmid}}$	Cross-section area using mid-section dimension after fracture
$\text{amp}_{\text{max}}$	Maximum amplitude of imperfection
2c	Crack length in circumferential direction in Figure 2.13
c	Material constant related to Armstrong-Fredrick non-linear kinematic hardening
$c_p$	Material constant representing true plastic strain ( $\varepsilon_p$ ) at the start of strain hardening or yield offset
$D_c$	Measure of damage state in CDM approach
D	Outer diameter of the pipe specimen
$d_1$	Distance between the surface of the base plate and the moment arm center
$d_2$	Distance between the application point of the jack load and moment arm center
e	Eccentricity of jack force ( $P_{\text{jack}}$ )
E	Modulus of elasticity of pipe material
k	Material constant describing the strain hardening behaviour of metal
L	Specimen length

$m$	Indication of internal pressure level i.e. $p_i/p_y$ ratio
$M_G$	Global moment
$M_L$	Local moment
$n$	Strain hardening exponent of Ramberg-Osgood Relation
$P$	Axial load applied to the top pivot of the pipe model
$P-\Delta$	Load-displacement
PEEQ	Equivalent plastic strain in ABAQUS post-processor
$p_i$	Applied internal pressure using water
$P_{cap}$	Cap force due to closed-end effect
$P_{jack}$	Force applied by off-centre loading jack
$P_{MTS}$	Axial load applied by the MTS testing machine
$p_y$	Internal pressure applied to the pipe such that the hoop stress reached to SMYS
$R_i$	Inside radius of the pipe specimen
SP1	Section point 1 representing the bottom surface of the shell
SP7	Section point 7 representing the top surface of the shell
$t$	Thickness of the pipe wall
$t_0$	Initial thickness of tension coupon at mid-section
$t_{mid}$	Thickness of tension coupon at mid-section after fracture
$u_1$	Displacement of the pipe model in global '1' axis
$u_2$	Displacement of the pipe model in global '2' axis
$u_3$	Displacement of the pipe model in global '3' axis
$V$	Transverse or shear load applied by a hydraulic jack

$w_0$	Initial width of tension coupon at mid-section
$w_{fmid}$	Width of tension coupon at mid-section after fracture
$Z$	Plastic sectional modulus or nominal plastic sectional modulus

### ***Greek Symbols***

$\alpha$	Parameter relating the yield strength of metal ( $\sigma_y$ ) with material constant k
$\alpha_{ij}$	Back-stress tensor
$\alpha_{ij}^{dev}$	Deviatoric part of the back-stress tensor
$d\alpha$	Increment of back-stress in uniaxial form
$\varepsilon_c$	Average strain on the compression side of the cross-section
$\varepsilon_{ij}$	Strain tensor
$\varepsilon_{ij}^p$	Plastic strain tensor
$\varepsilon_t$	Average strain on the tension side of the cross-section
$\varepsilon_t^{crit}$	Ultimate tensile strain capacity of the pipe wall or weldment
$\varepsilon_{tf}$	Factored tensile strain in the longitudinal or hoop direction
$\varepsilon_y$	Yield engineering strain
$\bar{\varepsilon}^p$	Equivalent plastic strain
$d\varepsilon^p$	Uniaxial true plastic strain increment or the equivalent plastic strain increment
$d\varepsilon_{ij}^p$	Incremental plastic strain
$\bar{\varepsilon}_c^p$	Critical equivalent plastic strain

$\epsilon_{nom}$	Nominal or engineering strain
$\epsilon_{ln}^{pl}$	True logarithmic plastic strain
$\epsilon_{ln}$	True logarithmic total strain
$\epsilon_p$	Plastic component of true strain
$\delta_{ij}$	Kronecker Delta
$\Delta$	Axial displacement or axial shortening or MTS stroke
$\Delta_C$	Axial displacement at which the plastic strain reaches the critical strain limit ( $\bar{\epsilon}_c^p$ )
$\Delta_i$	Axial displacement at which self-contact at the interior of the pipe wall is initiated
$\Delta_v$	Vertical distance above the foot of the wrinkle where the horizontal jack force is applied
$\Delta_h$	Lateral deflection of the pipe specimen after the application of jack force
$\sigma_{ij}$	Cauchy stress tensor
$\sigma_{nom}$	Nominal or engineering stress
$\sigma_y$	Yield strength of steel
$\sigma_{ys}$	Static yield stress or SMYS of pipe material
$\sigma_{ij}$	Cauchy stress tensor
$\sigma_{true}$	True stress
$\sigma_{v.m.}$	Uniaxial true stress or the von Mises stress
$\sigma_u$	Ultimate stress of material
$S_{ij}$	Deviatoric stress tensor

$\theta_1$	Rotation of the pipe model about global ‘1’ axis
$\theta_2$	Rotation of the pipe model about global ‘2’ axis
$\theta_3$	Rotation of the pipe model about global ‘3’ axis
$\theta_{avg}$	Locking Rotation, an average of top and bottom end rotations measured during testing or analysis
$\theta_{top}$	Rotation measured at top end of pipe specimen during test
$\theta_{bot}$	Rotation measured at bottom end of pipe specimen during test
$\varphi_G$	Global curvature
$\varphi_L$	Local curvature
$\phi_{\varepsilon_t}$	Resistance factor for tensile strain
$\eta^+$	Direction of normal indicating outer surface of the pipe specimen
$\eta^-$	Direction of normal indicating inner surface of the pipe specimen
$\lambda$	Half wavelength of axisymmetric pipe wrinkle or imperfection
$d\lambda$	Material constant based on incremental theory
$\pi$	Pi ( $\approx 3.141592$ )
$\gamma$	Material constants for Armstrong-Fredrick non-linear kinematic hardening
$\nu$	Poisson’s ratio

### ***Abbreviations***

API	American Petroleum Institute
CDM	Continuum damage mechanics

CSA	Canadian Standards Association
DAR	Damage accumulation rule
DNV	Det Norske Veritas
D/t	Outside diameter to thickness ratio
FEA	Finite element analyses
LCF	Low cycle fatigue
LVDT	Linear variable differential transducer
L/D	Length to outside diameter to thickness ratio
MTS	Material testing system
NPS	Nominal pipe size or diameter
NTSB	National Transportation Safety Board
RVDT	Rotational variable differential transformer
SP	Section Point
SMYS	Specified minimum yield strength

# 1. INTRODUCTION

## 1.1 Problem Statement

Unprecedented demand of hydrocarbons has pushed all the limits through increasing exploration and extraction activities even in the remotest regions of the world, especially Arctic and sub-Arctic regions of the Canadian North. Steel pipelines are the most efficient mode for transporting and distributing these resources from production field to the market place. In Canada alone, there is over 700,000 km of energy pipelines in operation (Yukon Government updated on March 27, 2006). A number of major onshore pipeline projects, such as the Mackenzie Gas Project worthing over \$16 billion, and the Alaska Highway Pipeline Project worthing over \$30 billion, will be underway in near future (Calgary Herald ; Fair Trade Info, cited on March 3, 2010). The majority of these onshore pipelines are buried pipelines. These pipelines, particularly buried in cold region, often subjected to a combination of large axial and bending deformations because of extreme geo-environmental effects, which may cause the pipes to buckle or wrinkle. Under continued presence of these effects, some of these buckling or wrinkling waves can grow rapidly, and, eventually, the pipes can undergo large inelastic deformations. In addition, the wrinkle formation process can be accelerated by the presence of geometric imperfections due to manufacturing tolerances, dents, corrosion, etc. The size of these wrinkles can substantially restrict product flow or prohibit the passage of intelligent in-line inspection tools required for proper maintenance, hence jeopardize the safe operation of the pipelines. Furthermore, the wrinkle deformations may be severe enough to cause fracture in the pipe wall. Consequently, the safety and integrity of the pipelines can become an issue.

In order to avoid undesirable accidents and environmental hazards through loss of containment, the pipeline operators usually dig up the deformed pipe and replace

the wrinkled portions, even though such remedial action can be very costly and may not always be necessary (Murray 1997; Das 2003). However, presently, there is no reliable measure to safe guard against leaks or fractures of these wrinkled pipes in terms limiting fracture strain values, critical fracture condition, and other related information within these wrinkles. A review of the current design codes and practices (American Petroleum Institute (API 5L) 2004; Canadian Standards Association (CSA Z662) 2007; Det Norske Veritas (DNV OS-F101) 2007) has revealed that design provisions as well as design philosophy can be overly conservative. Because prior research observations (Zhou and Murray 1993b; Zimmerman et al. 1995; Dinovitzer and Smith 1998; Das 2003) have indicated that pipes transporting energy are highly ductile and do not lose operational safety and structural integrity due to wrinkle formation.

Previous research observations have also indicated that occurrence of fractures in pipe wrinkle is rare for monotonically controlled deformation processes in the laboratory and the norm for the deformation configuration of these wrinkles is essentially axisymmetric (Das et al. 2002). Under the continued presence of these deformation processes, there will be stacking up of wrinkles developing an “accordion” configuration, as shown in Figure 1.1a, and conceptually, there will be no danger of fracture at the wrinkle location (Das 2003). A cyclic deformation/loading producing plastic strain reversals in wrinkle location is necessary to generate fracture in the wrinkled pipe, as can be seen from Figure 1.1b (Das et al. 2007a).

However, a recent field fracture was observed within the sharp fold of wrinkle in an NPS10 (10 inches nominal pipe diameter) energy pipe operated by WestCoast Energy Inc. in British Columbia, Canada, as shown in Figure 1.2a (Das et al. 2002). Field observations had indicated that there were no significant strain reversals in the wrinkled pipe segment. The final failure was a “tearing” failure resulting from monotonic application of an axial load not aligned with the axis of the pipe. In order to verify this failure mechanism and determine the characteristics contributing to its formation, a full-scale test applying axial load

and a shear load with appropriate boundary conditions was carried out on an NPS12 pipe (with a wall thickness of 6.84 mm and a grade of X52) at the University of Alberta (Das et al. 2002). A failure mode similar to the field was observed in the test, as can be seen from Figure 1.2b. Successful simulation of this behaviour in the laboratory has underscored the need for more rigorous investigation which seeks to answer some fundamental questions regarding this unique mode of failure and hence, to establish a failure criterion under telescopic tearing action.

## **1.2 Research Objectives, Scope, and Significance**

This research program is designed to develop the failure criteria to predict the onset of tearing fracture/failure of wrinkled steel pipe under variable loading conditions. The primary objective of this program is to provide a better understanding of this unique failure mechanism and, hence, to identify the key factors responsible for this failure mode. The analytical and experimental results obtained from this study are used to develop the failure criteria to predict the onset of this unique failure mode.

The scope of this research program consists of:

1. Preliminary investigation of the failed field and test specimens (Das et al. 2002), which includes developing a full-pipe finite element (FE) model to simulate the behaviour of the failed field and test specimens, for identifying the key factors responsible for tearing fracture and hence, proposing a preliminary tearing failure criterion;
2. Reanalyzing all the test results obtained from the full-scale ‘pipe wrinkling’ test program (Aydin 2007) to address the objectives of this research program;

3. Simulating the behaviour of all the tests (Aydin 2007) using the half-pipe FE model developed in this research program and, thus, providing confidence to use this numerical model for further investigation.
4. Developing failure criteria to predict the failure modes of all the test specimens included in this study and hence, demonstrating the acceptability of the proposed failure criteria;
5. Performing a parametric study using the calibrated numerical model on the key parameters identified in this research program and providing a specific range under which the tearing failure may/can exhibit.

The set objectives and goals identified for this research project, which once met, will provide a number of significant enhancements in safety, reliability and integrity management of current/future buried pipelines. In addition, this research program will definitely have a positive impact on the economic and environmental demands on the exploitation of oil and natural gas reserves in the arctic and sub-arctic regions of the Canadian north.

### **1.3 Research Approach**

To achieve the objectives and goals set for this research project, this research program was divided into four major phases. The methodology adopted during these phases is summarized herein.

As a first step, a proof of concept test was carried out by Das et al. (2002) to simulate the tearing fracture observed in the field. The test successfully simulated the field behaviour. The first phase was focused on understanding and simulating the complex behaviour observed in field and laboratory, and then, to propose a preliminary failure criterion responsible for this failure mode. In this phase, a nonlinear full-pipe finite element (FE) model was developed by the author using ABAQUS. Using this FE model, a detailed numerical investigation was carried out to verify and validate the test and field behaviour. Results of this phase has

identified the presence of ‘localized strain reversals’ even for monotonically applied load, as one of the key parameters for generating such tearing failure. (Based on the numerical results of this phase, a preliminary failure criterion was proposed).

As a second step towards providing more rigorous insight on this unique failure mechanism, a full-scale ‘pipe wrinkling’ test program was carried out (Aydin 2007) concurrent to this research project. Six full-scale tests in two different sizes of pipes and two different grades of pipes were undertaken in this experimental program. Results of this test program have indicated that the tearing failure can be one of the possible ultimate limit states of wrinkled pipes, and hence, provided motivation for the next phase. The second phase of this research work was to reanalyze all of the test results, and to perform detailed numerical validation of all the tests using the FE model developed in the first phase.

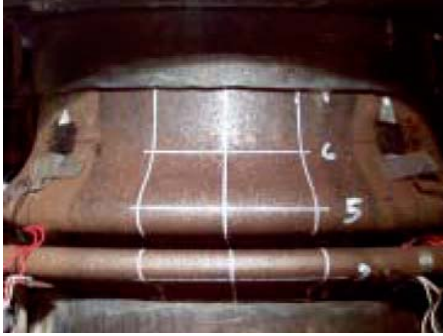
The third phase of this research was focused on developing the failure criteria to predict the tearing failure mode of wrinkled pipe. In this phase, a ‘Critical Strain Limit’ along with ‘strain reversal criterion’ were chosen as the failure criteria. Results of this phase have shown that the proposed failure criteria can predict the tearing mode with acceptable accuracy.

As the last component of this research project, a parametric study was designed and carried out to study the effects of different parameters on different failure modes of wrinkled pipe under monotonic loading. Results of this phase have indicated that some of the parameters can expedite the telescopic tearing action, whereas some can delay this failure mechanism.

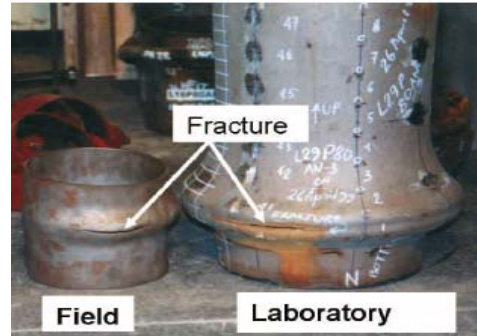
#### **1.4 Organization of Thesis**

The thesis is broken into five major chapters and two other small chapters: Chapter 1 – introduction and Chapter 7 – summary, conclusions, and recommendation. This thesis has been written using ‘Paper Format’ for the major chapters. Therefore, there will be some repetitions in this thesis, specifically in the

preamble of each major chapter. Chapter 2 summarizes the findings obtained from the literatures on the issues such as behaviour of wrinkled pipe, fracture or failure of pipe wrinkles, and current pipelines design guidelines and practices. Chapter 3 discusses the development of the numerical model of the full-scale pipe and also portrays the comparisons of behaviour obtained from experiments and numerical simulations. In this chapter, the key factors responsible for the tearing failure mechanism of wrinkled pipe are identified. Chapter 4 describes the full-scale test program and the results obtained from the tests. This chapter also includes a detailed discussion regarding the numerical verification of all the test results. In the next chapter, a double failure criterion is proposed to predict the onset of tearing failure mode under monotonic load–deformation. This chapter also deals with the demonstration of the acceptability of the failure criteria. In chapter 6, effect of different parameters on the failure modes of the wrinkled pipe is presented. This chapter also describes the range of parameters under which the tearing mechanism can/may exhibit.



(a)

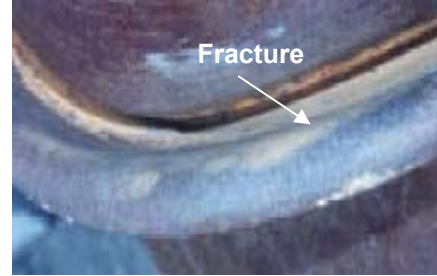


(b)

Figure 1.1 (a) Accordion type failure under monotonic loading (Das et al. 2002); and (b) fractures under cyclic deformation (Das et al. 2007c).



(a)



(b)

Figure 1.2 Pipe segment showing tearing fracture at wrinkle location obtained from (a) WestCoast Energy, and (b) Experimental work performed at University of Alberta (Das et al. 2002)

## **2. LITERATURE REVIEW**

### **2.1 General**

The objectives of this review are to cite literature that will help to built-up knowledge regarding all possible failure modes of onshore energy pipelines due to wrinkling in the pipe wall, and hence, to provide some necessary information to guide this research program. Emphasis has been given to better understand the tearing failure mode which is very unique and new failure mechanism that may challenge the northern pipeline operators in more frequent basis, as they are pushing more and more in the discontinuous permafrost regions of Canadian North. This review will cover brief discussion on several topics including geo-environmental loading, pipeline integrity, consequences of pipeline failures, history of onshore pipeline research, and different failure modes of wrinkled pipes.

### **2.2 Geo-Environmental Loading and Pipeline Integrity**

The design, construction and maintenance of northern pipelines are notably different from southern pipelines mainly due to the remoteness and environmental sensitivity of the region (Tanaka et al. 2009). Several successfully constructed and operated pipelines in northern Canada and Alaska cross geologically active or potentially active regions which can pose significant challenges to pipeline integrity (Morgan et al. 2004). These challenges will be even more, as the pipeline industry in North America has been actively advocating for major natural oil and gas pipeline development opportunities in Arctic and sub-Arctic regions. The presence of continuous or discontinuous permafrost in these regions can be critical for design, operation and maintenance of these pipelines (Oswell 2002).

The onshore steel pipelines, especially buried in discontinuous permafrost, often respond to thermal strains due to differential temperatures, stress cycles due to internal pressure condition, and/or geotechnical movement. Pipeline movement associated to geo-movement can be caused by factors such as slope instability, thaw settlements, frost heave, landslides, earthquakes, etc. (Oswell 2002). Field observations of buried pipelines have indicated that pipeline/ground movement due to geo-hazards along with or without thermal load can induce large forces and displacements on these pipelines resulting in localized curvature and strains in the pipe wall (Morgan et al. 2004). Often these local deformations result in local buckling known as pipe 'wrinkling'. During its post-wrinkling response, these local buckles or wrinkles can grow under sustained deformations. These wrinkles usually form under the combination of internal pressure and axial load with or without bending deformation (Yoosef-Ghodsi et al. 1995). The shape of these wrinkles can be nearly axisymmetric (see Figure 2.1a) under the presence of internal pressure and axial deformation. Whereas, the shape of these wrinkles may become non-axisymmetric (see Figure 2.1b), due to the presence of shear and/or bending deformation (Das et al. 2008). Therefore, a wrinkled pipeline may then be subjected to various load combinations and load hysteresis including monotonically increasing deformations, and/or cyclic axisymmetric or non-axisymmetric deformations, etc. The behavioural characteristics one may expect from a wrinkle, such as possible fracture or benign deformation, will depend on the driving mechanism associated with the wrinkle deformation and the continued presence of the driving mechanism. Consequently, there is possibility of a fracture or rupture at pipe wrinkle, jeopardizing the safe operations of the field pipelines and hence, causing environmental hazard.

Figure 2.2 illustrates the schematic view of some of the geo-hazards commonly observed in Northern environment. For pipeline routed in geologically unstable slopes, as shown in Figure 2.2a, external loading caused by pipe interacting with a moving soil mass can pose threat to the integrity on the buried pipeline (Martens et al. 2009). A large soil mass moving along the slip/sliding plane can induce significant displacement or strain to the pipeline. This displacement controlled

loading process is monotonic in nature. A number of existing pipelines located in Horseshoe Canyon Formations in central Alberta, known for slope stability problems, can have issues with pipeline integrity (Martens et al. 2009). The buried pipeline operated by Enbridge Pipelines Inc., transmitting crude oil from Norman wells, Northwest Territories to Zama, Alberta, has faced similar geo-hazard challenges (Wilkie et al. 2001). This route runs through regions of discontinuous permafrost. A schematic showing the effect of discontinuous permafrost on a buried pipeline is presented in Figure 2.2b. Slope stability was a concern for a segment of this pipeline running through a region known as Slope 92 (Wilkie et al. 2001). Several incidents of pipe wrinkle were reported and one of them is presented in Figure 2.3.

In order to maintain adequate safety and integrity and to minimize the environmental impact, the pipeline industry have shown increasing interest to use the chilled pipelines for transporting natural oil and gas from northern energy fields (Tanaka et al. 2009). The primary purpose of a chilled gas pipeline is to prevent thawing of permafrost through which the pipeline traverses. Similar approach was adopted for the Norman Wells-Zama pipelines, where the crude oil with a pour point of  $-30^{\circ}\text{C}$  was chilled for the most northern section and could be pumped even in the surrounding ground temperatures of the pipeline of  $-8^{\circ}\text{C}$  (Wilkie et al. 2001). Although this concept is preventing the thawing of frozen ground, a new problem can arise with freezing of unfrozen susceptible soil, thus causing frost heave, as shown in Figure 2.2c. Frost heave could have a serious impact on a cold buried pipeline. As the ground around the pipe freezes with time, wet soils could freeze and expand and lift or laterally deflect the pipe (Tart Jr. 2007). Since frost heaving is usually a perennial event, the load-deformation mechanism is more cyclic in nature. However, frost heave has limited impact on a buried warm pipeline because seasonal freezing rarely occurs below a warm pipe and all the soils in contact with a warm pipe are usually thawed.

Thaw settlement is another well-known geo-hazard for a pipeline passing through regions of continuous and discontinuous ice-rich permafrost (Tart Jr. 2007). This

can be a result of the thawing of ice layers or ice-rich strata through seasonal air temperature changes, warming from heated structures e.g. buried pipelines, and/or removal of insulating vegetation. Due to thawing of ice-rich region, the soil in thaw-unstable regions can settle while that in adjacent thaw stable regions may retain its original configuration, as shown in Figure 2.2d (Murray 1997). This discontinuity in the support of the pipe at the transition zone of a thaw-stable and thaw-unstable region can induce significant axial as well as bending deformation to the pipe wall. The process of thaw settlement usually occurs very slowly and monotonically and may continue over several years until it reaches a large magnitude, thus posing a threat to pipeline integrity.

### **2.3 Consequences of Pipeline Failure Incidents**

The risk factors associated with the loss of containment of an energy pipeline can be significant, as it can involve not only environmental hazards but also public safety. Recent documentation has cited the staggering costs of pipeline failures. The legal cost associated with one fatality on a recent failure was \$280 million (Koch et al. 2002). Property damage costs for liquid and natural gas transmission pipelines from 1994-1999 totalled \$279 million. This section includes some of the pipeline failures reported in recent years to provide a broader spectrum regarding the type of failure modes as well as the consequences of these failures.

#### ***2.3.1 Morgan Falls Landfill***

The failure of a 40 inch (1016 mm) diameter steel pipeline with leakages was discovered on March, 1998 at Morgan Falls Landfill, Sandy Springs, Georgia, USA (NTSB 1999). This pipeline was operated by Colonial Pipeline Company to transmit refined petroleum products. The cleanup cost associated to this failure incident was over \$3.2 million. A significant reduction of line pressure (2.65 MPa) was observed at site of failure. After excavating the failed pipeline, a pipe wrinkle (buckle) was observed at the compression side of the pipe (see Figure

2.4a). Visual examination of the cut segment (about 3m long) obtained from the field also revealed the presence of circumferential and longitudinal cracks, in some instances through-thickness cracks, at the outer surface of the pipe (see Figure 2.4b). No damage such as dents, gouges, or corrosion was reported in the area of these cracks. Crack arrest marks were also noticed within this region indicating the propagation of cracks in several phases over time. Cracking in the pipe was consistent with stress damage due to soil settlement beneath the pipe.

### ***2.3.2 Winchester, Kentucky***

A 24 inch (610 mm) diameter pipeline operated by Marathon Ashland Pipe Line experienced a rupture in January 2000 near Winchester, Kentucky, USA (NTSB 2001). Approximately 11,644 barrels of crude oil were released from the pipeline as a result of this rupture. Marathon Ashland had to spend over \$7.1 million in response to the accident. At the rupture location, the pipeline ran through a layer of shale and rested on Styrofoam pillows to prevent direct contact between shale and pipe. An earlier inspection through the entire pipeline, conducted in 1997 using inline inspection tool, had showed an anomaly at the rupture site. This anomaly was interpreted as a dent in the pipe wall. However, the reported dent was not considered as significant and therefore, no measure was taken for repair. The rupture was found on the bottom of the pipe, as shown in Figure 2.5. Post-accident laboratory examination of the pipe showed transgranular cracks with appearance typical of fatigue progression. Primary and secondary origin areas of fatigue cracking were found at the edges of a dent in the pipe wall. The dent was consistent with contact with a hard object, although no hard object (such as a rock) was found during the investigation. The probable cause of the accident was fatigue cracking due to the presence of a dent in combination with fluctuating pressures within the pipe, producing high localized stress cycles in the pipe wall.

### **2.3.3 *Prince George's County***

A failure incident in an oil pipeline system was reported on April 2000 at the Chalk Point generating station in south-eastern Prince George's County, Maryland, USA (NTSB 2002). The failed pipe was 12.75 inch (323 mm) in diameter with a wall thickness of 0.203 inch (5.15 mm) and American Petroleum Institute (API) 5L grade X42 or X52 steel pipes. Approximately 140,400 gallons of fuel oil were released into the surrounding wetlands, creek and river due to this loss of containment. The consequence of this failure incident was significant, involving cost of over \$71 million for environmental responses and clean-up operations. The laboratory observation of the cut segment (about 53 in or 1.35 m long) of the failed pipe indicated that the pipe was considerably bent with an outward-protruding wrinkle on the inside radius or compression side of the bend (see Figure 2.6a). The angle of the bend at wrinkle location was found to be in the range of 5~6 degrees. Notable cross-sectional distortion or ovalization was also reported. An open crack with a length of approximately 6 in (165 mm) and width of 0.374 in (9.5 mm) was observed at the crest of the buckle or wrinkle (see Figure 2.6b). Microscopic examination indicated that there was no external corrosion present on the failed pipe segment. The interior surface of the pipe in the location of wrinkle crest contained a number of shallow secondary cracks. All the cracks were circumferentially oriented, confined to the permanently deformed area of the pipe, had blunt tips, and were filled with corrosion products. Some of these cracks exhibited slight branching. Laboratory observations also indicated that the appearance of these cracks was typical of corrosion fatigue cracking in low carbon steels, resulting from exposure to high stress amplitudes.

## **2.4 History of Pipeline Research in Wrinkling**

The subjects of onset of pipe buckling/wrinkling and post-wrinkling behaviour, or in other words structural stability and performance of steel pipes, have dominated the research of buried onshore pipelines over the past few decades. The topics covered the structural behaviour of pipeline including the buckling resistance of

pipes, the critical buckling strain, and the ultimate rupture/fracture of pipes. The parameters investigated included different loading combinations, which included axial load or deformation, bending moment or curvature, shear force or lateral deflection, variable internal pressure condition; pipe geometry (outside diameter to thickness or  $D/t$  ratio), pipe material, and the presence of girth weld in the buckled region.

Majority of these researches were focused on understanding the behaviour related to initiation and formation of wrinkles under monotonic load-deformation conditions that buried pipelines experience in the field (Bouwkamp and Stephen 1973; Bushnell 1981; Bushnell 1984; Gresnigt 1986; Mohareb et al. 1993; Dorey et al. 2001). Consequently, most of the current pipeline design standards and practices recommend various limit state design methods for energy pipelines based on noticeable cross-sectional deformation and formation of local buckling/wrinkling corresponding to the critical buckling strain limit ranging from 0.5% to 2.0% (American Petroleum Institute (API 5L) 2004; Canadian Standards Association (CSA Z662) 2007; Det Norske Veritas (DNV OS-F101) 2007). Because of limited knowledge on the post-wrinkling behaviour of pipelines, the present practice of the pipeline operators is to dig up the deformed pipe and replace the wrinkled portions in order to minimize the risk of any undesirable accident and environmental hazards due to pipe rupture. However, prior research observations on the post-wrinkling behaviour (Zhou and Murray 1993b; Zimmerman et al. 1995; Dinovitzer and Smith 1998; Das 2003) have indicated that current design provisions as well as design philosophy can be overly conservative, as the occurrence of buckling or wrinkling does not necessarily affect the safety and integrity of pipelines if the pipes possess sufficient ductility against fracture. Consequently, recommendations have also been made to relax the current pipeline limit state design approaches (Murray 1997; Das 2003). All pipe segments tested at the University of Alberta (Mohareb et al. 1993; Zhou and Murray 1993a; Yoosef-Ghodsi et al. 1995; Murray 1997; Mohareb et al. 2001; Myrholm 2001; Das et al. 2002; Das 2003; Dorey et al. 2001; Dorey et al. 2006) developed large deformations localized in a single wrinkle or multiple wrinkles

without loss of containment. Researchers elsewhere have drawn the same conclusion (Bouwkamp and Stephen 1973; Schneider 1998).

Wilkie et al. (2001) had documented a case study involving the diagnosis and exposure of a wrinkle in a NPS 12 pipe (305 mm or 12 in. nominal diameter) at Norman Wells-Zama Pipeline, located in the Mackenzie valley of the Northwest Territory of Canada, operated by Enbridge Pipeline Inc. According to the current design and maintenance practices, the pipeline operation was shut down and the wrinkled portion of the pipeline was dug out and replaced to avoid any probable environmental disaster and safety hazard. This repair operation resulted in considerable loss of revenue and interruption of pipeline operation for several days. This repair could have been delayed or even avoided if there was a clear direction regarding the post-wrinkling behaviour of field pipeline. Therefore, there is a great demand among the pipeline industries for a rationale design procedure addressing the remaining capacity of the wrinkled pipe without compromising the pipeline safety and integrity. In order to exploit the pipe capacity with high utilization of the pipe material (advocating strain-based design) as well as to have a safe design, it is utmost important to have a clear understanding of all possible failure modes of wrinkled pipe under variable load conditions.

## **2.5 Failure Modes of Wrinkled Pipe**

A wrinkled pipeline may be subjected to various load combinations and load hysteresis such as: monotonically increasing axial (axisymmetric), bending (nonaxisymmetric), and/or shear deformations; cyclic axisymmetric or nonaxisymmetric deformations (Zhang and Das 2008b). However, there are two principal fracture limit states for a wrinkled pipe — 'low cycle fatigue (LCF)' mode under cyclic load-deformation and 'tearing' failure mode caused by very large deformation and/or curvature applied monotonically. Under monotonic load/deformation, there is another possible failure mode known as 'Accordion' failure mode where there will be no fracture. However, the excessive cross-

sectional deformation associated to this failure mode can threaten the movement of inspection and cleaning tools (e.g. geopig), thus, hindering the operation of a field pipeline (Das et al. 2008).

### ***2.5.1 Low Cycle Fatigue***

Buried pipeline can undergo cyclic load/deformation process during its service life. Cyclic load/deformations are due to temperature variation, cyclic freezing and thawing of ground, fluctuations of operating pressure, and the seismic movement if the pipe line is routed in seismic regions (Das et al. 2002; Oswell 2002; Palmer and Williams 2003; Oswell et al. 2005; Tart Jr. 2007). Recent studies at University of Alberta and elsewhere (Das et al. 2001; Myrholm 2001; Das et al. 2007a; Das et al. 2007b; Das et al. 2008) have shown that a wrinkled pipeline can be susceptible to fracture if subjected to cyclic load/deformation history. The cyclic deformation can be involved with either axial or bending deformation. This loading process can generate a hysteresis of plastic strain reversals in the vicinity of wrinkle, thus leading to a fracture. Under cyclic axial deformation, the deformed shape is axisymmetric or bulge type, and the fracture can be triggered along the crest of the wrinkle, as shown in Figure 2.7 (Das et al. 2007a). The failed field specimen obtained from Gold Creek gas pipeline in northern Alberta operated by WasCana Energy Inc. has shown similar deformed shape with the presence of fracture at wrinkle crest (Das et al. 2007a). Under cyclic bending deformation, the deformed shape will be non-axisymmetric (see Figure 2.8) and the fracture can trigger at the wrinkle crest located at the compression side of the pipe (Das et al. 2008). Similar failure mode was observed for a failed field specimen obtained from an NPS12 oil pipeline in south-eastern Prince George's County, Maryland, USA, as shown in Figure 2.6b (NTSB 2002). The number of cycles required to generate this fracture in the laboratory (Das 2003; Das et al. 2007a; Das et al. 2007b) are very low, ranging from 4 to 9 cycles. This indicates that the remaining life of a wrinkled pipe can be significantly reduced if it is subjected to cyclic loading. Using all the LCF test results

conducted at University of Alberta (Myrholm 2001; Das 2003), an extensive research program is being carried out by Zhang (Zhang 2010) to develop models to predict the LCF lives of wrinkled pipe. Results of Zhang's work (Zhang 2010) have shown that the proposed accumulated damage models predict the remaining life of a wrinkled pipe with reasonable accuracy.

### **2.5.2 *Accordion Wrinkles***

Recent research observations have indicated (Das et al. 2002; Zhang and Das 2008b) that the occurrence of fractures in pipe wrinkle is rare for monotonically controlled deformation processes in a laboratory environment and the shape of these wrinkles is essentially axisymmetric (see Figure 2.1a). Under the presence of continued deformation, the half-wave length of the wrinkle decreases as a result of the deformation until the interior surfaces of the wrinkle come into contact and the wrinkle “closes”, as shown in Figure 2.9. At this stage the force in the pipe wall bypasses the wrinkle by following the path formed by the direct contact of the inner surface at the ends of the wrinkle. Therefore, a second wrinkle may develop adjacent to the first and the process may be repeated while the fold of the second wrinkle develops (see Figure 2.10). Conceptually, this may lead to stacking of wrinkles, i.e. accordion wrinkles, and there will not have a danger of fracture at the wrinkle location.

This phenomenon can also be explained using the load-displacement (P- $\Delta$ ) response obtained from the test of an NPS12 pipe with an wall thickness of 6.84 mm and X52 grade of steel with specified minimum yield strength (SMYS) of 358 MPa (Das 2003; Zhang and Das 2008a). As can be seen from the P- $\Delta$  plot in Figure 2.11, the pipe specimen was yielded at Point 'Y' and reached its maximum load carrying capacity or limit point at Point 'H1'. At point 'H1', the wrinkle became visible, and under continued displacement, the pipe specimen started to soften. Thus, the amplitude of the wrinkle increased significantly and the load carrying capacity decreased rapidly until Point 'L1' (see Figure 2.11). At this point, some part of the pipe interior at wrinkle location came into contact (i.e.

wrinkle closure occurred) providing a direct load path. The load path then bypasses the bends in the wrinkle. Consequently, the pipe capacity started to pick up again as indicated by load path 'L1-H2' of Figure 2.11. The test was then continued by applying more axial displacement. The test specimen then reached its second limit point 'H2'. At this point, the second wrinkle was formed and came in contact at the inside surfaces of the wall at point 'L2'. The two wrinkles then formed a shape that looks like an 'accordion of wrinkles'. After closing of 2nd wrinkle, the test was discontinued. During the test, no rupture or fracture was observed. Therefore, it can be said that the pipe specimen can exhibit extreme ductility under large deformation applied monotonically and is able to maintain its integrity even after formation of multiple wrinkles. In this research program for both experiment (Aydin 2007) and FE model, it is assumed that when the load carrying capacity of pipe specimen (see load path 'L1-H2' in Figure 2.11) starts to increase significantly after the formation of first wrinkle, the 'Accordion' failure mode does exist.

### ***2.5.3 Telescopic Tearing***

As mentioned before, the occurrence of fractures in pipe wrinkle is rare for monotonically controlled deformation processes (Das et al. 2002). However, a recent field fracture was observed within the fold of a wrinkle in an NPS10 (10 inches or 254 mm nominal pipe diameter) energy pipe operated by WestCoast Energy Inc. in British Columbia, Canada (see Figure 1.2a) (Das et al. 2002). Field observations had indicated that the final failure was a "tearing" failure resulting from monotonic application of an axial load not aligned with the axis of the pipe. The initial bulging wrinkle of the field sample occurred at an unpressurized location, and had been squashed to the point that the wrinkle became essentially flat, so that its interior surfaces came into contact over most of the extent of the wrinkle. This was followed by a deformation where one side of the top segment of the pipe slipped inside the bottom segment in a 'telescoping' manner. In so

doing it created a fold in the pipe wall and the tear in the pipe wall occurred at the sharpest bend within this fold.

In order to verify this failure mechanism and determine the characteristics contributing to its formation, a proof of concept test was carried out at University of Alberta (Das et al. 2002). The full-scale proof of concept test was carried out on an NPS12 pipe with a wall thickness of 6.84 mm and a grade of X52 by applying axial load and a shear load with appropriate boundary conditions. A deformation configuration similar to the field specimen was observed during the test, as can be seen from Figure 2.12. Similar to the failed field specimen, a tearing in the pipe wall at the sharpest bend of the wrinkle fold was observed during the test (see Figure 1.2). It was also reported that there was no fracture at the crest of wrinkle. Similar failure phenomenon was observed by Bouwkamp et al. (1973). They fractured large diameter pipes (1219 mm diameter) with wall thickness of 11.73 mm wall by applying very large curvatures. According to their observation, the failure mode was the tearing shear failure of pipe wall (Bouwkamp and Stephen 1973). Successful simulation of this behaviour in the laboratory has underscored the need for more rigorous investigation which seeks to answer fundamental questions regarding this unique failure mode.

Being motivated from the results of the proof of concept test, the first phase of this research program is objected to understand and simulate the test behaviour numerically and hence, to establish a preliminary failure criterion. A detailed discussion including loading and boundary conditions as well as load-deformation behaviour of this test is included in Chapter 3. However, results obtained from the proof of concept test (Das et al. 2002) were very much constrained to the load-displacement (P- $\Delta$ ) plot and the final deformed shape of the failed specimens. No detailed information was documented regarding the dimensions of the pipe wrinkle formed in the full-scale test or in the field. Therefore, more detailed investigation was beyond the scope of that test program. In order to provide a complete understanding of the tearing failure mechanism as well as to establish

the failure criteria in terms of limiting strain values to predict the existence of this failure mode, more rigorous investigation was felt necessary.

A full-scale 'pipe wrinkling' experimental program were carried out on NPS16 (16 in. or 406.4 mm nominal pipe diameter) and NPS20 (20 in. or 508 mm nominal pipe diameter) specimens with two different pipe materials under sustained axial deformation with constant curvature (Aydin 2007). It has been a challenge to generate the tearing fracture in the laboratory controlled environment. The loading procedure involving a constant curvature under monotonically increasing axial deformation to generate the desirable deformation configuration suitable for telescoping tearing did require significant effort and understanding. To date, only the University of Alberta pipeline research group has focused its research on this problem, and the loading procedure adopted herein is unique, and never applied before elsewhere. A detailed discussion of this test program (Aydin 2007) is included in Chapter 4. Results of this test program have indicated that the pipe specimens had exhibited very ductile behaviour with significant plastic deformation. However, the presence of several circumferential cracks in test specimens was reported (Aydin 2007), and a significant fracture in the pipe wall was observed at the wrinkle fold of one of the NPS16 specimens. The occurrence of this fracture has confirmed the observations of the initial experimental work (Das et al. 2002). Results of all these experimental programs have recognized that the tearing failure can be one of the possible ultimate limit states of wrinkled pipes. Although the safety and the integrity of wrinkled pipes may not be a problem for line pipes with good ductility under normal service conditions, the tearing type failure can happen under significantly large curvature and/or axial deformation. Therefore, it is necessary to conduct a rigours research program to address the existence of this failure mode and hence, to provide a better understanding of this failure mechanism.

## 2.6 Ductile Fracture of Steel

According to current design codes and practices for designing energy pipelines (American Petroleum Institute (API) 2004; Canadian Standards Association (CSA) 2007; Det Norske Veritas (DNV) 2007), limit states fall into two categories: ultimate limit states and serviceability limit states. Ultimate limit states refer to burst or collapse of pipe including rupture, yielding due to primary loads (internal pressure, self-weight of line pipe and its content, soil over burden, external hydrostatic pressure, and buoyancy), buckling resulting collapse or rupture (e.g. hydrostatic collapse, unstable local buckling, some upheaval buckling modes). Whereas, serviceability limit states refer to the state that restricts normal operation or affect durability.

The focus of this research program is the ultimate limit states of wrinkled pipe under monotonic loading. The primary objective is to develop a failure criterion to predict the tearing failure mode of wrinkled pipe. It is relevant to add that a new clause has been included in the latest edition of oil and gas pipeline systems (Canadian Standards Association (CSA) 2007). A new minimum longitudinal tensile strain requirement is being included in this clause (reference: clause C.6.3) to prevent membrane rupture. The minimum strain requirement is given as:

$$2.1) \quad \phi_{\varepsilon_t} \varepsilon_t^{crit} \geq \varepsilon_{tf}$$

where,  $\phi_{\varepsilon_t}$  refers to resistance factor for tensile strain,  $\varepsilon_t^{crit}$  refers to ultimate tensile strain capacity of the pipe wall or weldment, and  $\varepsilon_{tf}$  refers to factored tensile strain in the longitudinal or hoop direction.

Several provisions are given in (Canadian Standards Association (CSA) 2007) to compute the ultimate tensile strain capacity of the pipe wall or weldment ( $\varepsilon_t^{crit}$ ). This strain capacity in this clause is limited to the presence of surface-breaking defects and/or buried defects, as shown in Figure 2.13. However, the failure criteria developed /established in this research work is dealing with the ultimate

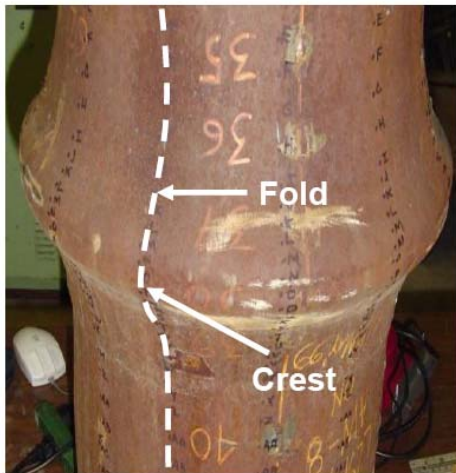
capacity of the plain pipe relating to ductile fracture of steel under monotonic quasi-static loading. The constitutive model by Khoo (2000) is utilized to develop the failure criteria for this study.

Ductile fracture is a result of microvoid coalescence, as shown in Figure 2.14. Microvoids within a metal start to nucleate at a certain stage of deformation, and then, these voids can grow and coalesce. Rupture can initiate as these void join together to create a macro crack. This classical phenomenon is investigated physically by a number of researchers during 1960's and 1970's (McClintock 1968; Rice and Tracey 1969; Hancock and Mackenzie 1976). There are several approaches available to model ductile fracture based on the observation of physical tests. These approaches utilize different parameters (including the critical damage state in a continuum damage mechanics model, the critical void fraction, the critical void growth rate, the absorbed energy till fracture or other parameters that are integrated over the plastic strain, etc.) as the measure of fracture.

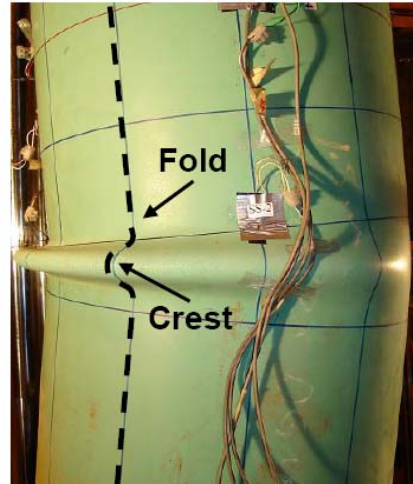
One of these approaches (Gillemot 1976; Matic et al. 1987) used the absorbed (critical) strain energy density till fracture as a measure of the fracture toughness. In this model, the fracture can occur when the material is assumed to absorb a critical strain energy density. Void volume fraction criteria (Gurson 1977) is another available constitutive model which takes into account the nucleation and growth of voids in ductile fracture. In this model, there is a volume change associated with plastic deformation as a result of void growth. This approach utilizes parameters such as the critical void fraction and/or the critical void growth rate as a measure of fracture.

Another popular approach is to use continuum damage mechanics (CDM) to model ductile fracture (Lemaitre 1984; Lemaitre 1985). In this model, the effect of void and crack formation is reflected in parameter  $D$ , which is a measure of damage state. In general, values of  $D$  range between 0 and 1, where 0 represents no damage, and 1 signifies complete damage (Bhattacharya and Ellingwood 1998). Local rupture occurs when  $D$  attains a critical value. The constitutive

model developed by Khoo (2000) has utilized the concept of CDM and incorporated material dilation to predict ductile fracture of steel. In this model, damage was assumed to be isotropic, and was a function of the state of stress and the plastic strain increment. Parameters used in this model are calibrated with data obtained from tension coupon tests. In this research program, similar approach along with some simplification is adopted to predict the tearing fracture of wrinkled pipe. It is assumed that the tearing fracture will initiate as the equivalent plastic strain ( $\varepsilon^p$ ) reaches a critical strain limit,  $\bar{\varepsilon}_c^p$ . Application of this plastic strain ( $\bar{\varepsilon}_c^p$ ) value as a fracture limit was adopted successfully by a number of researchers (Cheng et al. 1998; Martinez-Saucedo et al. 2006; Zhao et al. 2009) in the FE analyse of round slotted hollow steel sections (HSS). This critical plastic strain ( $\bar{\varepsilon}_c^p$ ) value corresponds to a point well beyond the peak load and the initiation of necking of a tensile coupon tests, but before the complete fracture of those test coupons (Cheng et al. 1998). In this approach, it is assumed that fracture has initiated in advance of the complete fracture, and  $\bar{\varepsilon}_c^p$  represents the limit at which the onset of fracture will occur. A detail discussion regarding the approach adopted herein is presented in Chapter 5.

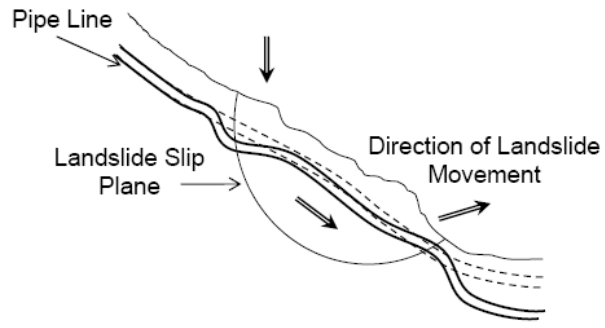


(a) Axisymmetric

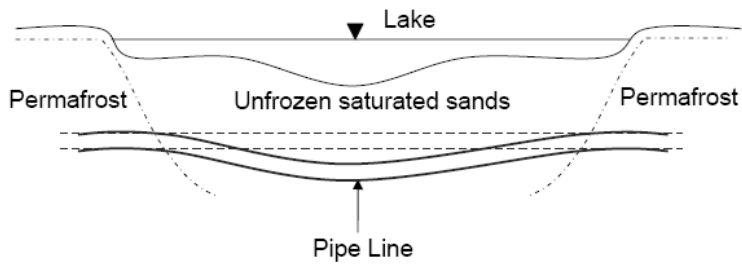


(b) Non-axisymmetric

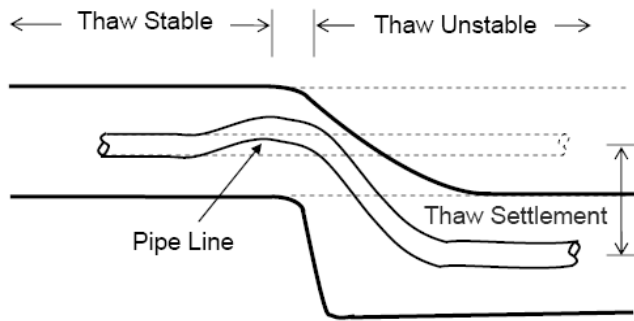
Figure 2.1 Typical Wrinkle Shapes (Das 2003; Aydin 2007)



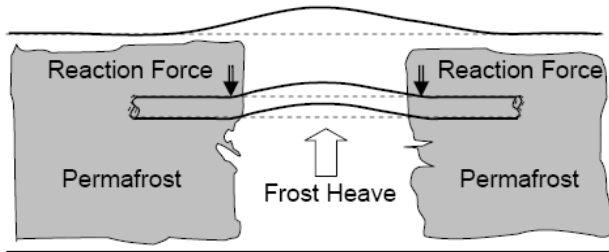
(a) Slope Instability



(b) Discontinuous Permafrost



(c) Thaw Settlement



(d) Frost Heave

Figure 2.2 Schematic views showing different geo-hazards on pipelines buried in cold environments (Murray 1997; Tart Jr. 2007; Martens et al. 2009; Tanaka et al. 2009)

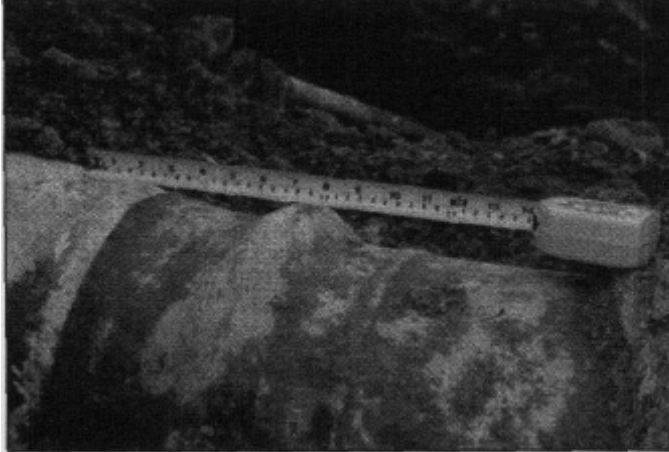


Figure 2.3 Exposed wrinkle of Norman wells pipeline at Slope 92 (Wilkie et al. 2001)



Figure 2.4 (a) Wrinkle (buckle) in a 40 inch diameter steel pipe with (b) close-up view of wrinkled pipe showing through-the-wall cracks (NTSB 1999)

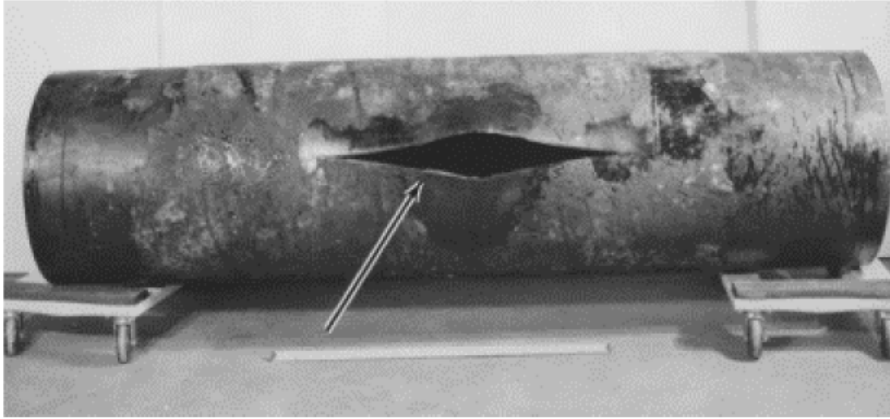


Figure 2.5 Rupture of an energy pipe due to presence of dent along with operating pressure fluctuations (NTSB 2001)



(a)



(b)

Figure 2.6 (a) Wrinkle or buckle location in the failed pipe, (b) Presence of significant crack at the wrinkle crest (NTSB 2002)

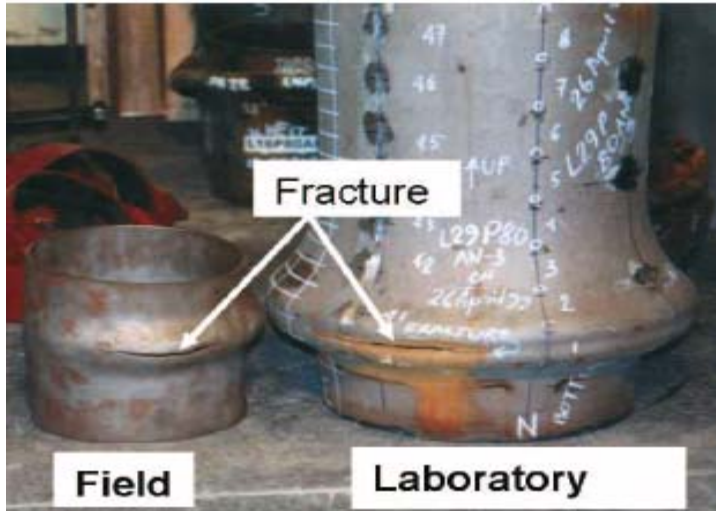


Figure 2.7 Fracture of wrinkled pipe under cyclic axial loading (Das et al. 2007a)



Figure 2.8 Non-axisymmetric wrinkles under bending deformation (Das et al. 2008)

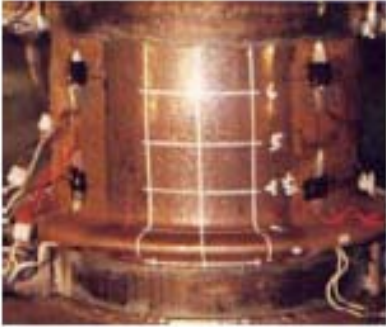


Figure 2.9 Deformed shape after closing of 1<sup>st</sup> wrinkle under monotonic loading (Zhang et al. 2008a)

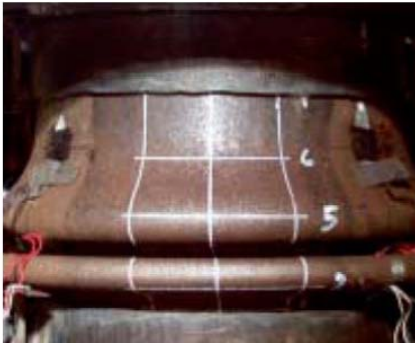


Figure 2.10 Accordion type of failure under monotonic loading (Das et al. 2002)

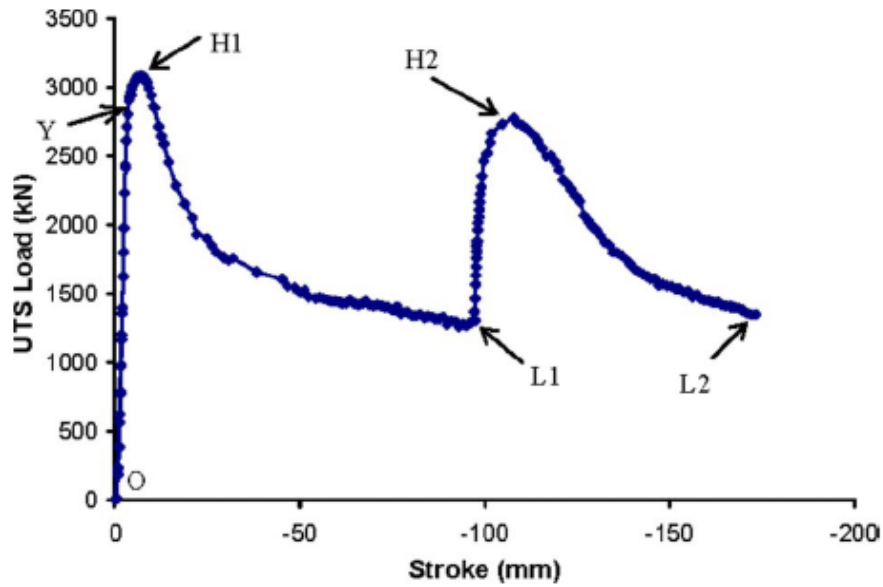


Figure 2.11 Load-displacement response of an NPS12 pipe under monotonic deformation (Das 2003; Zhang and Das 2008a)

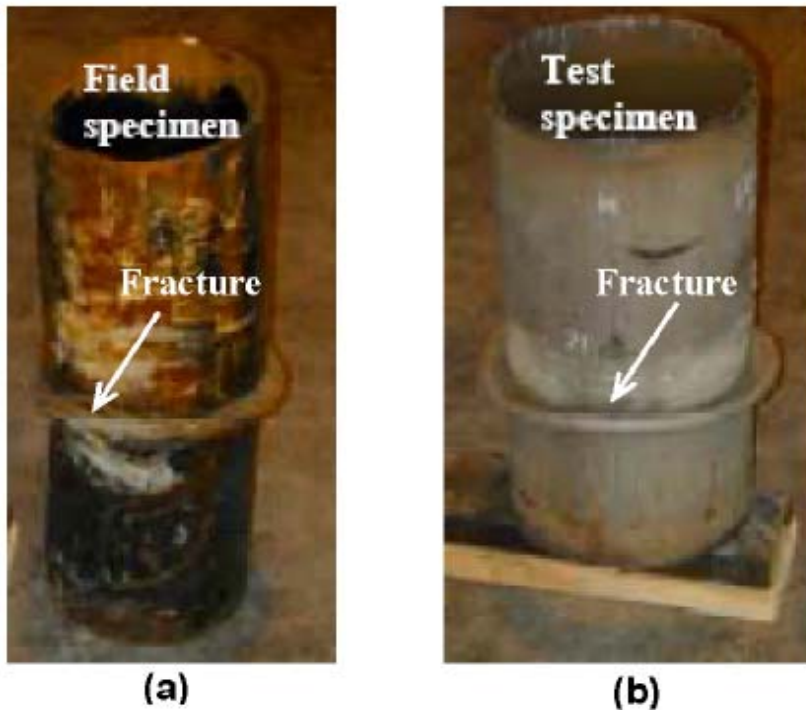


Figure 2.12 Final deformed shapes of the specimens obtained from (a) the WestCoast Energy Inc. and (b) the test (Das et al. 2002)

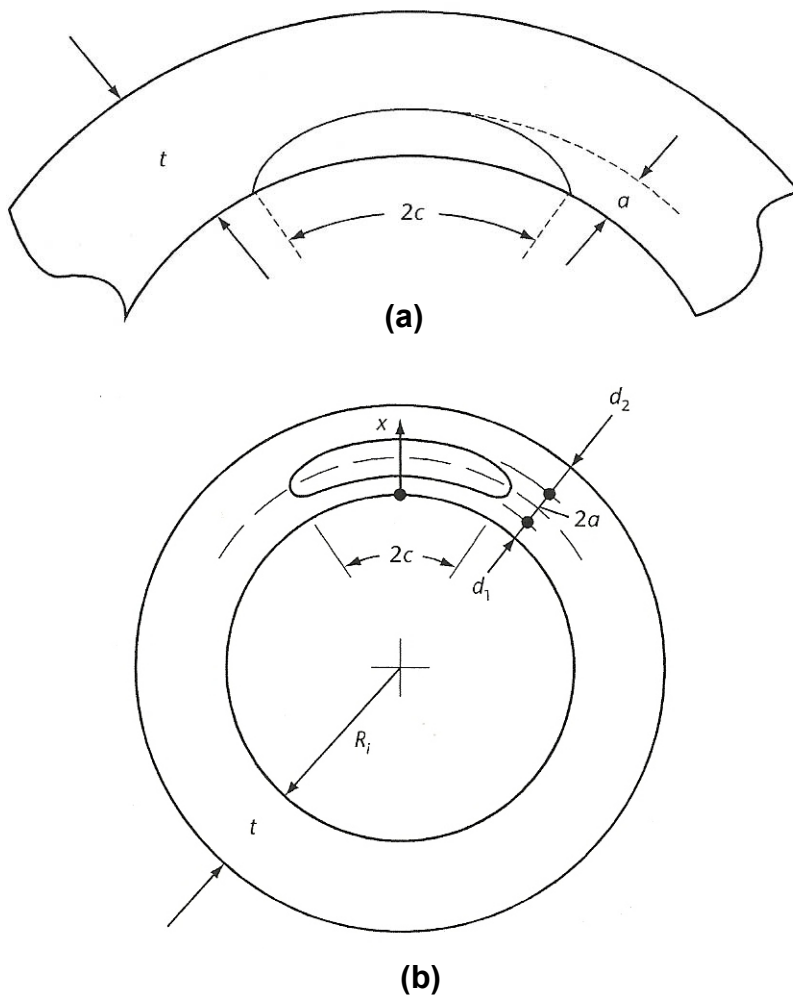


Figure 2.13 Schematic of (a) surface-breaking, and (b) buried defects in the pipe wall (Canadian Standards Association (CSA) 2007)

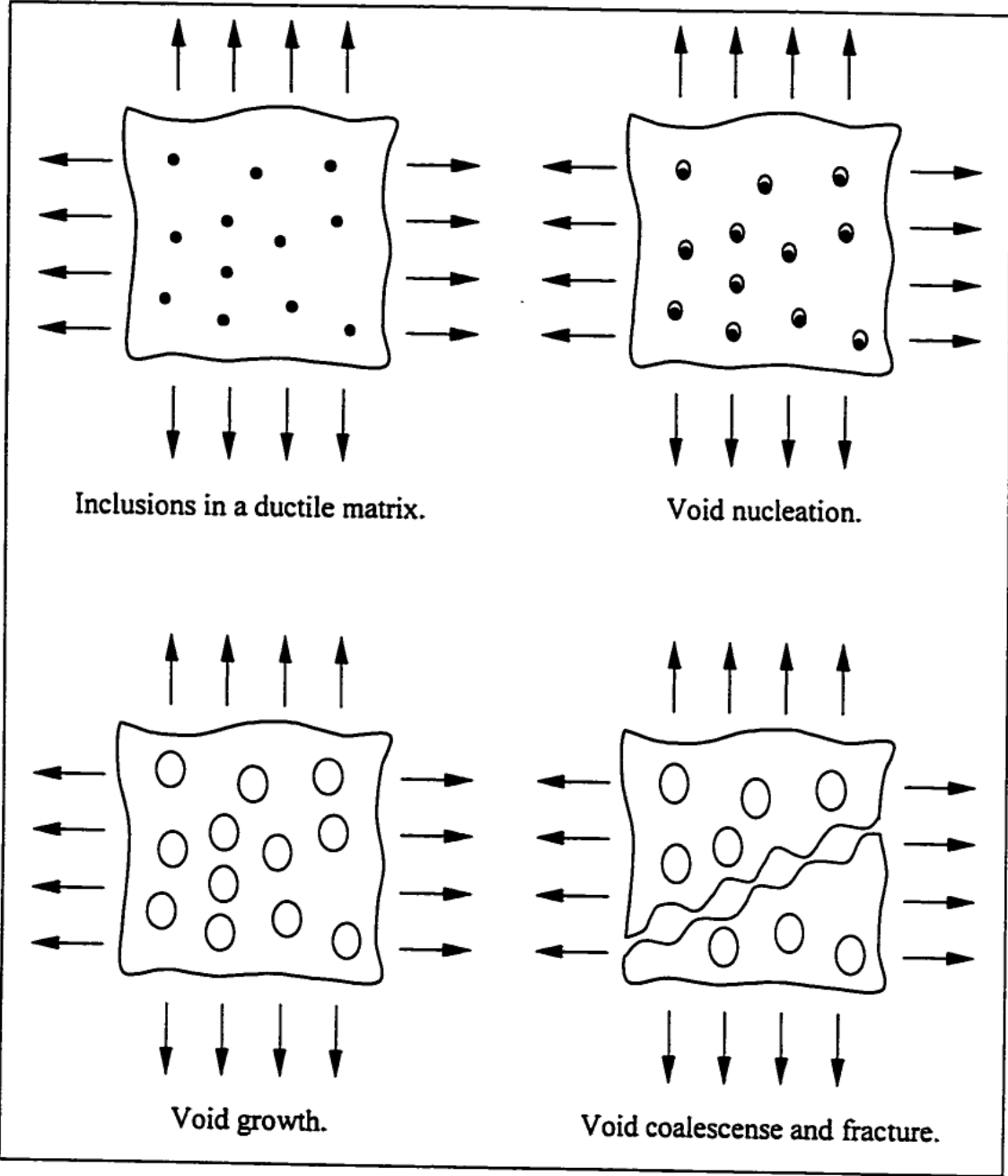


Figure 2.14 Mechanism of ductile fracture in metal (Khoo 2000)

## 2.7 References

- American Petroleum Institute (API). 2004. Specification for line pipe. API 5L, American Petroleum Institute, Washington, D.C.
- Aydin, M. 2007. Tearing fracture of energy pipelines under monotonic loading conditions. M.Sc. dissertation, University of Alberta, Edmonton, AB, Canada.
- Bhattacharya, B. and Ellingwood, B. 1998. Continuum damage mechanics analysis of fatigue crack initiation. *International Journal of Fatigue*, 20: 631-9.
- Bouwkamp, G.J. and Stephen, M.R. 1973. Large diameter pipe under combined loading. *American Society of Civil Engineers, Transportation Engineering Journal*, 99: 521-536.
- Bushnell, D. 1981. Elastic-plastic bending and buckling of pipes and elbows. *Computers and Structures*, 13: 241-8.
- Bushnell, D. 1984. Computerized analysis of shells-governing equations. *Computers and Structures*, 18: 471-536.
- Calgary Herald. Mackenzie project gets review panel support [online]. Available from <http://www.calgaryherald.com/business/> [cited 3/3 2010].
- Canadian Standards Association (CSA). 2007. Oil and gas pipeline systems. Z662-07, Canadian Standards Association, Mississauga, ON, Canada.
- Cheng, J.J.R., Kulak, G.L., and Khoo, H-A. 1998. Strength of slotted tubular tension members. *Canadian Journal of Civil Engineering*, 25: 982-991.
- Das, S. 2003. Fracture of wrinkled energy pipelines. PhD in Structural Engineering, University of Alberta, Edmonton, AB, Canada.

- Das, S., Cheng, J.J.R., and Murray, D.W. 2007a. Behaviour of wrinkled steel pipelines subjected to cyclic axial loadings. *Canadian Journal of Civil Engineering*, 34: 598-607.
- Das, S., Cheng, J.J.R., and Murray, D.W. 2007b. A test method to determine low-cycle-fatigue behaviour of wrinkled pipe. *Journal of Testing and Evaluation*, 35: 1-9.
- Das, S., Cheng, J.J.R., and Murray, D.W. 2007c. Prediction of fracture in wrinkled energy pipelines subjected to cyclic deformations. *International Journal of Offshore and Polar Engineering*, 17: 205-212.
- Das, S., Cheng, J.J. R., and Murray, D. W. 2002. Fracture in wrinkled linepipe under monotonic loading. *In Proceedings of the 4th International Pipeline Conference, Sep 30-Oct 3 2002, Vol. B, pp. 1613-1618.*
- Das, S., Cheng, J.J.R., Murray, D.W., Wilkie, S., A., and Zhou, Z.J. 2001. Wrinkle behaviour under cyclic strain reversal in NPS12 pipe. *In 20th International Conference on Offshore Mechanics and Arctic Engineering; Polar and Arctic Pipeline Technology, Jun 3-8 2001, Vol. 4, pp. 129-138.*
- Das, S. 2003. Fracture of wrinkled energy pipelines. Ph.D. Thesis, University of Alberta Edmonton, Alberta, Canada.
- Das, S., Cheng, J.J.R., Murray, D.W., and Nazemi, N. 2008. Effect of monotonic and cyclic bending deformations on NPS12 wrinkled steel pipeline. *Journal of Structural Engineering*, 134: 1810-1817.
- Det Norske Veritas (DNV). 2007. DNV offshore standard OS-F101: Submarine pipeline systems. Det Norske Veritas, Hovik, Norway.
- Dinovitzer, A., S. and Smith, J., R. 1998. Strain-based pipeline design criteria review. *In Proceedings of the 1998 International Pipeline Conference, IPC. Part 2 (of 2), Jun 7-11 1998, Vol. 2, pp. 763-770.*

- Dorey, A.B., Murray, D.W., and Cheng, J.J.R. 2006. Critical buckling strain equations for energy pipelines - A parametric study. *Journal of Offshore Mechanics and Arctic Engineering*, 128: 248-255.
- Dorey, A.B., Cheng, J.J.R., and Murray, D.W. 2001. Critical buckling strains in energy pipelines. Dept. of Civil and Environmental Engineering, University of Alberta, Edmonton.
- Fair Trade Info. Companies say Alaska gas pipeline could cost \$41B on fairtradeinfo.com [online]. Available from <http://www.fairtradeinfo.com/> [cited 3/3 2010].
- Gillemot, L.F. 1976. Criterion of crack initiation and spreading. *Engineering Fracture Mechanics*, 8: 239-53.
- Gresnigt, A.M. 1986. Plastic design of buried steel pipelines in settlement areas. Netherlands.
- Gurson, A.L. 1977. Continuum theory of ductile rupture by void nucleation and growth. I. yield criteria and flow rules for porous ductile media, *Transactions of the ASME. Series H, Journal of Engineering Materials and Technology*, 99: 2-15.
- Hancock, J.W. and Mackenzie, A.C. 1976. On the mechanisms of ductile failure in high-strength steels subjected to multi-axial stress-states. *Journal of the Mechanics and Physics of Solids*, 24: 147-69.
- Khoo, H.A. 2000. Ductile fracture of steel. PhD Thesis, University of Alberta, Edmonton, AB, Canada.
- Koch, G.H., Brongers, M.P.H., Thompson, N.G., Virmani, Y.P., and Payer, J.H. 2002. Corrosion cost and preventive strategies in the United States, NTIS, U.S. Department of Commerce, United States.

- Lemaitre, J. 1985. A continuous damage mechanics model for ductile fracture. Transactions of the ASME. Journal of Engineering Materials and Technology, 107: 83-9.
- Lemaitre, J. 1984. How to use damage mechanics [nuclear reactors]. *In* 7th International Conference on Structural Mechanics in Reactor Technology (SMiRT-7), Vol. 80, pp. 233-45.
- Martens, M., Kania, R., Kare, R., Topp, D., and Sander, F. 2009. Strain relief of a buried pipeline due to slope movement. *In* 2008 ASME International Pipeline Conference, IPC 2008, September 29, 2008 - October 3, Vol. 2, pp. 835-842.
- Martinez-Saucedo, G., Packer, J.A., and Willibald, S. 2006. Parametric finite element study of slotted end connections to circular hollow sections, Engineering Structures, 28: 1956-1971.
- Matic, P., Kirby, G.C., and Jolles, M.I. 1987. Relationship of tensile specimen size and geometry effects to unique constitutive parameters for ductile materials (NRL-MR-5936), NTIS, U.S. Department of Commerce, United States.
- McClintock, F.A. 1968. Criterion for ductile fracture by growth of holes. *In* ASME Meeting APM-14, pp. 9.
- Mohareb, M., Kulak, G.L., Elwi, A., and Murray, D.W. 2001. Testing and analysis of steel pipe segments. Journal of Transportation Engineering, 127: 408-417.
- Mohareb, M., Alexander, S.D.B., Kulak, G.L., and Murray, D.W. 1993. Laboratory testing of line pipe to determine deformational behaviour. *In* Proceedings of the 12th International Conference on Offshore Mechanical and Arctic Engineering (OMAE 1993), Jun 20-24 1993, Vol. 5, pp. 109-114.

- Morgan, V., Kenny, S., Power, D., and Galling, R. 2004. Monitoring and analysis of the effects of ground movement on pipeline integrity. *In* International Conference on Terrain and Geohazard Challenges facing Onshore Oil and Gas Pipelines: Evaluation, Routing, Design, Construction, Operation, June 2, 2004 - June 4, Vol. 2004, pp. 701-712.
- Murray, D.W. 1997. Local buckling, strain localization, wrinkling and postbuckling response of line pipe. *Engineering Structures*, 19: 360-371.
- Myrholm, B.W. 2001. Local buckling and fracture behaviour of line pipe under cyclic loading. M.Sc., University of Alberta, Edmonton, Alberta, Canada.
- NTSB. 2002. Rupture of piney point oil pipeline and release of fuel oil near chalk point, Maryland, April 7, 2000. Pipeline Accident Report: NTSB/PAR-02/01, National Transportation Safety Board, Washington, D.C. 20594, USA (<http://www.nts.gov/publictn/2002/PAR0201.htm>).
- NTSB. 2001. Pipeline accident brief: Winchester, Kentucky, 2000 (PAB 0102). PAB0102, National Transportation Safety Board, Washington, D.C. 20594, USA (<http://www.nts.gov/publictn/2001/PAB0102.htm>).
- NTSB. 1999. Pipeline accident brief: Morgan falls landfill, sandy springs, Georgia, 1998. PAB9901, National Transportation Safety Board, Washington, D.C. 20594, USA (<http://www.nts.gov/publictn/1999/PAB9901.htm>).
- Oswell, J.M. 2002. Geotechnical aspects of northern pipeline design and construction. *In* Proceedings of the 4th International Pipeline Conference, September 30, 2002 - October 3, Vol. A, pp. 555-562.
- Oswell, J.M., Skibinsky, D., and Cavanagh, P. 2005. Discussion of "Frost heave and pipeline upheaval buckling". *Canadian Geotechnical Journal*, 42: 323-324.

- Palmer, A.C. and Williams, P.J. 2003. Frost heave and pipeline upheaval buckling. *Canadian Geotechnical Journal*, 40: 1033-1038.
- Rice, J.R. and Tracey, D.M. 1969. On the ductile enlargement of voids in triaxial stress fields. *Journal of the Mechanics and Physics of Solids*, 17: 201-17.
- Schneider, S.P. 1998. Flexural capacity of pressurized steel pipe. *Journal of structural engineering* New York, N.Y., 124: 330-340.
- Tanaka, T., Haung, S., Fukuda, M., Bray, M.T., and Akagawa, S. 2009. A study on cold region pipeline design based on full-scale field experiment. *In* 2008 ASME International Pipeline Conference, IPC 2008, September 29, 2008 - October 3, Vol. 4, pp. 211-219.
- Tart Jr., R.G. 2007. Pipeline geohazards unique to northern climates. *In* 2006 6th International Pipeline Conference, IPC 2006, September 25, 2006 - September 29, Vol. 1, pp. 909-916.
- Wilkie, S.A., Doblanko, R.M., and Fladager, S.J. 2001. Northern Canadian pipeline deals with effects of soil movement, *Oil & Gas Journal*, 99: 62.
- Yoosef-Ghodsi, N., Kulak, G.L., and Murray, D.W. 1995. Some test results for wrinkling of girth-welded line pipe. *In* Proceedings of the 14th International Conference on Offshore Mechanics and Arctic Engineering. Part 5 (of 5), Jun 18-22 1995, Vol. 5, pp. 379-387.
- Yukon Government. updated on March 27, 2006. Pipeline and transportation infrastructure [online]. .
- Zhang, J. 2010. Development of LCF life prediction model for wrinkled steel pipes. Ph.D., Thesis, University of Alberta, Edmonton, AB, Canada.

- Zhang, Y. and Das, S. 2008a. Failure of X52 wrinkled pipelines subjected to monotonic axial deformation. *Journal of Pressure Vessel Technology*, 130: 021702-1.
- Zhang, Y. and Das, S. 2008b. Failure of X52 wrinkled pipeline subjected to monotonic bending deformation and internal pressure. *International Journal of Offshore and Polar Engineering*, 18: 50-55.
- Zhao, R., Huang, R., Khoo, H.A., and Cheng, J.J.R. 2009. Parametric finite element study on slotted rectangular and square HSS tension connections. *Journal of Constructional Steel Research*, 65: 611-621.
- Zhou, Z.J. and Murray, D.W. 1993a. Behaviour of buried pipelines subjected to imposed deformations. *In Proceedings of the 12th International Conference on Offshore Mechanical and Arctic Engineering (OMAE 1993)*, Jun 20-24 1993, Vol. 5, pp. 115-122.
- Zhou, Z.J. and Murray, D.W. 1993b. Towards rational deformation limit states for buried pipelines. *In Proceedings of the Third (1993) International Offshore and Polar Engineering Conference*, Jun 6-11 1993, pp. 18-24.
- Zimmerman, T.J.E., Stephens, M.J., DeGeer, D.D., and Chen, Q. 1995. Compressive strain limits for buried pipelines. *In Proceedings of the 14th International Conference on Offshore Mechanics and Arctic Engineering*, Part 5 (of 5), June 18, 1995 - June 22, Vol. 5, pp. 365-378.

### 3. PRELIMINARY INVESTIGATION OF TEARING FAILURE<sup>1</sup>

#### 3.1 General

An ever increasing demand to exploit oil and natural gas reserves has amplified extraction activities even in the most remote regions of the Arctic and sub-Arctic of the Canadian North. Steel pipelines have proven to be the most efficient mode for transporting and distributing these resources to urban areas. There have been more than 700,000 km of energy pipeline in operation in Canada alone, and future pipeline projects totalling more than CAD \$30 billion have been planned for the next five years in order to transport natural gas and petroleum products from Alaska and the Northwest territories to market places in Canada and the United States (Yukon Government updated on March 27, 2006). The majority of these pipelines are buried pipelines. As pipelines, especially those buried in regions of discontinuous permafrost, often respond to geotechnical movements and/or thermal strains, there is a great variety of field conditions that may develop to cause the pipe to buckle or wrinkle. Wrinkling is a local buckling phenomenon that may result from thermal expansion or as a part of a plastic collapse bending mechanism induced by soil settlements resulting from slope movements, frost heave, and thaw settlements. The behavioural characteristics one may expect from a wrinkle (such as possible fracture or benign deformation) will depend on the driving mechanism associated with the wrinkle deformation and the continued presence of the driving mechanism. Consequently, it is often difficult, if not impossible, to predict with assurance what the risk factor will be with respect to the possibility of a fracture occurring under continuing deformation.

According to earlier research observations, since fracture in the laboratory only rarely occurs for monotonically controlled deformation processes, the norm for

---

<sup>1</sup> Part of this chapter has been published in the Journal of Offshore Mechanics and Arctic Engineering, ASME, February 2010, volume 132, issue 1, 011302-1-10.

wrinkle bending behaviour appears to be the development of a benign bulge wrinkle; the deformation configuration will be essentially axisymmetric (Das et al. 2002). Under a continually increasing axial displacement due to monotonic geotechnical movement, the half-wave length of the wrinkle decreases until the interior surfaces of the wrinkle come into contact and the wrinkle “closes”. At this stage, the force in the pipe wall bypasses the wrinkle by following the path formed as a result of the direct contact of the inner surfaces at the ends of the wrinkle. Accordingly, a second wrinkle may develop adjacent to the first and the process may be repeated while the fold of the second wrinkle develops. Conceptually, this may lead to stacking of wrinkles, (i.e., accordion wrinkles as shown in Figure 3.1), and there will be no danger of fracture at the wrinkle location.

The present work has been initiated because of a field fracture observed within the wrinkle location in an NPS10 (10 inches nominal pipe diameter) energy pipe operated by WestCoast Energy Inc. in British Columbia, Canada (as shown in Figure 3.2). Similar failure mode of a laboratory specimen was observed in a study carried out at the University of Alberta (Das et al. 2002). A description of the field load history and an inspection of the deformed geometry and the fracture surface had shown that there were no significant strain reversals in the wrinkled pipe segment. The final failure was a “tearing” failure resulting from monotonic application of an axial load not aligned with the axis of the pipe. According to the initial assessment of the failed field specimen, an initial bulging wrinkle occurred at an unpressurized location, probably through soil movement in the direction of the pipe. Subsequent or simultaneous shear force generated from the soil movement acting on the wrinkle region had forced the initial axisymmetric wrinkle to squash to the point that the wrinkle became essentially flat. As a result of this, the interior surfaces of the wrinkle came into contact with each other. This was followed by a deformation where one side of the top segment of the pipe slipped inside the bottom segment in a “telescoping” manner. In so doing it created a fold in the pipe wall and the tear in the pipe wall occurred at the sharpest bend within this fold. To verify this unique failure mechanism and determine the

characteristics contributing to its formation, two full-scale tests applying axial load and a shear load with appropriate boundary conditions were carried out on NPS12 pipe at the University of Alberta (Das et al. 2002). Successful simulation of this behaviour in the laboratory has emphasized that fractures can be triggered at wrinkle locations by monotonic loading histories with appropriate boundary conditions and has thus provided the motivation to carry out the present study.

However, there are some fundamental questions that still need to be answered, as the results obtained from the full-scale test mentioned above were very much constrained to the load-displacement plot of the MTS (Material Testing System) universal testing machine and the final deformed shape of the failed specimen. In order to investigate the behaviour of the failed field and test specimens, a finite element (FE) model has been developed in this study. The FE simulator, ABAQUS, which is capable of accounting for material nonlinearity effects, large displacements, large rotations, initial imperfections, and possible complex contact surfaces, was used to develop the model. The present model has been developed based on the finite-membrane-strain formulation in order to account for finite strains as well as the effects of plate thinning. This chapter includes a brief description of the experimental work done by Das et al. (Das et al. 2002), which is relevant to characterize this tearing mode of failure in buried pipelines. This chapter also describes the development of the FE model, for which every effort has been made to simulate the behaviour of the pipe observed during the full-scale test conducted at the University of Alberta under complex loading history with different boundary conditions. Results of this analytical work include the global and local deformation patterns and a detailed assessment of the stresses and strains at wrinkled location.

### **3.2 Previous Experimental Investigation**

Two full-scale tests applying axial load and shear load with different boundary conditions were carried out on NPS12 pipes (Das et al. 2002). The diagnoses of the field fracture at the wrinkled location of a pipeline operated by WestCoast

Energy Inc. had identified that failure was resulting in a monotonic application of axial loading not aligned with the axis of the pipe. Two pipe specimens of 12.75 inches OD (outer diameter), 6.84 mm thickness and Grade X52 steel were used for this testing program. The test set-up used was a very simple arrangement where the specimen was welded to the base plates at top and bottom. Figure 3.3 shows the schematic view of the test set-up, indicating the application of loading at different stages of the test. The axial load ( $P_{\text{MTS}}$ ) was applied by the MTS universal testing machine with a capacity of 6000kN, and the transverse load ( $V$ ) was applied by a hydraulic jack (in the proximity of the wrinkle developed at about mid-span of the pipe specimen) at a desired location as shown in Figure 3.3.

### ***3.2.1 Loading Steps***

The application of loading at different stages of the test and the changes in the boundary conditions corresponding to those stages were completed in several steps. In the first step, the axisymmetric axial load ( $P_{\text{MTS}}$ ) was applied using the displacement control method until the first identifiable wrinkle had formed at about mid-span of the pipe specimen. During this step, the two ends of the specimen were fully clamped against rotation, as can be seen in Figure 3.3a. In the second step, the specimen was unloaded and the end boundary conditions were changed to a pin-pin condition with the aid of knife edge support, as shown in Figure 3.3b. In the third step, after changing the boundary conditions, the axial load ( $P_{\text{MTS}}$ ) was reloaded until it reached the previous level. After this reloading, the transverse shear force ( $V$ ) was applied with a horizontal jack at a distance of  $\Delta_v$  ( $\approx 30.0$  mm) above the foot of the wrinkle location. In the final step, the end conditions were changed to a clamped-clamped condition as shown in Figure 3.3c, which was followed by a gradual increase in the MTS load ( $P_{\text{MTS}}$ ) with simultaneous unloading of the jack force ( $V$ ). Finally, the MTS stroke was applied incrementally until the specimen failed.

### 3.2.2 Test Results

The load-deformation behaviour of the test specimen is shown in Figure 3.4. The pipe specimen reached its maximum load carrying capacity (limit point) at Point  $c'$  and at this point, a wrinkle at about pipe mid-span became visible. Subsequently, as the stroke or axial displacement increased beyond the limit point, the pipe specimen was softened with the amplification of the wrinkle and the load carrying capacity decreased at a rapid rate, as shown by path  $c'-d'$ . During this step, the ends of the specimen were fully clamped against rotation. Following this, the specimen was unloaded as indicated by path  $d'-b'$  in order to facilitate the change in boundary condition from clamped to pinned (see Figure 3.3b). In the next step, the pipe specimen was reloaded (path  $b'-d'$ ), followed by application of the jack force ( $V$ ) at the closest possible proximity to the wrinkle. During this stage, the MTS load ( $P_{MTS}$ ) began to drop and continued in the same manner (path  $d'-e'$ ) as the jack load ( $V$ ) increased. The jack load ( $V$ ) was gradually increased up to point  $e'$ , where a suitable offset was formed between the upper and lower parts of the pipe with a relative rotation of  $\Theta$  ( $\approx 3.4^\circ$ ) and a lateral deflection of  $\Delta_h$  ( $\approx 20$  mm) as shown in Figure 3.3c. As described by Das et al., the rationale for creating this suitable offset was to generate non-axisymmetric axial loading and thus to initiate the process of generating tearing failure in the pipe specimen in a similar to the case shown in Figure 3.2.

In the final stage of the test, the ends of the pipe specimen were changed to fixed-fixed condition by locking the MTS heads, a step which was followed by the gradual increase of the MTS stroke and simultaneous unloading of the jack force ( $V$ ), as shown by path  $e'-f'-k'$ . At point  $g'$  in Figure 3.4, the MTS load began to pick up again. The reason for this increase in load carrying was the closing of the wrinkle fold on the compression side. During the load path  $g'-h'$ , the wrinkle began to fold on the compression side and the upper portion of the specimen began to telescope into the bottom portion with the increase of the MTS stroke. At point  $h'$ , the MTS load ( $P_{MTS}$ ) began to drop again, even with the increase of MTS stroke suggesting the occurrence of a fracture in the pipe wrinkle. At some stage,

the “tearing” fracture (in terms of long through-thickness separation) was triggered in the sharp fold of the wrinkle as shown in Figure 3.5. The failed laboratory specimens have indicated that, in the presence of telescopic action, monotonic loading can result in tearing-type failure in buried line pipe.

### **3.3 Development of the Numerical Model**

The objective of the first part of this research program this study is to investigate the behavioural characteristics of buried pipelines under variable loading conditions applied in a monotonic manner as described in previous sections, focusing on the tearing failure mode at telescopic wrinkles. In order to achieve the aforementioned objective, a finite element (FE) model has been developed which considers all possible nonlinearity effects. The ABAQUS program (Hibbitt, H.D., Karlsson, B.I., and Sorensen, P., 2006) has been chosen for this analytical work, as it possesses features essential for simulating post-buckling response of line pipe. In particular, it can model an elasto-plastic isotropic hardening material suitable for the constitutive modeling of the pipe material, as well as the effects of finite strains and plate thinning through finite membrane strain formulation, nonconservative applied loads, and possible complex contact surfaces (Murray 1997). Its element library includes a certain element type which is capable of accounting for large displacement, large rotation, and initial imperfections (Mohareb et al. 2001). This program has both load control and displacement control capabilities, both of which are required in order to simulate the test loads and post processing capabilities that allow the user to view deformed configurations, contour lines for a variety of variables, and plots relating selected variables. Figure 3.6 shows a schematic view of the developed FE model with initial boundary conditions. Points A and B are pivot points at which axial displacement/load (P) had been applied. Lines CD and EF represent end plates. The portions between Point A and Line CD and between Point B and Line EF have been modeled in such a way that they will act as a rigid body. The jack load (V) shown in Figure 3.6 was applied following the formation of the initial wrinkle

at close proximity to the pipe's mid-span. The numerical development of a pipe segment includes appropriate selection of element type, element mesh generation and optimization, proper boundary and loading conditions, material properties, and solution scheme.

### ***3.3.1 Element Selection***

Selection of an appropriate finite element is critical to the successful simulation of the post-wrinkling behaviour of pipes with large deformations. For the development of the present numerical model, 4-noded quadrilateral doubly curved general purpose shell elements (S4R) with reduced integration were chosen. Each node of these shell elements has three translational and three rotational degrees of freedom. Their formulation is based on finite-membrane-strain formulation, and can account for the effect of plate thinning as a function of in-plane deformation (Hibbitt, H.D., Karlsson, B.I., and Sorensen, P., 2006). The use of finite strain formulation is necessary and justifiable for modeling large displacement, large rotation, and softening behaviour of wrinkled pipe under complex loading conditions, as the total equivalent plastic membrane strains were found to be extremely large (as high as 100%) at the wrinkle zone (Mohareb et al. 2001) in some locations.

As discussed above, for these shell elements, membrane strains follow finite strain formulation, whereas bending strains are predicted using small strain assumptions. However, strains normal to the shell surface are assumed to be constant along shell thickness. Transverse shear strain components of these elements are calculated at midpoints of element edges (Hibbitt, H.D., Karlsson, B.I., and Sorensen, P., 2006). Seven section points, as can be seen in Figure 3.7, have been chosen through the thickness of each element in order to facilitate numerical integration and to properly capture the plasticity resulting from extreme local bending occurring in the vicinity of the telescoping wrinkle. Figure 3.7 describes the configuration of section points in a numerically integrated shell and also

shows the positive normal ( $\eta$ ) given by the right-hand rule. In Figure 3.7, Section Point 7 (SP7) represents the top surface of the shell, i.e., the outer surface of the pipe wall, whereas Section Point 1 (SP1) represents the bottom surface of the shell, i.e., the inner surface of the pipe wall. These elements have an isoparametric formulation, meaning that the same interpolation functions are used for both displacements and position vectors (Mohareb et al. 2001).

### ***3.3.2 Mesh Sensitivity***

The major objective of performing a mesh sensitivity analysis for any numerical work is to optimize the mesh configuration yielding the acceptable result with the largest possible number of elements in the shortest possible computational time. In order to achieve this objective in the present case, the element size and aspect ratio of the elements were kept in consideration during the mesh generation of the developed model. It is a generally accepted practice to aim for non-uniform mesh discretization for problems like this, for which more refined mesh could be used in the region of the pipe where strain localization usually occurs and coarser mesh for the rest of the pipe segment. However, previous numerical works had shown that local buckling initiation had triggered at the boundary separating two sets of elements with different mesh sizes (Mohareb et al. 2001; Das et al. 2007b). Considering the above discussion, uniform mesh size was chosen for the pipe model, in both longitudinal and circumferential directions, at minimal expense in terms of computational time. Selection of uniform mesh in the longitudinal direction was found to be reasonable as it allowed for the capture of any dominant buckling/wrinkling anywhere along the pipe segment. Under the complex loading combination of axial load through thermal strain and/or geotechnical movement and bending moment through lateral soil thrust, wrinkles can expand in the circumferential directions to cover the entire circumference which justifies the use of uniform mesh in that direction.

Element size for the present model has been chosen so as to fulfill the direction given by Bruschi et al. (Bruschi et al. 1995). According to their investigation,

there should be at least four 2<sup>nd</sup> order shell elements in the longitudinal direction for capturing the buckling half-wavelength ( $\lambda$ ), whereas at least 12 elements should be generated on the half circumference subtending an angle less than 15°.

During this mesh study, the focus was given on both global behaviour and local behaviour. Based on the results of this sensitivity analysis, the coarser mesh can provide reasonable prediction concerning the onset of buckling behaviour and the global behaviour. However, the refinement of the mesh will become critical while analyzing the post buckling behaviour of a wrinkled pipe as well as localized stress-strain relationship, as a coarser mesh will not have the capacity to simulate/predict this behaviour as effectively as will a finer mesh. However, the use of too refined a mesh will increase the computational time to several folds. Furthermore, if the aspect ratio of any element in the developed model is abnormally high, there are more possibilities introduced which will fail to converge to the desired solution. As such, the element's size should be kept small enough to yield reliable results and yet large enough to reduce computational time. Keeping the above discussion in mind, the element size was chosen for this study that such the aspect ratio never exceeded a value of 3.0.

The mesh used in the present model was obtained from a series of analyses using gradually refined mesh. The mesh study was conducted along both the circumferential direction and the longitudinal (or axial) direction.

### ***3.3.3 Circumferential Direction***

When conducting the mesh study in this direction, the number of elements along the longitudinal direction was kept constant at 122, and the number of elements in the circumferential direction was changed gradually or incrementally from 32 to 188. The effect of mesh refinement along the circumferential direction on the load-displacement (P- $\Delta$ ) response is presented in Figure 3.8.

In Figure 3.8,  $P_{MTS}$  represents the reaction force at pivot point A in Figure 3.6, and  $\Delta$  represents the applied axial displacement at point A. Figure 3.8 illustrates that a mesh size as sparse as  $32 \times 122$  can give satisfactory maximum or axial load and stable onset of buckling behaviour. But to get a steady postbuckling behaviour for even higher axial displacement, the mesh size has to be at least as fine as  $126 \times 122$ . For higher mesh refinement such as  $188 \times 122$  in the present case, the change in the P- $\Delta$  response is not significant whereas the computational time increases to several folds. This will be more critical for larger pipe deformation history. Therefore, this analytical work conservatively used 126 elements along the circumferential direction.

#### ***3.3.4 Longitudinal Direction***

To study the effect of mesh refinement in longitudinal direction, the number of elements in the circumferential direction was kept constant as 126, and the number of elements along the longitudinal direction was changed from 30 to 180. The results are presented in Figure 3.9. According to Figure 3.9, it can be concluded that a mesh size of  $126 \times 122$  is fine enough to obtain stable and satisfactory load-displacement response at reasonable accuracy and computational time.

Based on these two mesh studies, a mesh size of  $126 \times 122$  was chosen to conduct the subsequent FEA.

#### ***3.3.5 Modeling of End Plates and Collars***

The end plates of the pipe specimen represented as Lines CD and EF in Figure 3.6 were 75 mm in thickness and experienced elastic deformation only at a very small scale during the test conducted by Das et al. (Das et al. 2002). The loading arms and the end plates were so robust in nature, as indicated by the authors (Das et al. 2002), that it was deemed reasonable to model them as a rigid body during the

numerical simulation. The end plates were modelled using 3-node, three dimensional (3D) rigid elements. The pivot/load points A and B were connected to the end plates as indicated in Figure 6, i.e., lines CD and EF respectively, using rigid ties so that the degrees of freedom of the nodes on the end plates were constrained to the degrees of freedom of the pivot points. Therefore, the portions between the end plates and the pivot points became essentially rigid. Due to this rigid body motion, the end plates were subjected to the same kinematic boundary conditions that had been applied to their corresponding pivot points. The distance from the pivot point to the corresponding end plate was about 333 mm, as shown in Figure 3.10, a fact which bears little significance considering that the portions between the pivot point and the end plates behaved as a rigid body.

In the tests, two confining collars, 75 mm long and made of the same pipe material, were attached next to the end plates to prevent the pipe from buckling and/or fracturing locally due to the end conditions. There are several ways to incorporate these collars in the numerical model. The realistic way would be to model the collar–pipe interaction as a contact problem with a compromise of convergence issue and computational cost. In a bid to circumvent that complicated step and thereby optimize the computational time, it is reasonable to aim for a more simplified approach. One approach could be to model the top and bottom locations of the pipe specimen indicated as collars in Figure 3.6 and Figure 3.10 as linear elastic using the same material properties as that of the pipe steel, thereby preventing local buckling at the specimen ends. However, the approach used in the present model was to increase the thickness of the pipe at the top and bottom collar locations, a strategy which forced the inelastic local buckling to develop away from the specimen ends. A similar scenario occurred during the test conducted by Das et al. (Das et al. 2002) due to the presence of the collars. This modeling simplification was therefore judged not to compromise the integrity of the analytical model (Mohareb et al. 2001).

### 3.3.6 Material Modeling

The full-scale specimens used for the tests performed by (Das et al. 2002) were taken from a grade X52 steel pipe with a specified minimum yield strength of 358 MPa. The actual yield strength at 0.5% strain was found to be 357 MPa. Four tension coupon tests were conducted by (Das 2003)) and the measured average engineering stresses and strains obtained from those coupon tests for grade X52 materials were taken as input data for the present model. The following two expressions (Hibbitt, H.D., Karlsson, B.I., and Sorensen, P., 2006) were used to determine the true stress–true logarithmic plastic strain behaviour in order to model the constitutive behaviour of the pipe material,

$$(2) \quad \sigma_{true} = \sigma_{nom} (1 + \varepsilon_{nom})$$

$$(3) \quad \varepsilon_{ln}^{pl} = \ln(1 + \varepsilon_{nom}) - \frac{\sigma_{true}}{E}$$

Where,  $\sigma_{nom}$  is the nominal or engineering stress,  $\varepsilon_{nom}$  is the nominal or engineering strain recorded from the coupon (material) tests, E is the modulus of elasticity,  $\sigma_{true}$  is the true stress, and  $\varepsilon_{ln}^{pl}$  is the true logarithmic plastic strain.

The true stress versus true logarithmic plastic strain curve shown in Figure 3.11 demonstrates an initial elastic behaviour subsequent to the gradual development of plastic flow with strain hardening. Assuming the pipe material had been comprised of an isotropic metal, the classical von Mises yield criterion was used to predict the yield surface in the present model. According to this criterion, the yield surface assumes that the yield of steel is independent of the hydrostatic stress. It was also assumed that the material model used in the present work obeyed the associated flow rule in relating the plastic strain increments to the current stress increments followed by yielding. An isotropic stress-strain hardening model has been chosen for the present analysis. As the loading history

obtained from the field and the physical test did not involve any cyclic loading, an isotropic hardening was found to be reasonable.

However, the stress-strain relations obtained from these numerical analyses, presented in the later part of this chapter (see sub-section 3.5.2), have shown the presence of localized strain reversal at the wrinkle location. Therefore, applicability of isotropic hardening can be arguable. According to classic metal plasticity, kinematic hardening would be more appropriate for this phenomenon. There are two types of kinematic hardening models, linear and nonlinear, available to consider this effect. The nonlinear kinematic hardening model, also known as combined isotropic hardening model, usually provides a more accurate approximation to the stress-strain relation .

Figure 3.12 shows the yield surface of the combined isotropic-kinematic hardening model. The evolution laws of kinematic hardening model describe the translation of the yield surface in stress space through the back-stress tensor ( $\alpha$ ), as shown in. Whereas, the isotropic hardening component describes the change of the yield stress defining the size of the yield surface, where,  $\sigma^0$  as a function of plastic deformation. According to the well-known ‘Armstrong-Fredrick’ kinematic hardening law, the center of the von Mises circle stays in a limiting circle. When the back-stress saturates and reaches the value of  $c/\gamma$  (see Figure 3.13), and under a state of proportionally increased loading, any hardening after the saturation of kinematic hardening will be only due to isotropic hardening.

In the present context, since, the strain reversal has occurred at a very large plastic strain value (sub-section 3.5.2), theoretically, the back stress has saturated at the point of strain reversal and, any hardening after this saturation will be only due to isotropic hardening. Therefore, it seems reasonable to assume that the plasticity of the pipe material can be predicted using isotropic hardening model.

Residual stresses can have significant effect on the inelastic behaviour of structural steel, as it can inherent some residual stresses through manufacturing

process. During pipe manufacturing process, plates are usually formed into pipes by UOE process in several steps. In the U stage, a punch with an adapted radius is pushed into mid section of the plate. Then, the O press completes the process of forming an almost round open seam tube. During the U and O processes on the base of circumferential direction, inner parts of pipe deform in compressive mode while, outer parts deform as tensile. The amount of deformation is dependent on the diameter and wall thickness of the pipe; the more  $D/t$  ratio is, the less deformation occurring during the U and O processes.

The last forming step consists of the expansion stage, E that improves the roundness and straightness of the pipes. Expansion leads to circumferential tensile plastic strains throughout the pipe wall. As a result of pre-straining in UOE process, the presence of residual stresses in the pipe wall is minimized. Therefore, effect of residual stresses is not considered in the material model of this study.

### ***3.3.7 Boundary Conditions and Loading Sequence***

Special attention and appropriate selection of boundary conditions and loading sequence are required in order to predict a complex load history such as this and then generate the deformed shape observed in the field specimen. During the test (Das et al. 2002), the axial load ( $P_{MTS}$ ) was applied at the top pivot using an MTS universal testing machine, as shown in Figure 3.3. The kinematics of the test was such that the top and bottom end of the pipe remained circular following the formation of a wrinkle at approximately mid-height of the pipe segment, as those ends had been welded to infinitely rigid end plates. The portion between the MTS head and the top pivot were essentially rigid and thus were modelled as a rigid body facilitating rigid body motion ( $\theta_I$ ) about pivot points A and D at a certain stage of the numerical analysis. In the numerical model, the axial loading was applied using displacement control at the top pivot while the bottom pivot remained stationary. A transverse force ( $V$ ) was applied at the closest possible proximity to the wrinkle to simulate the jack load. This transverse force ( $V$ ) had been applied as a series of nodal forces in the FE analysis. Both in the test and in

the FE analysis, zero internal pressure was applied to the pipe specimen, as the field fracture reported by West Coast Energy Inc had occurred when the line pipe was not in service.

The boundary conditions and applied loading history in the numerical analysis were divided into a number of steps. These load steps were chosen in such a way as to remain consistent with the test (Das et al. 2002). In the first step, an initial axial displacement (30 mm) was applied at the top pivot, A, in the negative “3” direction, keeping the top and bottom ends of the pipe fully restrained. During this step, a wrinkle formed at about mid-height of the specimen. In the second step, the initial displacement was released, meaning that the specimen was unloaded in order to facilitate the change in the boundary condition from fixed to pinned, as required in the next step. After releasing the initial displacement, the boundary condition was changed from fixed to pinned condition to allow rotation about “1” axis (i.e.  $\Theta_1 \neq 0$ ) in Step 3. In Step 4, a transverse force, V, was applied to a set of nodes in the global “2” direction located approximately 30 mm above the wrinkle location. Simultaneously, the axial displacement at the top of the pipe was increased to 42 mm. In Step 5, the boundary conditions at the top and bottom pivots were changed by keeping the rotations about global “1” axis fixed at their current level. In the subsequent step, the axial displacement at top pivot A was increased until it reached the final deformation as indicated by the test results of the pipe specimen.

### ***3.3.8 Initial Imperfection Model***

Incorporation of initial imperfections in the present FE model was of mere importance, as influence of initial imperfections on the global and local behaviour of the line pipe was found to be significant (Bushnell 1981; Dinovitzer and Smith 1998; Dorey et al. 2002; Dorey et al. 2006). Presence of initial imperfection can reduce the load carrying capacity as well as trigger the onset of buckling much earlier for imperfect shell structures in comparison to the behaviour of perfect shell structures as illustrated in Figure 3.14 (Bushnell 1981). Since there was no

imperfection data available from the proof of concept test (Das et al. 2002), the initial imperfection patterns assumed based on the recommendation provided by Dorey et al. (2006) had been applied to the present model.

Three different patterns of assumed initial imperfection, “Ring”, “Half-Ring”, and “Blister” type were established by Dorey et al. (2006) as illustrated in Figure 3.15. The extent of imperfections in the direction of X-axis (see Figure 3.15) should be taken as  $0.5D$ ; where  $D$  is the outer diameter of the pipe (Dorey et al. 2006). According to their numerical investigation, the maximum amplitude for an assumed “blister” or “ring” type initial imperfection for NPS12 specimens with a nominal  $D/t$  ratio of 51 should be about 2% of the pipe wall thickness ( $t$ ). Based on the recommendation revealed from this study (Dorey et al. 2006), the “blister” type initial imperfection pattern with maximum amplitude of 0.56mm (8% of  $t$ ), as shown in Figure 3.16a, and the “ring” type initial imperfection pattern with maximum amplitude of 0.28mm (4% of  $t$ ), as shown in Figure 3.16b, had been tried in the present FE model. These smooth curves (look like bulge) as indicated in Figure 3.16 had been established using a cosine function with the maximum amplitude located at the mid span of the pipe specimen. In the present context of load-deformation history, the “ring” type initial imperfection with the maximum amplitude of 4% of  $t$  has given closer match to experimental results and found reasonable to be used as an initial imperfection model.

### **3.3.9 Contact Formulation**

Since the pipe went through a large deformation during the load-deformation history, there is a possibility of self-contact among various portions of the pipe at the wrinkle location as the wrinkle closes. This propensity rationalizes the incorporation of contact formulation in the present FE analysis. A contact surface, as can be seen in Figure 3.19, has been defined on the interior surface ( $\eta^-$ ) of the pipe wall within the middle-third of the pipe where the possible self-contact is expected. Since this is a self-contact problem, the master surface and the slave

surface represent the same contact surface. After defining the contact surface, a surface interaction definition which specifies the constitutive properties and the constraint enforcement methods is assigned to the contact pair. Since the selection of the contact discretization and the tracking approach can have a significant impact on solution costs during analysis, careful attention has been given to the choosing of these parameters during contact formulation. For the present problem, the “node-to-surface” contact discretization, rather than the “surface-to-surface” contact discretization, has been adopted in order to optimize the solution cost. The “finite-sliding”, rather than a “small-sliding” tracking approach, has been incorporated in the current formulation, as it is often difficult to predict which regions will be involved in the contact or how they will move relative to each other during self-contact. The augmented Lagrange method has been used for enforcing the constraint and ensuring convergence of this 3D self-contact problem, since this approach can resolve contact conditions easily and prevent problems with over-constraints while keeping penetrations small.

### ***3.3.10 A Brief Note on Solution Strategy***

A numerical analysis of shell structures such as buried pipelines may have to address severe nonlinearities due to large displacement effects, nonlinear material properties, and/or boundary nonlinearities such as self-contact of pipe wrinkles. The deformation history for this thin shell structure includes the formation of local buckling/wrinkling, leading to softening behaviour in the post-buckling region until collapse (Zhou and Murray 1995), necessitating the adoption of a robust solution technique to capture this type of behaviour.

The nonlinear static stress analysis with the option of automatic stabilization provided by the ABAQUS simulator was adopted to solve the initial part of the analysis dealing with local instabilities such as surface wrinkling. During this process, stabilization was achieved by applying damping throughout the model in such a way that the viscous forces introduced were sufficiently large to prevent instantaneous buckling or instability but small enough not to affect the behaviour

significantly while the problem was stable. The classical Newton-Raphson algorithm with displacement control was been used for this solution process. During the final stage of the analysis prior to failure, a solution technique based on an equilibrium iterative procedure combined with an arc-length control technique (referred to as the modified Riks method (Riks 1979)) was adopted to carry out the post-buckling analysis. Because the Riks method can be suitable for solving ill-conditioned problems such as the snap-through problem, unstable collapse, and/or unstable problems which exhibit softening behaviour at the post wrinkling stage.

### **3.4 Verification of the FE Model**

The performance of the FE modeling technique adopted in the present numerical work was verified using the data obtained from the full-scale test (Das et al. 2002). Results obtained from the full-scale test mentioned earlier were very much constrained to the load-displacement plot of the MTS and the final deformed shape of the failed specimen. The load-deformation responses obtained from the experiment (Das et al. 2002) and the plot of the reaction force for the displaced node A at the top of the pipe obtained from the nonlinear FE analysis are shown in Figure 3.17. In general, there was a fairly good agreement between the analytically predicted values and the test behaviour, as can be seen from Figure 3.17. The overall trend of the load-displacement response also matched reasonably well. However, there were some variations in the actual loads, and they were significant in some instances. The yielding of the pipe specimen and the formation of the wrinkle appeared to develop earlier in the FE analysis and the maximum load value (Point *c*) obtained from numerical analysis was noticeably lower. These conditions may be attributed to the assumed initial imperfection or the application of the circumferential loading at the axial centre line of the wrinkle in order to ensure the formation of wrinkle at the desired location. Also, the stiffness of the elastic loading curve in the *a-c* region obtained from the numerical analysis is higher than that obtained from the test. The stiffness of the FEA

loading paths in the  $c-d$ ,  $d-e$ ,  $e-f$ , and  $f-g-h$  regions were always found to be relatively lower than those of the physical experiment ( $c'-d'-e'-f'-g'-h'$ ) at most locations. This may be due to the effect of the material properties, test boundary conditions, and the assumed imperfections pattern used in the numerical model. However, for key points such as Points  $d$ , (the point at which the unloading of the pipe was performed),  $e$ ,  $f$ ,  $g$ , and  $h$  on the plot, the analytical result appeared to be generated in a similar manner to the test. When the pipe specimen reached Point  $g$  on the  $P-\Delta$  curve obtained from the FEA, the contact pressure at the wrinkle location due to self-contact at the interior of the pipe wrinkle was tracked, and the load carrying capacity of the deformed pipe started to pick up. In the actual test, the closing of the wrinkle (Point  $g'$ ) seemed to occur early in comparison to the case of the FEA. Since simplifications and assumptions had been adopted in the contact formulation in order to optimize solution cost, this variation can be considered reasonable. Figure 3.18a, Figure 3.18b and Figure 3.18c all show the deformed shapes of Specimen obtained from the present analytical work, the test, and the field, respectively. It can be seen that the FE model produces a deformation configuration with characteristics closely resembling the post-wrinkling configuration observed both in the experiment and in the field. However, more detailed comparisons were not possible as no detailed data were available regarding the dimensions of the pipe wrinkle formed in the full-scale test or in the field. While the actual values of the applied loads may vary due to differences in material properties (Dorey et al. 2002) and initial imperfections (Dorey et al. 2006) and slight variations in loading sequence, the global trends and magnitude can be considered to be fairly accurate. As such, it is sufficiently reasonable to carry out further analysis using this numerical model to predict the stresses and strains at localized wrinkle locations in order to investigate this unique failure mode in energy pipeline observed in the field.

### 3.5 Discussion of Analytical Results

The fundamental objectives during this stage of this research project were to simulate the deformational behaviour observed in the field and the laboratory and then to develop better understanding of this unique failure mechanism. Keeping those aforementioned objectives under consideration, the analytical results obtained from this study focused on the evolution of the deformation pattern, the assessment of the wrinkle profile on the compression side of the pipe, and a detailed assessment of the longitudinal stress-strain relationship of some critical elements on the sharp fold of the wrinkle.

#### 3.5.1 Deformed Configuration

Figure 3.20 shows the development of the pipe wrinkle at different stages of the analysis as the deformation became amplified. As can be seen, there was a continuous change in the formation of the post buckling shape as the pipe specimen softened and wrinkling progressed. The individual frames of Figure 3.20, shifting from Figure 3.20a to Figure 3.20d sequentially from top to bottom, were keyed to the letters on the load-deformation curve of Figure 3.17. An initial outward bulging shape (Dinovitzer et al. 2004) of wrinkle developed, as shown in Figure 3.20a, as the pipe specimen reached Point *d* on the load-displacement (P- $\Delta$ ) curve of Figure 3.17. Then, the diamond shape (Dinovitzer et al. 2004) of the wrinkle in Figure 3.20b, which is typical for unpressurized pipe, began to develop as the jack force (*V*) reached its maximum value and the pipe reached Point *e* on the P- $\Delta$  curve of Figure 3.17. Figure 3.20c illustrates the deformed configuration of the pipe specimen at the moment it reached Point *g* on the P- $\Delta$  curve of Figure 3.17. At this point, the load carrying capacity of the deformed pipe began to increase again as there had been self-contact at the inside surface on the compression side of the wrinkled pipe. This has substantiated the observation of Das et al. (Das et al. 2002), that “the wrinkle fold on the compression side closed.” Figure 3.20d represents the final deformed configuration of the pipe

reaching Point  $h$  on the P- $\Delta$  curve of Figure 3.17, where the analysis was stopped due to the non-convergence issue.

Four strips were isolated from the compression side of the wrinkled pipe at the location of the dashed lines  $xx'$  indicated in Figure 3.20. These strips are presented in Figure 3.21 for the purpose of tracking and understanding the progression of the wrinkle formation mechanism at different stages of the load-displacement history. The deformed configuration of the selected strips included the four key points indicated in the P- $\Delta$  curve of Figure 3.17. Element numbers were incorporated into the wrinkle profiles in order to facilitate the tracking of the relative curvature or change in curvature between key load steps at a given element. As reported by Das et al. (Das et al. 2002), the tearing fracture with a long through-thickness separation was encountered in the sharp fold within the wrinkle. Based on this description of the failure and the visual inspection/assessment of the wrinkle profiles, the potentially critical elements in Figure 3.21 were considered to be Elements 8411, 8537, 8663, 8789, and 8915. These elements were identified at the end or “foot” of the wrinkle in the initial stage of loading as shown in Figure 3.21a, and then at the bottom of the fold of the wrinkle in Figure 3.21c, finally ending up at the location where telescopic tearing had the potential to occur (see Figure 3.21d). Element 7655, located at the mid-height of the wrinkle, recognized as the “crest” of the wrinkle, was also selected in order to compare the stress-strain results obtained for the aforementioned critical elements.

### ***3.5.2 Stress-Strain History***

In general, tearing fractures such as the one exhibited in the experimental specimen should occur under tensile stresses. At some of the critical elements highlighted in Figure 3.21c, the tensile stresses/strains would be greatest on the inner surface of the pipe wall and the outer surface would still be under compressive stresses/strains. However, there is a possibility of reversal of the

tensile stresses/strains on the outer surfaces of some of those critical elements indicated in Figure 3.21d at the final stage of the analysis. Given that reversed plastic bending in the vicinity of the telescoping wrinkle was anticipated, seven section points through the thickness of the shell element were incorporated during the development of the present pipe model. In Figure 3.7 and Figure 3.22, Section Point 7 (SP7) represents the top surface of the shell, (i.e., the outer surface of the pipe wall with  $\eta^+$ , as indicated in Figure 3.21c), whereas Section Point 1 (SP1) represents the bottom surface of the shell, (i.e., the inner surface of the pipe wall with  $\eta^-$ , as indicated in Figure 3.21b).

Figure 3.22 shows the true longitudinal stress-strain relationships obtained from the inner surface (SP1) and the outer surface (SP7) of the critical elements outlined in the previous section. The plots of the true stress-strain histories presented in Figure 3.22 have indicated that, although the applied loading was applied in a monotonic manner, due to the complex nature of the deformations experienced during the formation of wrinkle the local stress-strain histories—specifically at the compression side of the wrinkle in the vicinity of elements 8411, 8537, and 8663—were not monotonic and exhibited strain reversal behaviour. Results obtained from the study conducted for the purpose of understanding the post-wrinkling behaviour of energy pipelines under cyclic loadings (Das et al. 2007a) have shown the cyclic behaviour to be extremely low cycle in nature, where the number of cycles varied from four to nine. The authors (Das et al. 2007a) have also revealed that it was the strain reversals under cyclic deformations that were primarily responsible for the formation of fractures/cracks at the crest of the wrinkle. In the present case, as can be seen in Figure 18, Element 7655, located at the crest of the wrinkle, did not go through the strain reversal process. This explains why there was no fracture observed at the crest of the wrinkle of the failed field and laboratory specimens. However, the plots of the stress-strain histories for Elements 8537 and 8663, as shown in Figure 3.22c and Figure 3.22d, have illustrated that the inner faces (SP1) of each those elements were under tensile strains at an increasing rate/pattern during the early stages of P-

$\Delta$  history and then eventually began reversing, i.e., the tensile strains began decreasing during the later stages of the P- $\Delta$  history. On the other hand, the outer face (SP7) of those elements started with compressive strains in the initial stages and finally reversed towards tensile strains by the end of the analysis. Finally, for Element 8537, the strain at SP7 did actually reverse from compressive to tensile strain at the final stage of the stress-strain history; for Element 8663, the strain at SP1 was still within the tensile region. Elements 8789 and 8915, which were present at the bottom of the wrinkle fold, did not go through the strain reversal process, as can be seen from Figure 3.22e and Figure 3.22f, respectively. This fact suggests the possibility of the initiation of a fracture from the outer surface of the pipe wrinkle near Elements 8537 and 8663 and eventually the fracture of the pipe at the same location under tearing action, which was also evident in the failed field and test specimens (see Figure 3.2 and Figure 3.5).

### **3.6 Discussion of Failure Phenomena**

This preliminary investigation was focused on examining the deformations of NPS12 line pipe, which is representative of typical western Canadian pipelines, under variable loads. Although earlier research observations have shown that pipeline under monotonically increasing axial or bending strain may show accordion wrinkles (which are generally benign in nature), fracture incidents were encountered within the vicinity of a telescopic wrinkle both in a field line pipe segment and in a laboratory specimen. Based on the load-displacement histories obtained from those two incidents, monotonic non-axisymmetric loading in conjunction with a transverse load arising from the soil displacements could generate large wrinkles in the buried energy line pipes and eventually cause fracturing on the sharp folds of telescopic wrinkles located at the compressed side of the line pipe.

For simulating the complex load-deformation behaviour observed in the field and in the laboratory, a FE model was developed. The final deformed shapes obtained from the present numerical work and from the laboratory specimen (Das et al.

2002) appeared to be identical. Reasonable agreement was found in the load-deformation relationships obtained from the analytical work and from the test result. The stress-strain relations obtained from this study in the sharp fold of telescopic wrinkles on the compression side of the pipe identified the presence of the strain reversals, even for monotonic non-axisymmetric loading. This explains how a complex loading history similar to the one that arose for the field pipeline, because of harsh geo-environmental conditions, can produce strain reversals. These strain reversals could be considered key factors triggering the fracture initiating from the outer surface of the pipe wall and eventually failure of the pipeline under tearing action.

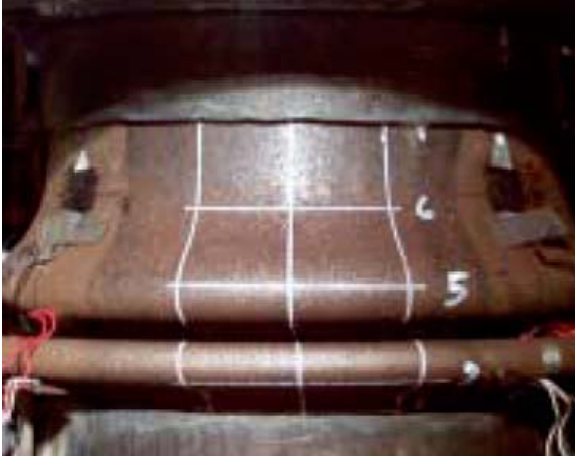


Figure 3.1 Accordion type failure under monotonic loading (Das et al. 2002)



Figure 3.2 Pipe segment showing tearing fracture at wrinkle location obtained from WestCoast Energy (Das et al. 2002)

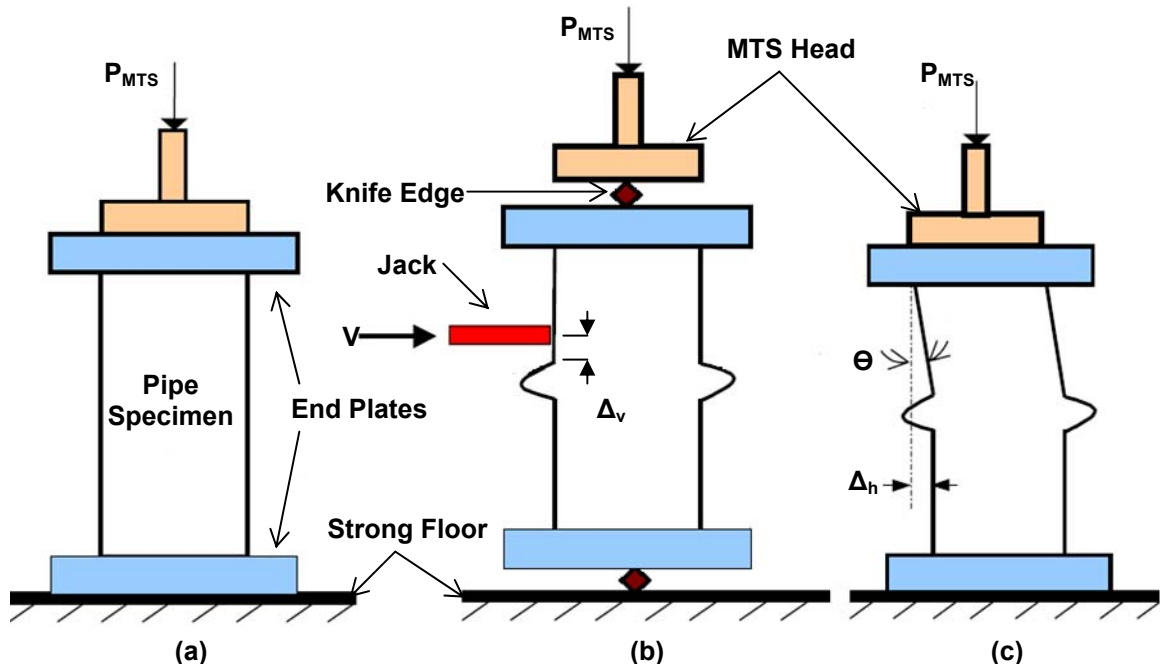


Figure 3.3 Schematic view of the test set with sequence of applied axial and transverse load (Das et al. 2002)

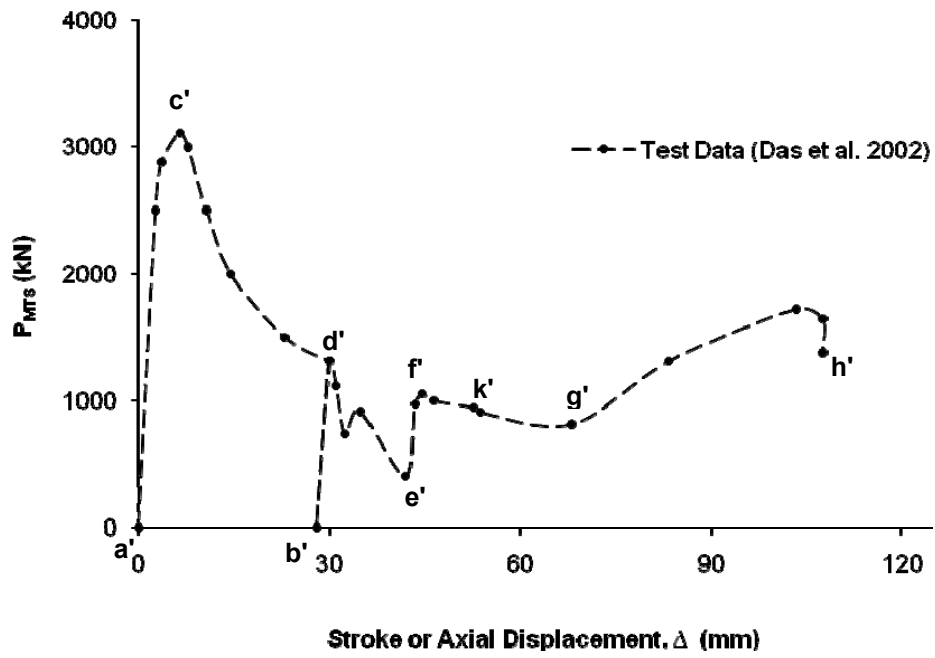


Figure 3.4 Load-displacement response for the test specimen (Das et al. 2002)



Figure 3.5 Fracture (through-thickness crack) in the wrinkle fold of the pipe specimen (Das et al. 2002)



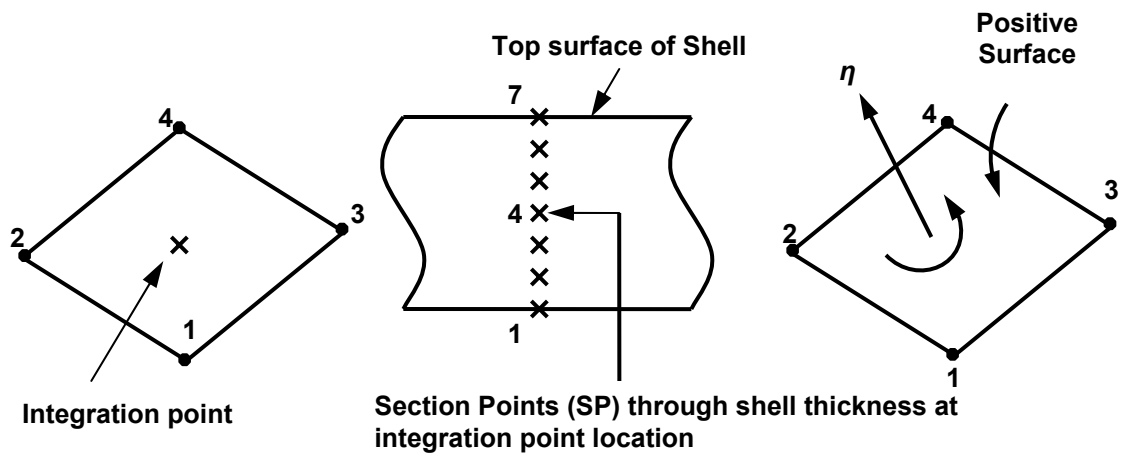


Figure 3.7 Configuration of section points in a homogeneous shell element (Hibbitt, H.D., Karlsson, B.I., and Sorensen, P., 2006)

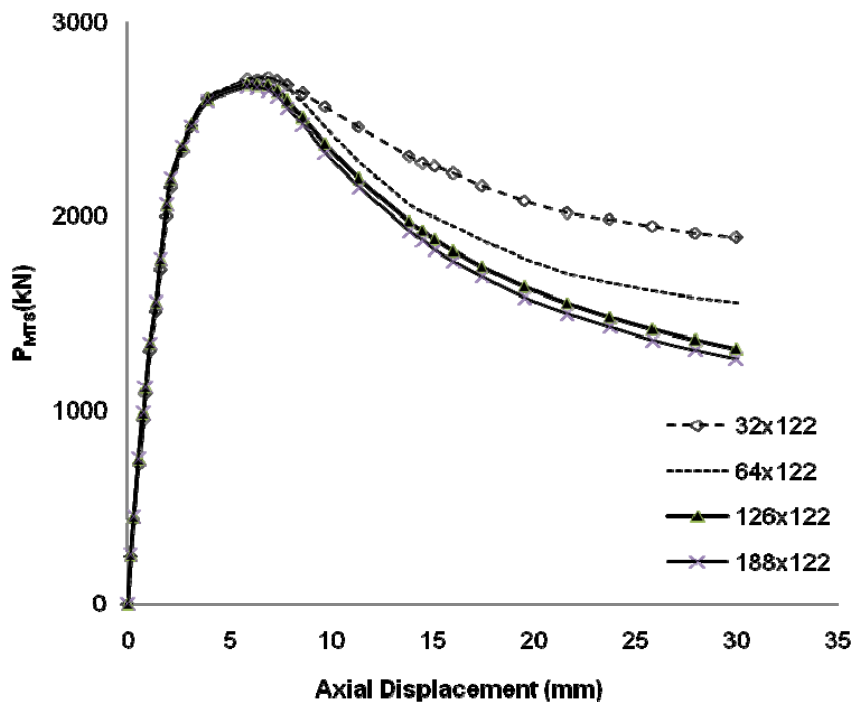


Figure 3.8 Effect of mesh refinement in circumferential direction on axial load-displacement response

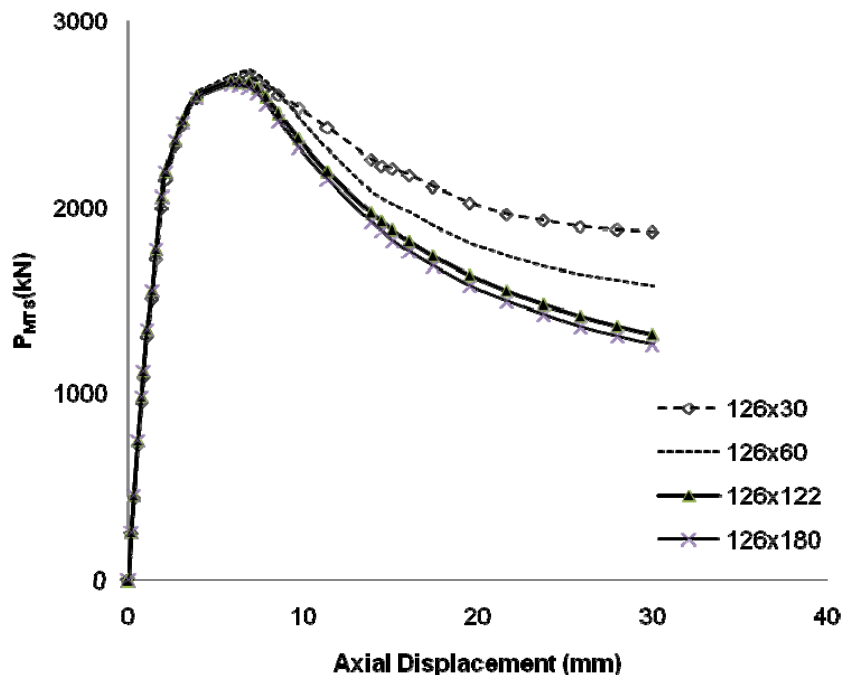


Figure 3.9 Effect of mesh refinement in longitudinal direction on axial load-displacement response

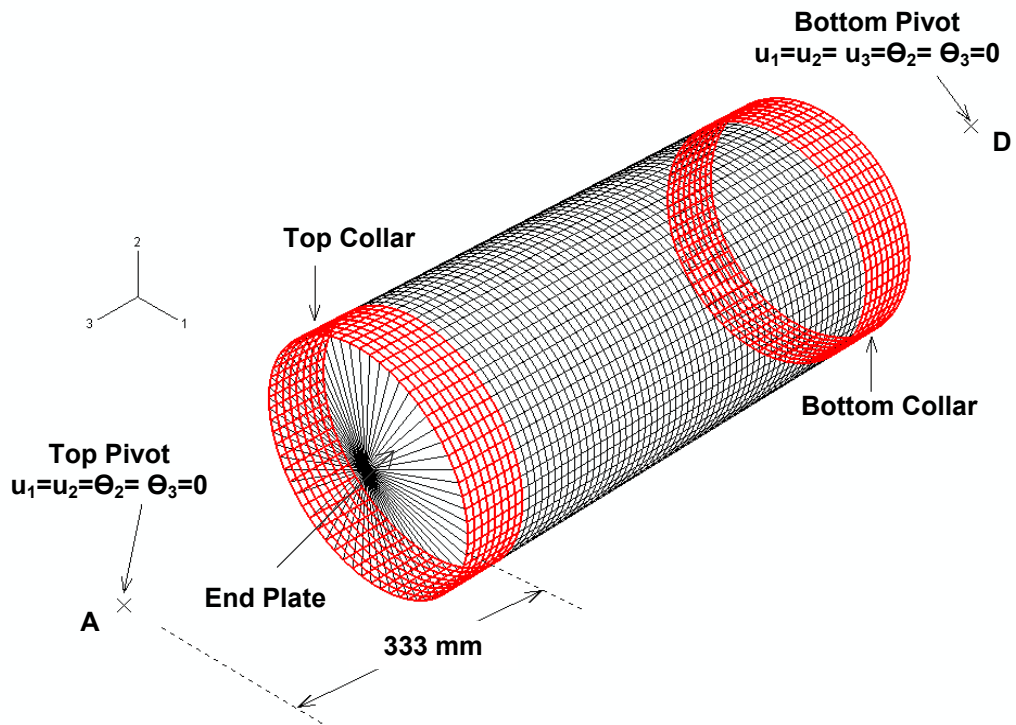


Figure 3.10 Typical geometry and initial boundary condition for the full-pipe model

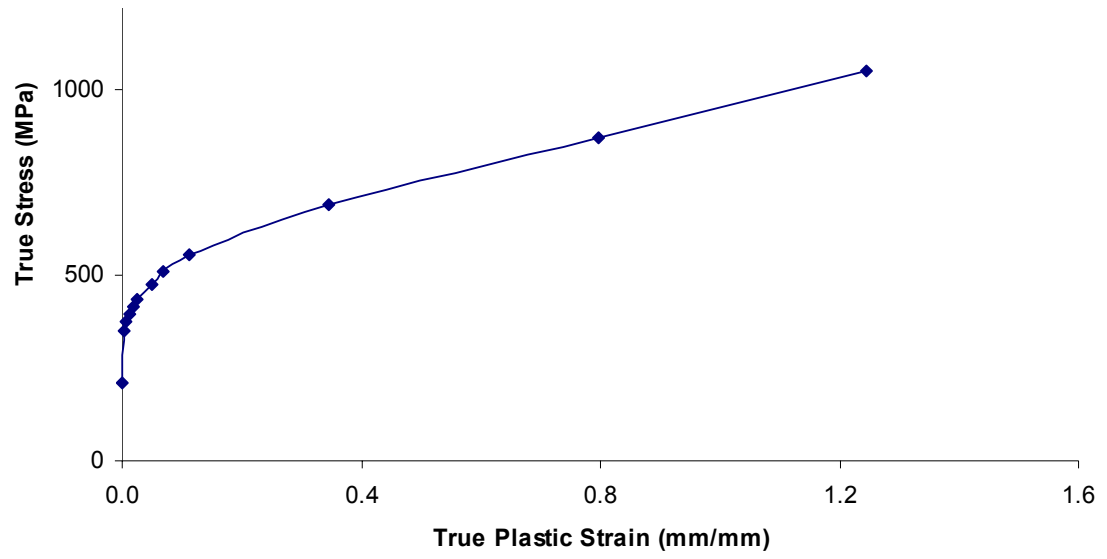


Figure 3.11 True stress versus true plastic strain behaviour until failure

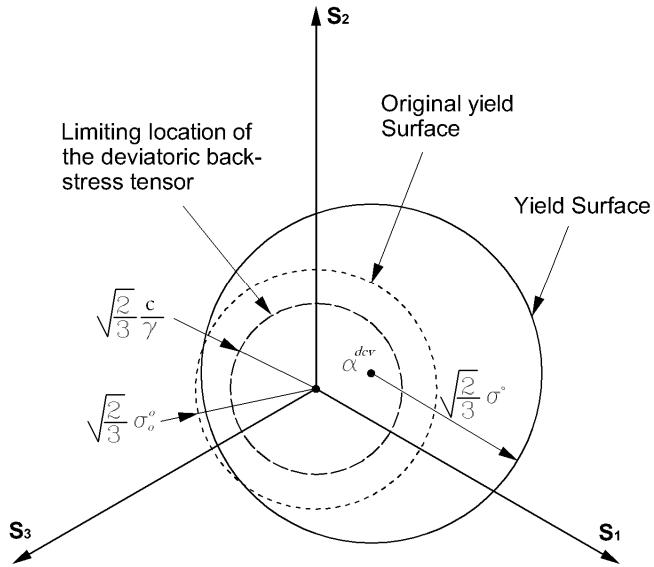


Figure 3.12 Nonlinear kinematic hardening illustrating evolution of yield surface in the stress space

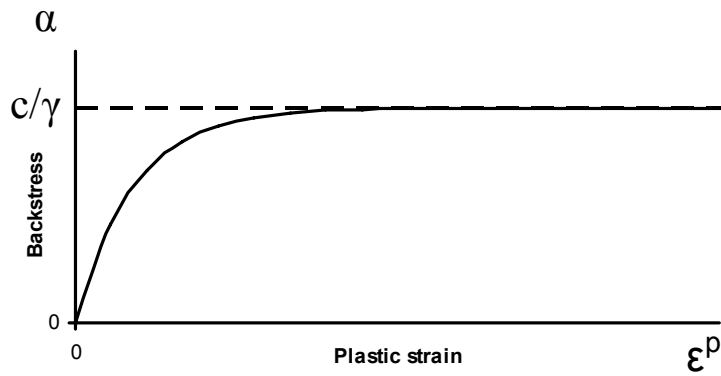


Figure 3.13 Evolution of back-stress using kinematic hardening model saturating at  $c/\gamma$ .

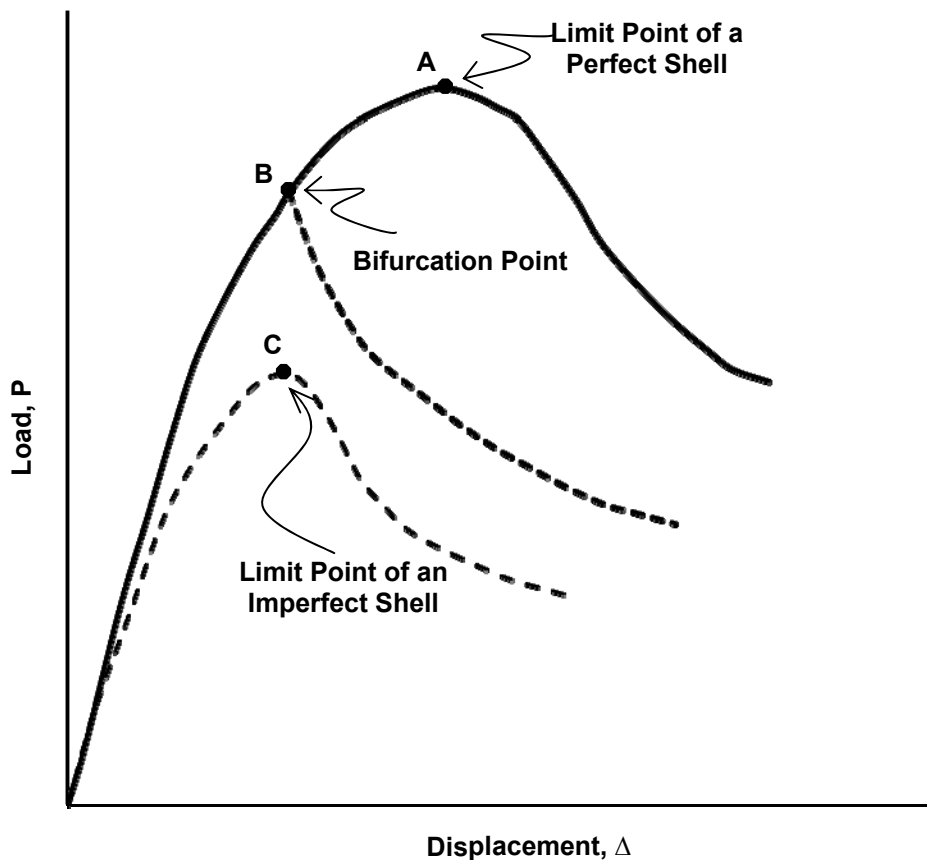


Figure 3.14 Load versus displacement response of shell structures (Bushnell 1981)

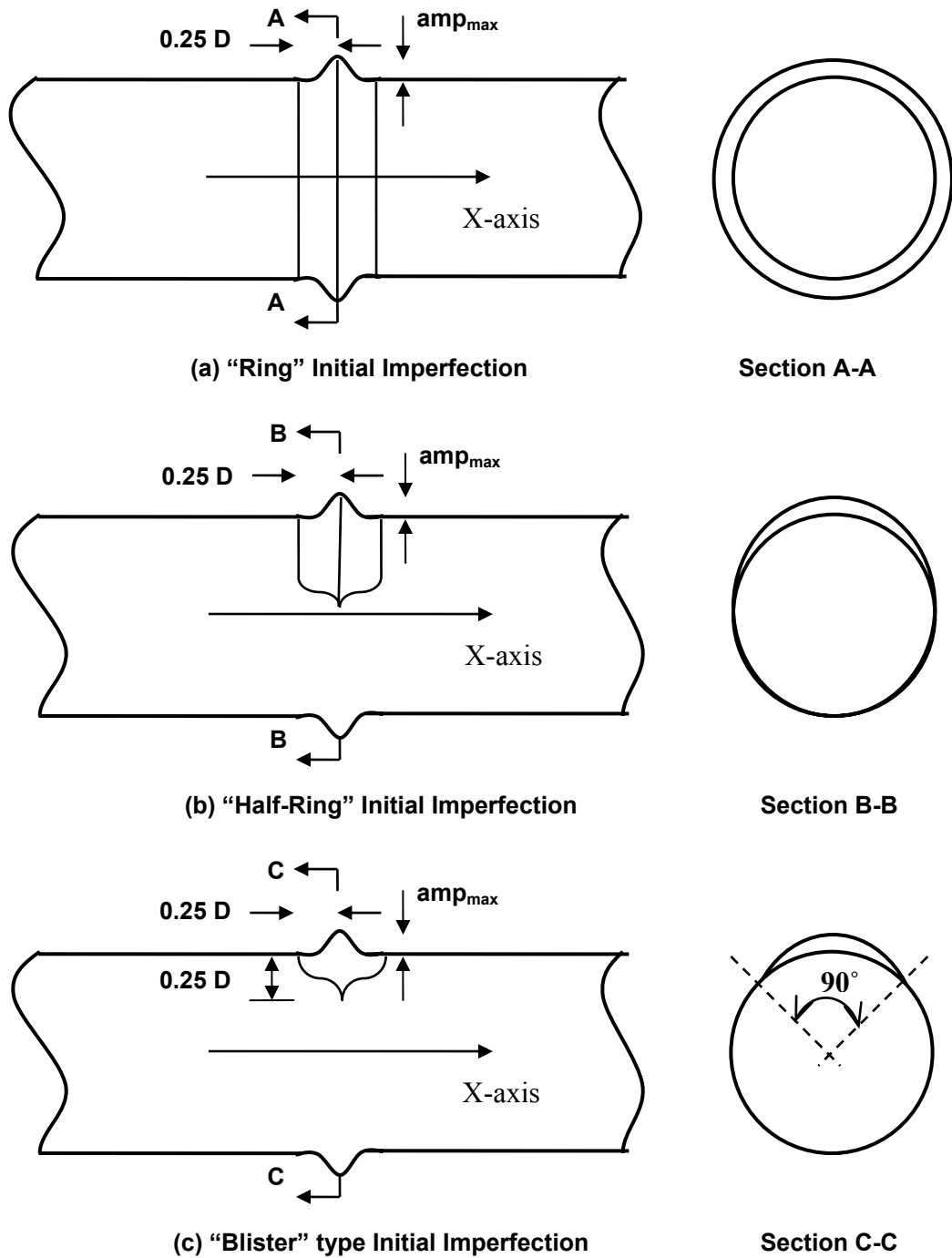
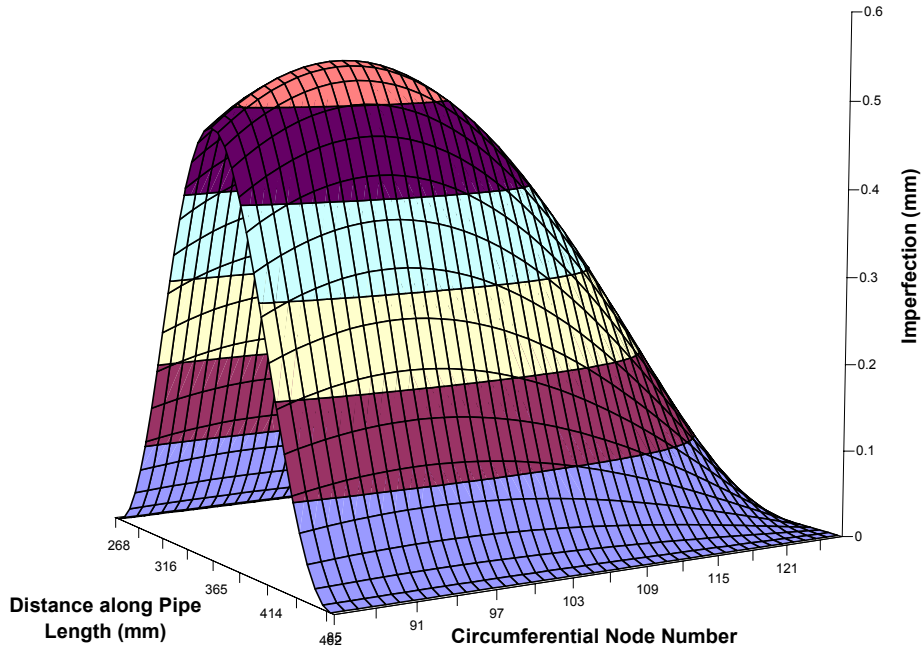
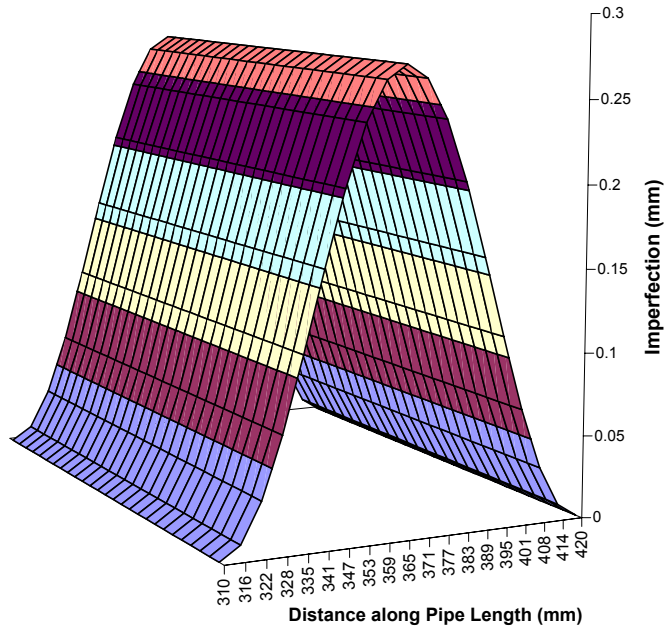


Figure 3.15 Schematic views of assumed initial imperfection patterns where X-axis represents the longitudinal direction of pipe (Dorey et al. 2006)



**(a) Blister Type Imperfection**



**(b) Radial Type Imperfection**

Figure 3.16 Imperfections Patterns adopted in the present FE Model

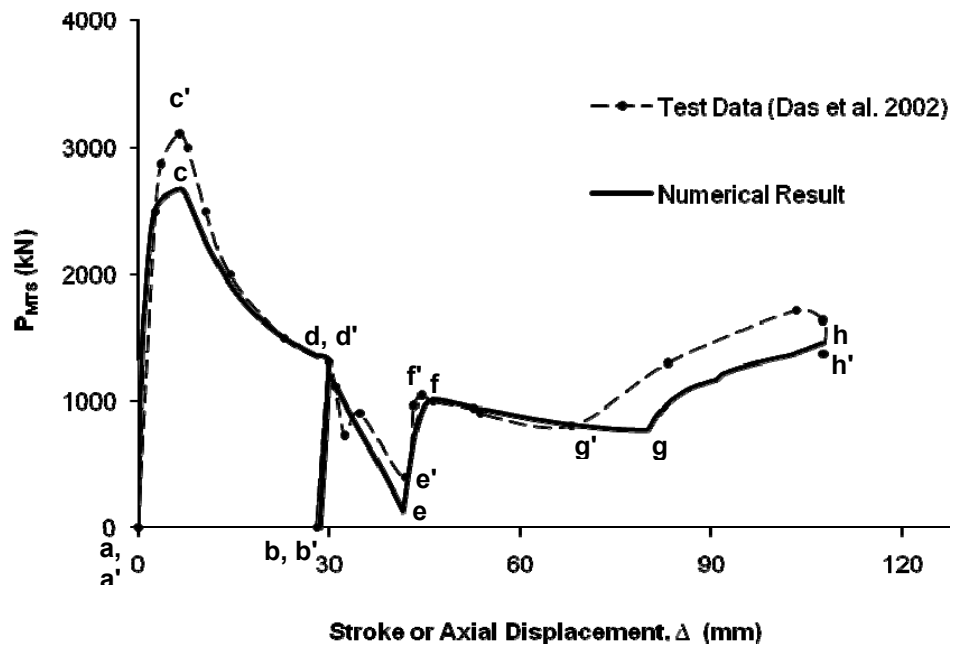


Figure 3.17 MTS load—displacement relationship obtained from FE Analysis and test result (Das et al. 2002)

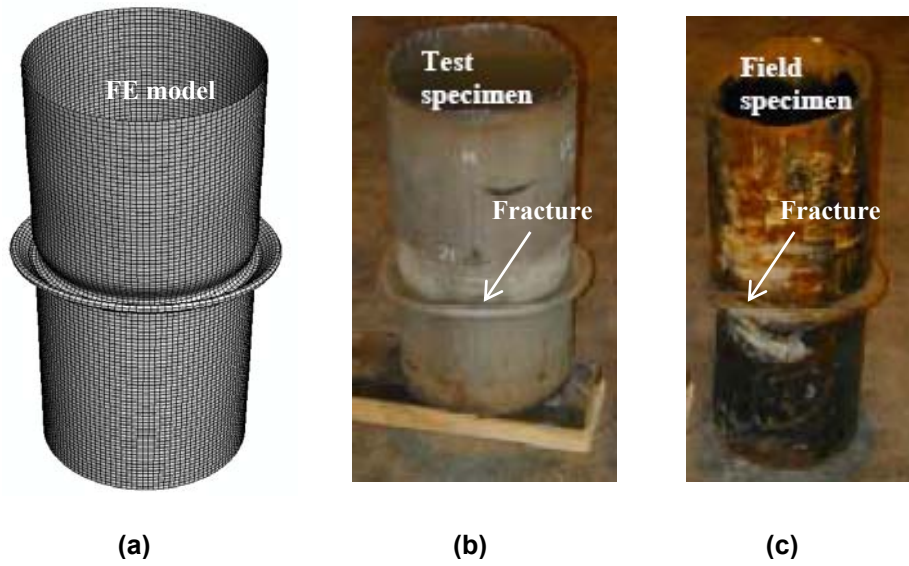


Figure 3.18 Comparison of Deformed shapes of the specimen obtained from (a) the present analytical work, (b) the experiment, and (c) the WestCoast Energy Inc.(Das et al. 2002)

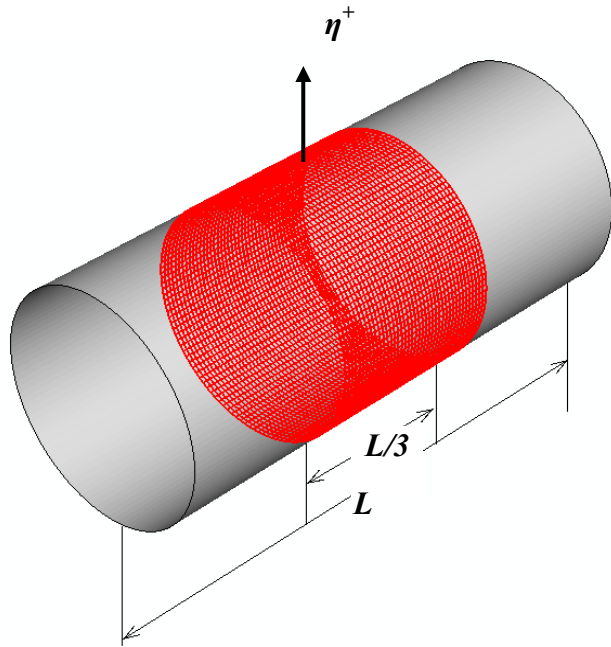


Figure 3.19 Predicted location of self-contact between inner surfaces of pipe wall ( $\eta^+$  is the direction of normal indicating outer surface of the pipe)

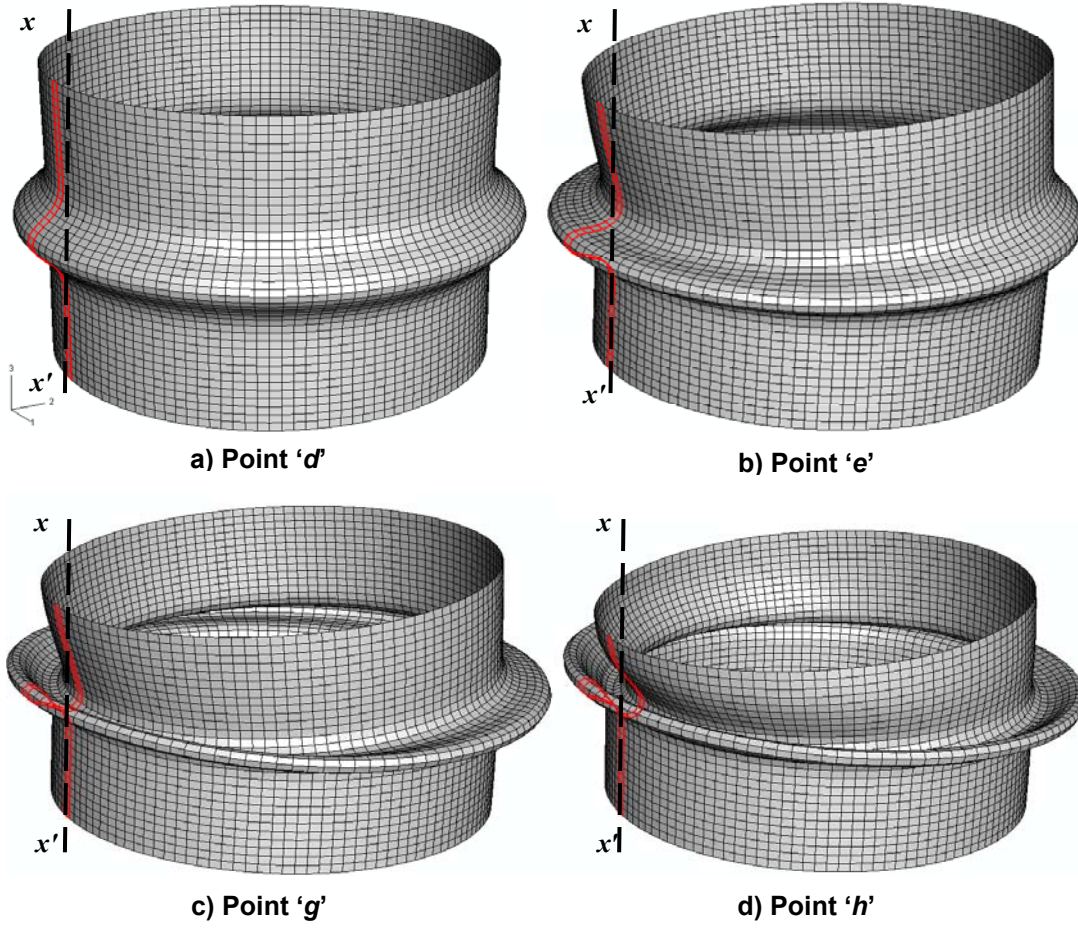


Figure 3.20 Predicted progression of deformed configuration for the pipe specimen

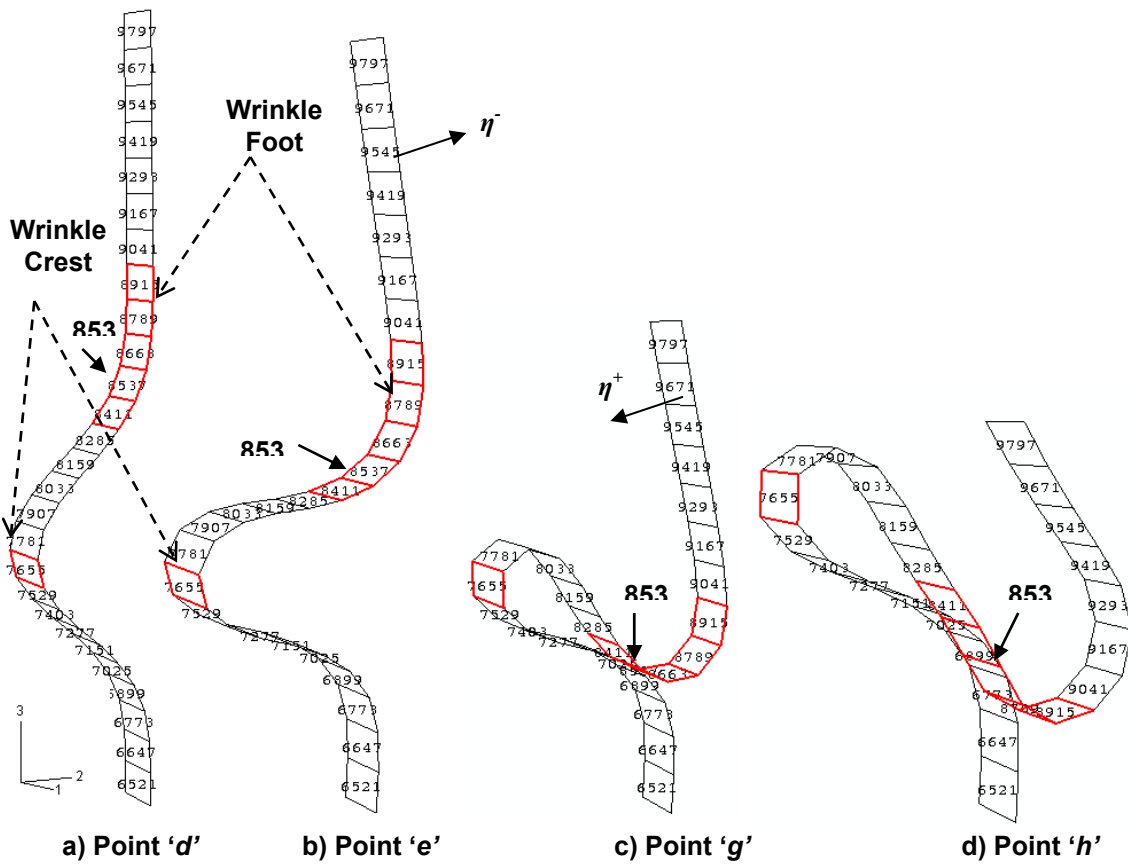


Figure 3.21 Predicted wrinkle formation process on the compression side of the pipe

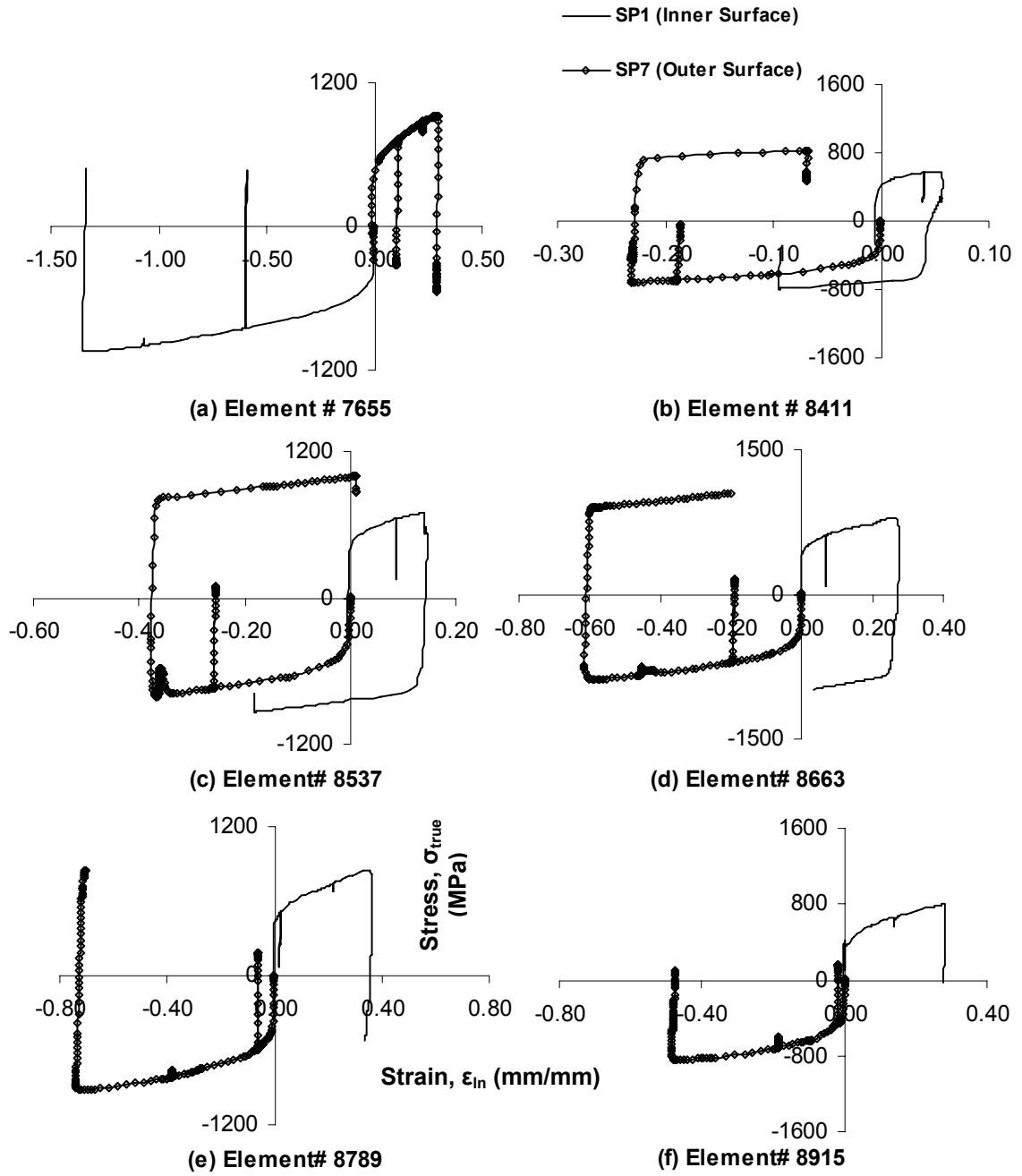


Figure 3.22 Longitudinal Stress-Strain relationship at some selected elements

### 3.7 References

- Bruschi, R., Monti, P., Bolzoni, G., and Tagliaferri, R. 1995. Finite element method as numerical laboratory for analysing pipeline response under internal pressure, axial load, bending moment. *In* Proceedings of the 14th International Conference on Offshore Mechanics and Arctic Engineering, Part 5 (of 5), Vol. 5, pp. 389-401.
- Bushnell, D. 1981. Buckling of shells-pitfall for designers. *AIAA Journal*, 19: 1183-226.
- Das, S. 2003. Fracture of wrinkled energy pipelines. PhD Thesis, Structural Engineering, University of Alberta, Edmonton, AB, Canada.
- Das, S., Cheng, J.J.R., and Murray, D.W. 2007a. Behaviour of wrinkled steel pipelines subjected to cyclic axial loadings. *Canadian Journal of Civil Engineering*, 34: 598-607.
- Das, S., Cheng, J.J.R., and Murray, D.W. 2007b. Prediction of fracture in wrinkled energy pipelines subjected to cyclic deformations. *International Journal of Offshore and Polar Engineering*, 17: 205-212.
- Das, S., Cheng, J.J.R., and Murray, D.W. 2002. Fracture in wrinkled linepipe under monotonic loading. *In* Proceedings of the 4th International Pipeline Conference, Sep 30-Oct 3 2002, Vol. B, pp. 1613-1618.
- Dinovitzer, A., Fred, A., Lazor, R., and Doblanko, R. 2004. Development and validation of a pipeline buckle and wrinkle assessment model. *In* Proceedings of the 5th Biennial International Pipeline Conference, IPC: Compression and Pump Technologies; Corrosion; Design and Construction; Environmental Issues; GIS/Database Development; Innovative Projects and Emerging Issues, Oct 4-8 2004, Vol. 2, pp. 1219-1228.

- Dinovitzer, A.S. and Smith, J.R. 1998. Strain-based pipeline design criteria review. *In* Proceedings of the 1998 International Pipeline Conference, IPC. Part 2 (of 2), Jun 7-11 1998, Vol. 2, pp. 763-770.
- Dorey, A.B., Murray, D.W., and Cheng, J.J.R. 2002. Material property effects on critical buckling strains in energy pipelines. *In* Proceedings of the 4th International Pipeline Conference, Sep 30-Oct 3 2002, Vol. A, pp. 475-484.
- Dorey, A.B., Murray, D.W., and Cheng, J.J.R. 2006. Initial imperfection models for segments of line pipe. *Journal of Offshore Mechanics and Arctic Engineering*, 128: 322-329.
- Hibbitt, H.D., Karlsson, B.I., and Sorensen, P. 2006. ABAQUS version 6.6 - theory manual.
- Mohareb, M., Kulak, G.L., Elwi, A., and Murray, D.W. 2001. Testing and analysis of steel pipe segments. *Journal of Transportation Engineering*, 127: 408-417.
- Murray, D.W. 1997. Local buckling, strain localization, wrinkling and postbuckling response of line pipe. *Engineering Structures*, 19: 360-371.
- Riks, E. 1979. An incremental approach to the solution of snapping and buckling problems. *International Journal of Solids and Structures*, 15: 529-551.
- Yukon Government. accessed on March 27, 2006. Pipeline and transportation infrastructure [online]. .
- Zhou, Z.J. and Murray, D.W. 1995. Analysis of postbuckling behaviour of line pipe subjected to combined loads. *International Journal of Solids and Structures*, 32: 3015-3036.

## 4. NUMERICAL VERIFICATION OF EXPERIMENTAL RESULTS<sup>2,3,4</sup>

### 4.1 General

Steel pipelines, either onshore or offshore, have been one of the most efficient modes for transporting and distributing hydrocarbons in North America. In Canada alone, there is over 700,000 km of energy pipelines in operation. A number of major onshore pipeline projects, such as the Mackenzie Delta Gas Pipeline Project and the Alaska Highway Pipeline Project, are proposed to be constructed in near future (Yukon Government updated on March 27, 2006). The majority of these onshore pipelines are buried pipelines. Field observations have indicated that these pipelines, especially buried in cold regions, can often undergo large deformations under displacement controlled loading process; such as slope movement, thaw settlement, frost heave, and thermal strain etc.; resulting in localized wrinkles in the pipe wall (Wilkie et al. 2001). These wrinkles usually form under the combination of internal pressure and axial load with or without bending deformation (Yoosef-Ghodsi et al. 1995). The shape of these wrinkles can be nearly axisymmetric (see Figure 4.1a) under the presence of internal pressure and axial deformation. Whereas, the shape of these wrinkles may become non-axisymmetric (see Figure 4.1b), due to the presence of shear and/or bending deformation (Das et al. 2008). However, the detriment behavioural characteristics can be expected from these wrinkles such as possible fracture (eventually a loss of containment) or benign deformation (resulted in serviceability problems), depending on the driving mechanism associated with the wrinkle formation and deformation process.

---

<sup>2</sup> Part of this chapter has been published and presented the 28<sup>th</sup> international conference on Ocean, Offshore and arctic Engineering (OMAE2009), ASME, May 2009, Honolulu, Hawaii, USA.

<sup>3</sup> Part of this chapter has been accepted in July 9, 2010 for publication in the Journal of Pressure Vessel Technology, ASME.

<sup>4</sup> Part of this chapter is in preparation for possible publication in the Journal of Offshore Mechanics and Arctic Engineering, ASME.

Previous research observations have indicated that occurrence of fracture in pipe wrinkle is rare for monotonically controlled deformation processes and the shape of these wrinkles is essentially axisymmetric, as shown in Figure 4.1a (Das et al. 2002; Zhang and Das 2008). Under the continued presence of these deformation processes, there will be stacking up of wrinkles developing an “accordion” configuration (see Figure 4.2a) and conceptually, there will be no danger of fracture at the wrinkle location (Das 2003). A cyclic deformation controlled loading history producing plastic strain reversals in the wrinkle location is necessary to generate fracture in the wrinkled pipe, and the fracture usually triggered at the crest of the wrinkle, as can be seen from Figure 4.2b (Das et al. 2001; Das et al. 2007a; Das et al. 2007b). However, a field fracture was observed recently within the wrinkle location in an NPS10 (10 in or 254 mm nominal pipe diameter) energy pipe operated by WestCoast Energy Inc. in British Columbia, Canada, as shown in Figure 4.3a (Das et al. 2002). Field observations had indicated that there were no significant strain reversals in the wrinkled pipe segment. The final failure was a “tearing” failure resulting from monotonic application of an axial load not aligned with the axis of the pipe. In order to verify this failure mechanism and determine the characteristics contributing to its formation, a proof of concept test under the combination of axial and shear load with appropriate boundary conditions was carried out at the University of Alberta (Das et al. 2002). The full-scale test was conducted on an NPS12 (12 in or 305 mm nominal pipe diameter) pipe with a wall thickness of 6.84 mm and a grade of X52 steel with specified minimum yield strength (SMYS) of 358 MPa. Reasonable similarity was observed between the failed laboratory and field specimens, as can be seen in Figure 4.3a and Figure 4.3b. Successful simulation of this behaviour in the laboratory had emphasized that fractures could be generated at wrinkle locations under monotonic load-deformation process with appropriate boundary conditions.

Being motivated from the results of the proof of concept test, a detailed numerical investigation was carried out to answer some fundamental questions regarding this unique failure mode (Ahmed et al. 2010). In this analytical work, a finite

element (FE) model was developed to simulate the complex load-deformation behaviour observed in the field and in the laboratory. Figure 4.3a, Figure 4.3b, and Figure 4.3c illustrates the comparison of the final deformed shapes of the specimens obtained from the field, the laboratory, and the analytical work, respectively. It can be seen that the FE model had produced a deformation configuration with characteristics closely resembling the post-wrinkling configuration observed both in the experiment and in the field. Reasonable agreement was found in the load-deformation relationships obtained from the analytical work and from the test result (Ahmed et al. 2010). The stress-strain relations obtained from the sharp fold of telescopic wrinkle located at the compression side of the pipe had identified the presence of the strain reversals, even for monotonic non-axisymmetric loading. It is important to add that there was no significant strain reversal at the crest of the wrinkle. Results of this analytical work had explained how a complex loading history similar to the one that arose for the field pipeline due to the presence of harsh geo-environmental conditions can produce strain reversals (Ahmed et al. 2010). These strain reversals could be considered as key factors for triggering the onset of fracture in the pipe wall and eventually, to fail the pipeline under tearing action.

Results obtained from the aforementioned full-scale test (Das et al. 2002) were very much constrained to the load-displacement plot and the final deformed shape of the failed specimens. No detailed information was documented regarding the dimensions of the pipe wrinkle formed in the full-scale test or in the field. However, more rigorous investigation was felt necessary to establish the failure criteria for predicting this tearing failure mechanism. Therefore, a full-scale experimental program was carried out on NPS16 (16 in or 406.4 mm nominal pipe diameter) and NPS20 (20 in or 508 mm nominal pipe diameter) specimens under sustained axial deformation with constant curvature (Aydin 2007). Results of this test program have indicated that the pipe specimens had exhibited very ductile behaviour with significant plastic deformation. However, the presence of small circumferential cracks in several test specimens was reported (Aydin 2007), and a significant fracture in the pipe wall was observed at the wrinkle fold of one

of the NPS16 specimens (D16P40A7-3) (Ahmed et al. 2009). The occurrence of this fracture has provided agreement with the observations of the initial analytical work presented in Chapter 3 (Ahmed et al. 2010), and thus, endowed with motivation to carry out further investigation under this research program.

The present research work has been undertaken to better understand the complete post-wrinkling behaviour and hence, to identify the failure modes of wrinkled line pipes under monotonic axial and bending deformations. Therefore, the performance of the developed FE model needs to be verified comprehensively. To underscore this specific need, the results of this experimental program have been utilized extensively to verify the acceptability of the numerical results. It is important to add that a significant portion of this test program, to be specific, the global moment-curvature response as well as pipe wall strain values which were not being addressed in the report (Aydin 2007), are reanalyzed from the raw test data of this experimental work and presented in this chapter in detail. Therefore, this chapter includes a detail description of the full-scale test program as well as a detail discussion regarding the verification of the analytical results using the test results.

## **4.2 Experimental program**

Six full-scale tests were undertaken in this experimental program. Two sizes of pipe, NPS16 supplied by Tokyo Gas Ltd. and NPS20 supplied by TransCanada Pipelines Ltd., representative of those used in pipelines for transmission of petroleum products, were tested under internal pressures ranging from zero to high with monotonically increasing axial deformation under constant curvature. These full-scale tests were carried out on three X60-grade (SMYS of 414 MPa) pipes with a diameter-to-thickness ratio of 34 and three X65-grade (SMYS of 448 MPa) pipes with a diameter-to-thickness ratio of 79. The length of 16 in. (406 mm) and 20 in. (508 mm) pipe specimens were 1550 mm and 1800 mm, respectively. It has been a challenge to generate tearing type of failure at the pipe wrinkle under laboratory controlled environment. Since, there are no well-defined

test procedures and/or analytical tools available to simulate such kind of fracture, it is hard to design and set values for the test parameters such as  $D/t$ ,  $L/D$ , internal pressure, and end rotations ( $\theta_{avg}$ ) required during the full-scale test. Therefore, a preliminary analysis was carried out to design the test parameters (Aydin 2007). Table 1 summarizes the test matrix for the six full-scale test specimens with pipe geometry, load values and internal pressure conditions. Each specimen has been given a designation that can be interpreted to identify the most of the attributes of the test. Each of the six tests is designated by a descriptor of the form of DxxPxxAxx-Z, where “Dxx” designates the outside diameter of the pipe in inch, “Pxx” is the descriptor of the level of the internal pressure as a percentage of  $p_y$ , where,  $p_y$  is equal to the internal pressure applied to the pipe such that the hoop stress reached to SMYS, “Axx” indicates the average of the applied end rotations ( $\theta_{avg}$ ) at which two ends of the specimen are locked in degree, and Z indicates the test specimen number. The test setup, instrumentation, and loading procedure adopted in the test program are described in the following sub-sections.

#### **4.2.1 Test Setup**

The experimental program was carried out in the I.F. Morrison Structural Engineering Laboratory at the University of Alberta. The test setup, shown in Figure 4.5, was designed such that the required internal pressure, concentric axial load-deformation, and large bending deformation or end rotations ( $\theta$ ) could be applied and controlled simultaneously. The axial load ( $P_{MTS}$ ) was applied by the 6,000 kN capacity MTS (universal testing) machine. The end moment was introduced by applying jack forces with the aid of an off-centre hydraulic jack at an eccentricity of  $e$  to the centerline of the pipe specimen. The end rotations were facilitated with the rotating heads at top and bottom of MTS. Two ends of the pipe specimens were machined to a bevel angle of  $45^\circ$  to satisfy the ‘full penetration groove weld’ between the 75 mm thick end plates of grade X70 (SMYS of 484 MPa) and the pipe. These end plates were required to contain the water pressure. In order to ensure the formation of wrinkle positioned approximately in the

middle of the pipe length, a set of six collars (three at the top and three at the bottom) were installed around the pipe specimen, as can be seen in Figure 4.5. These collars were 75 mm long and made out of the same pipe specimen. One of the objectives of installing these collars was to avoid triggering local buckling influenced by the end conditions (residual stress and stress concentration due to end welding). The full-scale laboratory tests were performed under internal pressures ranging from zero ( $0.0p_y$ ) to high ( $0.8p_y$ ). During the experiment, the internal pressure was applied through an air-driven fluid pump and monitored with the aid of a pressure transducer.

#### **4.2.2 Instrumentation**

For structures responding to load-deformation (P- $\Delta$ ) linearly, strain gauges can provide a convenient mean of measurement to the response of the structure in a global sense, as strain distributes proportionally to the magnitude of P- $\Delta$ . Whereas, for structures that undergo significant plastic deformation similar to the present case, it is difficult to characterize the structural response by focusing on point specific strains obtained by strain gauges, as strain redistributes and localizes during the P- $\Delta$  process. Under such condition, “average strains” over a reasonable length may be more meaningful. Therefore, instalment of several types of strain measuring devices with different gauge lengths was felt necessary.

For NPS16 pipe specimens, 28 strain gauges (5 mm gauge length) and, for NPS20 pipe specimens, 20 strain gauges were installed used to measure the local strains in longitudinal and circumferential directions. 18 Demec points (203.2 mm gauge length) for NPS16 pipes and 14 Demec points (254 mm gauge length) for NPS20 pipes were installed to measure average strains between two Demec points along tension and compression sides of specimens. Typical layouts of strain gauges and Demec points installed on 16 in. and 20 in. pipe specimens are shown in Figure 4.6a and Figure 4.6b, respectively. The characters ‘Dc’ and ‘Dt’ in Figure 4.6 represent the Demec points on compression and tension sides of the specimens, respectively. The characters ‘SC’ and ‘ST’ indicate the locations of strain gauges

to measure longitudinal strains on compression and tension sides of the specimens, respectively. The characters ‘SN’ and ‘SS’ indicates the location of strain gauges on the north and south side of the specimens, respectively. The strain gauges-‘HC’, ‘HT’, ‘HN’, and ‘HS’ were installed to measure circumferential (hoop) strains. Demec points were shifted 8 mm apart in circumferential direction from the adjacent strain gauge at the corresponding locations. Punch holes were stamped beside Demec points. One of the reasons for marking these punch holes was to facilitate measurement of distance between punch marks using a divider and a calliper, in case of dropping off an Demec point during the test. In addition, when the distances between Demec points were out of range of the mechanical Demec gauges, the strains were measured with the aid of a divider and a calliper.

Eight Linear Variable Displacement Transducers (LVDTs) were installed to measure the lateral movement of the pipe specimens. Seven Rotational Variable Differential Transducers (RVDTs) was of great importance during the tests because the end rotations of the pipe specimens were monitored through them in order to establish the locking angles of the pipes. Seven cable transducers were mounted on the bottom end plate to determine the relative rotations of the base plate in-plane and out-of-plane directions, and measure the shortening of the pipes. A data acquisition system was used to record all the loads and corresponding strokes and deformations.

### **4.3 Loading Procedures**

These tests were carried out using a loading procedure designed to mimic a wrinkle formation process and eventually fracture or rupture in the pipe wall at post-wrinkling stage under tearing action similar to that field failure discussed earlier. However, for specimen 1 (D16P0A4.5-1), the test had to be terminated prematurely, as the out-of-plane bending of the wrinkled pipe was observed during the test. The important contribution of this test was to modify the test set-up. An additional lateral bracing system was incorporated to the test assembly to

prevent out-of-plane instability. The modified test set-up was used for the rest of the tests and no out-of-plane movement was observed for the other five tests. In order to get better understanding of the specimen's behaviour, the load-deformation (P- $\Delta$ ) responses, as shown in Figure 4.7 and Figure 4.8, are chosen to describe the loading sequences and change in boundary condition during the test. In these plots, positive displacement refers to axial shortening of the pipe and positive load refers to axial compression. A summary of the major load steps in the test procedure is described in the following paragraphs.

In step one, the pipe specimen was filled with water. Then, an internal pressure of  $0.4p_y$  (11.9 MPa for NPS16 and 5.3 MPa for NPS20) was applied to all specimens, except for specimen 6 (D20P80A4-6), such that the hoop stress was to 40% of SMYS. For specimen 6, an internal pressure of  $0.8p_y$  (10.6 MPa) was applied, as the internal pressure of an operating field pipeline may vary from  $0.4p_y$  to  $0.8p_y$ , depending on the location of the pipe from the pump station. The applied internal pressure ( $p_i$ ) was obtained using Equation 4.1. In step two, an initial axial load ( $P_{cap}$ ), can be obtained by Equation 4.2, was applied to the pipe through the MTS machine, while internal pressure was adjusted to keep it constant at  $0.4p_y$  or  $0.8p_y$ . The purpose of applying  $P_{cap}$  was to compensate the effect of internal pressure on the end plates.

$$4.1) \quad p_i = np_y = n \frac{\sigma_{ys} t}{R_i}$$

$$4.2) \quad P_{cap} = \pi R_i^2 p_i$$

In the above expressions,  $p_i$  is the applied internal pressure in MPa,  $n$  is the indication of pressure level (0.4 or 0.8),  $\sigma_{ys}$  is the static yield stress or the specified minimum yield strength (SMYS) of the pipe material in MPa,  $t$  is the pipe wall thickness in mm, and  $R_i$  is the inside radius of the pipe in mm.

In the next step, an additional axial compression load was applied by MTS, making the total axial load on specimen 2 (D16P0A5-2) and specimen 3 (D16P40A7-3) of 3424 kN (Point ‘b’ on P- $\Delta$  curve in Figure 4.7). The initial axial load for other specimens is reported in Table 4.1. This additional load was applied to reduce the demand on the eccentric hydraulic jack for wrinkle formation, as the jack had a limiting capacity. This load combination was intended to reproduce the stresses in a normal operating pipeline in which there were no imposed geotechnical displacements.

In step four, the jack force ( $P_{jack}$ ) was applied monotonically to apply global moment ( $M_G$ ) or rotations  $\theta_{top}$ , and  $\theta_{bot}$  to the top and bottom ends of the pipe, respectively. The jack force ( $P_{jack}$ ) increased monotonically using a load controlled method almost until it reached point ‘c’ in Figure 4.7 and Figure 4.8. Beyond this point, the load carrying capacity of the pipe started to drop. Due to high  $D/t$  ratio, the drop in the load carrying capacity was considerably rapid in case of 20 in. pipes in comparison to 16 in. pipes, as can be revealed from Figure 4.7 and Figure 4.8. The first peak point (‘c<sub>4</sub>’ or ‘c<sub>5</sub>’ or ‘c<sub>6</sub>’) was observed distinctly for 20 in. specimens. Subsequently, a displacement controlled method was used to apply increasing monotonic bending deformation. This process was continued until a sizable wrinkle was formed with reasonable offset between top and bottom end of the pipe to ensure telescoping action. Experience obtained from previous experimental and analytical works suggests that the size of wrinkle, dependent of end rotation, can play significant role on the tearing failure of wrinkled pipe. However, the magnitude of these end rotations was limited by the test assembly and the capacity of the eccentric jack. The average end rotations ( $\theta_{avg}$ ) for different specimens are reported in Table 4.1. The end of this step is indicated by point ‘d’ on the P- $\Delta$  curve. The location of point ‘d’ on the P- $\Delta$  curve was dependent on the magnitude of the end moments or end rotations. During these stages of test, all six collars were present around the pipe specimen to ensure the formation of wrinkle away from the rigid constraint at the ends of the pipe.

In step five, both the top and bottom rotating heads were locked at an angle of  $\theta_{avg}$  (e.g.  $7^\circ$  for specimen 3). During this stage, lower two collars from top end and upper collar from bottom end were removed for allowing the growth of the wrinkle for specimen 3. Similar approach was applied for the other tests depending on the wrinkle location. By locking these two heads, the end condition became fixed-fixed which can be identified by the jump in the P- $\Delta$  curve (see path ‘d-e’ in Figure 4.7 and Figure 4.8). During this stage, the internal pressure was kept constant at  $0.4p_y$  for specimen 3 and 4, at  $0.8p_y$  for specimen 6; whereas the internal pressure was released to  $0.0p_y$  for specimen 2 and 5 to consider the effect of unpressurized condition.

In the final step, the axial displacement or MTS stroke was applied monotonically under constant curvature until the failure of the specimen. In order to keep constant curvature, the hydraulic jack force had reversed from compression to tension to keep constant curvature. With the increase of the MTS stroke, the capacity of the pipe started to drop following the path ‘e-f’ in Figure 4.7 and Figure 4.8. The load capacity of the pipe dropped significantly for the unpressurized ones (path ‘e<sub>2</sub>-f<sub>2</sub>’ or ‘e<sub>5</sub>-f<sub>5</sub>’) in comparison to the pressurized ones (path ‘e<sub>3</sub>-f<sub>3</sub>’, ‘e<sub>4</sub>-f<sub>4</sub>’, or ‘e<sub>6</sub>-f<sub>6</sub>’). At point ‘f’, the MTS load started to pick up again, as the wrinkle fold on the compression side started to close. Similar trend was observed in the previous experimental work (Das et al. 2002). During this phase (path ‘e-g’), the upper part of the specimen began to telescope into the bottom part of the specimen and at about point ‘g’, there was initiation of tearing fracture in the pipe wall as expected. However, the test was stopped or terminated, as the wrinkle in the tension side folded and the load capacity of the pipe started to pick up again as shown by the path ‘g-h’ in Figure 4.7 and Figure 4.8. The maximum values of the axial load ( $P_{MTS}$ ) observed during the test are reported in Table 4.1.

## 4.4 Test Results

### 4.4.1 Moment-Curvature Relationships

The free body diagram of the moment arm of the test setup is presented in Figure 4.9. This diagram was used to facilitate the calculation of end moments and curvatures. The global end moment ( $M_G$ ), the global curvature ( $\phi_G$ ), the local moment ( $M_L$ ), and the local curvature ( $\phi_L$ ) were calculated using the equations 4.3 to 4.6. The maximum moment and the maximum curvatures for all the specimens are reported in Table 4.1 and Table 4.2, respectively. The global moment-curvature ( $M-\phi$ ) behaviour of all the specimens except the specimen 1 are illustrated in Figure 4.10 and Figure 4.11. It can be observed from Figure 4.10 that the pipe specimen started to yield at about point 'Y' and reached its maximum moment carrying capacity or limit point at point 'H<sub>2</sub>' or 'H<sub>3</sub>'. Similar trend was observed for specimen 4 (D20P40A3.5-4) and specimen 5 (D20P0A5-5), as shown in Figure 4.11. However, the specimen 6 yielded much earlier (see point 'Y<sub>6</sub>' in Figure 4.11) in comparison to the other 20 in. pipes due to the presence of high internal pressure. It can also be added that the peak moment (point 'H<sub>6</sub>') was found to be significantly lower and appeared at much higher curvature in comparison to the other cases. Beyond point 'H', the wrinkle was started to become visible for all the specimens. As the curvature increased beyond the limit point, the pipe specimen softened with the increase of the wrinkle amplitude and the pipe capacity decreased rapidly. However, there is a significance difference in the post-wrinkling behaviour between NPS16 and NPS20 pipes. Since the  $D/t$  ratio is considerably high for NPS20 specimens, the moment capacity decreases exponentially. When the rotation angle reached the set value tabulated in parameter Table 4.1 (e.g. about 7° for specimen 3), the pipe capacity had dropped significantly and in most instances, very close to zero as identified by points 'L<sub>2</sub>' to 'L<sub>6</sub>' in Figure 4.10 and Figure 4.11. Beyond this point, the moment started to drop sharply, as the end rotations or curvature were kept constant until the end of the test.

The relation between the local ( $M_L$ ) or global moment ( $M_G$ ) with local curvature ( $\varphi_L$ ) for specimen 3 and specimen 5 is illustrated in Figure 4.11. The local moment and local curvature were determined at the wrinkled locations, while the global values were measured at the end plate locations. By making a pictorial comparison between the global and local M- $\varphi$  relationship, it is noticeable that the softening point or the limiting point of the pipe seemed to be observed at the same load step in both cases. However, due to the second order effects which produced the local moments, the local moments seemed to decrease at a slower rate with increasing deformation than that of the global end moments. Figure 4.11 also indicates that the second order effect was more pronounced in case of smaller  $D/t$  ratio.

$$4.3) \quad M_G = P_{jack} [\cos \theta_{top} \cdot e + \sin \theta_{top} (d_2 - d_1)] + P_{MTS} \cdot \sin \theta_{top} \cdot d_1$$

$$4.4) \quad \varphi_G = \frac{\theta_{top} + \theta_{bot}}{L}$$

$$4.5) \quad M_L = P_{MTS} \cdot \delta_h + P_{jack} \cdot (e \cdot \cos \theta_{top} + d_2 \cdot \sin \theta_{top} - \delta_h)$$

$$4.6) \quad \varphi_L = \frac{|\varepsilon_c| + |\varepsilon_t|}{D}$$

#### 4.4.2 *Wrinkle Location*

Figure 4.4 represents the initial wrinkled shape of the deformed pipe specimens prior to load step 5 i.e. just before locking the top and bottom rotating heads. In this figure, specimens 2-5 are lined up from left to right in chronological order. Due to the presence of internal pressure during the formation of wrinkle, an outward bulge type wrinkle was observed for all the specimens as expected (Murray 1997). Since the pipe was under bending deformation, axisymmetric wrinkles were formed on the compression side of the specimens. With the use of

collars during the wrinkling stage, the wrinkle locations for all the specimens were observed close to the mid span of the pipes (see Figure 4.4).

For specimen 2, the wrinkle was observed between the Demec points Dc3 and Dc4 (see Figure 4.6). The wrinkle crest was located 623 mm above from the bottom end of the specimen and approximately 150 mm below the mid-height, as illustrated in Figure 4.4. Whereas for specimen 3, the wrinkle was developed between the Demec points Dc6 and Dc7. At this stage, the crest of the wrinkle was located 625 mm below from the top end of the specimen and approximately 150 mm above the mid-height of the pipe. For specimen 4 and 5, the wrinkle was formed between the Demec points Dc1 and Dc2. For both specimens, the approximate location of the wrinkle crest was about 1200 mm from the top end and about 300 mm below the mid span of the specimen. For specimen 6, the wrinkle was initiated very close to the Demec point Dc6. The elevation of the wrinkle was about 254 mm above the mid-section of the pipe specimen.

## **4.5 Comments on Strains**

### **4.5.1 Strain Gauge Strains**

The maximum strain values obtained from different measuring devices are summarized in Table 2. It can be noted that the maximum longitudinal compressive strains obtained from strain gauges were ranged from 2.7% to 3.0% for all the test specimens. The maximum circumferential tensile strains obtained from NPS16 and NPS20 specimens were 2.57% (specimen 3) and 1.45% (specimen 6), respectively. Typical longitudinal and circumferential strain variations plot are presented in Figure 4.13 to Figure 4.15. The salient points marked on Figure 4.10 and Figure 4.11 are also shown in these plots. From Figure 4.13, it can be seen that the maximum local compressive strains for specimens 2 and 4 (16" pipe) occurred at much higher curvature due to low  $D/t$  ratio. However, the sudden jump in curvature values in strain variation plots (see Figure 4.13) has

indicated the onset of wrinkling for all the test specimens. It is important to note that the current pipeline design standards and practices conservatively recommend various limit states based on formation of wrinkle that corresponds to material strain of 0.5-2% (American Petroleum Institute (API) 2004; Canadian Standards Association (CSA) 2007; Det Norske Veritas (DNV) 2007). The maximum compressive strains at the onset of wrinkles of the test specimens are comparable to the values recommended by the codes. However, the strain values obtained from other devices (see Table 4.1) were found to be several times higher than these limit strain values.

The circumferential strain distributions for specimens 2 and 3 are presented in Figure 4.14. At strain gauge location 'HN-7' on specimen 3, there was sudden change in the strain values as indicated by points 'k<sub>3</sub>' and 'm<sub>3</sub>' in Figure 4.14. This indicates the onset of wrinkle at that location. Whereas, at strain gauge location 'HC-5', no change in strain values was observed as indicated by point 'H<sub>3</sub>' or point 'H<sub>2</sub>'. The circumferential strain distributions for specimens 4, 5 and 6 are presented in Figure 4.15. As can be seen from Figure 4.15, the strain value for specimen 6 (point 'H<sub>6</sub>') was much higher in comparison to other cases (point 'H<sub>4</sub>' or 'H<sub>5</sub>'). This was attributed due to the presence to high internal pressure for specimen 6.

#### **4.5.2 Demec and Calliper Strains**

The gauge lengths of the mechanical Demec gauges (or extensometer) and the callipers were varied in each specimen to fit the wavelength of the wrinkle. However, the gauge length of the Demec gauges and the callipers was approximately equal to the half of the outside diameter ( $D$ ) for all specimens. The relationships between the Demec (longitudinal compressive) strains and the global curvature at wrinkle locations are shown in Figure 4.16. One of the salient points of Figure 4.10 and Figure 4.11 ('L'), at which the MTS heads were locked, is indicated on this plot. As can be seen from Figure 4.16, the position of 'L' on the plot is not only dependent on the magnitude of the applied bending deformation,

but also dependent on D/t ratio (compare the relative position of 'L<sub>2</sub>' and 'L<sub>5</sub>') and internal pressure (compare the relative position of 'L<sub>4</sub>' and 'L<sub>6</sub>'). Unlike the strain gauge, these Demec gauges measured the strain over the whole length of wrinkle. For instance, the wrinkle was initiated between Demec points Dc3 and Dc4 for specimen 2, as shown in Figure 4.4. Therefore, the strain values measured between Dc3-5 can be considered as the wrinkle strain for specimen 2. When the wrinkle strain value reached a certain magnitude (e.g. 30.28% for specimen 2, as reported in Table 4.1), no more reading was possible to record using the Demec gauges due to the deformation configuration of the wrinkle region. Figure 4.16 also represents the plot of the global curvature versus the local compressive strain obtained from the calliper. The points 'm' and 'k' in Figure 4.16 indicate the start and end of recording the calliper readings.

As discussed earlier, the calliper readings were taken, when it was not possible to capture the whole wrinkle length using the Demec gauges. The maximum wrinkle strain recorded from the calliper was about 61.2% ('Dc 5-8' indicates gauge length of 0.75D in Figure 4.16) and 55.52% ('Dc 5-8' gauge length of D in Figure 4.18) for specimen 3. It can be addressed that the strain values from the field pipeline inspection devices (pig or geopig) would be comparable to these wrinkle strains. In the present case, the wrinkle strain is much higher than any value considered acceptable according to the current pipeline design and practices (American Petroleum Institute (API) 2004; Canadian Standards Association (CSA) 2007; Det Norske Veritas (DNV) 2007). Pipelines in present days can often undergo very significant deformation without material failure due to higher toughness and ductility. Similar trend was found in the present case. From Figure 4.7, it can be seen that the final shortening of specimen 3 reached about 220 mm over the specimen length of 1550 mm, which exhibited a significant axial ductility with an overall or global strain of 15% before partial cracking or tearing in the wall of the pipe specimen. The compressive strain growth with the axial displacement history is presented in Figure 4.17 and Figure 4.18. As can be seen from Figure 4.17, there are reasonable similarity in the development of strain with axial shortening for specimens 2 and 3, and for specimens 4 and 5. However, the

effect of  $D/t$  ratio can be considerable, as the rate of strain growth of specimens 4 or 5 was noticeably higher than that of specimens 2 or 3. It can also be observed from Figure 4.17 that the presence of high internal pressure (in case of specimen 6) can be reduce the rate of strain growth significantly at least in the initial stages of the deformation process. On the other hand, during the final stages of load-deformation process, the internal pressure did not have any significant effect on the strain growth rate among different specimens, as shown in Figure 4.18.

### ***4.5.3 Final Deformed Configurations and Failure Modes***

The final deformed configurations of different pipe specimens under sustained monotonic axial shortening with constant curvature were presented in Figure 4.19a, and Figure 4.19b for unpressurized and pressurized pipes, respectively. By observing Figure 4.19a, a pictorial comparison can be drawn between specimens 2 and 5, as most of the test parameters were identical except the  $D/t$  ratio. In both cases, the final shape of the wrinkle closely resembles the shape of a “Cowboy Hat” with a diamond buckling mode (Murray 1997), typically observed for unpressurized condition. However, a circumferential crack or rupture in the outer surface of the pipe wall at the wrinkle fold was identified during the test of these specimens. In Figure 4.19b, a pictorial comparison was made drawn between specimens 3 and 6. In both cases, internal pressure was present until the end of the test. Some similarities can be observed in the final deformed shapes, as the telescoping action (i.e. one segment of the pipe slipped inside the other segment) was present in both cases. However, for specimen 6, another wrinkle was started to become visible due to the presence of high internal pressure and lower curvature, thus leading to ‘accordion’ failure mode.

Figure 4.20 represents the cut segment of the pipe wrinkle obtained from the compression side of specimen 2 and 3. It can be seen form Figure 4.20 that there was an initiation of crack or rupture at location of ‘X’ for specimen 2. However, the geometric constrains developed from the applied test parameters did not allow the crack to propagate. On the other hand, there was significant cracking in the

pipe wall at location ‘X’ on the compression side of the wrinkle fold of specimen 3, as shown in Figure 4.20. After inspecting the final deformed shape and the cut segment from the compression side of the wrinkled pipe, it can be said that the interior surfaces of the pipe wrinkle came into contact with each other as wrinkle closed. This was followed by an axial deformation where one side of the top segment of the pipe slipped inside the bottom segment in a “telescoping” manner. In so doing it created a fold in the pipe wall and, eventually, significant tearing in the pipe wall was occurred at the proximity of the sharpest bend within this fold. But, the crack was not completely torn apart due to the sealing of the buckle lips on the tension side of the wrinkle under axial load.

However, the final deformed shape and the shape of the crack for specimen 3, as shown in Figure 4.20, have provided an evidence of this unique failure mode, as similar trends were found in the previous experimental (Das et al. 2002) and analytical work (Ahmed et al. 2010). The presence of tearing fracture in the sharp fold of the wrinkle is shown by ‘X’ location in Figure 4.21a, and Figure 4.21b for the failed field and test specimen respectively. According to the observation from the earlier analytical work (Ahmed et al. 2010), severe strain reversals could occur in the vicinity of the sharp fold of the telescopic wrinkle even for monotonic non-axisymmetric loading, and eventually, could onset the fracture initiating from the outer surface of the pipe wall (see location ‘X’ in Figure 4.21c). Similar scenario can be observed in the present case, where the cracking had initiated from the outer surface of the pipe wall and then propagated through the thickness of the pipe wall under tearing action.

#### **4.6 Summary of Experimental Results**

Six full-scale tests with different internal pressures were carried out under monotonically increasing axial deformation with constant curvature on X60 grade NPS16 pipelines with a D/t ratio of 34 and on X65 grade NPS20 pipelines with a D/t ratio of 79. A detailed discussion of load-deformation response, moment-

curvature relation, strain growth and the deformation configurations obtained from the tested specimens are presented in this chapter.

Test results have indicated that the tested pipes were found to be very ductile and had exhibited significant plastic deformation up to a certain stage of load-deformation history. The maximum longitudinal and circumferential strain values obtained from the strain gauges were in the range of 2.92% and 2.54%, respectively. The maximum wrinkle strain values varied between 30.48 to 61.21%. These strain values are much larger than the permissible strain values in the current design and maintenance practices (American Petroleum Institute (API) 2004; Canadian Standards Association (CSA) 2007; Det Norske Veritas (DNV) 2007) and thus indicates the current pipeline design standards and maintenance practices based on wrinkle limit strain may be conservative. However, one incident of significant fracture and a several incidents of rupture initiating from the outer surface of the pipe wall at the sharp fold of the wrinkle process under monotonic axial and bending deformations were observed during this test program. Consequently, this rupture in the pipe wall along with the excessive cross-sectional deformation can put the safe operation of a field line pipe in danger. The results of all the tests has also identified that the post-wrinkling behaviour and tearing fracture of a wrinkled pipe are dependent on the amount of the curvature ( $\theta_{avg}$  i.e. locking angle),  $D/t$  ratio, and internal pressure.

The results of this test program have provided a valuable database for conducting a comprehensive analytical investigation to better understand the tearing mode of failure for wrinkled pipe and hence, to formulate a guideline to predict a limiting parameter for this unique mode of failure.

#### **4.7 Numerical Studies**

Test data obtained from the above mentioned experimental program (Aydin 2007) were used extensively in the calibration and verification of the developed FE model. In addition, the true stress ( $\sigma_{true}$ ) – true plastic strain ( $\epsilon_p$ ) relation of both

X60-grade and X65-grade pipe materials up to fracture were established to simulate the complete post-wrinkling behaviour.

As discussed in the previous chapter, the first phase of this research program was focused on understanding and simulating the complex behaviour of the proof concept test (NPS12 pipe specimen) (Das et al. 2002), and then, to identify key factors responsible for this failure mode. For achieving these objectives, a numerical investigation was carried out to develop and analyze a FE model using ABAQUS (Hibbitt, H.D., Karlsson, B.I., and Sorensen, P., 2006). The FE model developed in Chapter 3 along with some modifications has been utilized to replicate the behaviour of NPS16 and NPS20 pipe specimens.

#### ***4.7.1 Description of FE Model***

In Chapter 3, a full-pipe (NPS12) segment was divided into a number of discrete elements to represent the geometry in the FE model, as shown in Figure 4.22. The mid-surface of the pipe wall was modelled using four-node general purpose shell element with reduced integration. Seven section points (SP) were chosen through the thickness of each element in order to facilitate numerical integration and to properly capture the plasticity resulting from extreme local bending occurring in the vicinity of the telescoping wrinkle. Figure 4.22 represents the initial boundary conditions of the full pipe model. The displacements  $u_1$  and  $u_2$ , and the rotations  $\theta_2$  and  $\theta_3$  were restrained for the top pivot point A, whereas,  $u_1$ ,  $u_2$ ,  $u_3$ ,  $\theta_2$  and  $\theta_3$  were restrained for the bottom pivot point B.

All the test specimens used in this experimental program (Aydin 2007) had a plane of symmetry in the geometry, boundary and loading conditions. Consequently, for NPS16 and NPS20 pipe specimens, only half of the pipe along its longitudinal axis was modeled instead of the full pipe to optimize or reduce the computation time. A typical geometry and initial boundary conditions that were used in the numerical analyses of the NPS16 specimens is shown in Figure 4.23. Accordingly, displacements  $u_1$ , and rotations  $\theta_2$  and  $\theta_3$  were restrained at all nodes

along the longitudinal plane of symmetry. Other than using the symmetric boundary condition, major features of the half-model were very much similar to that of the full-model. It is important to note that an initial imperfection (Dorey et al. 2006) was incorporated in the half-model in order to initiate the wrinkle numerically. Similar approach was adopted for the full-model. However, the number of collars used during the test of NPS16 and NPS20 were different to that of NPS12. In this case, the effect of collars was included in the finite element model through the use of a set of additional elements representing the collars, which were removed at the appropriate load step through the use of element death. The finite element mesh shown in Figure 4.23 has been selected based on the approach similar to the mesh study used in Chapter 3 which showed that a further refinement of the mesh did not significantly change the numerical results. Since the pipe went through a large deformation during the load-deformation history, there is a possibility of self-contact among various portions of the pipe at the wrinkle location as the wrinkle closes. Therefore, a self-contact formulation is incorporated in this FE model. Similar approach was also adopted for the full-pipe model.

#### ***4.7.2 Boundary Conditions and Loading Sequences***

The boundary conditions and loading sequences used in FEA were divided into a number of steps. A summary of the load steps adopted for NPS16 and NPS20 specimens (Half-pipe) is included below:

- Apply an internal pressure (ranging between  $0.4p_y$  and  $0.8p_y$ ) at the inside surface of the pipe wall.
- Apply an initial axial load (e.g. 1712 kN for NPS16 pipe specimens), which is half of the experiment value (Aydin 2007) shown in Table 4.1, to the top pivot ‘A’ in the negative global “3” direction (see Figure 4.23).

- Apply end moments or end rotations about global “1” axis incrementally to the pivot points ‘A’ and ‘B’, until  $\theta_{avg}$  (an average of  $\theta_{top}$  and  $\theta_{bot}$ ) reaches the specified value in Table 4.1 (e.g.  $7^\circ$  for D16P40A7-3). During this stage, a non-axisymmetric wrinkle was formed at the compression side of the pipe (see Figure 4.1).
- Change the end conditions of top and bottom pivots by keeping the rotations about global “1” axis fixed at their current level with the aid of a torsional spring at the top and bottom pivot point. During this stage, lower two collars from top end and upper collar from bottom end were removed for allowing the growth of the wrinkle for specimen 3 (D16P40A7-3). Similar approach was applied for the other test specimens depending on the wrinkle location.
- Release the internal pressure for specimen 2 and specimen 5, or keep the internal pressure at the same level ( $0.4p_y$  or  $0.8p_y$ ) for other specimens.
- Finally, increase the axial displacement at ‘A’ until it reaches the final axial-shortening as indicated by the test results of the pipe specimen.

#### **4.7.3 True Stress-True Plastic Strain Curves**

As mentioned earlier, the NPS16 pipe specimens were taken from a grade X60 steel pipe with specified minimum yield strength (SMYS) of 414 MPa, whereas the NPS20 pipe specimens were taken from a grade X65 steel pipe with specified minimum yield strength (SMYS) of 448 MPa. However, for X60 pipe material, the actual yield strength at 0.5% strain was found to be 488 MPa, and for X65 pipe material, the actual yield strength at 0.5% strain was found to be 495 MPa, which are significantly higher than SMYS. Six tension coupons, three for X60 grade and three X65 grade, were tested in this research program. The measured mechanical properties of both X60 and X65 pipe materials are tabulated in Table 4.3. The measured engineering stresses and strains obtained from these coupon tests are presented in Figure 4.24a and Figure 4.24b. The average of these

engineering stress and strain values were used for computing the input data for the half-pipe model of NPS16 and NPS20 pipes.

The following two expressions (Hibbitt, H.D., Karlsson, B.I., and Sorensen, P., 2006) were used to determine the true stress – true (logarithmic) plastic strain behaviour in order to model the constitutive behaviour of the pipe material,

$$4.7) \quad \sigma_{true} = \sigma_{nom} (1 + \varepsilon_{nom})$$

$$4.8) \quad \varepsilon_p = \varepsilon_{ln}^{pl} = \ln(1 + \varepsilon_{nom}) - \frac{\sigma_{true}}{E}$$

Where,  $\sigma_{nom}$  is the nominal or engineering stress,  $\varepsilon_{nom}$  is the nominal or engineering strain recorded from the coupon (material) tests, E is the modulus of elasticity,  $\sigma_{true}$  is the true stress, and  $\varepsilon_p$  or  $\varepsilon_{ln}^{pl}$  is the true logarithmic plastic strain.

Figure 4.25a and Figure 4.25b, representing the true stress – true plastic strain values for X60 and X65 respectively, were obtained directly from the initial segment of the engineering stress-strain data (up to peak load). After the peak load, the true stress versus true plastic strain curves (see Figure 4.26), were generated using a power-law equation by rearranging the well-known Ramberg–Osgood relation (Ramberg and Osgood 1943; Canadian Standards Association (CSA) 2007). Similar approach was taken by several researchers (Cheng et al. 1998; Khoo 2000; Zhao et al. 2009). In its original form, the Ramberg–Osgood relation (Ramberg and Osgood 1943) for total strain ( $\varepsilon$ ) is given by Equation 4.9. In Equation 4.9, the first term on the right side, ' $\sigma/E$ ', represents the elastic part of the strain, whereas the second term, ' $k(\sigma/E)^n$ ', accounts for the plastic part. The parameters k and n, describing the strain hardening behaviour of metal, are constants that depend on the material being considered. Now, by introducing the yield strength of the material ( $\sigma_y$ ), a new parameter,  $\alpha$  can be defined, which is related to k (see Equation 4.10).

$$4.9) \quad \varepsilon = \frac{\sigma_{true}}{E} + k \left( \frac{\sigma_{true}}{E} \right)^n$$

$$4.10) \quad \alpha = k \left( \frac{\sigma_y}{E} \right)^{n-1}$$

Now, by relating expression 4.9 and expression 4.10, the Ramberg–Osgood equation can be rewritten as shown in Equation 4.11. After rearranging the expression 4.11, the plastic strain ( $\varepsilon_p$ ) can be obtained using Equation 4.12. Now, by introducing another material constant  $c_p$ , the plastic strain ( $\varepsilon_p$ ) can be obtained using expression 4.13. In this ‘power-law’ relationship between true stress and plastic strain, the hardening behaviour of the material depends on the material constants  $c_p$  and  $n$ .

$$4.11) \quad \varepsilon = \frac{\sigma_{true}}{E} + \alpha \frac{\sigma_y}{E} \left( \frac{\sigma_{true}}{\sigma_y} \right)^n$$

$$4.12) \quad \varepsilon_p = \varepsilon - \frac{\sigma_{true}}{E} = \alpha \frac{\sigma_y}{E} \left( \frac{\sigma_{true}}{\sigma_y} \right)^n$$

$$4.13) \quad \varepsilon_p = c_p \left( \frac{\sigma_{true}}{\sigma_y} \right)^n$$

The parameter,  $c_p$  in Equation 4.13, represents the true plastic strain at the start of strain hardening or yield offset. By forcing Equation 4.13 to pass through the true stress and true plastic strain corresponding to the peak load as indicated by plots X-60 (FEA) and X-65 (FEA) in Figure 4.25a, and Figure 4.25b, respectively, the true stress versus true plastic strain curve after the peak load were generated by adjusting ‘ $n$ ’ alone. The trial true stress versus true plastic strain relationship was adjusted iteratively until the numerical simulation agreed with coupon test results, similar to the iterative procedure proposed by Matic (Matic 1985).

The parameters,  $c_p$  and  $n$ , used to obtain the material model curve for the half-pipe model as shown in Figure 4.26, are tabulated in Table 4.4. As can be seen from Figure 4.25 and Figure 4.26, there is an initial elastic relationship between the true stress-true plastic strain values followed by a gradual development of plastic flow with strain hardening for both materials. Assuming the pipe material had been comprised of an isotropic metal, the classical von Mises yield criterion was used to predict the yield surface in the present model. Since there was no involvement of cyclic loading in the loading histories obtained from the field and the laboratory tests, an isotropic hardening was found to be reasonable in this study.

## **4.8 Verification of FE Model**

The performance of the half-pipe model and the methodology adopted in this FEA was validated using the test results of NPS16 and NPS20 pipe specimens reported in Table 4.2, including load-displacement ( $P-\Delta$ ) response, moment-curvature ( $M-\phi$ ) relation and the initial and final deformed shapes. A comparison of all the test and analytical results describing the efficiency or accuracy of the present FE model are presented in Table 4.5

### **4.8.1 Load-Displacement ( $P-\Delta$ ) Response**

#### **4.8.1.1 NPS16 Specimens**

The load-deformation ( $P-\Delta$ ) behaviours obtained from tests and finite element analyses (FEA) of specimen 2 (D16P0A5-2) and specimen 3 (D16P40A7-3) are shown in Figure 4.27. As can be seen, the overall trend of the load-displacement responses has matched reasonably well. Initially an axial load along with the internal pressure ( $0.4p_y$ ) was applied in specimens 2 and 3, as indicated by path 'a-b'. At point 'b', the end moments were applied until it reached the desired end rotation (e.g. point 'd<sub>2</sub>' for specimen 2). During this load-path ('b-d<sub>2</sub>'), the maximum load value predicted from FEA, indicated by point 'c' in Figure 4.27, was about 2% higher than the value obtained from the test as indicated by point

'c'. When the specimen 2 reached point 'd<sub>2</sub>' in the  $P-\Delta$  curve, the internal pressure was released, as indicated by the load drop in Figure 4.27. Similar scenario was observed in the FE simulation of specimen 2 (see point  $d'_2$ ). At this point, the end rotations were locked at their present level i.e. the end conditions became fixed-fixed, which can be identified by the jump in the  $P-\Delta$  plot. Both path 'd<sub>2</sub>- e<sub>2</sub>' and path ' $d'_2$ -  $e'_2$ ' have matched reasonably well. After locking the end rotations, the maximum load value at point ' $e'_2$ ' obtained from FEA was about 5% lower than the value obtained from the test (point 'e<sub>2</sub>').

In case of specimen 3, the internal pressure was kept constant at  $0.4p_y$  and hence, there was no drop in the pipe capacity at point 'd<sub>3</sub>'. However, the end rotations seemed to be locked little earlier in the FEA as indicated by point  $d'_3$ . After reaching the peak load, the load carrying capacity of specimen 2 (path 'e<sub>2</sub>-f<sub>2</sub>' or path ' $e'_2$ - $f'_2$ ') had dropped more sharply, in both test and analysis, compared to specimen 3 (path 'e<sub>3</sub>-f<sub>3</sub>' or path ' $e'_3$ - $f'_3$ '), due to unpressurized condition. After locking the end rotations for specimen 3, the maximum load value (see point ' $e'_3$ ') obtained from FEA was about 2% higher than the value obtained from the test (see point 'e<sub>3</sub>'). When the pipe specimen reached point ' $f'_2$ ' or point ' $f'_3$ ' on the  $P-\Delta$  curve obtained from the FE analyses, the contact pressure at the wrinkle location was tracked due to self-contact at the interior surface of the pipe wall, and the load carrying capacity of the deformed pipe started to pick up again (see path ' $f'_2$ - $h'_2$ ' or ' $f'_3$ - $h'_3$ '). In the actual tests, the closing of the wrinkle (point 'f<sub>2</sub>' or point 'f<sub>3</sub>') seemed to occur slightly away from the location observed in the FEA. Since simplifications and assumptions were adopted in the contact formulation to optimize solution cost, this variation can be considered reasonable. The analyses were stopped at point ' $h'_2$ ' or point ' $h'_3$ ', when the specimens reached close to the final axial shortening (point 'h<sub>2</sub>' or point 'h<sub>3</sub>') observed during the tests. In summary, a good correlation between the test behaviour and numerical prediction was obtained, and for the key points  $c'$ ,  $d'$ ,  $e'$ ,  $f'$ ,  $h'$  on the plot, the analytical result appeared to be generated in a similar manner to the test.

#### 4.8.1.2 NPS20 Specimens

The load-deformation ( $P$ - $\Delta$ ) behaviours obtained from the tests and the FE analyse of NPS20 specimens are shown in Figure 4.28. As can be seen, the overall trend of the load-displacement responses has matched reasonably well. Initially an axial load along with the internal pressure ( $0.4p_y$ ) was applied in specimens 4 (D20P40A3.5-4) and specimen 5 (D20P0A3.5-5), whereas, an initial axial load along with the internal pressure ( $0.8p_y$ ) was applied in specimens 6 (D20P80A4-6). After applying the initial axial load and internal pressure, the end moments were applied until it reached the desired end rotation (e.g. point 'd<sub>4</sub>' for specimen 4). For specimen 4, during this load-path ('a-c<sub>4</sub>-d<sub>4</sub>'), the maximum capacity predicted from FEA (see point 'c'<sub>4</sub>' in Figure 4.28) was almost at the identical location observed during the test as indicated by point 'c<sub>4</sub>'. Similar observation can be made for the other two specimens (see point 'c'<sub>5</sub>' and 'c'<sub>6</sub>'). At point 'd'<sub>4</sub>', the end rotations were locked at their present level as can be identified by the jump in the  $P$ - $\Delta$  plot. Both path 'd<sub>4</sub>- e<sub>4</sub>' obtained from test and path 'd'<sub>4</sub>- e'<sub>4</sub>' obtained from FEA have matched reasonably well.

In case of specimen 5, the internal pressure was released at point 'd'<sub>5</sub>', as indicated by the load drop in Figure 4.28. However, there was no evidence of load drop in the  $P$ - $\Delta$  plot obtained from the test result. It is important to mention that, with the full release of the internal pressure ( $0.4p_y$ ), the final deformed shape did not match with the deformation configuration obtained from the test. Therefore, three different trials, i) with full release ( $0.4p_y$ ), ii) with partial release ( $0.2p_y$ ), and iii) with no release ( $0.0p_y$ ) of internal pressure, were applied to resemble the test deformed shape as well as to obtain the  $P$ - $\Delta$  response closer to the test value. A pictorial comparison of  $P$ - $\Delta$  responses for these different conditions is illustrated in Figure 4.29. As can be seen from Figure 4.29, the  $P$ - $\Delta$  plot with partial release of internal pressure did resemble the test behaviour with reasonable accuracy. A comparison of the final deformed shapes, which will be presented later in this chapter, also matched well in the case of partial release. Although a reasonable correlation can be observed (see FEA-5 in Figure 4.28), due to this assumption,

the load drop indicated by path ' $d'_5$ -  $e'_5$ ' was not as significant as observed in the test (see path ' $d_5$ -  $e_5$ ').

For specimen 6, the initial peak, indicated by ' $c'_6$ ' or ' $c_6$ ', was significantly high due to the presence of high internal pressure. After locking the end rotations (see point ' $d'_6$ '), the pipe reached its maximum load carrying. After reaching the peak load (see point ' $e'_6$ '), the load carrying capacity of specimen 6 (path ' $e_6$ - $f_6$ ' or path ' $e'_6$ - $f'_6$ ') did not drop as sharply as the other NPS20 specimens. It can also be observed from Figure 4.28 that the wrinkle closed for specimen 6 much later as compared to the other two specimens due to the presence of higher internal pressure (see path ' $e'_4$ - $f'_4$ ', path ' $e'_5$ - $f'_5$ ', and path ' $e'_6$ - $f'_6$ '). After comparing Figure 4.27 and Figure 4.28, It can also be added that the initial contact for the NPS20 specimens was earlier than that of the NPS16 specimens. This may be attributed due to higher D/t ratio for NPS20 pipe specimens. However, for all the test specimens, the closing of the wrinkle (point ' $f_2$ ', ' $f_3$ ', ' $f_4$ ', ' $f_5$ ', ' $f_6$ ') seemed to occur slightly earlier from the location observed in the FEA. As mentioned earlier, due to simplifications and assumptions adopted in the contact formulation in order to optimize solution cost, these variations can be considered reasonable.

The maximum load value at point ' $e$ ' for all the FE analyses is presented in Table 4.5 along with the corresponding test results for comparison. As can be seen from Table 4.5, the FE model did predict the test behaviour with reasonable efficiency. In summary, a good correlation between the test behaviour and numerical prediction was obtained, and for the key points  $c'$ ,  $d'$ ,  $e'$ ,  $f'$ ,  $h'$  on the plot, the analytical result appeared to be generated in a similar manner to the test.

#### **4.8.2 Moment-Curvature ( $M$ - $\phi$ ) Response**

The global end moment ( $M_G$ )-global curvature ( $\phi_G$ ) relationships obtained from tests and FE analyses for NPS16 specimens and NPS20 specimens are presented in Figure 4.30 and Figure 4.31. For NPS16 specimens, the yielding of the pipe specimens (point ' $Y$ ' in Figure 4.30) appeared to develop slightly earlier in the FE

analyses. Similar observation can also be made for NPS20 specimens. The maximum moment values (see point ‘*H*’ in Figure 4.30 and Figure 4.31) obtained from numerical analysis presented in Table 4.5 along with the corresponding test results. As shown in Table 4.5, the FEA predicted the moment capacity with reasonable accuracy.

However, some variations can be observed in the post-peak or post-wrinkling behaviour, as indicated by path '*H-L*'. Also, initial stiffness of *M-φ* plot obtained from FEA was always found to be slightly lower than those of the physical experiment. These variations may be attributed due to the effect of the material properties, the discrepancy between test and FEA in terms boundary conditions and application of end moments, and the assumed imperfections pattern used in the numerical model. It should also be added that, although the peak moments (see point ‘*H*’) were observed at the curvature very close to the test values for most of the specimens, the peak moment for specimen 6 seems to occur at a smaller curvature value (see Figure 4.31) This may be attributed due to the isotropic behaviour of the FE model, as material anisotropy can be considerable under high internal pressure. Since the focus of this present study is mostly dealing with the post-wrinkling behaviour and hence, the ultimate limit state, assuming isotropic behaviour seems reasonable. However, the overall trend of the *M-φ* responses has matched reasonably well.

Beyond point ‘*H*’, the wrinkle was started to become visible during the tests as well as the FE analyses of both specimens. As the curvature increased beyond the limit point, the pipe specimen softened with the increase of the wrinkle amplitude and the pipe capacity decreased rapidly both in test and numerical analyses (see path ‘*H-L*’ or path ‘*H'-L'*”). When the rotation angle reached the set value tabulated in parameter Table 4.1 (e.g. about 7° for specimen 3 in Figure 4.30), the pipe capacity had dropped significantly as identified by point ‘*L*<sub>3</sub>’. Beyond this point, the moment started to drop sharply, as the end rotations or curvature were kept constant until the end of the test or the FEA of specimen 3. However, the end rotations were locked at a smaller value for specimen 2, as identified by point ‘*L*<sub>2</sub>’

for test or ' $L'_2$ ' for FEA in Figure 4.30. Similar observation can be made for NPS20 specimens. However, in the post-wrinkling behaviour, a significance difference was noticed in both test and FEA between NPS16 pipes and NPS20 pipes with moderate internal pressure. Since the  $D/t$  ratio was considerably higher for NPS20 specimens, the moment capacity decreases significantly (see path ' $H'_3-L'_3$ ' in Figure 4.30 and path ' $H'_4-L'_4$ ' in Figure 4.31). The global curvature ( $\phi_G$ ) values at point ' $L$ ' in Figure 4.30 and Figure 4.31 were obtained from numerical analysis and presented in Table 4.5 along with the corresponding test values. As shown in Table 4.5, the FEA predicted the global curvature with reasonable accuracy.

In general, a good correlation was observed in the post wrinkling behaviour of the test specimens and the FE model. Although the actual values of the applied loads or moments may vary due to differences in material properties (Dorey et al. 2002) and initial imperfections and slight variations in loading sequence, the global trends and magnitude observed in the FEA can be considered to be fairly accurate.

### ***4.8.3 Comparison of Deformed Shapes***

#### **4.8.3.1 Initial Deformed Shapes**

Figure 4.32a and Figure 4.32b represent the initial wrinkle shapes obtained from the tests and FE analyses of specimen 2 and specimen 3, respectively. Figure 4.33 represent the initial deformed shapes of the deformed pipe specimen 4 and specimen 5, respectively. These deformed shapes were attained at point 'd' on the  $P-\Delta$  curve or at point 'L' on the  $M-\phi$  diagram i.e. just before locking the top and bottom rotating heads. For all test and FEA specimens, due to the presence of internal pressure up to point 'd' on the  $P-\Delta$  plots, an outward bulge type wrinkle was observed for all the specimens as expected (Murray 1997). Since the pipe was under bending deformation, axisymmetric wrinkles were formed on the compression side of the specimens (see Figure 4.32 and Figure 4.33).

For specimen 2, the wrinkle was observed between the Demec points DC-3 and DC-4 during the test, as shown in Figure 4.32a. Whereas, the wrinkle was developed between the Demec points DC-6 and DC-7 during the test of specimen 3, as shown in Figure 4.32b. The wrinkles were noticed almost at the identical locations of both specimens in the developed FE models (see Figure 4.32). For specimen 4 and 5, the wrinkle was formed between the Demec points Dc1 and Dc2 as indicated in Figure 4.33a and Figure 4.33b, respectively. Similar trend was observed in the deformed configurations of FE analyses of those specimens. For specimen 6, it was reported that the onset of buckling or pipe wrinkling initiated between the Demec points DC-5 and DC-7 during the test (Aydin 2007). During the FEA of specimen 6, the wrinkle was observed at similar location. However, since there was no photograph available for the specimen 6 at point 'd<sub>6</sub>' on the *P-Δ* curve (see Figure 4.28), it was not possible to compare the initial deformed shape of FEA-6.

#### **4.8.3.2 Final Deformed Shapes**

The final deformed configurations obtained from test and FEA of pipe specimen 2 and specimen 3 were presented in Figure 4.34 and Figure 4.35, respectively. A pictorial comparison can be made between test and FEA by observing the views from the compression and tension sides of the pipe specimens, as shown in Figure 4.34a and Figure 4.35a; and in Figure 4.34b and Figure 4.35b, respectively. For specimen 2, in both test and FEA, the final shapes of the wrinkle closely resemble the shape of a “Cowboy Hat” with a diamond buckling mode (Murray 1997), typically observed for unpressurized condition. However, as internal pressure was present until the end of the test and FEA of specimen 3, the presence of telescoping action (i.e. one segment of the pipe slipped inside the other segment) was noticed.

The final deformed configurations obtained from test and FEA of specimen 4 are presented in Figure 4.36. As shown in Figure 4.36, the FEA of specimen 4 was able to simulate the post-wrinkling shape observed during the test. However,

although internal pressure condition of specimen 4 was similar to specimen 3, both in test and FEA, the presence of telescoping action was not as prominent as specimen 3. This may be attributed due to high  $D/t$  ratio, as cross-section deformation was more significant in specimen 4 compared to specimen 3.

The final deformed configurations obtained from test and FEA of specimen 5 are presented in Figure 4.37 and Figure 4.38. As mentioned in section 4.8.1.2, different internal pressure conditions was applied in the FE analyses of specimen 5 and the  $P-\Delta$  plot with partial release of internal pressure came close to the test behaviour. A comparison of the final deformed shapes obtained from the FE analyses with partial release and full release of internal pressure is presented in Figure 4.37. As can be seen, the deformation configuration with no internal pressure has more pronounced diamond buckling mode (Murray 1997) and significant cross-sectional distortion compared to the deformed shape with partial release of internal pressure. However, the FEA with partial release of internal pressure produced the deformed shape comparable to the post-buckling shape observed during the test, as shown in Figure 4.38.

Figure 4.39 illustrates a pictorial comparison of the final deformed shapes obtained from the test and FEA of specimen 6. As can be seen, the FE model did predict the deformed shape with reasonable accuracy. It can be added that although internal pressure was present for both specimen 4 and 6, due to presence of higher internal pressure for specimen 6, the presence of telescoping action was noticeably similar to specimen 3 (see Figure 4.35 and Figure 4.39). However, formation of second wrinkle was observed much earlier in both test and FEA of specimen 6, which justifies why no fracture was observed in the wrinkle fold. In summary, it can be said that the FE model produced a deformed shape with features closely resembling the post-wrinkling shape observed during the test of all specimens.

#### 4.8.4 Comparison of Strain Values

As discussed in section 4.4, during the physical tests, both local and global pipe wall strain values were obtained using different measuring devices. Some of these strain measurements were used as further validation of the FE analyses results. Since one of the fundamental objective of this research program is to understand the complete post-wrinkling behaviour (up to failure) of the deformed pipes, only the global strain values obtained mechanical Demec (or extensometer) and calliper readings were selected for discussion. The comparison between the experimental and predicted longitudinal compressive strains along with axial shortening of NPS16 and NPS20 pipes are presented in Figure 4.40 and Figure 4.41, respectively. As shown in Figure 4.40 and Figure 4.4, in general the strain values obtained from the FE analyses are in good agreement with the measured experimental strains, providing a reasonable estimate of both the general behaviour and the maximum wrinkle strain values.

For specimen 2, since the wrinkle was initiated between Demec points Dc3 and Dc4 (see Figure 4.32a), the strain values measured between Dc3-5 (with a gauge length  $\approx 0.5D$ ) and Dc2-5 (with a gauge length  $\approx 0.75D$ ) were considered for comparison. Similarly, the strain measurements between Dc5-7 and Dc5-8 were considered for comparison for specimen 3 (see Figure 4.32a). For specimen 4, the strain values obtained between Dc1-3 were used (see Figure 4.33), whereas the measurements between Dc5-7 and Dc4-7 (see Figure 4.6 for location of Demec points) were considered for specimen 6. Although the general trends were reasonably matched, the FEA predicted the strain values slightly higher in the initial stages of deformation history for specimens 2, 3, and 4 (see Figure 4.40 and Figure 4.41), whereas, for specimen 6, the FEA predicted the strain values noticeably higher in the earlier part of displacement history. One of the reasons for these dissimilarities was the difference in the gauge length used in the test and analyses, as the gauge length used in FEA is dependent of mesh size used in the FE model. This may also occur due to the slight variations in the location and the wave length of the wrinkle observed during test and FEA, and this could be even

critical in the early stages of deformation history. However, the variation between the analytically predicted values and the test measurements were not significant under large deformation, as can be seen from Figure 4.40 and Figure 4.41. It is also important to add that the effect of the variation in gauge length is found to be more sensitive for the smaller gauge length (e.g. 0.5D) compared to the higher gauge length.

The relationships between the experimental and predicted longitudinal compressive strains – global curvature ( $\phi_g$ ) responses of NPS16 and NPS20 pipes are presented in Figure 4.42 and Figure 4.43, respectively. One of the salient points ('L' or 'L<sup>n</sup>') of global moment – global curvature ( $M-\phi_g$ ) relations (see Figure 4.30 and Figure 4.31), at which the pivot points were locked in both FEA and tests, is indicated on these plots. As can be seen from Figure 4.42 and Figure 4.43, the general trends for most of the specimens, except Dc5-7 of specimen 6, were found to be in good agreement with the values obtained from tests. Moreover, the locations of the key point 'L<sup>n</sup>' on the FEA plots were very close to the test measurements (compare the relative positions of 'L<sub>2</sub>' and 'L<sub>2</sub><sup>n</sup>', 'L<sub>3</sub>' and 'L<sub>3</sub><sup>n</sup>', and, 'L<sub>4</sub>' and 'L<sub>4</sub><sup>n</sup>').

#### **4.9 Summary of Numerical Results**

Based on the comparison drawn in 4.8, the numerical analyses provided a fairly good prediction of the test behaviour of all specimens in terms the load-displacement response, and the moment-curvature relation. In addition, the FE analyse has successfully captured both local and global behaviour of the test specimens in terms of the deformation configurations as well as strain measurements. Hence, it seems reasonable to carry out further analyses using this numerical model to predict the localized stresses and strains at wrinkle locations of all NPS16 and NPS20 specimens for developing the failure criteria to predict for the failure modes of all these specimens.

Table 4.1 Full-scale Test Matrix and Load Values

Specimen Designation	Steel grade			Initial	Maximum	Maximum	Locking	Internal
	[SMYS (MPa)]	$D/t$	$L/D$	Axial Load (kN)	Axial Load, $P_{MTS}$ (kN)	Moment, $M_G$ (kN-m)	Rotation, $\theta_{avg}$ (Degrees)	Pressure (% of <sup>a</sup> $p_y$ )
D16P0A4.5-1				3424	5556	770	4.5	0
D16P0A5-2	X60 [414]	34	3.8	3424	5245	706	5.0	0
D16P40A7-3				3424	5700	711	7.0	40
D20P40A3.5-4				1540	2800	641	3.5	40
D20P0A5-5	X65 [448]	79	3.5	1540	2150	618	5	0
D20P804-6				2560	3000	430	4	80

<sup>a</sup>Indicates that  $p_y$  = the internal pressure (in MPa) applied to the pipe such that the hoop stress reached to SMYS or  $\sigma_{ys}$ .

Table 4.2. Maximum Curvature and Strain Values

Specimen Designation	Maximum Curvature		Maximum Strain (%)			
	Global, $\phi_G$ ( $1 \times 10^{-6}$ /mm)	Local, $\phi_L$ ( $1 \times 10^{-6}$ /mm)	Strain Gauge		Demec Strain (*G.L. $\approx$ $\frac{1}{2}$ D)	Caliper Strain ( <sup>a</sup> G.L. $\approx$ $\frac{2}{3}$ D, D)
			Longitudinal Strain	Circumferential Strain		
D16P0A5-2	129.2	579.6	-2.82	+2.34	-30.28	-58.83
D16P40A7-3	165.9	835.6	-2.81	+2.57	-34.4	-61.21, -55.52
D20P40A3.5-4	68.3	531.3	-2.92	+0.98	-48.82	
D20P0A5-5	98.6	733.0	-2.71	+1.17	-40.36	
D20P80A4-6	80.7	634.0	-2.73	+1.45	-5.42	-59.92

<sup>a</sup> G.L. = Gauge Length in mm, D = Outer Diameter of Pipe in mm

Table 4.3 Material Properties of Test Specimens from Coupon Tests

<b>Measured properties</b>	<b>X-60</b>	<b>X-65</b>
Young Modulus, E (GPa)	201	208
Static Yield Stress, $\sigma_y$ (MPa)	488	495
Static Ultimate Stress, $\sigma_u$ (MPa)	543	557
$\sigma_u/\sigma_y$	1.114	1.125
Elongation (%) (Gage Length= 200 mm)	33.4	24

Table 4.4 Assumed Material Properties

<b>Assumed Properties (Power Law Equations)</b>	<b>X-60</b>	<b>X-65</b>
$N$	14.5	12.5
$c_p$	0.002654	0.002567

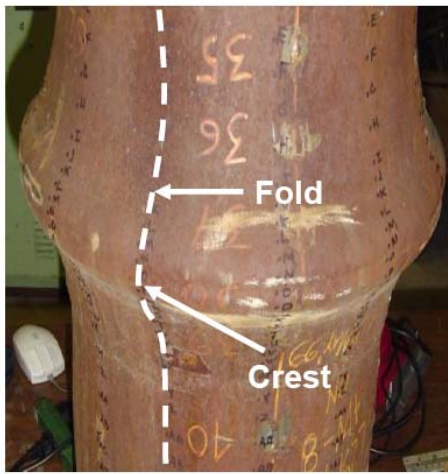
Table 4.5 Comparison of Test and Analytical Results

Specimen	Maximum Axial Load, $P_{MTS}$ (kN) <sup>a</sup>			Maximum End Moment, $M_G$ (kN-m)			Maximum Global Curvature, $\phi_G$ (kN-m) <sup>a</sup>		
	Test	FEA	$\lambda = \frac{\text{Test}}{\text{FEA}}$	Test	FEA	$\lambda = \frac{\text{Test}}{\text{FEA}}$	Test	FEA	$\lambda = \frac{\text{Test}}{\text{FEA}}$
D16P0A5-2 (FEA-2)	5233	4997	1.047	706	728	0.970	113.5	116	0.978
D16P40A7-3 (FEA-3)	5031	5137	0.979	711	733	0.970	156	157.6	0.990
D20P40A3.5-4 (FEA-4)	2450	2357	1.039	641	633	1.013	68.3	69.82	0.978
D20P0A5-5 (FEA-5)	1915	1890	1.013	618	637	0.970	96.3	95.76	1.006
D20P80A4-6 (FEA-6)	3091	3105	0.995	430	426	1.009	80.7	81.7	0.988

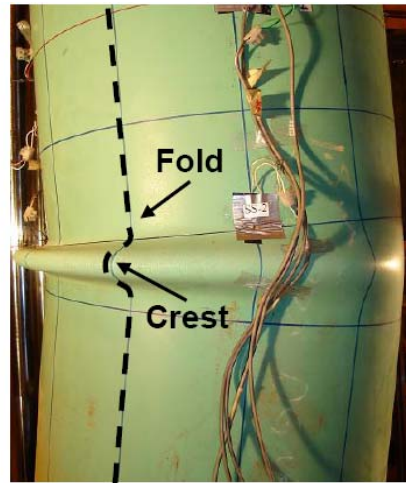
<sup>a</sup>Note: The term, ' $\lambda$ ', represents the efficiency of the present FEA

The term, ' $P_{MTS}$ ', represents the maximum axial load at point 'e' or 'e' in  $P$ - $\Delta$  plots (see Figure 4.27 and Figure 4.28)

The term, ' $\phi_G$ ', represents the maximum end moment at point 'L' or 'L' in  $M$ - $\phi$  plots (see Figure 4.30 and Figure 4.31)

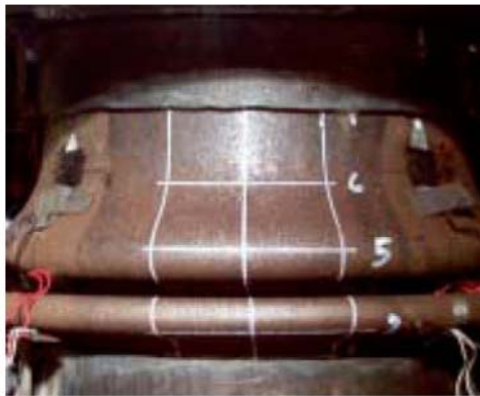


(a) Axisymmetric

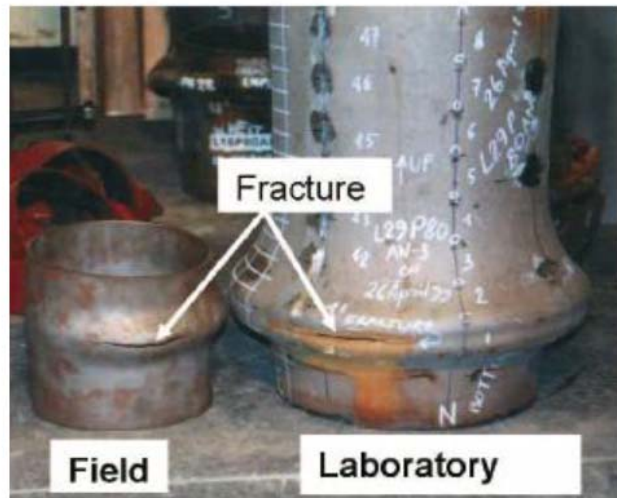


(b) Non-axisymmetric

Figure 4.1 Typical Wrinkle Shapes (Das 2003; Aydin 2007)



(a)



(b)

Figure 4.2 (a) Accordion type failure under monotonic loading (Das et al. 2002); and (b) fractures under cyclic deformation (Das et al. 2007b).

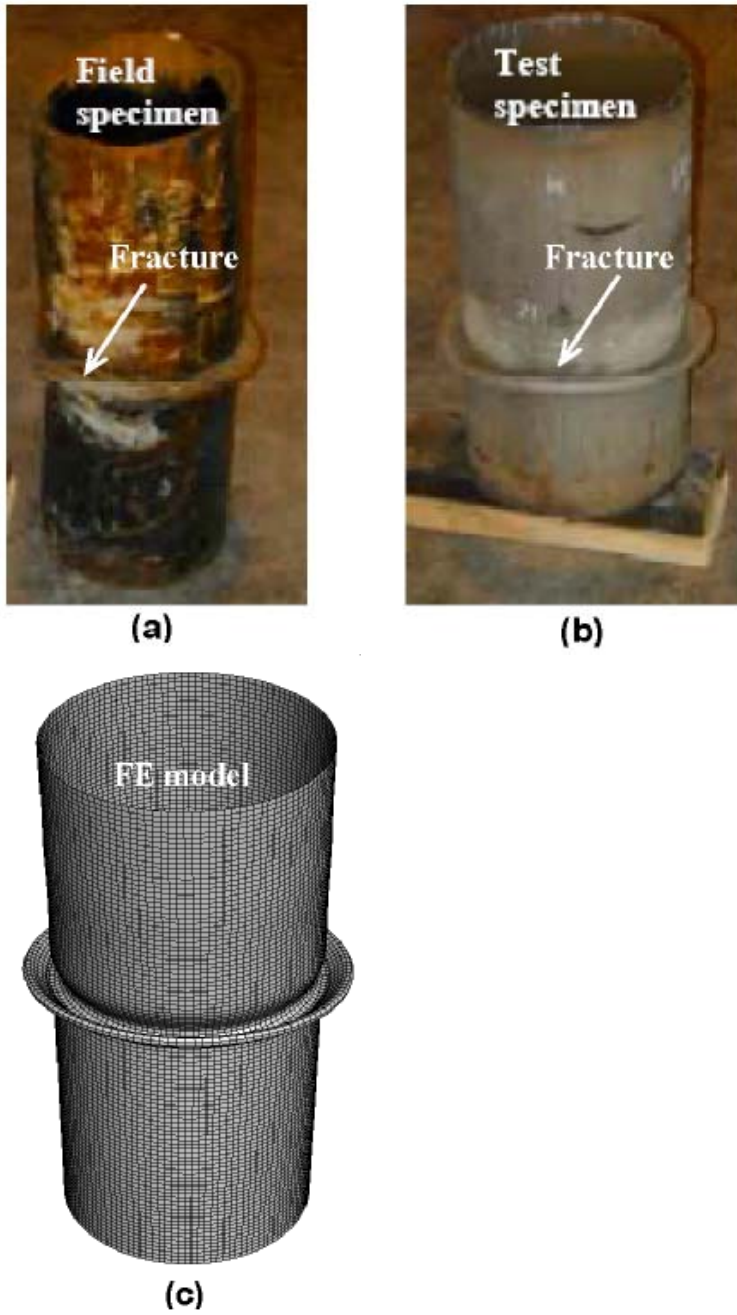


Figure 4.3 Final deformed shapes of the specimens obtained from (a) the WestCoast Energy Inc. (Das et al. 2002) , (b) the test (Das et al. 2002), and (c) the numerical work (Ahmed et al. 2010)



**D16P0A5-2**



**D16P40A7-3**



**D20P40A3.5-4**



**D20P0A5-5**

Figure 4.4 Initial deformed configurations of Specimen 2, 3, 4, and 5

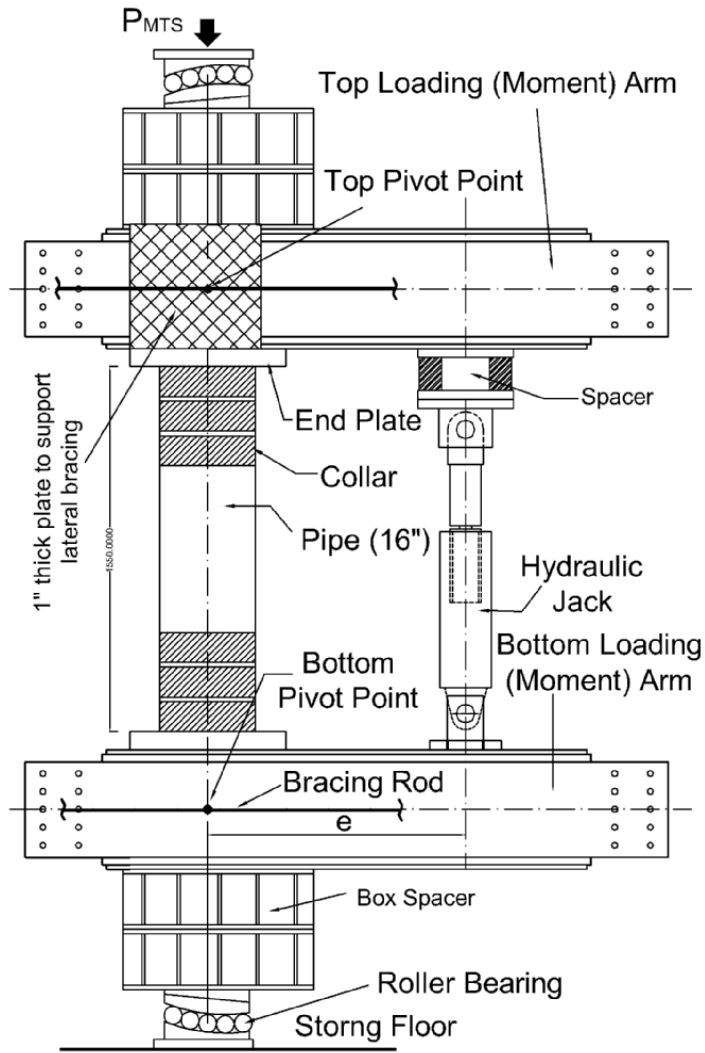
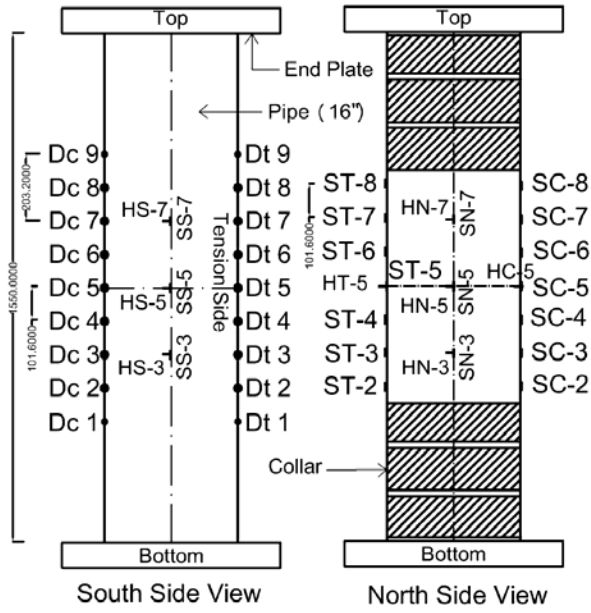
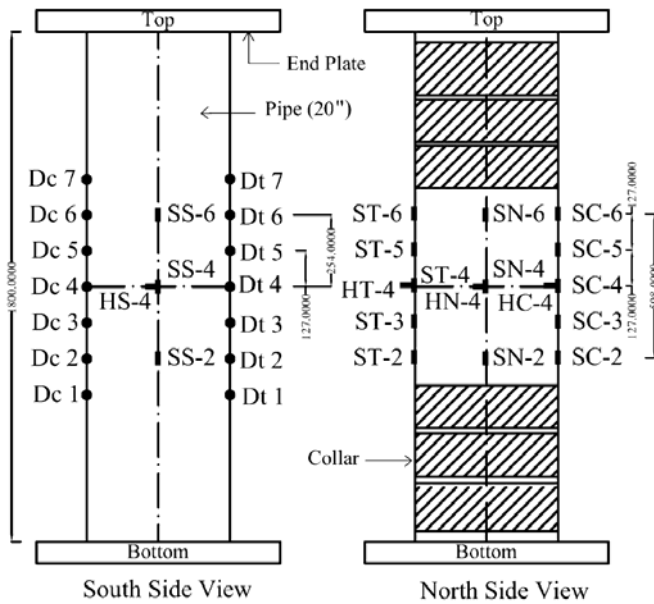


Figure 4.5 Schematic of test setup



(a) 16" (508 mm) Pipe



(b) 20" (508 mm) Pipe

Figure 4.6 Typical layouts of strain gauges and Demec points

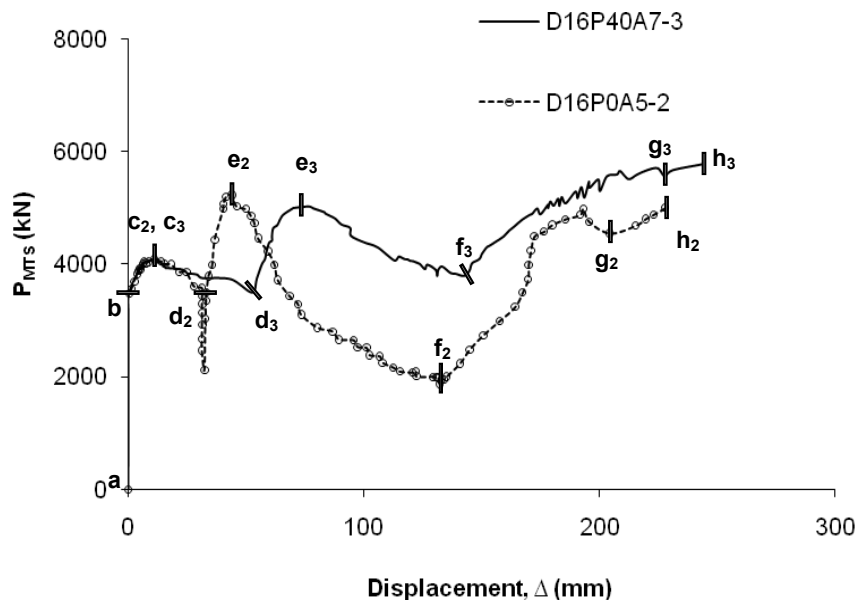


Figure 4.7 MTS load versus displacement response of Specimen 2 and 3

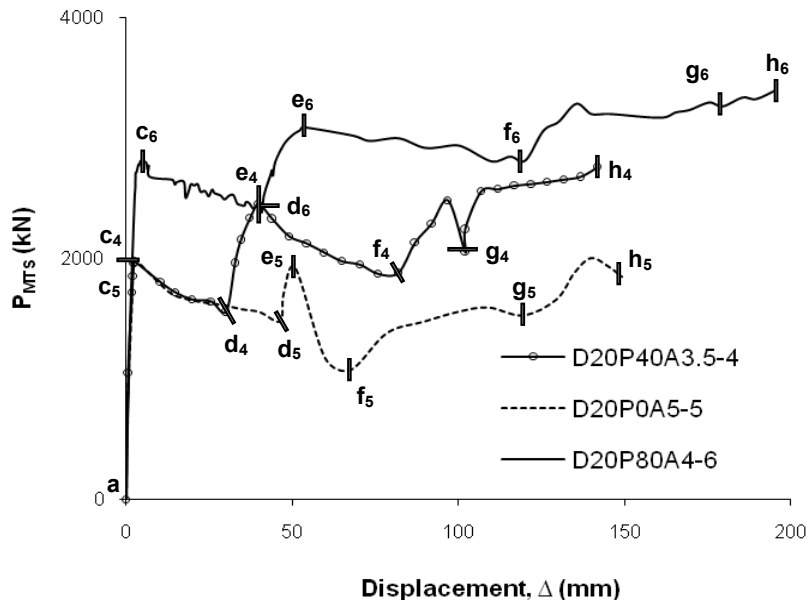


Figure 4.8 MTS load versus displacement response of Specimen 4, 5 and 6

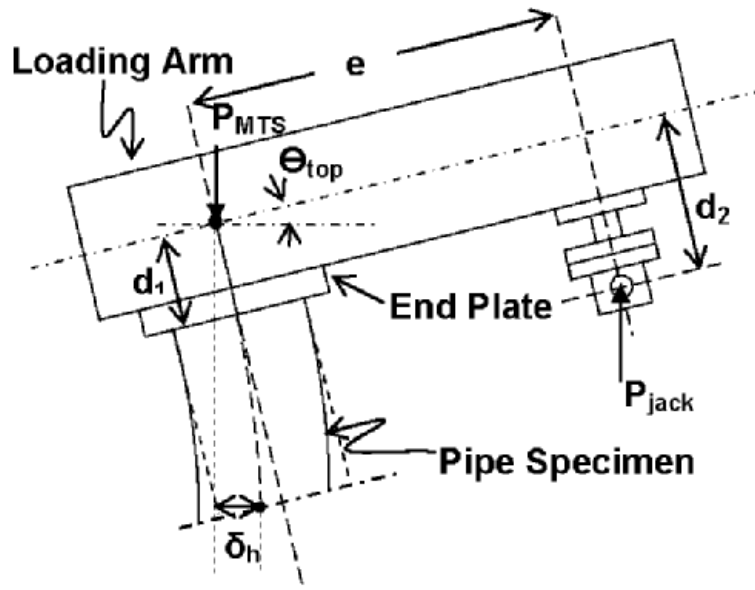


Figure 4.9 Free body diagram of the moment arm for calculating global and local end moment

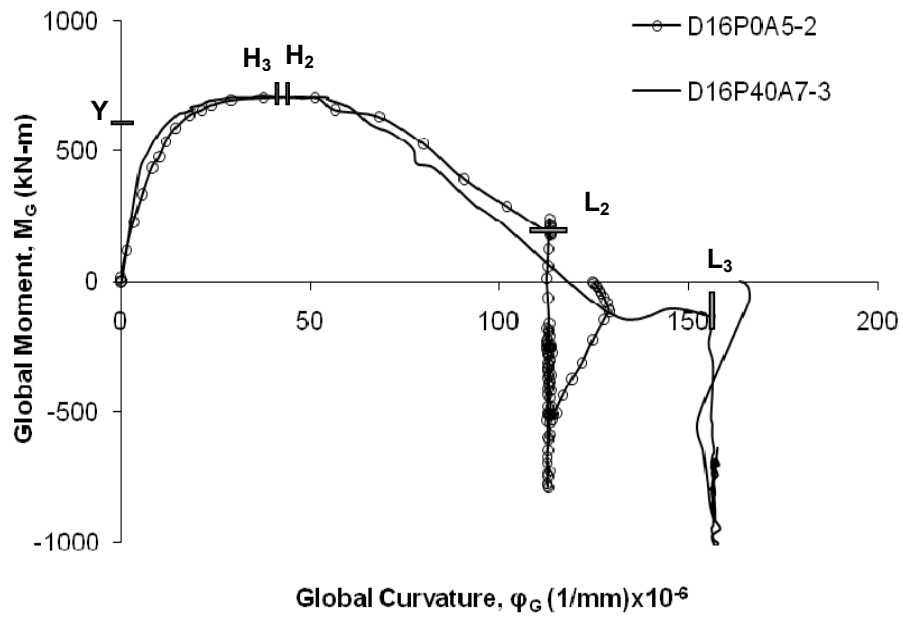


Figure 4.10 Global moment curvature behaviour of Specimen 2 and 3

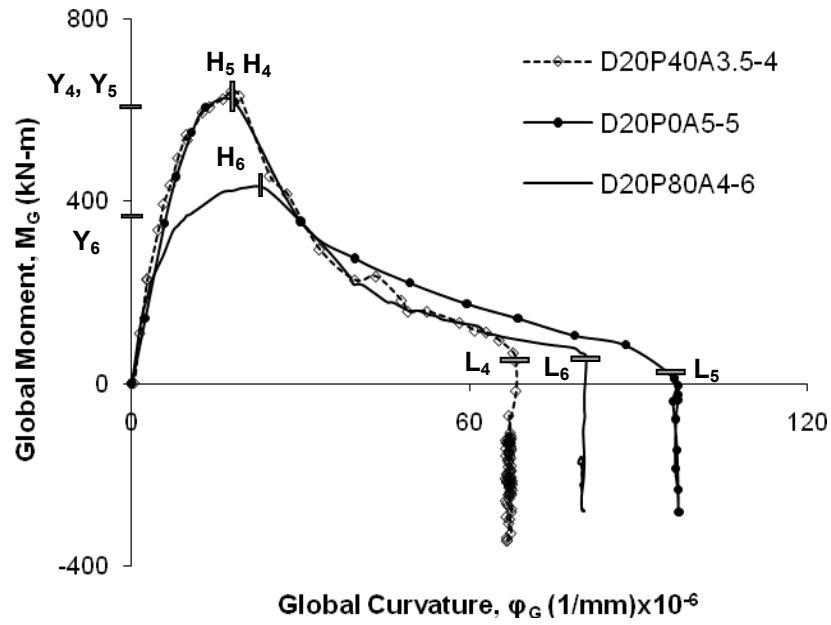


Figure 4.11 Global moment curvature behaviour of Specimen 4, 5 and 6

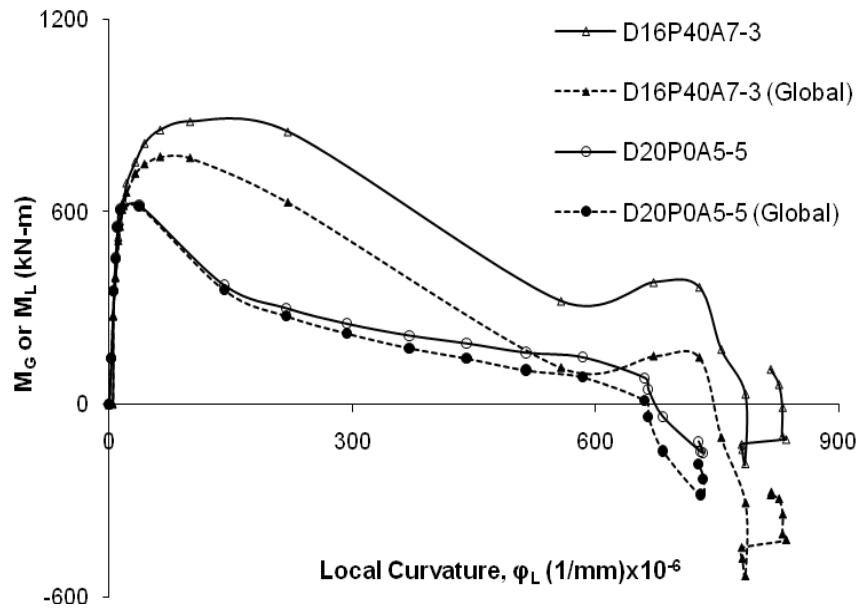


Figure 4.12 Local moment curvature behaviour of Specimen 3 and 5

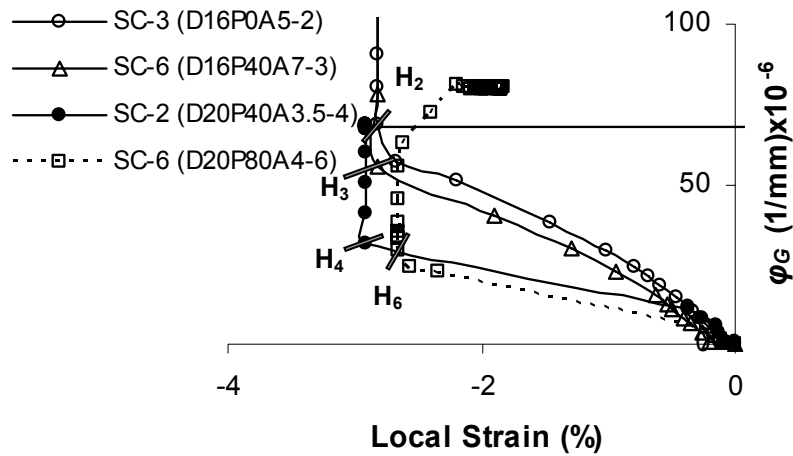


Figure 4.13 Local longitudinal strains versus global curvature for specimens 2, 3, 4 and 6

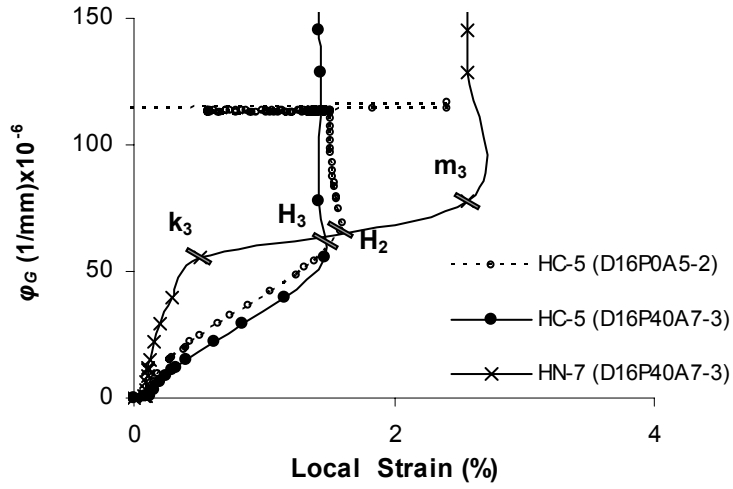


Figure 4.14 Local circumferential strains versus global curvature for 16" pipes

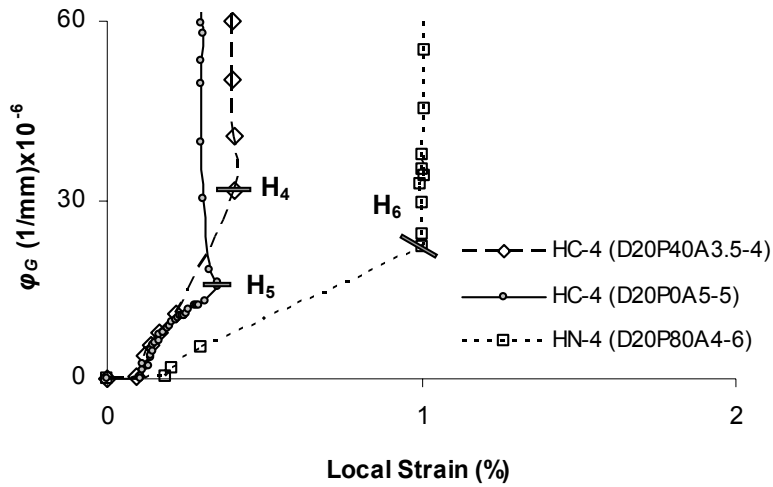


Figure 4.15 Local circumferential strains versus global curvature for 20" pipes

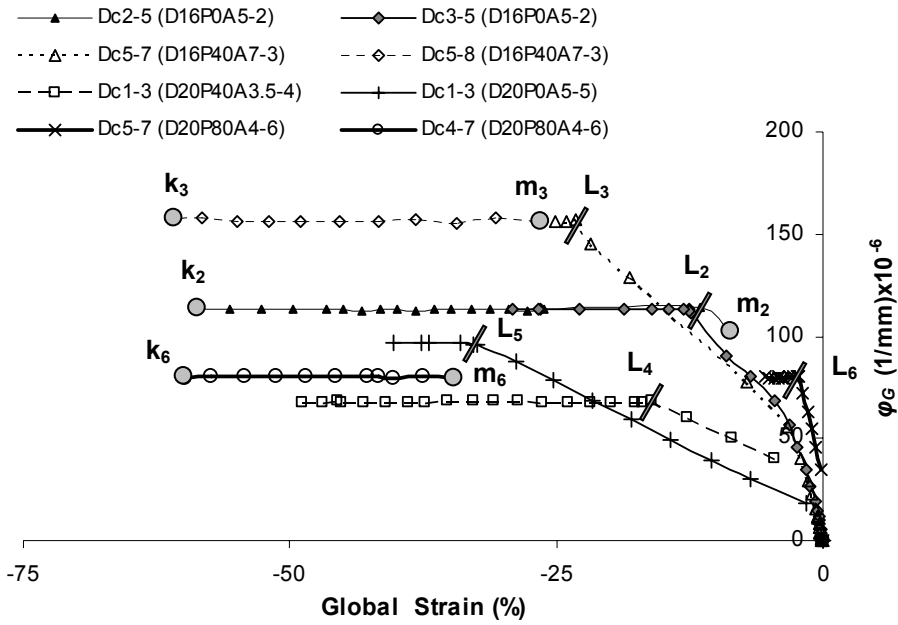


Figure 4.16 Global curvature- global longitudinal compressive strain relationships for specimens 2-5

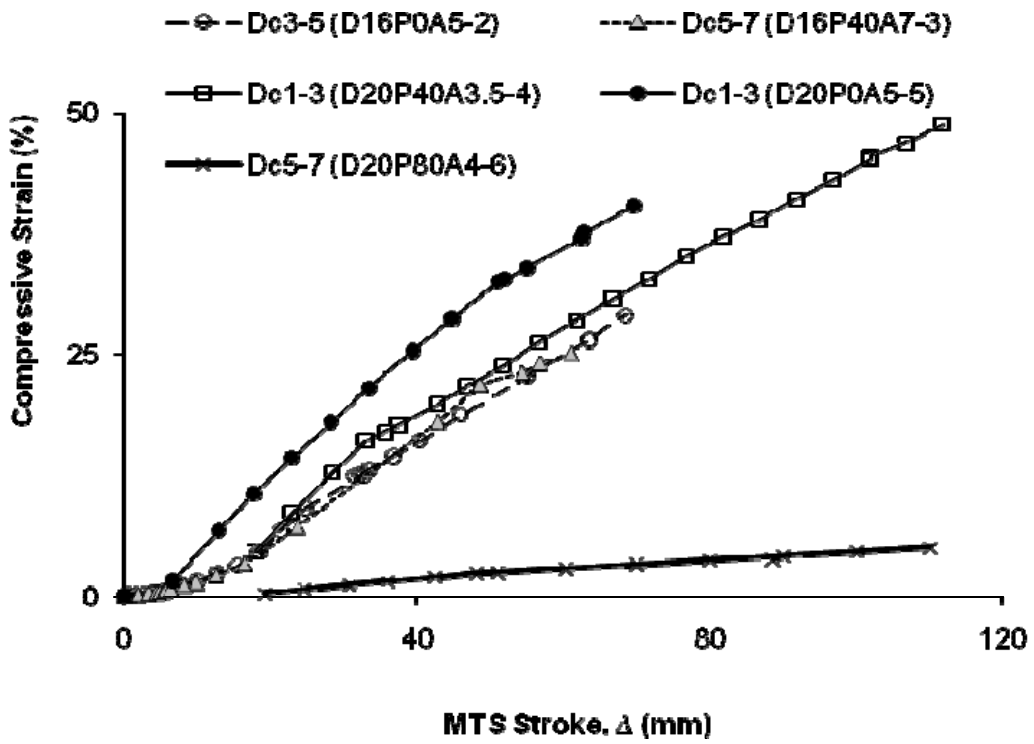


Figure 4.17 Global longitudinal compressive (Demec) strain growth with axial shortening

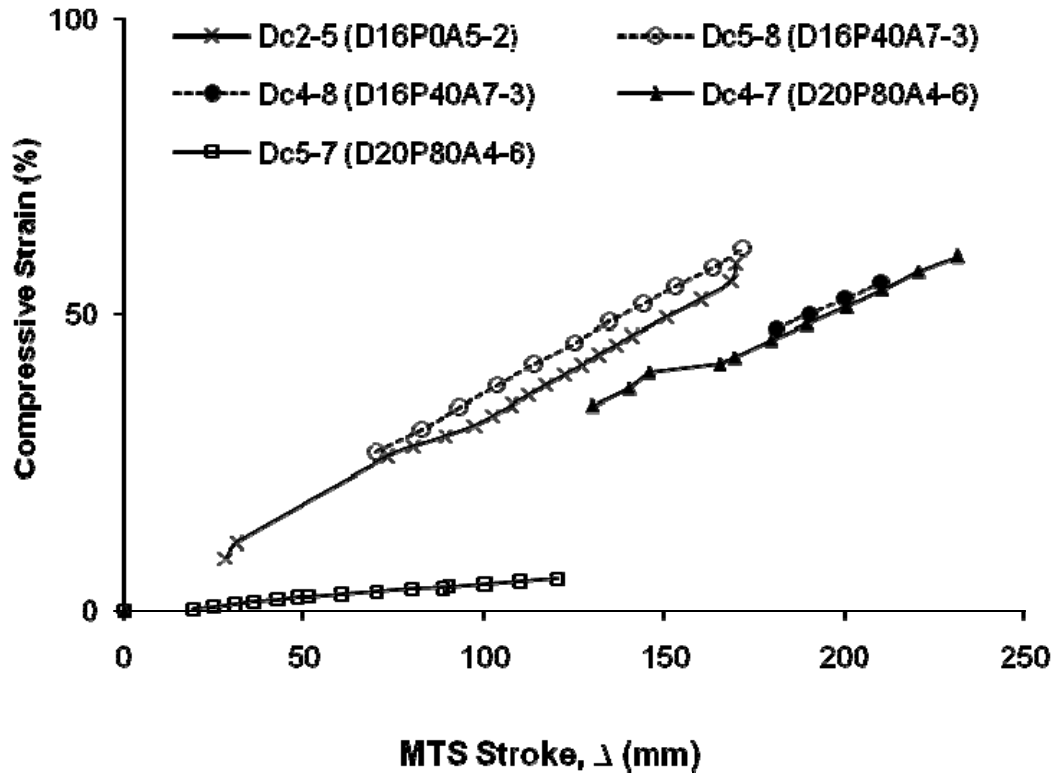
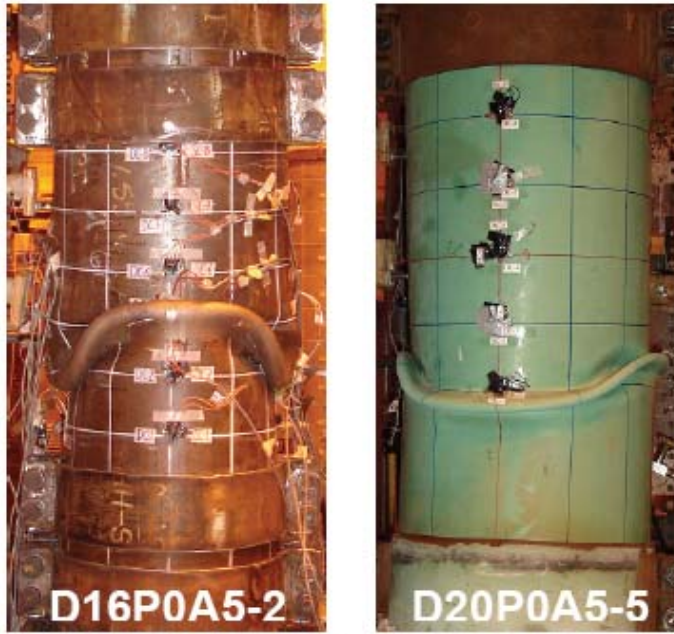


Figure 4.18 Global longitudinal compressive (Caliper) strain growth with axial shortening



(a)



(b)

Figure 4.19 Comparison of final deformed shapes between (a) Specimen 2 and 5, and (b) Specimen 3 and 6



Figure 4.20 Cut segment from the compression side of Specimen 2 and 3

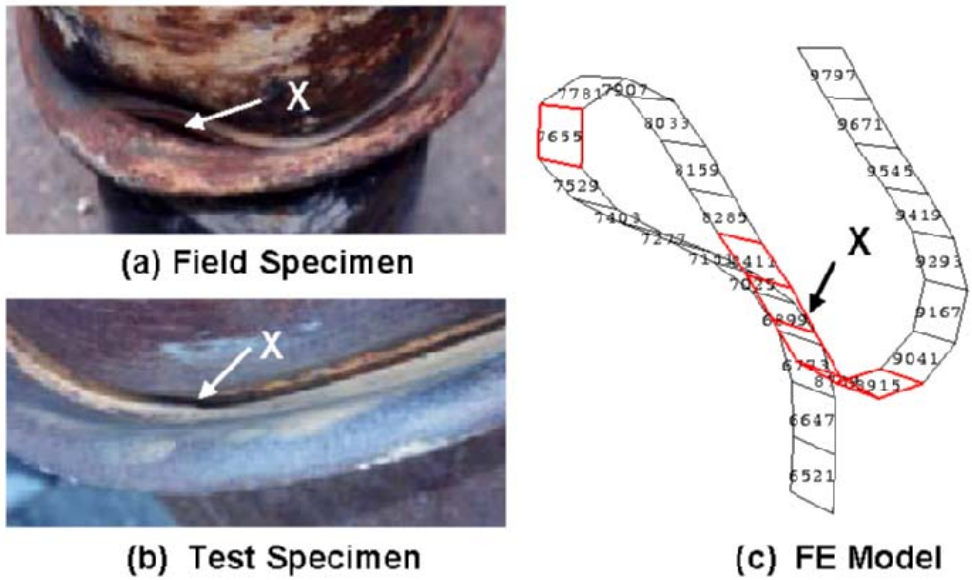


Figure 4.21 Fracture in the wrinkle fold of (a) the field (Das et al. 2002), and (b) the test specimen (Das et al. 2002); and location of strain reversal in FE model (Ahmed et al. 2010).

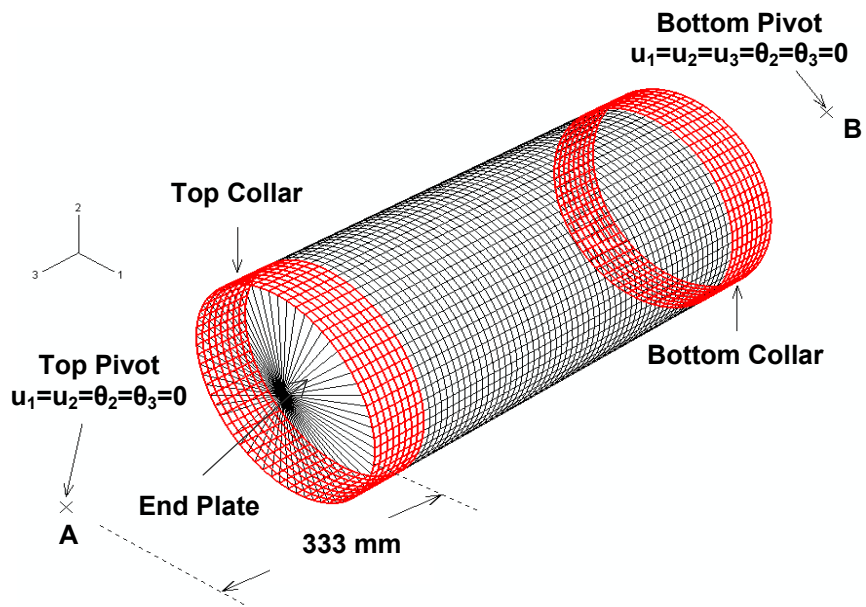


Figure 4.22 Typical geometry and initial boundary condition for full-pipe model

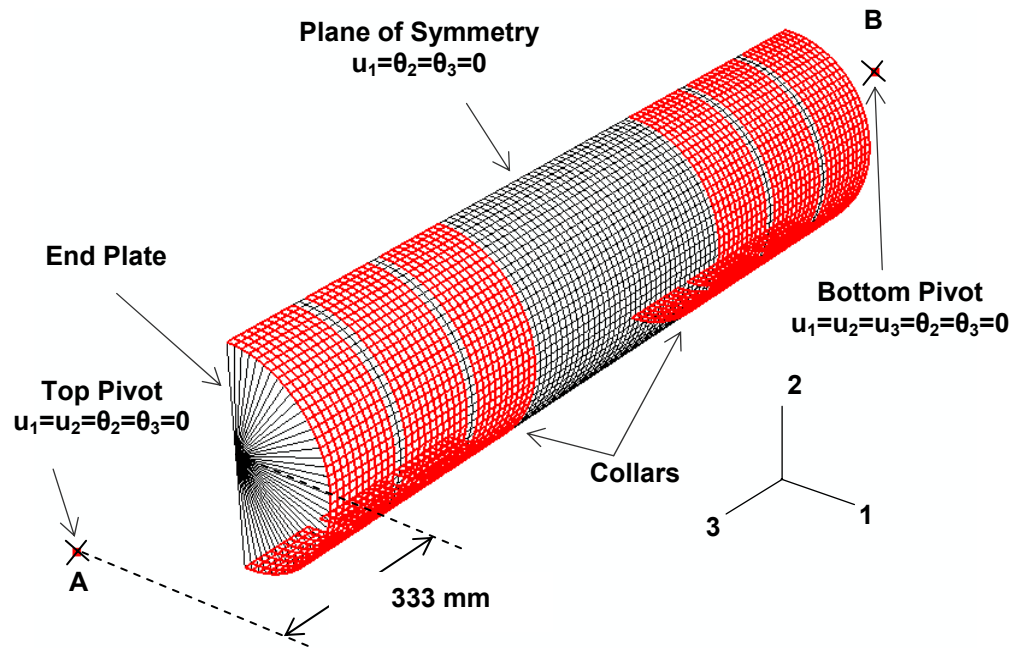
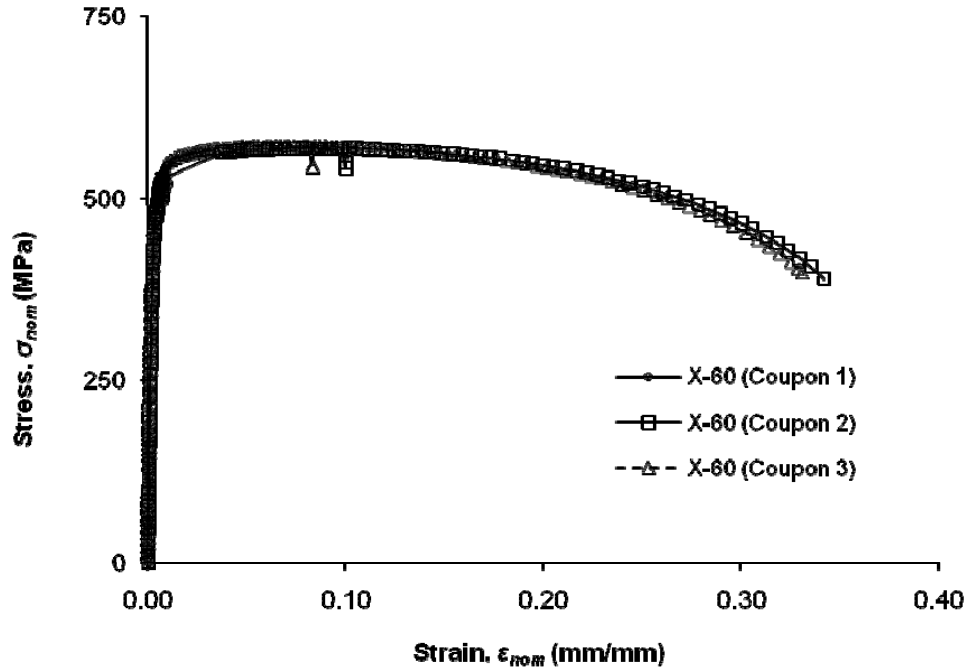
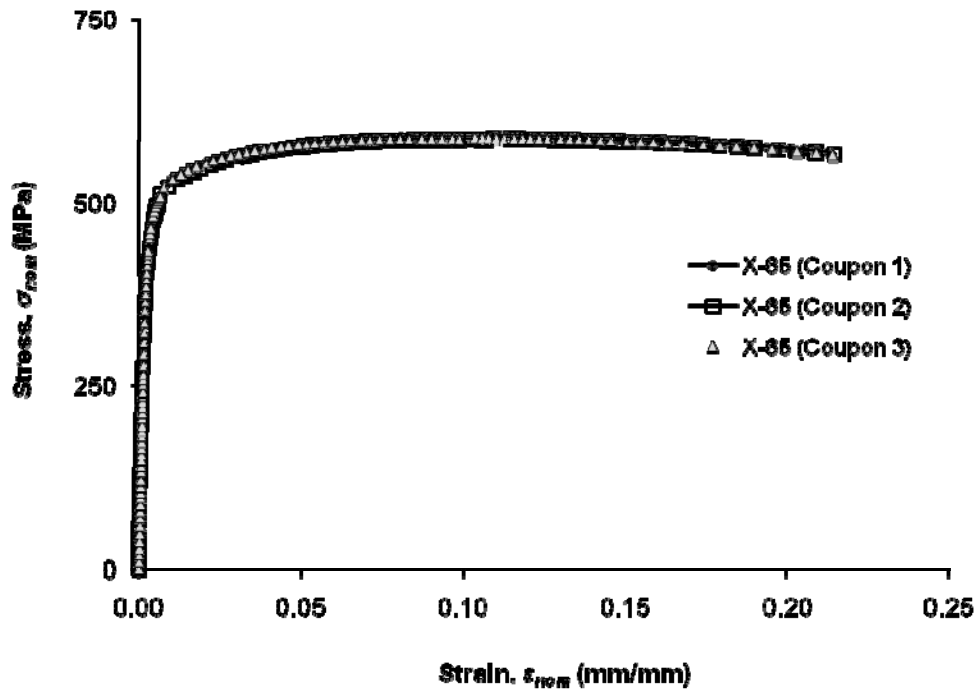


Figure 4.23 Typical geometry and initial boundary condition for half pipe model

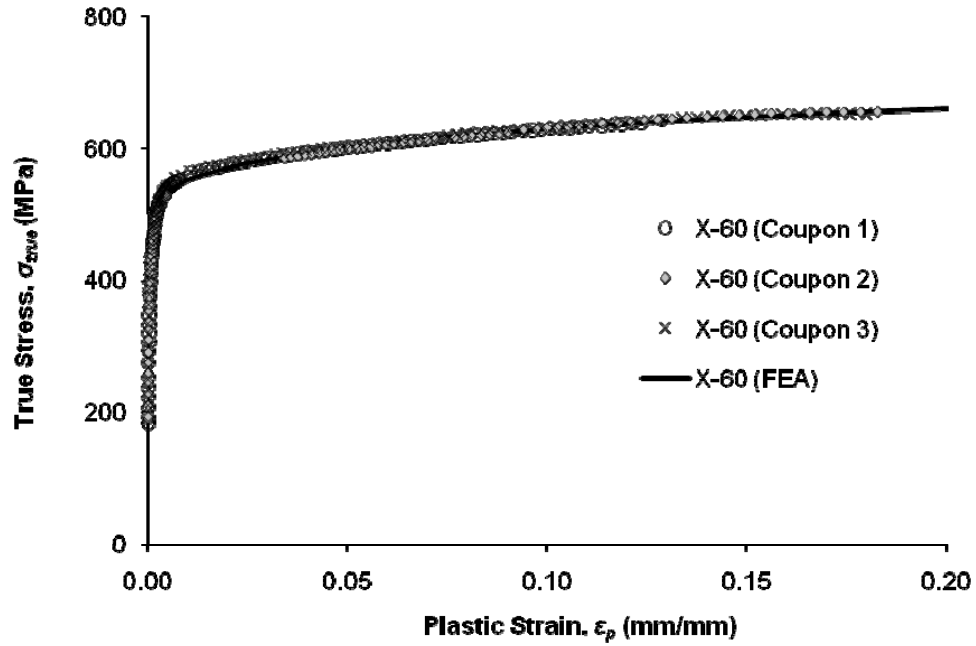


(a)

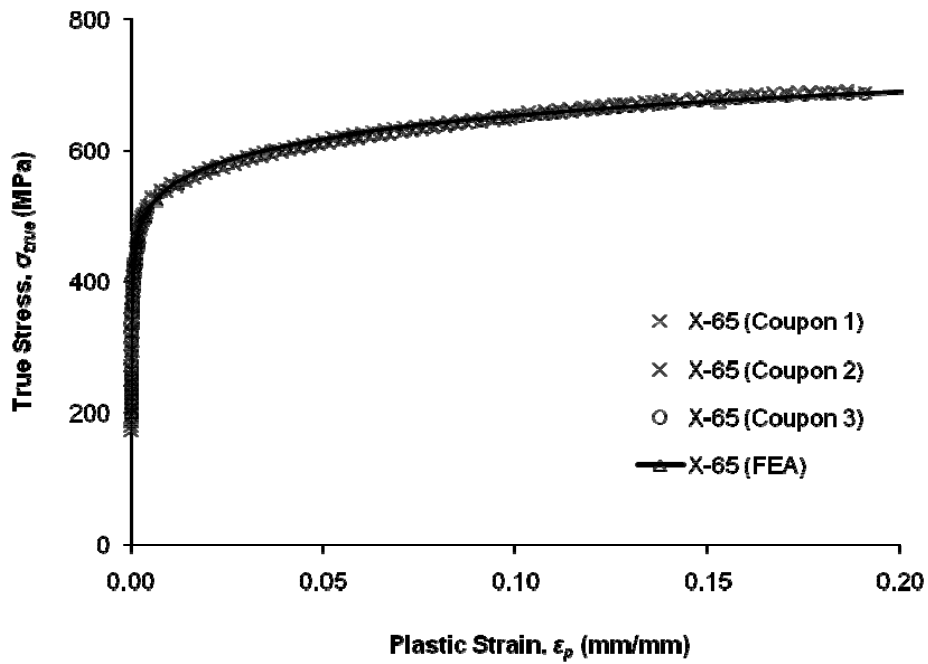


(b)

Figure 4.24 Engineering stress-strain plot of X60 and X65 grade steel obtained from tension coupon test



(a)



(b)

Figure 4.25 True stress-true plastic strain behaviour of X-60 and X-65 grade steel (up to 20% strain)

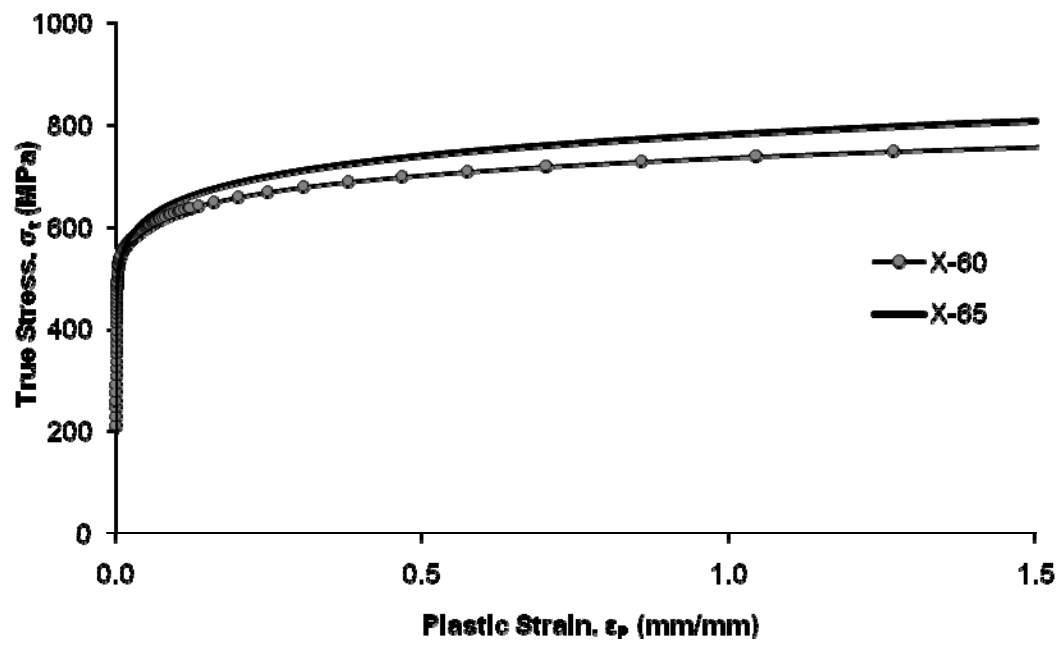


Figure 4.26 True stress-true plastic strain behaviour of X-60 and X-65 grade steel (up to failure)

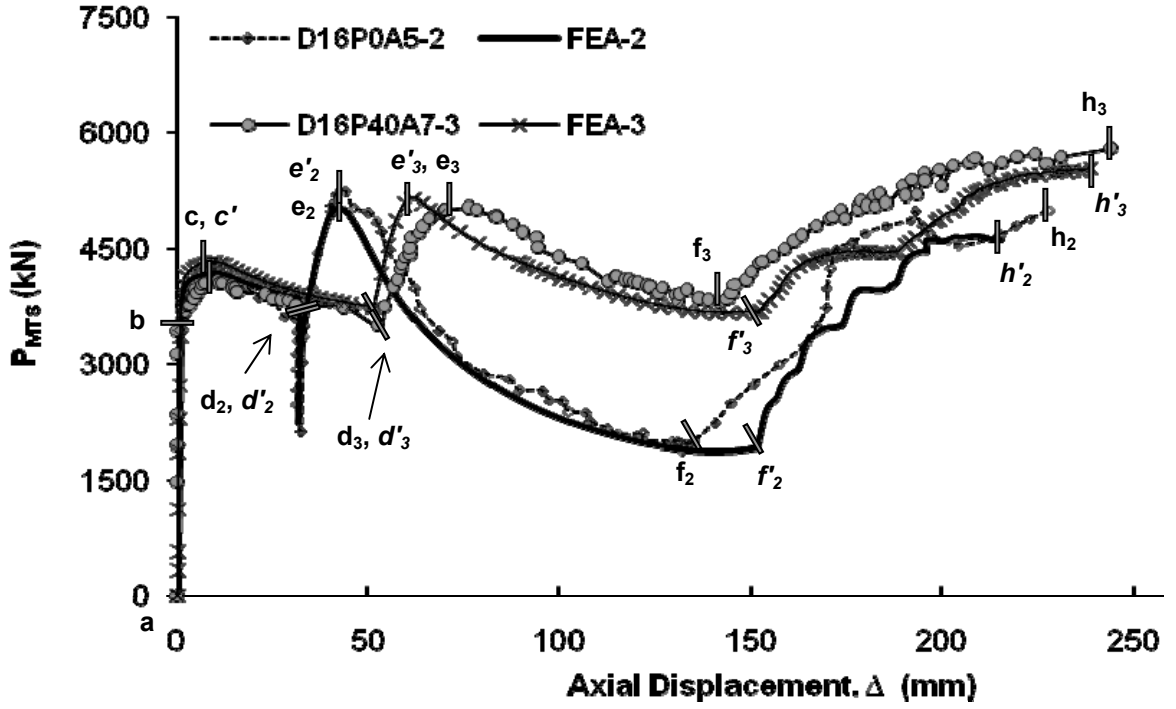


Figure 4.27 MTS load—displacement relationship obtained from FE analyses and test results of NPS16 pipes

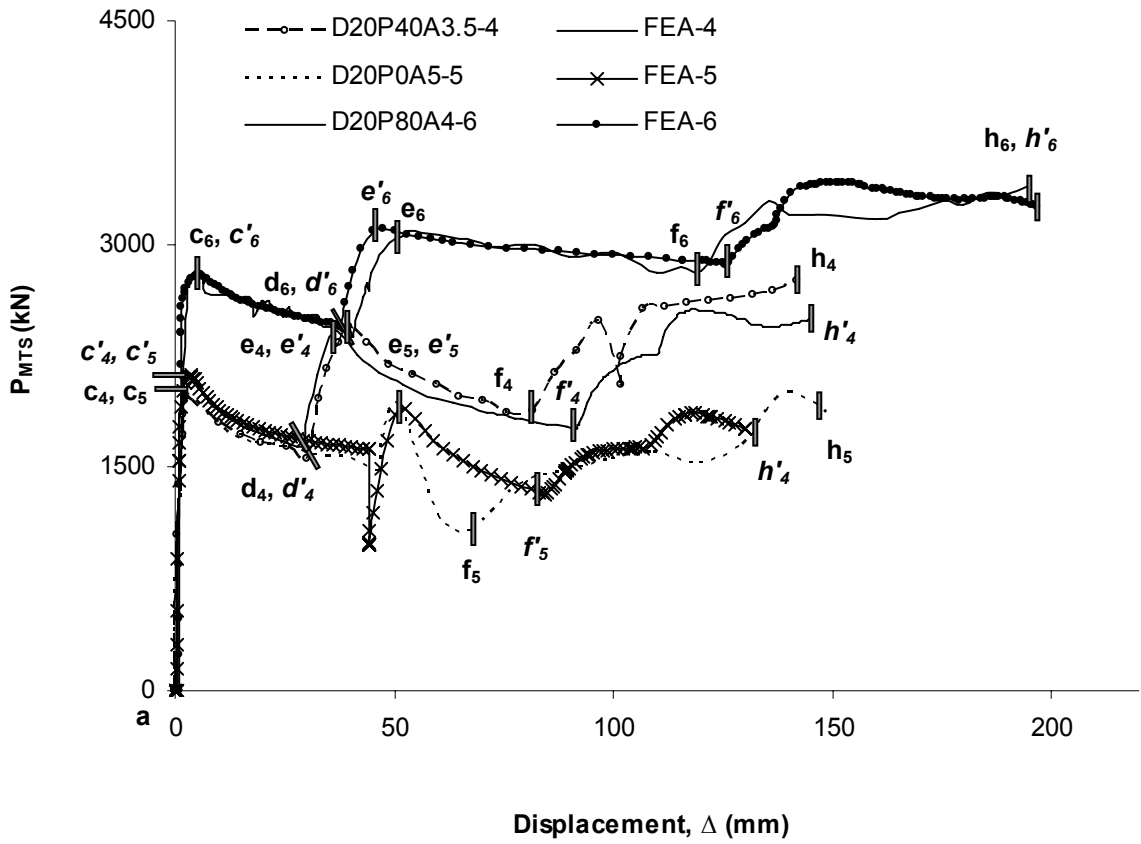


Figure 4.28 MTS load—displacement relationship obtained from FE analyses and test results of NPS20 pipes

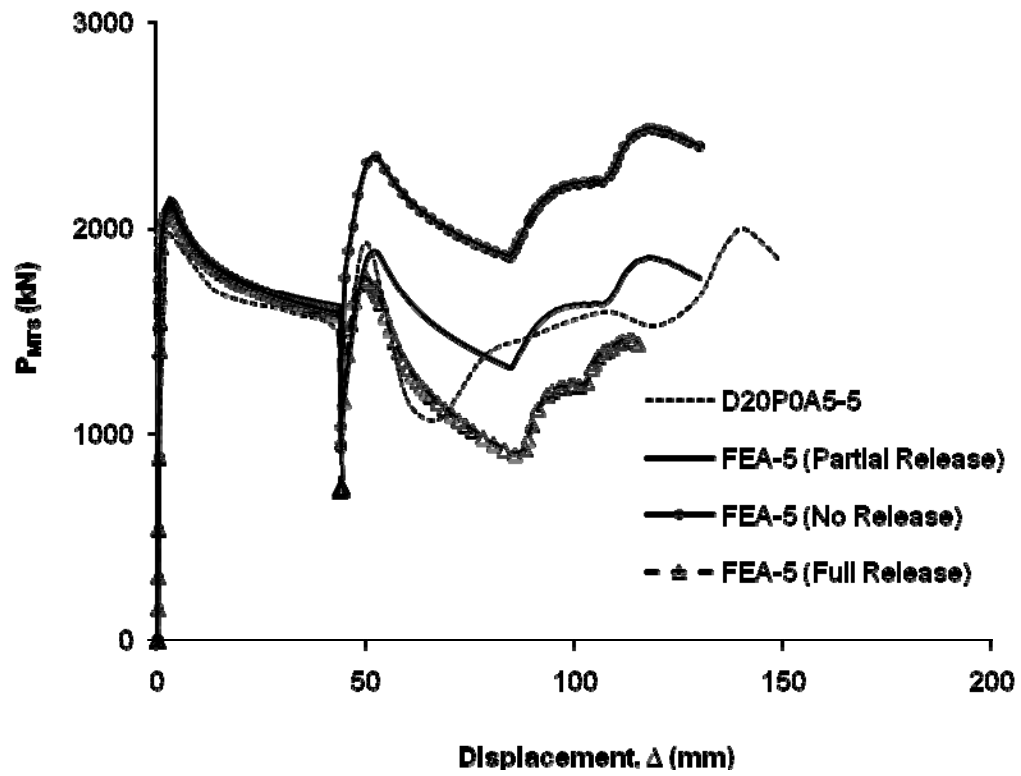


Figure 4.29 MTS load—displacement relationship obtained from FE analyses and test results of specimen 5 for different load condition

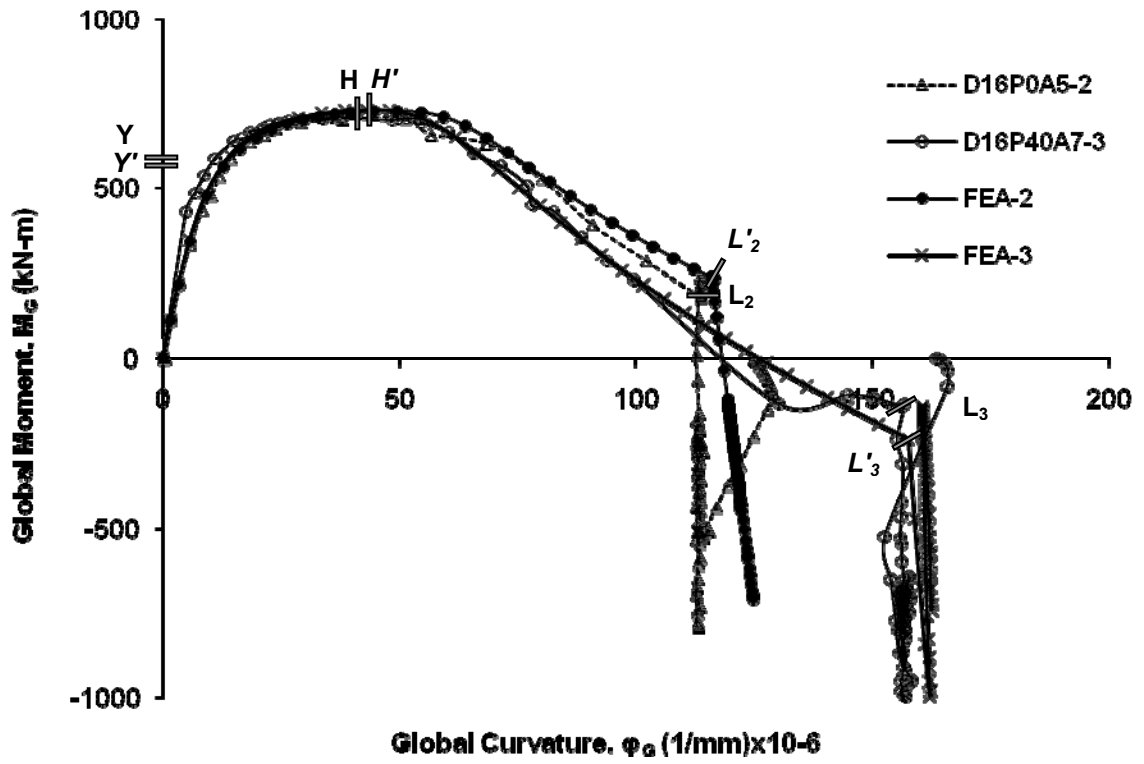


Figure 4.30 Global moment—global curvature relationship obtained from FE analyses and test results of NPS16 Pipes

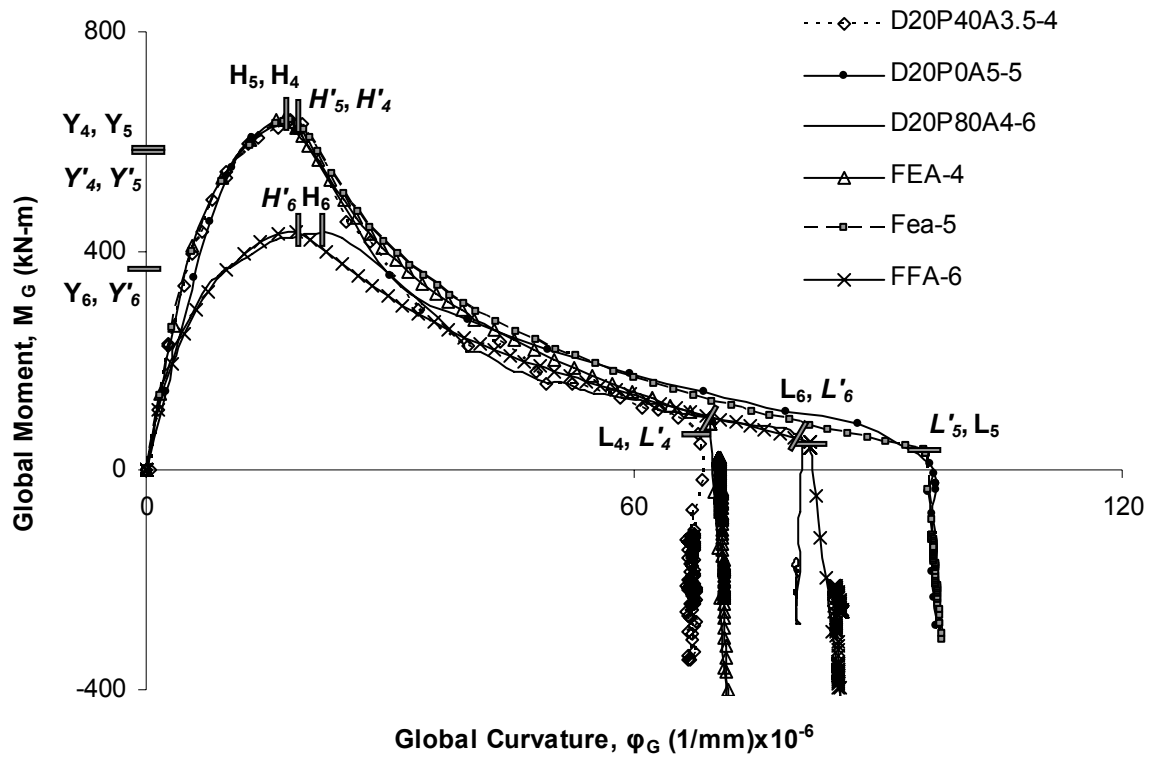
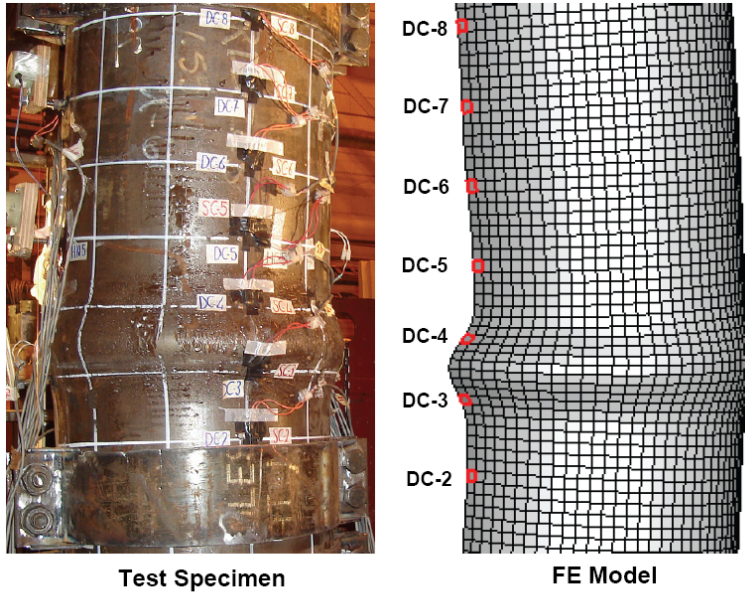
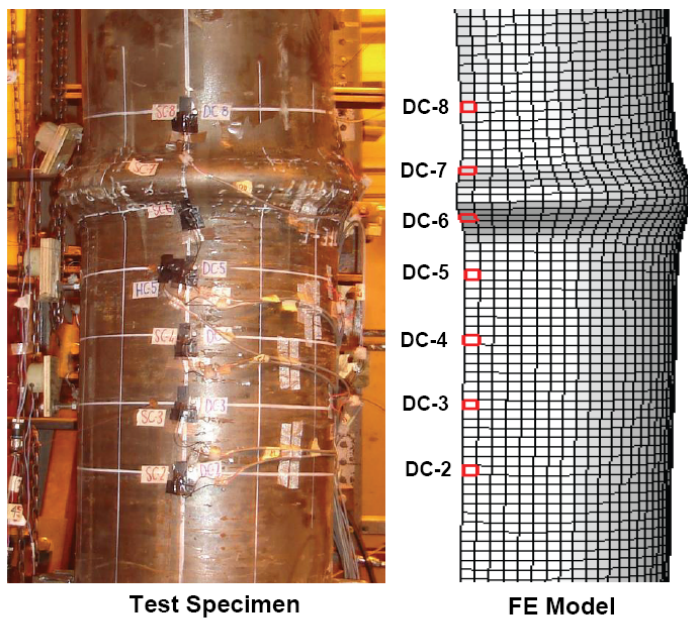


Figure 4.31 Global moment—global curvature relationship obtained from FE analyses and test results of NPS20 Pipes

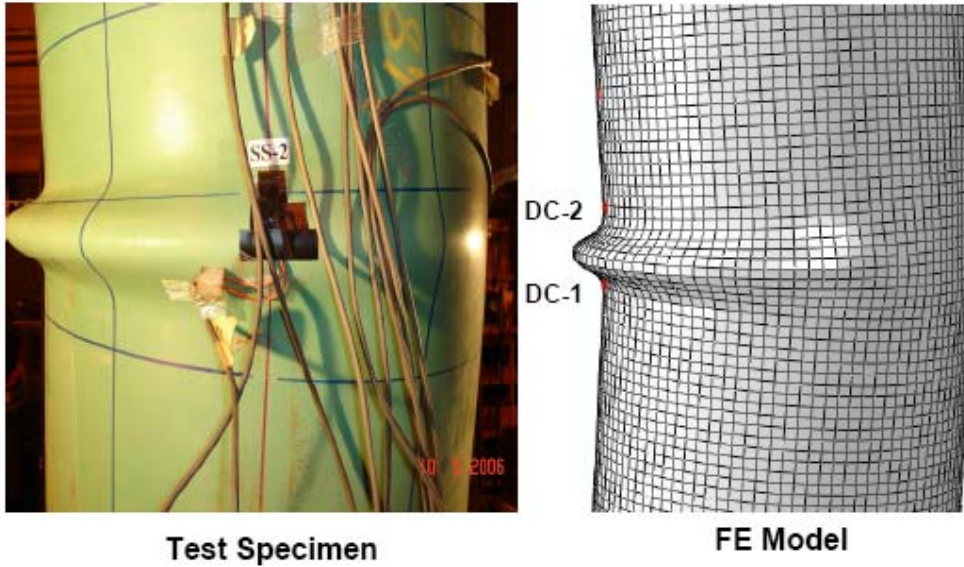


a) D16P0A5-2

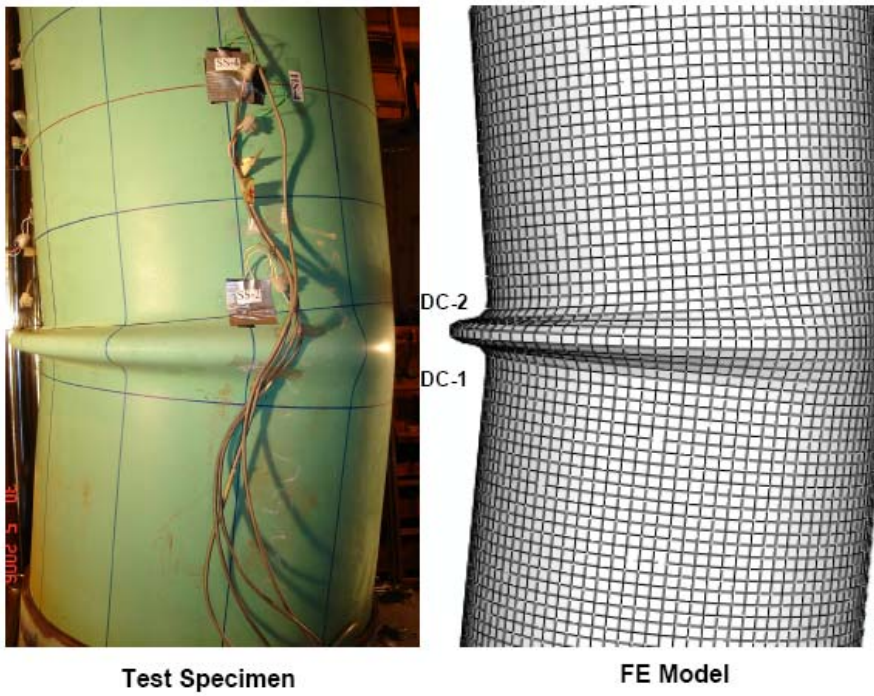


b) D16P40A7-3

Figure 4.32 Comparison of initial deformed shapes of specimen 2 and 3

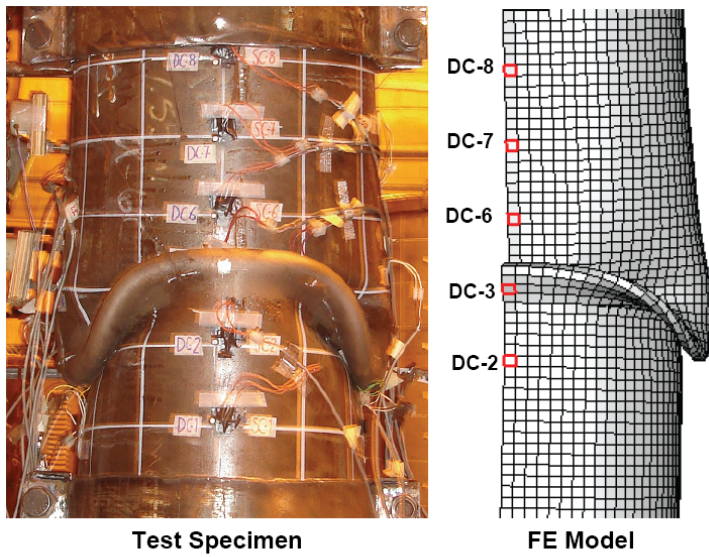


**a) D20P40A3.5-4**



**b) D20P0A5-5**

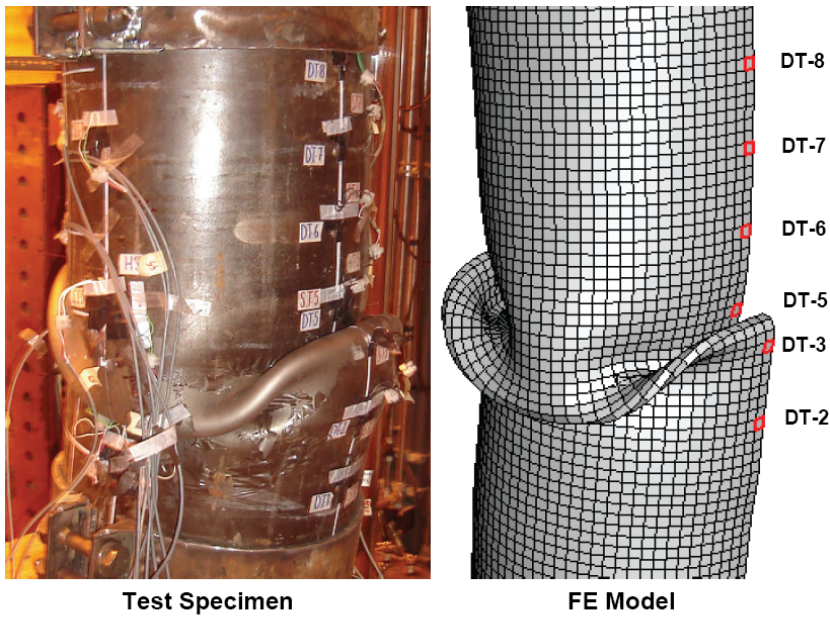
Figure 4.33 Comparison of initial deformed shapes of specimen 4 and 5



**Test Specimen**

**FE Model**

**a) Compression Side View**



**Test Specimen**

**FE Model**

**b) Tension Side View**

Figure 4.34 Comparison of final deformed shapes of specimen 2 (D16P0A5-2)

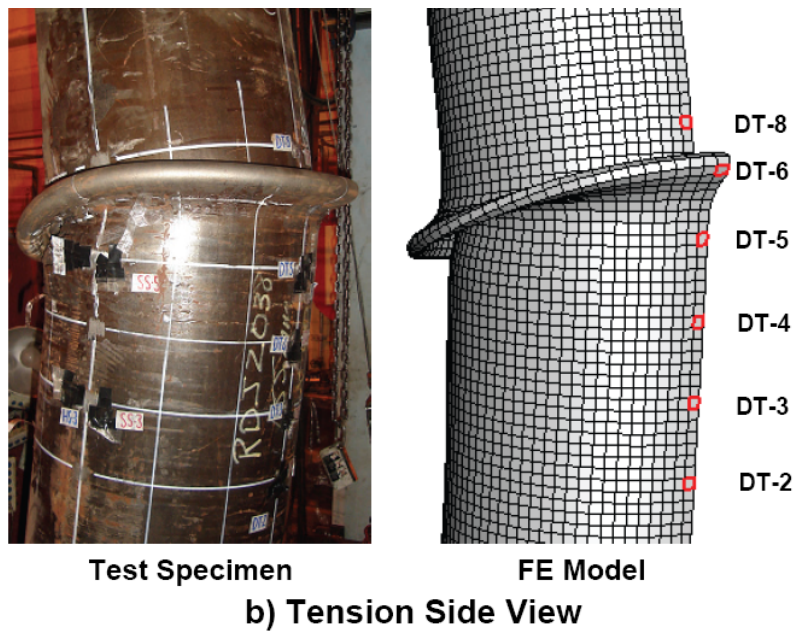
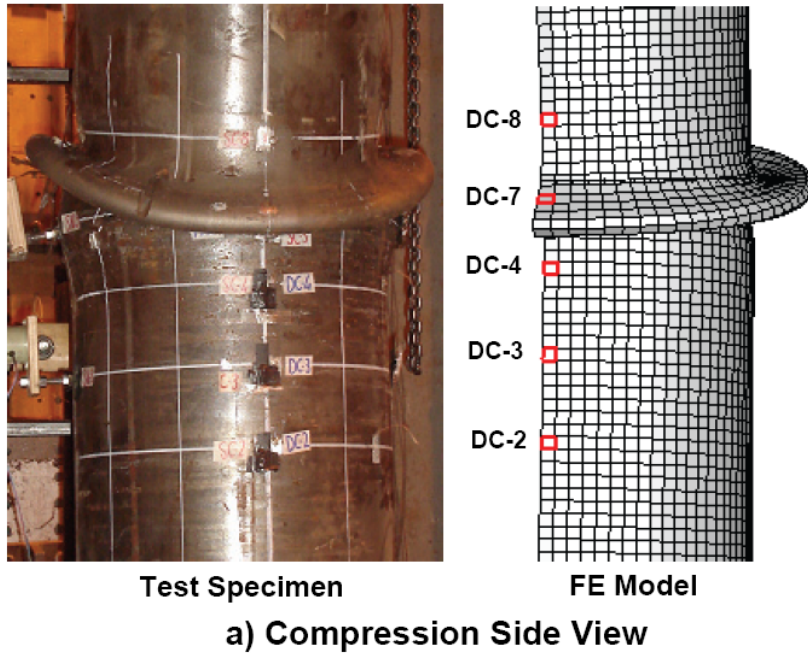
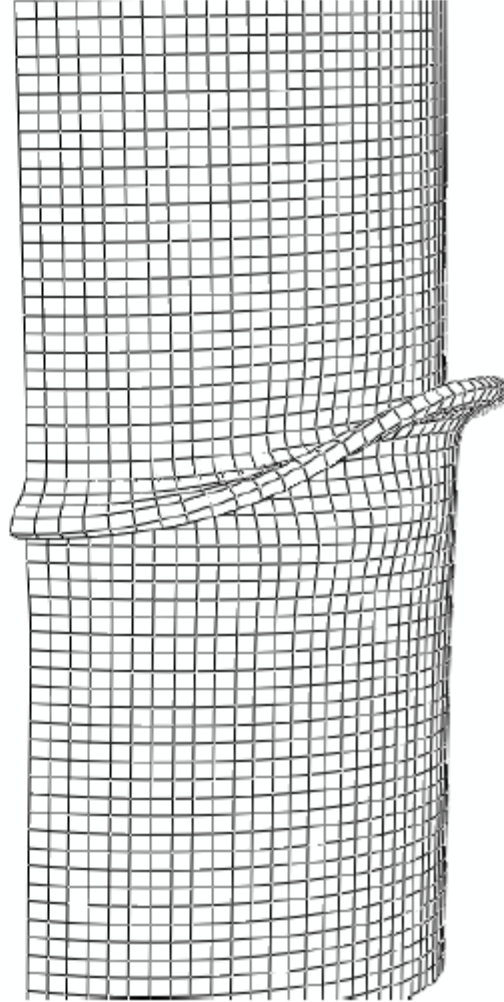


Figure 4.35 Comparison of final deformed shapes of specimen 3 (D16P40A7-3)



**D20P40A3.5-4**



**FEA-4**

Figure 4.36 Comparison of final deformed shapes of specimen 4

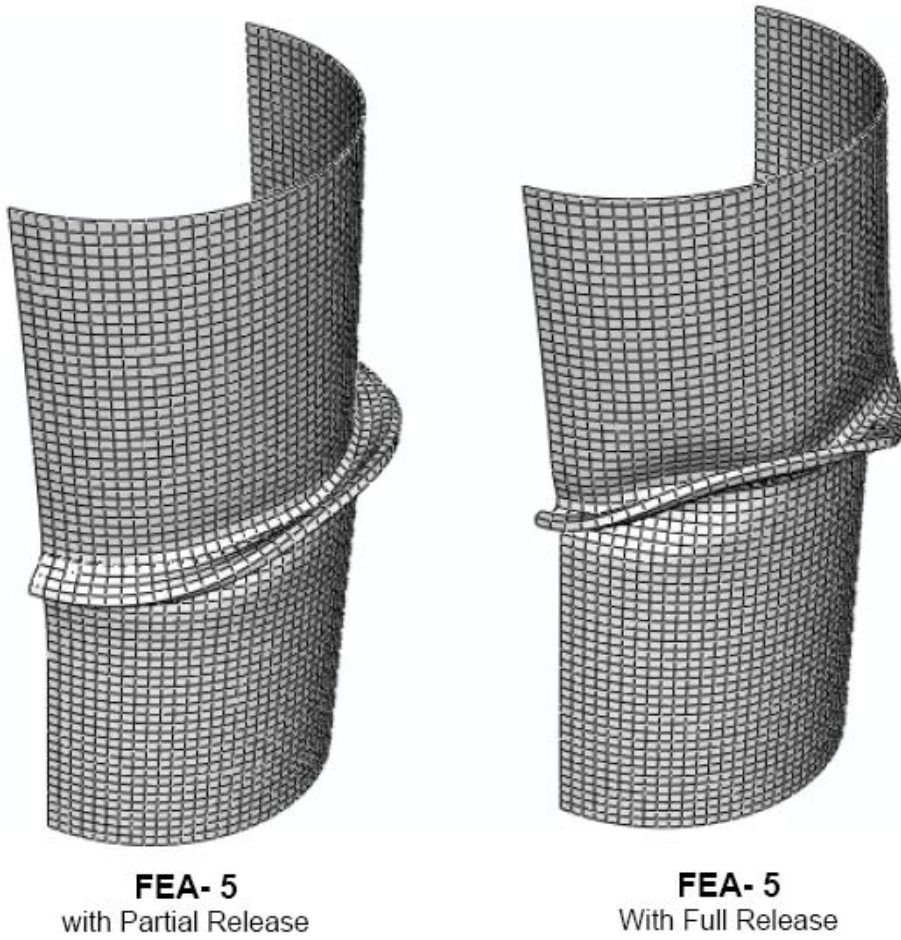
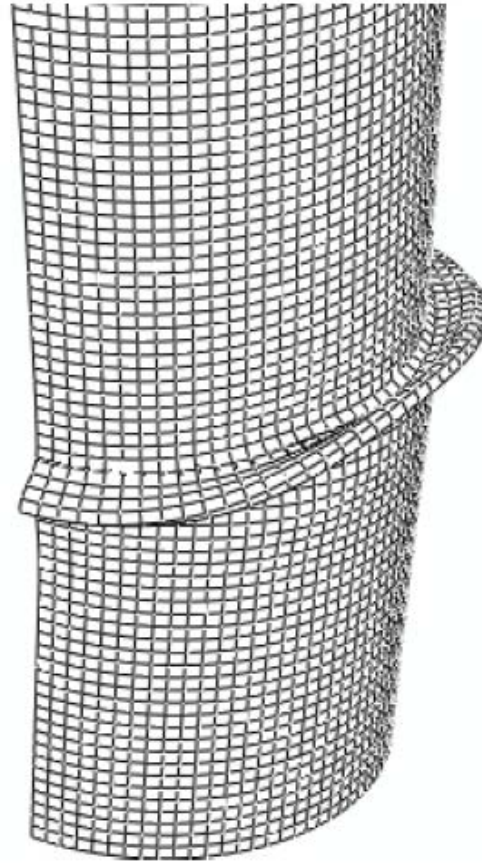


Figure 4.37 Comparison of final deformed shapes from FE analyses of specimen 5 with two different internal pressure conditions



**D20P0A5-5**

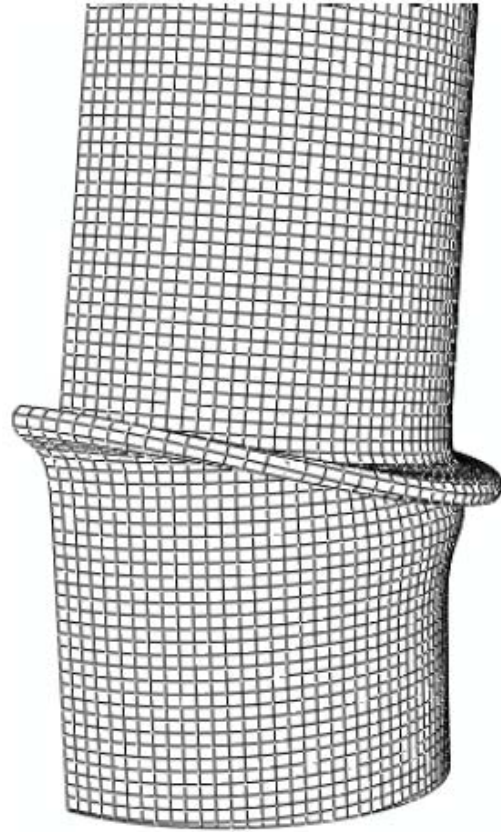


**FEA-5**

Figure 4.38 Comparison of final deformed shapes of specimen 4



**D20P80A4-6**



**FEA-6**

Figure 4.39 Comparison of final deformed shapes of specimen 6

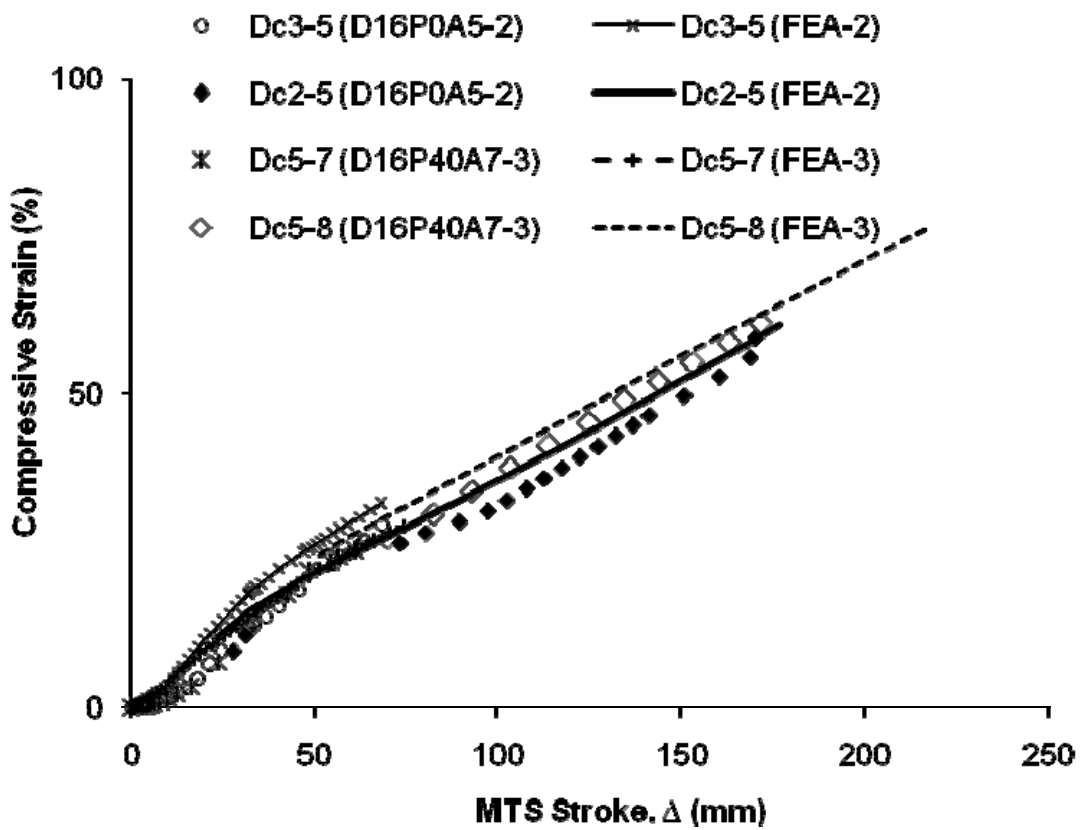


Figure 4.40 Comparison of global longitudinal compressive (Caliper) strain —axial shortening response of NPS16 specimens

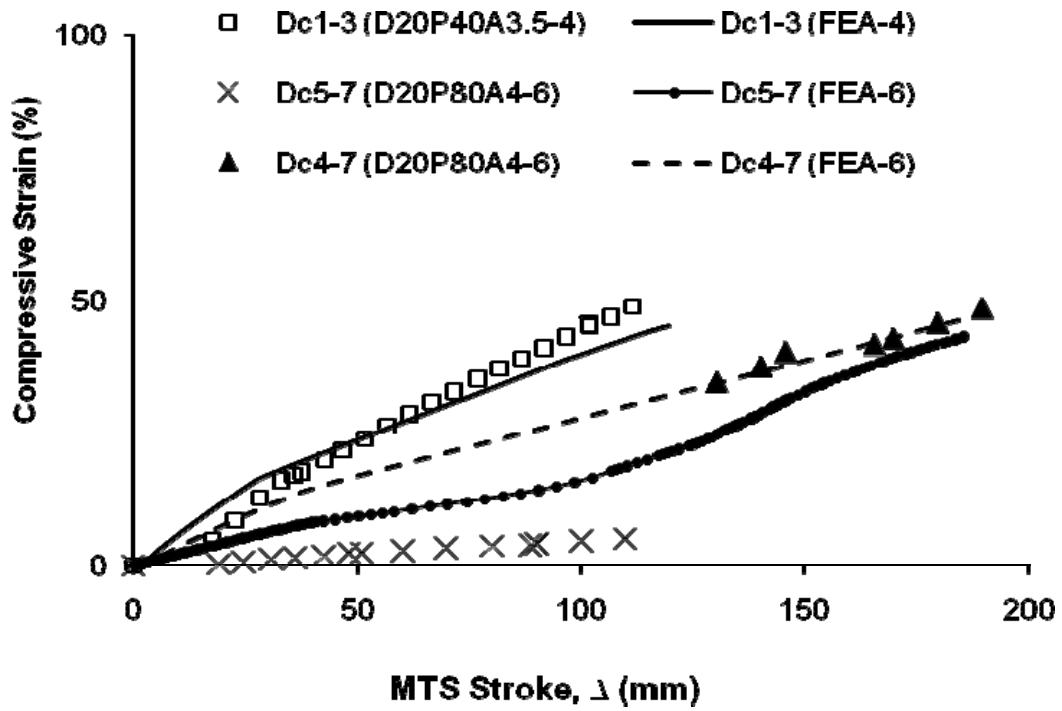


Figure 4.41 Comparison of global longitudinal compressive (Caliper) strain—axial shortening response of NPS20 specimens

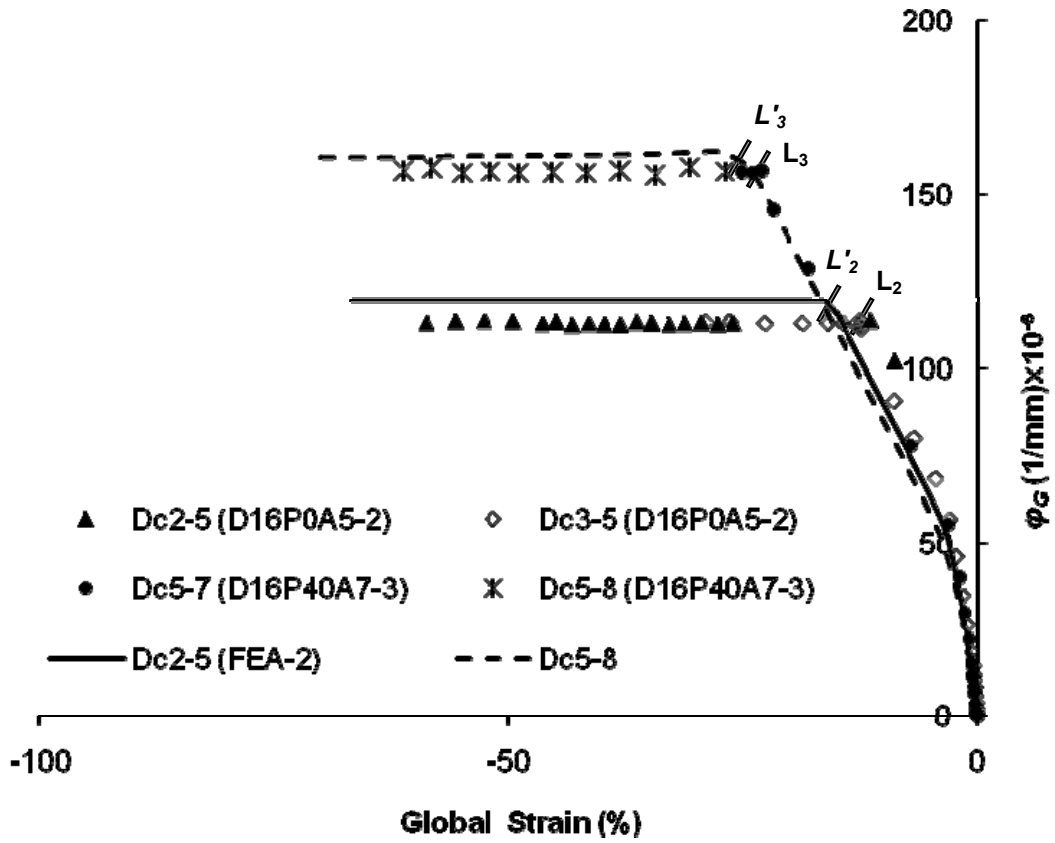


Figure 4.42 Comparison of global curvature-longitudinal compressive strain response for NPS16 specimens

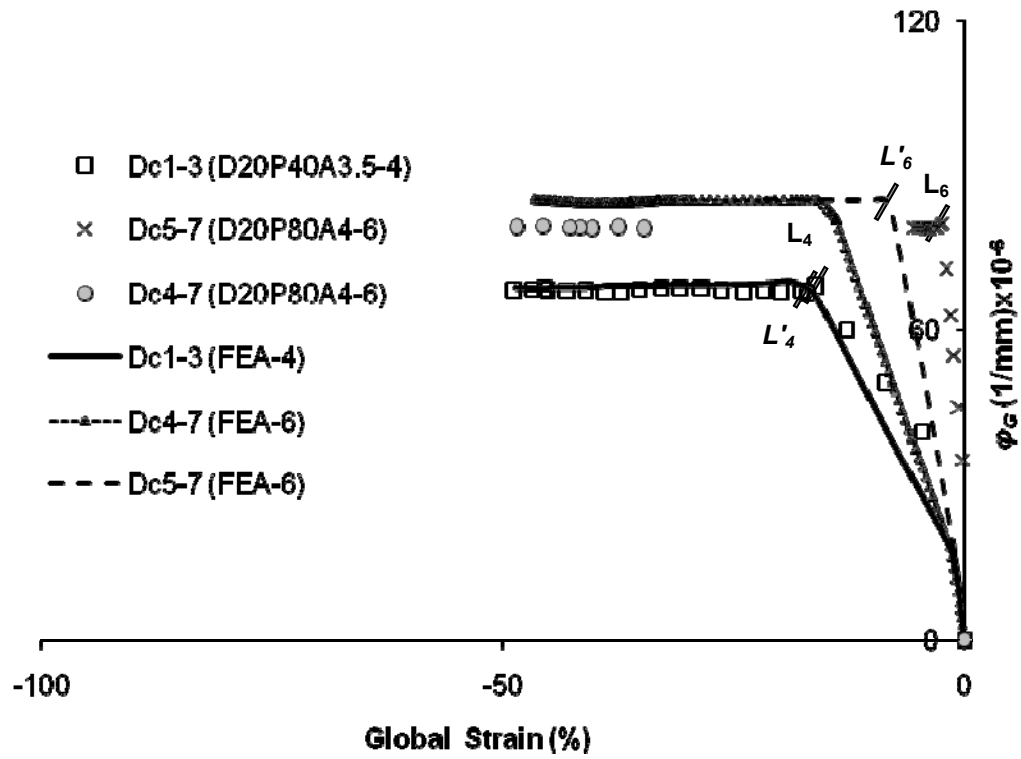


Figure 4.43 Comparison of global curvature-longitudinal compressive strain response for NPS20 specimens

#### 4.10 References

- Ahmed, A., Das, S., and Cheng, J.J.R. 2010. Numerical investigation of tearing fracture of wrinkled pipe. *Journal of Offshore Mechanics and Arctic Engineering*, 132: 011302-1.
- Ahmed, A., Aydin, M., Cheng, J.J.R., and Zhou, J. 2009. Experimental investigation of fracture in wrinkled pipelines under monotonic axial and bending deformation. *In Proceedings of the ASME 28th International Conference on Ocean, Offshore and Arctic Engineering*, Honolulu, Hawaii, USA.
- American Petroleum Institute (API). 2004. Specification for line pipe. API 5L, American Petroleum Institute, Washington, D.C.
- Aydin, M. 2007. Tearing fracture of energy pipelines under monotonic loading conditions. M.Sc. dissertation, University of Alberta, Edmonton, AB, Canada.
- Canadian Standards Association (CSA). 2007. Oil and gas pipeline systems. Z662-07, Canadian Standards Association, Mississauga, ON, Canada.
- Cheng, J.J.R., Kulak, G.L., and Khoo, H.-A. 1998. Strength of slotted tubular tension members. *Canadian Journal of Civil Engineering*, 25: 982-991.
- Das, S. 2003. Fracture of wrinkled energy pipelines. PhD in Structural Engineering, University of Alberta, Edmonton, AB, Canada.
- Das, S., Cheng, J.J.R., and Murray, D.W. 2007a. Behaviour of wrinkled steel pipelines subjected to cyclic axial loadings. *Canadian Journal of Civil Engineering*, 34: 598-607.

- Das, S., Cheng, J.J.R., and Murray, D.W. 2007b. Prediction of fracture in wrinkled energy pipelines subjected to cyclic deformations. *International Journal of Offshore and Polar Engineering*, 17: 205-212.
- Das, S., Cheng, J.J.R., and Murray, D.W. 2002. Fracture in wrinkled linepipe under monotonic loading. *In Proceedings of the 4th International Pipeline Conference*, Sep 30-Oct 3 2002, Vol. B, pp. 1613-1618.
- Das, S., Cheng, J.J.R., Murray, D.W., Wilkie, S.A., and Zhou, Z.,J. 2001. Wrinkle behaviour under cyclic strain reversal in NPS12 pipe. *In 20th International Conference on Offshore Mechanics and Arctic Engineering; Polar and Arctic Pipeline Technology*, Jun 3-8 2001, Vol. 4, pp. 129-138.
- Das, S., Cheng, J.J.R., Murray, D.W., and Nazemi, N. 2008. Effect of monotonic and cyclic bending deformations on NPS12 wrinkled steel pipeline. *Journal of Structural Engineering*, 134: 1810-1817.
- Det Norske Veritas (DNV). 2007. DNV offshore standard OS-F101: Submarine pipeline systems. Det Norske Veritas, Hovik, Norway.
- Dorey, A.B., Murray, D.W., and Cheng, J.J.R. 2002. Material property effects on critical buckling strains in energy pipelines. *In Proceedings of the 4th International Pipeline Conference*, Sep 30-Oct 3 2002, Vol. A, pp. 475-484.
- Dorey, A.B., Murray, D.W., and Cheng, J.J.R. 2006. Initial imperfection models for segments of line pipe. *Journal of Offshore Mechanics and Arctic Engineering*, 128: 322-329.
- Hibbitt,H.D., Karlsson, B.I., and Sorensen, P.,. 2006. ABAQUS version 6.6 - theory manual. .
- Khoo, H.A. 2000. Ductile fracture of steel. PhD Thesis, University of Alberta, Edmonton, AB, Canada.

- Matic, P. 1985. Numerically predicting ductile material behaviour from tensile specimen response, *Theoretical and Applied Fracture Mechanics*, 4: 13-28.
- Murray, D.W. 1997. Local buckling, strain localization, wrinkling and postbuckling response of line pipe. *Engineering Structures*, 19: 360-371.
- Ramberg, W. and Osgood, W.R. 1943. Description of stress-strain curves by three parameters. National Advisory Committee for Aeronautics (United States Advisory Committee for Aeronautics), Washington, DC, United States.
- Wilkie, S.A., Doblanko, R.M., and Fladager, S.J. 2001. Northern Canadian pipeline deals with effects of soil movement. *In* , Vol. 99, pp. 62.
- Yoosef-Ghodsi, N., Kulak, G.L., and Murray, D.W. 1995. Some test results for wrinkling of girth-welded line pipe. *In* Proceedings of the 14th International Conference on Offshore Mechanics and Arctic Engineering. Part 5 (of 5), Jun 18-22 1995, Vol. 5, pp. 379-387.
- Yukon Government. updated on March 27, 2006. Pipeline and transportation infrastructure [online]. .
- Zhang, Y. and Das, S. 2008. Failure of X52 wrinkled pipeline subjected to monotonic bending deformation and internal pressure, *International Journal of Offshore and Polar Engineering*, 18: 50-55.
- Zhao, R., Huang, R., Khoo, H.A., and Cheng, J.J.R. 2009. Parametric finite element study on slotted rectangular and square HSS tension connections. *Journal of Constructional Steel Research*, 65: 611-621.

## 5. DEVELOPMENT OF FAILURE CRITERIA<sup>1,2</sup>

### 5.1 General

Under installation and operational conditions of onshore buried pipelines, it is very important to have a design procedure to account for different failure modes under variable load conditions. Moreover, it is essential to exploit the pipe capacity with high utilization of the pipe material, as well as to have a safe design. These conditions, which advocate strain-based design, may allow large plastic deformations in the pipe wall. However, more careful attention should be paid, as under severe geo-environmental loading conditions typical in Canadian North, these pipelines can often undergo large deformations due to displacement controlled loading process; thus resulting in large localized deformations (wrinkles). Consequently, the detrimental characteristics expected from these wrinkles, such as possible fracture (eventually a loss of containment) or benign deformation, will depend on the driving mechanism associated with the wrinkle formation and deformation process (Ahmed et al. 2010).

Previous research observations have indicated that the occurrence of fractures in pipe wrinkle is rare for monotonically controlled deformation processes and the shape of these wrinkles is essentially axisymmetric (Das et al. 2002; Zhang and Das 2008b). Under continued deformation, there will be stacking up of wrinkles developing an “accordion” configuration without any fracture at pipe wrinkle (Das 2003). However, a field fracture was observed recently within the wrinkle location in an NPS10 (10 in or 254 mm nominal pipe diameter) energy pipe operated by WestCoast Energy Inc. in British Columbia, Canada (Das et al.

---

<sup>1</sup> Part of this chapter has been published and presented the 8<sup>th</sup> International Pipeline Conference (IPC), ASME, September, 2010, Calgary, Alberta, Canada [Note: This paper has been nominated as one of the best seven student papers in IPC2010]

<sup>2</sup> Part of this chapter is presently under review for possible publication in the Journal of Structural Engineering, ASCE

2002). Field observations had indicated that the final failure was a “tearing” failure resulting from monotonic application of an axial load not aligned with the axis of the pipe. In order to verify this failure mechanism, a proof of concept test under the combination of axial and shear load with appropriate boundary conditions was carried out at the University of Alberta (Das et al. 2002). The full-scale test on an NPS12 (12 in or 305 mm nominal pipe diameter) pipe was successful to simulate a fracture at the wrinkle fold similar to field. Successful simulation of this unique behaviour in the laboratory had emphasized that fractures can occur at wrinkle locations even under monotonic load-deformation process with appropriate boundary conditions.

Being motivated from the proof of concept test results, a numerical investigation (as discussed in Chapter 3) was carried out to find the key factor responsible for this unique failure mechanism (Ahmed et al. 2010). In this analytical work, a full-pipe finite element (FE) model simulated the complex load-deformation behaviour observed in field and in laboratory with reasonable accuracy. According to the results of this numerical analysis, the stress-strain relations obtained from the wrinkle fold located at the compression side of the deformed pipe had identified the presence of the strain reversals, even for monotonic non-axisymmetric loading. It is important to add that there was no significant strain reversal at the crest of the wrinkle. These strain reversals were identified as one of the key factors to initiate fracture in the pipe wall and eventually, to fail the pipeline under tearing action. Therefore, in this chapter, the presence of strain reversal has been chosen as one of the failure criteria to predict the tearing fracture of wrinkled pipe.

Results obtained from the proof of concept test (Das et al. 2002) on an NPS12 pipe specimen were very much limited to the load-displacement ( $P-\Delta$ ) plot and the final deformed shape of the failed specimens. Since no detailed information was documented, it was not possible to broaden the scope of the preliminary analytical work (Ahmed et al. 2010). In order to establish the failure criteria for this failure mode, more rigorous investigation was felt necessary and hence, a full-scale

experimental program was carried out on NPS16 (16 in. or 406.4 mm nominal pipe diameter) and NPS20 (20 in. or 508 mm nominal pipe diameter) specimens under sustained axial deformation with constant curvature (Aydin 2007). Results of this test program (presented in Chapter 4) have indicated that although all the tested specimens did exhibit very ductile behaviour with significant plastic deformation, presence of small circumferential cracks in several test specimens was reported (Aydin 2007), and a significant fracture in the pipe wall was observed at the wrinkle fold of one of the NPS16 specimens (Ahmed et al. 2009). The occurrence of this fracture had provided an agreement with the observations of the preliminary numerical work (Ahmed et al. 2009). Results of this experimental program were used to verify the performance of the developed FE model comprehensively. Based on the comparison drawn in Chapter 4, the numerical analyses provided a fairly good prediction of the test behaviour of all specimens in terms the load-displacement response and moment-curvature relation. In addition, the FE analyses have successfully captured both local and global behaviour of the test specimens in terms of the deformation configurations as well as strain measurements.

Based on the comparisons drawn in Chapters 3 and 4, it seems reasonable to carry out further analyses using this numerical model to predict the localized stresses and strains at wrinkle locations of all test specimens including NPS12, NPS16 and NPS20 pipes. This chapter focuses on establishing the failure criteria utilizing the results of numerical analyses to predict this tearing failure mode. In conjunction with the strain reversal criterion discussed in Chapter 3, the critical equivalent plastic strain was used as the fracture or damage initiation limit in the FE model. A detail discussion on the development of the failure criteria, demonstrating the accuracy or acceptability of predicting this unique failure mechanism is presented in this chapter.

## 5.2 Development of Failure Criteria

In order to predict this tearing behaviour of wrinkled pipes, nonlinear numerical analyses were carried out using the finite element program ABAQUS (Hibbitt, H.D., Karlsson, B.I., and Sorensen, P., 2006). Test data obtained from the proof of concept test (Das et al. 2002) and the experimental work of Aydin (Aydin 2007) were used to validate the performance of the numerical model and the verification of all those results is presented in Chapter 3 and 4, respectively.

In the numerical analyses of all these full-scale tests, the pipe materials were assumed to behave according to the incremental isotropic hardening plasticity model. The hardening behaviour of these pipe materials can be described by a single parameter such as the hardening exponent according to a power hardening law (Zhang et al. 1999). In addition, the onset of tearing fracture is assumed to occur when the equivalent plastic strain ( $\bar{\epsilon}^p$ ) in any section point of any element in the FE model reaches a critical value,  $\bar{\epsilon}_c^p$ . The critical value of  $\bar{\epsilon}_c^p$  can be determined for each material from the results of the tension coupon tests. However, in order to define this critical limit, the true stress ( $\sigma$ ) – true plastic strain ( $\epsilon_p$ ) relation of the pipe material beyond the initiation of necking (up to fracture) of all the tested coupons obtained from different grade full-scale pipes have to be established (Yang et al. 1999; Zhao et al. 2009).

### 5.2.1 Tension Coupon Tests

True stress – true plastic strain curve including material response in both the pre- and post-plastic localization regime is essential when large deformation is considered, e.g. in the metal forming analysis, or in the analysis of ductile damage and fracture such as the present case (Zhang et al. 1999). To obtain these true stress – true strain curves, round tensile bars are usually recommended for thick sections (Zhang et al. 1999). However, for thin sections such as steel energy line pipes, it is more practical to use specimens with rectangular cross-section for

uniaxial tensile test (Zhang et al. 1999). Therefore, tension coupons with rectangular cross-section were preferred in this research program.

As discussed in Chapters 3 and 4, the NPS16 pipe specimens were taken from a grade X60 steel pipe with a specified minimum yield strength (SMYS) of 414 MPa, whereas the NPS20 pipe specimens were taken from a grade X65 steel pipe with a specified minimum yield strength (SMYS) of 448 MPa. Three tension coupons were cut from the NPS16 pipe, and three were taken from the NPS20 stock. All these coupons were cut along the longitudinal axis of the pipe. During the coupon tests, readings were taken at convenient intervals. These readings included static yield strength and static ultimate strength. Final elongation was measured from the failed specimens. The average material properties of the tested coupons are listed in Table 5.1. It is important to add that the actual yield strength at 0.5% strain was found to be significantly higher than SMYS for both X60 and X65 pipe materials.

As mention in Chapter 3, the NPS12 pipe specimen used for the proof concept test (Das et al. 2002) was taken from a grade X52 steel pipe with a specified minimum yield strength (SMYS) of 358 MPa. In this case, four tension coupon tests were conducted by Das et al. (Das 2003) and the measured average engineering stresses and strains obtained from those coupon tests were reported (Das 2003). The average material properties of these tested coupons are also listed in Table 5.1.

### ***5.2.2 True Stress –True Plastic Strain Curves***

Up to the peak load, the true stress – true plastic strain curves of all the pipe materials used in this study were obtained directly from the initial segment of the engineering stress – strain data. After the peak load, the true stress – true plastic strain curves were generated using a modified power-law equation by rearranging the well-known Ramberg–Osgood relation (Ramberg and Osgood 1943; Canadian Standards Association (CSA) 2007). Similar approach was taken by several researchers (Cheng et al. 1998; Khoo 2000; Zhao et al. 2009). A detail discussion

regarding the procedure to obtain material curves beyond peak load has been covered in Chapter 4.

Figure 5.1 represents the true stress – true plastic strain ( $\sigma - \varepsilon_p$ ) values until fracture for all the pipe materials used in this study. These true stress-true plastic strain values were used to define the material model of the full-pipe and half-pipe FE models used in Chapter 3 and Chapter 4, respectively. As can be seen from Figure 5.1, in general, there is an initial elastic relationship followed by a gradual development of plastic flow with strain hardening for all the materials. However, the strain hardening exponent for X52 material is much higher compared to X60 and X65 pipes. It is important to add that the  $\sigma - \varepsilon_p$  relation for X52 material shown in Figure 5.1 was obtained from literature (Das 2003) and was kept unmodified in this study. Along with the classical von Mises yield criterion, an isotropic stress-strain hardening model was chosen for all the numerical analyses of the full-scale test specimens.

### **5.2.3 Failure Criterion – Critical Plastic Strain ( $\bar{\varepsilon}_c^p$ ) Limit**

Before defining the critical strain limit as one of the failure criteria, a brief review regarding the development of the equivalent plastic strain is included in this section. In order to compute the equivalent plastic strain ( $\bar{\varepsilon}^p$ ) in the numerical simulations, a material constant ‘ $d\lambda$ ’ was computed using the equation 5.1, which is based on the incremental theory (Chen and Han 1988). In expression, the term ‘ $d\bar{\varepsilon}^p$ ’ is the uniaxial true plastic strain increment or the equivalent plastic strain increment and the term ‘ $\sigma_{v.m.}$ ’ is the uniaxial true stress or the von Mises stress in MPa, respectively. The values of these terms can be obtained from the uniaxial tension test data (Chen and Han 1988), and are included in the material models (see Figure 5.1). Once the value of  $d\lambda$  had been obtained at each time increment of the analysis, the incremental plastic strain ( $d\varepsilon_{ij}^p$ ) was computed using expressions 5.2 and 5.3. Then, the equivalent plastic strain ( $\bar{\varepsilon}_c^p$ ) values were obtained using

the numerical solution, given by the expression 5.4 (Hibbitt, H.D., Karlsson, B.I., and Sorensen, P., 2006) after each time increment.

$$5.1) \quad d\lambda = \frac{3}{2} \left( \frac{d\bar{\varepsilon}^p}{\sigma_{v.m.}} \right)$$

$$5.2) \quad d\varepsilon_{ij}^p = d\lambda(S_{ij})$$

$$5.3) \quad S_{ij} = \sigma_{ij} - \left( \frac{\sigma_{kk}}{3} \right) \delta_{ij}$$

$$5.4) \quad \bar{\varepsilon}^p = \int d\bar{\varepsilon}^p = \sum \left( \frac{2}{3} d\varepsilon_{ij}^p d\varepsilon_{ij}^p \right)^{\frac{1}{2}}$$

where,  $S_{ij}$  is the deviatoric stress tensor, given by the expression 5.3. In this expression,  $\delta_{ij}$  is the Kronecker Delta (Chen and Han 1988), and  $\sigma_{ij}$  is the Cauchy stress tensor (Hibbitt, H.D., Karlsson, B.I., and Sorensen, P., 2006).

As mentioned before, it is assumed that the tearing fracture will initiate as the equivalent plastic strain ( $\bar{\varepsilon}^p$ ) in any section point of any element in the FE model reaches a critical value,  $\bar{\varepsilon}_c^p$ . Application of this critical plastic strain ( $\bar{\varepsilon}_c^p$ ) value as a fracture limit was adopted successfully by a number of researchers (Cheng et al. 1998; Martinez-Saucedo et al. 2006; Zhao et al. 2009) in the FE analyse of round slotted hollow steel sections (HSS). This critical plastic strain ( $\bar{\varepsilon}_c^p$ ) value corresponds to a point well beyond the peak load and the initiation of necking of a tensile coupon tests, but before the complete fracture of those test coupons (Cheng et al. 1998), as shown in Figure 5.2. Since it is reasonable to assume that fracture has initiated in advance of the complete fracture, it is rational to use  $\bar{\varepsilon}_c^p$  as an onset of fracture limit.

An approximation of the critical equivalent plastic strain limit can be calculated from the measured cross-sectional area ratio ( $A_0/A_{fmid}$ ) at fractures using equation 5.5 (Zhao et al. 2009).

$$5.5) \quad \bar{\varepsilon}_c^p = \ln\left(\frac{A_0}{A_{fmid}}\right)$$

In equation 5.5,  $A_0$  represents the cross-section area on mid-section dimension before test in  $\text{mm}^2$ , and  $A_{fmid}$  represents the cross-section area on mid-section dimension after the fracture of the coupon in  $\text{mm}^2$ . Figure 5.3 represents a picture of typical tensile test coupon with schematic comparison of the cross-section before and after the test. The manual cross-sectional measurements before and after the test of grade X60 and grade X65 coupons are reported in Table 5.2. The computed values of  $A_0/A_{fmid}$  are also reported in Table 5.2. As can be seen from Table 5.2, the approximate  $\bar{\varepsilon}_c^p$  limit (obtained using equation 5.5) varies from 1.1 to 1.3 for all X60 test coupons, and from 0.96 to 1.05 for all X65 test coupons. Taking the medium of these ranges, the  $\bar{\varepsilon}_c^p$  limit of 1.2 and 1.0 could be selected for NPS16 and NPS20 specimens, respectively. As shown in Table 5.2, an average value of 1.0 for X52 grade steel obtained from literature (Das 2003; Zhang and Das 2008a; Zhang et al. 2008) could be chosen as  $\bar{\varepsilon}_c^p$  limit for NPS12 specimens.

However, in order to provide better understanding of the material behaviour as well as establishing confidence on this critical strain value, all the available test coupons results obtained from NPS16 pipes (X60) and NPS20 pipes (X65) have been analyzed numerically using FE simulator ABAQUS (Hibbitt, H.D., Karlsson, B.I., and Sorensen, P., 2006). However, as no detail information including the load-displacement response and cross-sectional dimension was available for X52 pipe material, the numerical analysis of X52 coupons is not possible in this case.

#### 5.2.4 Finite Element Models of Tension Test Coupons

Nonlinear three dimensional (3D) FE models of the tension test coupons of X60 and X65 grade steel have been developed using the general purpose commercial FE analysis program ABAQUS. The load-displacement plots along with the initial and final cross-section measurements obtained from the coupon test results of X60 and X65 are used to verify the performance of the FE simulation.

##### 5.2.4.1 Description of the FE model

One fourth (quarter) of the test coupon was used to build the 3D FE models for these two materials. The FE model with the dimensions in the plan view, the boundary conditions under uniaxial loading and the detailed mesh is presented in Figure 5.4. 8-noded 3D brick type elements (C3D8) were used in all the FE analyses. Similar to the full-scale pipe models, the incremental isotropic hardening along with the von Mises yield criterion was used for the material model of the coupons. A set of discrete data points of true stress –true plastic strain ( $\sigma - \varepsilon_p$ ), as shown in Figure 5.1, were used as the input data for the material model. Two linear elastic constants: modulus of elasticity ( $E$ ), and Poisson's ratio ( $\nu$ ) used in these models are listed in Table 5.1 for each material. The convergence rate of the computed results in terms of mesh density was checked to reach at the level with reasonable accuracy and computational time.

##### 5.2.4.2 Validation of the Coupon Models

The load-displacement ( $P-\Delta$ ) plots obtained from the tested coupon results of X60 grade and X65 grade steel were used to verify the performance of the FE simulation. The comparison between the experimentally measured and numerically predicted load-displacement response is drawn in Figure 5.5. In general, a good correlation can be observed between physical tests and FE analyses of both grades of materials. Up to peak load, as indicated by point 'P' on the FEA plots or 'P'' on the curves obtained from tested coupons in Figure 5.5,  $P-\Delta$  responses simulated by FE model are almost identical to test results. However,

in the post-peak load response, the FEA plots are found to be slightly softer than those obtained from the tested coupons. These dissimilarities may be attributed due to the approximation considered to model the coupon geometry and the simplification adopted in the assumed material behaviour. The simplification in the material behaviour implies that the tri-axial or bi-axial state of stress at the necking region has not been considered to modify the true stress values. Nevertheless, the FE model has predicted the test behaviour with acceptable accuracy. Hence, it seems reasonable to use the numerical results obtained from the FE analyses for further verification.

#### 5.2.4.3 Verification of Failure Criterion using Numerical Results

During the FE analyses of both materials, the approximate cross-sectional area at mid section of the coupon model was monitored. This cross-sectional area represents the instantaneous area at any specific point of the FE analysis. This area was obtained by multiplying the reduced width of the coupon ( $W_{mid}$ ) with the reduced thickness of the coupon ( $t_{mid}$ ) at any instant (see Figure 5.3a). For any specific material grade, e.g. X60 grade, these area values were compared with the average of three areas ( $A_{fmid}$ ) presented in Table 5.2. Points 'E<sub>1</sub>' and 'E<sub>2</sub>', as indicated on the displacement axis of the FEA  $P$ - $\Delta$  plots of X60 grade and X65 grade, respectively in Figure 5.5, represent the location at which the mid-sectional area has reached very close to test value. Figure 5.7a and Figure 5.7b illustrates the deformed shapes of X60 and X65, respectively, obtained at point 'E' on the  $P$ - $\Delta$  plots of Figure 5.5. For both materials, the neck region with moderate mesh distortion can be seen from Figure 5.7.

The equivalent plastic strain (PEEQ or  $\bar{\epsilon}^P$ ) distributions obtained at two specific displacement values (i.e. point 'E' and point 'C' in Figure 5.5) are presented in Figure 5.8 and Figure 5.9 for materials X60 and X65, respectively. The location of the maximum strain values are also indicated in those figures. The equivalent plastic strain ( $\bar{\epsilon}^P$ ) values, shown in Figure 5.8a and Figure 5.9a, are obtained at points 'E<sub>1</sub>' and 'E<sub>2</sub>', respectively, on the  $P$ - $\Delta$  curves. To be specific, the maximum

values of  $\bar{\epsilon}^P$  are 1.073 for X60 grade and 0.9375 for X65 grade. These values are representing the strain values at the point the coupons reached the cross-sectional dimension very close to the measured values reported in Table 5.2. Theoretically, these strain values should be selected as the critical strain limits ( $\bar{\epsilon}_c^P$ ) for these pipe material.

However, the equivalent plastic strain ( $\bar{\epsilon}^P$ ) values, obtained at points 'C<sub>1</sub>' and 'C<sub>2</sub>' on the  $P$ - $\Delta$  curves, are presented in Figure 5.8b and Figure 5.9b, respectively. At point 'C', the maximum values of  $\bar{\epsilon}^P$  are 1.201 for X60 grade and 1.055 for X65 grade. These values are very close to the values obtained using equation 5.5 and also not far away from the values at point 'E'. In summary, both point 'E' and 'C' lie between a point well beyond the initiation of necking and/or the peak load of the coupon tests, but before the complete fracture of those test coupons, as indicated by point 'F' on the  $P$ - $\Delta$  curves in Figure 5.5. Therefore, it can said that any of these two values, either at point 'E' or at point 'C', can be used as the critical strain limit. For simplicity and general applicability, the critical strain value,  $\bar{\epsilon}_c^P$ , obtained using equation 5.5 has been used as one of the failure criteria in this study.

The location of the critical strain limit for all the pipe material including X52, X60 and X65, are presented in Figure 5.10. As mentioned earlier, the position of  $\bar{\epsilon}_c^P$  for any specific grade of steel in Figure 5.10 represents a point which occurs well beyond the initiation of necking but before the complete fracture of the test coupons. The  $\bar{\epsilon}_c^P$  limits have been set as 1.0, 1.2, and 1.0 for NPS12 pipe with X52 grade, NPS16 pipe with X60 grade, and NPS20 with X65 grade, respectively.

### **5.3 Application of Failure Criteria— 'Double Criteria'**

The numerical analyses of all the full-scale pipe specimens, conducted and verified in Chapters 3 and 4, have provided a good prediction of the test

behaviour. Therefore, the results obtained from these FE analyses have been utilized to demonstrate the acceptability of the failure criteria — ‘Strain-Reversal Criterion’ and ‘Critical Plastic Strain Limit’, defined in the previous sections. For recapitulation and providing continuity, the full-scale test parameters used in the FE analyses conducted are reported in Table 5.3. For convenience, the proof of concept test (NPS12 specimen) under the combination of axial and shear loading (Das et al. 2002) has been designated as D12P0A3.4-1 or specimen 1 in Table 5.3. The full-scale tests on NPS16 and NPS20 specimens under constant curvature and monotonic increasing axial deformation (Aydin 2007) are also included in Table 5.3. Table 5.3 summarizes all the key features of these full-scale test programs. As mentioned before, each of these tests is designated by a descriptor of the form of  $D_{xx}P_{xx}A_{xx}-Z$ , where “ $D_{xx}$ ” designates the outside diameter of the pipe in inch, “ $P_{xx}$ ” is the descriptor of the level of the internal pressure as a percentage of  $p_y$ , where,  $p_y$  is equal to the internal pressure applied to the pipe such that the hoop stress reached to SMYS, “ $A_{xx}$ ” indicates the average of the applied end rotations ( $\theta_{avg}$ ) at which two ends of the specimen are locked in degree, and  $Z$  indicates the test specimen number. A detail discussion regarding the test matrix along with the loading and boundary conditions for all these specimens is presented in Chapters 3 and 4.

In order to facilitate the discussion regarding the development and application of failure criteria, the cut segments of the wrinkled pipes obtained from the compression side of the NPS16 specimens are presented in Figure 5.11. As can be seen, there was an initiation of crack or rupture at the bottom of the wrinkle fold identified as ‘X’ for specimen 2 (D16P0A5-2 in Table 5.3). Whereas a significant cracking in the pipe wall was observed at location of ‘X’ on wrinkle fold of specimen 3 (D16P40A7-3), as denoted in Figure 5.11. The inspection of the final deformed shapes and the close-up views of the cut segments have indicated that the interior surfaces of the pipe wrinkle came into contact with each other as wrinkle closed. Under continued axial deformation, the top segment of both pipe specimens had slipped inside the bottom segment in a ‘telescoping’ manner creating a sharp fold in the pipe wall. However, the presence of this “telescoping”

action was found to be more prominent for specimen 3. Eventually, significant fracture in the pipe wall of the specimen 3 was occurred near the sharpest bend of the wrinkle fold. However, the geometric constrains developed from the applied test parameters and loading conditions, to be specific the internal pressure condition, for specimen 2 did not allow the crack to propagate, as can be seen from Figure 5.11. It is important to add that the fracture was initiated from the outside of the pipe wall for both specimens, and eventually propagated through the thickness of the pipe wall for specimen 3.

The final deformed shape and the shape of the crack for specimen 3, as shown in Figure 5.11, have provided an evidence of tearing fracture. Similar trend was also observed in the NPS12 specimen (or D12P0A3.4-1) obtained from the proof of concept test and NPS10 specimen obtained from the field (Das et al. 2002). The presence of fracture at the sharp wrinkle fold is shown by ‘X’ mark in Figure 5.12a and Figure 5.12b for the failed field and test specimens, respectively. The results of the numerical simulation of D12P0A3.4-1 conducted in the earlier phase of this research project (Ahmed et al. 2010) have indicated that severe strain reversals could occur in the vicinity of the telescopic wrinkle fold, even for monotonic non-axisymmetric loading. Eventually, these strain reversals could be responsible for the onset of fracture initiating from the outer surface of the pipe wall at location ‘X’ in Figure 5.12c. Similar scenario was observed during the test of all three specimens, where a rupture had initiated from the outer surface of the pipe wall and eventually, propagated through pipe wall thickness for specimen 1 and specimen 3.

Therefore, the occurrence of severe strain reversals at any location of the developed FE model has been chosen as one of the criteria (designated as ‘Criterion-1’) indicating the possibility of tearing failure, while analysing the results of this numerical study. Along with ‘Criterion-1’, the equivalent plastic strain values (PEEQ or  $\bar{\epsilon}^p$ ) of the critical elements obtained after each time increment of the numerical analyses are monitored and then, compared with the ‘Critical Equivalent Plastic Strain ( $\bar{\epsilon}_c^p$ )’ limit defined in previous section. The  $\bar{\epsilon}_c^p$

limit was set as 1.0 for NPS12 and NPS20 pipes and 1.2 for NPS16 pipes. Once the  $\bar{\epsilon}^p$  value of any element in the FE model reaches or exceeds  $\bar{\epsilon}_c^p$  limit, it is assumed that the fracture has initiated in the pipe wall. This equivalent plastic strain limit is defined as ‘Criterion-2’ for the onset of fracture in the FE simulation. In this research work, the onset of fracture is assumed to exhibit at any specific location of the pipe wall, only if both ‘Criterion-1’ and ‘Criterion-2’ occur concurrently.

Finally, a prediction-based approach, which consists of checking of both ‘Criterion-1’ and ‘Criterion-2’ at any location of the wrinkle, was applied to all six test specimens reported in Table 5.3, in order to demonstrate the acceptability of these ‘Double Criterion’ for predicting this unique failure mechanism.

### **5.3.1 Specimen 1 (D12P0A3.4-1)**

A detail description regarding the evolution of the wrinkle, the assessment of the wrinkle profile, and the stress-strain relations at various locations of the wrinkle for specimen 1 is presented in Chapter 3. Figure 5.12c illustrates the final deformed shape of the specimen 1 obtained from the analysis of the full-pipe model. A strip was isolated from compression side of the wrinkled pipe at the location of the dashed lines AA’, as shown in Figure 5.12c, to facilitate the discussion. Results of some of the critical elements, as recognized in Chapter 3 (Ahmed et al. 2010), are included in this section to trace the presence of strain reversal, defined as ‘Criterion-1’. According to earlier numerical results, elements 8537 and 8663 were identified at the wrinkle foot in the initial stage of  $P$ - $\Delta$  history and then at the bottom of the wrinkle fold, finally ending up at location ‘X’ in Figure 5.12c, where telescopic tearing had the potential to occur (see Figure 5.12a and Figure 5.12b). Element 7655 located at the wrinkle crest (see Figure 5.12c) was also included for comparison, as fractures could occur (typically initiating from inside of the pipe wall) at the wrinkle crest under low cycle fatigue load-deformation (Das et al. 2001; Das et al. 2007).

### 5.3.1.1 Strain Reversal Criterion

The true longitudinal (along the longitudinal axis of the pipe) stress – logarithmic strain ( $\sigma$ - $\varepsilon_{ln}$ ) plots for elements 7655, 8537, and 8663 are presented in Figure 5.13. In the  $\sigma$ - $\varepsilon_{ln}$  plots, SP1 (section point 1) and SP7 (section point 7) represent the inner and the outer surface of the pipe wall, respectively. It is important to add that the any positive value in these plots indicates tensile stress or strain. As can be seen from Figure 5.13, although the applied loading was applied in a monotonic manner, the local true  $\sigma$ - $\varepsilon$  relations of elements 8537, and 8663 were not monotonic and exhibited strain reversal behaviour. Specifically, the outer face (SP7) of elements 8537 and 8663 were under compressive strains in the initial stages and finally, reversed towards tensile strains at the end of the analysis (see Figure 5.13b). Whereas the strain values at SP1 for those elements were found to be on the tensile region for the most part of the analysis, as indicated in Figure 5.13a. This fact suggested the possibility of the initiation of a fracture from the outer surface of the pipe wrinkle near Elements 8537 and 8663, which was also evident in the failed field and all three test specimens. However, the element 7655, located at the crest of the wrinkle, did not go through the strain reversal process, although it experienced severe plastic bending/deformation. This could provide an explanation, why there was no fracture observed at the wrinkle crest of the failed field specimen and test specimen 1.

### 5.3.1.2 $\bar{\varepsilon}_c^p$ Criterion

As elements 8537 and 8663 have gone through the strain reversal process meeting ‘Criterion-1’, it is justifiable to track the equivalent plastic strain ( $\bar{\varepsilon}^p$ ) of those elements and hence, check the ‘Criterion-2’. The true longitudinal stress versus equivalent plastic strain ( $\sigma$ - $\bar{\varepsilon}^p$ ) plots obtained from inner (SP1) and outer (SP7) surfaces of elements 7655, 8537, and 8663 are presented in Figure 5.14. It can be observed from Figure 5.14b that the equivalent plastic strain ( $\bar{\varepsilon}^p$ ) value obtained from the outer surface (SP7) of element 8663 (located at wrinkle fold) has exceeded the critical strain ( $\bar{\varepsilon}_c^p$ ) limit of 1.0 meeting ‘Criterion-2’. However, the

$\bar{\varepsilon}^p$  value at SP7 of element 7655 (located at wrinkle crest) was much smaller than the critical limit. On the other hand, the  $\varepsilon^p$  values obtained from the inner (SP1) surface of elements 7655 and 8663 (see Figure 5.14a), although did not reach the  $\bar{\varepsilon}_c^p$  value, were found to be significantly close to  $\bar{\varepsilon}_c^p$ . Moreover, the strain growth of element 8663 at both SP1 and SP7 was still evident in Figure 5.14. The contour plot of the equivalent plastic strain obtained from the outer surface of specimen 1 shown in Figure 5.15 also provides similar agreement. Based on the above discussion, it can be said that the stress-strain relations of element 8663 did meet both ‘Criterion-1’ and ‘Criterion-2’. Hence, it is reasonable to say that the onset of fracture was initiated from the outer surface of the pipe wall at the vicinity of element 8663 conforming the test observations (Das et al. 2002), and eventually, triggered the failure of the test specimen 1.

### 5.3.2 Specimen 2 (D16P0A5-2)

Figure 5.16a illustrates the close-up view of the final deformed shape of specimen 2 at wrinkle location. A strip was isolated from compression side at the location of dashed lines AA' in Figure 5.16a to facilitate the present discussion. The strip (or Line AA') in Figure 5.16a is equivalent to the strip obtained from the compression side of the test specimen in Figure 5.11a. The symbol ‘ $\eta+$ ’ in Figure 5.16a represents the outer surface of the pipe wall. Elements 4801 and 4901 located at the sharpest bend of wrinkle fold were anticipated to be critical in this case. Element 4301 located at wrinkle crest was also included for comparison to provide a comparison with the low cycle fatigue load-deformation (Das et al. 2001; Das et al. 2007).

#### 5.3.2.1 Strain Reversal Criterion

The true longitudinal stress – logarithmic strain ( $\sigma$ - $\varepsilon_{ln}$ ) plots obtained from SP1 (inner surface) and SP7 (outer surface) of elements 4301, 4801, and 4901 are presented in Figure 5.17a, and Figure 5.17b, respectively. As can be seen from Figure 5.17a representing the inside of the pipe (i.e. SP1), the strain reversal

process started for element 4801 located at the wrinkle fold, although the extent was not severe. However, the strain reversal process was not noticeable for the other two elements at the inside of the pipe. In contrast, the  $\sigma$ - $\varepsilon_{in}$  plots of element 4801 at the outside of the pipe (see Figure 5.17b) did exhibit considerable strain reversal behaviour, even under monotonically increased axial deformation with constant curvature. It is important to note that although the strain values of element 4901 were significantly high compare to that of element 4801, the extent of strain reversal in case of element 4901 was insignificant even at the outer surface of the pipe. Based on previous observation (Ahmed et al. 2010), it can be anticipated that there could be a possibility of fracture initiation at the proximity of element 4801. However, element 4301, located at wrinkle crest, did not go through the strain reversal process at both inner and outer surface of the pipe wall, which confirms the findings of specimen 1.

#### 5.3.2.2 $\bar{\varepsilon}_c^p$ Criterion

Now for checking the ‘Criterion-2’ of elements 4301, 4801, and 4901, the  $\sigma$ - $\bar{\varepsilon}^p$  plots at inner (SP1) and outer (SP7) surfaces of those elements were obtained and presented in Figure 5.18 a and Figure 5.18 b, respectively. Based on the previous discussion, element 4801 was anticipated to be critical, as it went through a reasonable strain reversal process. As can be seen Figure 5.18 a, the equivalent plastic strain ( $\bar{\varepsilon}^p$ ) value obtained at SP1 of element 4801 (located at wrinkle fold) was much smaller than the critical strain ( $\bar{\varepsilon}_c^p$ ) value, which was set as 1.2 for NPS16 pipes with X60 grade steel. Whereas,  $\bar{\varepsilon}^p$  at SP7 of element 4801 was found to be significantly close to  $\bar{\varepsilon}_c^p$  limit, as illustrated in Figure 5.18 b. The contour plot or distribution of equivalent plastic strain (PEEQ or  $\bar{\varepsilon}^p$ ) values obtained from outer surface of wrinkled pipe shown in Figure 5.19a, which was taken at the last increment of the FE analysis of specimen 2, also provides similar observation. This indicates that there is a possibility of fracture initiation from the outer surface of the pipe wall (SP7) at the location of element 4801.

It can also be observed from Figure 5.18 b that the  $\bar{\epsilon}^P$  value at SP7 of element 4901, located near the bottom of the wrinkle fold, reached very close to the critical limit ( $\bar{\epsilon}_c^P$ ). However, the presence of strain reversal process for element 4901 was insignificant (see Figure 5.17). After assessing the cut segment view of specimen 2 in Figure 5.11a, it can be said that although the fracture in the pipe wall did initiate close to the vicinity of element 4801 and 4901, the fracture did not propagate. This may be attributed due to the geometric constrains developed from the applied test and load parameters of specimen 2, specifically due to relatively smaller magnitude of end rotations (i.e.  $\theta_{avg}$  in Table 5.3), which were responsible for generating the curvature. Moreover, the geometry of the wrinkle shapes, observed during the final stage of test and FEA closely resembling the shape of a “Cowboy Hat” with a diamond buckling mode (see Chapter 4)(Murray 1997) due to zero internal pressure, did not allow to the exponentiation of strain reversal process as well as the growth of plastic strain. Therefore, no significant crack was observed for specimen 2. However, the  $\bar{\epsilon}^P$  values at both SP1 and SP7 of element 4301 (located at wrinkle crest) did not reach very close to the critical limit, and thus, did not meet both ‘Criterion-1’ and ‘Criterion-2’ similar to specimen 1.

### 5.3.3 Specimen 3 (D16P40A7-3)

For specimen 3, a strip was isolated from compression side at the location of dashed lines BB' in Figure 5.16b, for identifying the critical elements. The strip (or Line BB') in Figure 5.16b is equivalent to the strip obtained from the compression side of the test specimen in Figure 5.11b. Elements 5801 and 5901 located at wrinkle fold were anticipated to be critical in this case. The contour plot of the equivalent plastic strain ( $\bar{\epsilon}^P$ ) obtained from outer surface of pipe wrinkle of specimen 3 presented in Figure 5.19b, which was taken at an axial displacement of 205 mm (see the  $P$ - $\Delta$  plot of D16P40A7-3 in Chapter 4), also provides similar anticipation. According to the distribution of  $\bar{\epsilon}^P$  in Figure 5.19b, the outer edge (SP7) of element 5801 has reached the critical strain limit

( $\bar{\epsilon}_c^p \sim 1.20$ ) at a displacement notably earlier than the end of the analysis of specimen 3. In addition, element 6301 located at wrinkle crest was also included to compare with previous cases.

### 5.3.3.1 Strain Reversal Criterion

The true  $\sigma$ - $\epsilon_{in}$  plots obtained from SP1 (inner) and SP7 (outer) of elements 5801, 5901, and 6301 are presented in Figure 5.20 a and Figure 5.20 b, respectively. As can be seen from Figure 5.20 a illustrating the behaviour of pipe interior (SP1), the strain values reversed (from tensile to compressive strain direction) considerably for elements 5801 and 5901. Whereas, there was no strain reversal observed at the SP1 of element 6301, although the strain value was significantly higher compared to other elements. At the outer surface (SP7) of pipe wall as shown in Figure 5.20 b, both element 5801 and 5901 went through a considerable strain reversal process, whereas no strain reversal was observed for element 6301. The extent of strain reversal at both SP1 and SP7 of elements 5801 and 5901 was found more prominent comparing to the case of specimen 2. Therefore, it is reasonable to assume that there could be a strong possibility of fracture initiation at the proximity of elements 5801 and 5901. On the other hand, element 6301 at wrinkle crest did not go through the strain reversal process similar to specimen 1 and specimen 3, implying rare possibility of fracture at wrinkle crest.

### 5.3.3.2 $\bar{\epsilon}_c^p$ Criterion

Since both element 5801 and 5901 did go through significant strain reversal process meeting ‘Criterion-1’, the  $\sigma$ - $\bar{\epsilon}^p$  plots at inner (SP1) and outer (SP7) surfaces of those elements were obtained to apply the critical strain ( $\bar{\epsilon}_c^p$ ) limit criterion (see Figure 5.21). Based on earlier comments, both elements 5801 and 5901 were anticipated to be critical. As can be seen Figure 5.21a, the equivalent plastic strain ( $\bar{\epsilon}^p$ ) value at SP1 of element 5801 (located at wrinkle fold) reached very close to the critical strain ( $\bar{\epsilon}_c^p$ ) limit. The  $\bar{\epsilon}^p$  values obtained from SP7 of elements 5801 and 5901 reached or crossed the  $\bar{\epsilon}_c^p$  value with a reasonable

margin, as illustrated in Figure 5.21b. Similar observation can be made from the contour plot of  $\bar{\epsilon}^P$  on the outer surface of the wrinkled pipe (see Figure 5.19b). However, the  $\bar{\epsilon}^P$  values at both SP1 and SP7 of element 6301 (located at wrinkle crest) did not reach close to the critical limit, as predicted.

Since both ‘Criterion-1’ and ‘Criterion-2’ have been met for element 5801 located at wrinkle fold, it can be said that there is a strong possibility of onset of fracture initiating from the outer surface (SP7) of the pipe wall. The above anticipation does conform the test observation of specimen 3, where a significant crack was observed at the wrinkle fold (see the cut segment view of specimen 3 in Figure 5.11b).

#### 5.3.3.3 Plastic Strain Growth

Now by comparing the case of ‘no significant fracture’ for specimen 2 with the present situation, the test parameters of specimen 3, to be specific, the presence of relatively large end rotations (i.e.  $\theta_{avg}$  in Table 5.3) and internal pressure condition, might allow to the exponentiation of strain reversal process as well as the growth of plastic strain, and hence, might contribute considerably to trigger this unique failure mechanism.

To provide more insight regarding the above comments, the equivalent plastic strain growth of both specimen 2 and specimen 3 along their displacement history is presented in Figure 5.22. The strain growth of critical elements, including the outer surface of wrinkle fold (element 5801 for specimen 3, or element 4801 for specimen 2) and the inner surface of the wrinkle crest (element 6301 for specimen 3, or element 4301 for specimen 2), is presented in Figure 5.22a. As can be seen, the strain growth rate at both wrinkle crest and fold for specimen 3 was found to be close (or uniform) up to a significant part of the displacement history due to the presence of internal pressure. At the later stages of the displacement history, the strain growth rate became insignificant at the wrinkle crest. Whereas, the strain growth rate increased sharply at the wrinkle fold crossing the critical strain limit, as indicated in Figure 5.22a crest. However, for specimen 2, the growth of plastic

strain at wrinkle fold was found to be notably lower compared to the wrinkle crest in certain portion of the displacement history due to the release of internal pressure. The strain values of specimen 2 both at wrinkle crest and fold were slightly smaller compared to specimen 2, as anticipated, due to smaller end rotations. Although the strain growth rate picked up appreciably at the wrinkle fold of specimen 2 reaching very close to  $\bar{\varepsilon}_c^p$ , the strain values did not reach the critical strain limit. This justifies why there was no crack propagation for specimen 2, even after an initiation of crack at the bottom of the wrinkle fold (see Figure 5.11a).

The strain growth of critical elements, including the inner surface of wrinkle fold and the outer surface of the wrinkle crest is presented in Figure 5.22b. As can be seen, although the plastic strain value at wrinkle fold of specimen 3 was very close to  $\bar{\varepsilon}_c^p$ , none of the elements reached or crossed the critical limits. This gives explanation for why there was no through-thickness crack for specimen 3, even after having a significant cracking through the pipe wall (see Figure 5.11b).

#### **5.3.4 Specimen 4 (D20P40A3.5-4)**

Similar to the first three specimens, a strip was isolated from compression side at the location of dashed lines AA' in Figure 5.23, for identifying the critical elements of specimen 4. Elements 3401 and 3501 located at wrinkle fold, and Element 3801 or 3805 at wrinkle crest were selected for discussion.

##### **5.3.4.1 Strain Reversal Criterion**

The true  $\sigma$ - $\varepsilon_{ln}$  plots obtained from SP1 (inner) and SP7 (outer) of elements 3401, 3501, and 3805 are presented in Figure 5.24a and Figure 5.24b, respectively. According to Figure 5.24, the presence of strain reversal was evident at both inner and outer surfaces of elements 3401 and 3501 located at wrinkle fold. However, the extent of reversal is not as considerable as for specimen 1 or specimen 3. For

element 3805 located at wrinkle crest, no strain reversal was observed, as expected.

#### 5.3.4.2 $\bar{\epsilon}_c^p$ Criterion

Now for checking the ‘Criterion-2’ of elements 3401, 3501, and 3805, the  $\sigma$ - $\bar{\epsilon}^p$  plots at inner (SP1) and outer (SP7) surfaces of those elements were obtained and presented in Figure 5.25. Based on the previous discussion, element 3401 or 3501 could be critical, as both of the elements went through a reasonable strain reversal process. As can be seen Figure 5.25, the equivalent plastic strain ( $\bar{\epsilon}^p$ ) values obtained at both SP1 and SP7 of these elements were noticeably smaller than the critical strain limit,  $\bar{\epsilon}_c^p$ , which was set as 1.0 for X65 grade steel. The distribution of equivalent plastic strain ( $\bar{\epsilon}^p$ ) on the outer surface of specimen 4 as shown in Figure 5.26, also provides similar observation. It is also important to add that the growth of  $\bar{\epsilon}^p$  for these critical elements was monitored through the analysis, and was found to be exceedingly small at the later stage of the analyses. This might be attributed due to the formation of another wrinkle just beneath the critical elements, as indicated in Figure 5.26, at a reasonably smaller displacement history. In addition, the higher D/t ratio (see Table 5.3) could also contribute to this specific phenomenon. This explains why there was no initiation of fracture rather an evidence of accordion failure mode for specimen 4. In addition, the  $\bar{\epsilon}^p$  values obtained at both SP1 and SP7 of element 3805 were also appreciably small compared to  $\bar{\epsilon}_c^p$ , same as the other three specimens.

#### 5.3.5 Specimen 5 (D20P0A5-5)

Similar to specimen 4, a strip was isolated from compression side at the location of dashed lines BB’ in Figure 5.27, in order to identify the failure mode of specimen 5. Since only a certain percentage of internal pressure rather than full percentage was released in the FE analysis of specimen 5 (as explained in Chapter 4), the general behaviour in terms of deformed configuration as well as the stress-

strain relation was found to be very similar to specimen 4. Same as specimen 4, Elements 3401 and 3501 located at wrinkle fold, and Element 3801 at wrinkle crest were selected for discussion.

#### 5.3.5.1 Strain Reversal Criterion

The true  $\sigma$ - $\varepsilon_{ln}$  plots obtained from SP1 (inner) and SP7 (outer) of elements 3401, 3501, and 3805 are presented in Figure 5.28. According to Figure 5.28, the strain reversal process was observed at both inner and outer surfaces of elements 3401 and 3501 at wrinkle fold, as anticipated. Similar to specimen 4, there was no evidence of strain reversal at both SP1 and SP7 of element 3805 located at wrinkle crest.

#### 5.3.5.2 $\bar{\varepsilon}_c^p$ Criterion

In order to check the 'Criterion-2' for the above mentioned elements, the  $\sigma$ - $\bar{\varepsilon}^p$  plots at inner (SP1) and outer (SP7) surfaces are presented in Figure 5.29. As can be seen, the equivalent plastic strain ( $\bar{\varepsilon}^p$ ) values obtained at both SP1 and SP7 of elements 3401, 3501 and 3801 were markedly lesser than the critical strain limit ( $\bar{\varepsilon}_c^p$ ). The distribution of  $\bar{\varepsilon}^p$  on the outer surface of specimen 5 as shown in Figure 5.30, also provides similar observation. Similar to specimen 4, the growth of  $\bar{\varepsilon}^p$  for these critical elements was found to be very small at the later stage of the analyses. There was also an evidence of the formation of second wrinkle as indicated in Figure 5.30. Although some of the elements met the 'Criterion-1', none of the elements met 'Criterion-1' and 'Criterion-2' concurrently. This explains why there was no fracture observed during the test of specimen 5.

### 5.3.6 Specimen 6 (D20P80A4-6)

Similar to other NPS20 specimens, a strip was isolated from compression side at the location of dashed lines DD' in Figure 5.31, in order to explain the failure mode of specimen 6. In addition to the high D/t ratio (see Table 5.3), the internal

pressure condition for this specimen was significantly higher compared to all other specimens, which, in turn, might dominate the post-wrinkling behaviour of specimen 6. Elements 4801 and 4813 located at wrinkle fold, and Element 4201 at wrinkle crest were anticipated to be critical in this case.

#### 5.3.6.1 Strain Reversal Criterion

The true  $\sigma$ - $\varepsilon_{in}$  plots obtained from SP1 (inner) and SP7 (outer) of elements 4201, 4801, and 4813 are presented in Figure 5.32. According to Figure 5.32, the strain reversal process was observed at both inner and outer surfaces of elements 4801 and 4813 at wrinkle fold, as anticipated. The extent of reversal was found to be higher than the other NPS20 specimens. Similar to all other specimens, there was no evidence of strain reversal at both SP1 and SP7 of element 4201 located at wrinkle crest.

#### 5.3.6.2 $\bar{\varepsilon}_c^p$ Criterion

Since both element 4801 and 4813 did go through a significant strain reversal process meeting ‘Criterion-1’ comprehensively, the  $\sigma$ - $\bar{\varepsilon}^p$  plots at inner (SP1) and outer (SP7) surfaces of those elements were obtained to apply the critical strain ( $\bar{\varepsilon}_c^p$ ) limit criterion (see Figure 5.33). According to Figure 5.21, it is apparent that the equivalent plastic strain ( $\bar{\varepsilon}^p$ ) value at both SP1 and Sp7 of these elements did not even reach close to the critical strain ( $\bar{\varepsilon}_c^p$ ) limit. Similar observation can be made for element 4201 located at wrinkle crest. The contour of  $\bar{\varepsilon}^p$  plotted on the outer surface of specimen 6 as shown in Figure 5.34, also provides similar anticipation. Therefore, it can be said that since none of the elements did meet both ‘Criterion-1’ and ‘Criterion-2’ concurrently, there is a strong possibility of no fracture in the pipe wall of specimen 6. The above anticipation does conform the test observation, where no fracture or crack was observed in the pipe wall of the test specimen.

Although the final deformed shape of specimen 3 (where a significant crack was observed) was essential same as the specimen 6, the magnitude of internal

pressure as well as the end rotations in addition to the higher D/t ratio may attribute to the post-wrinkling behaviour of specimen 6. To put more insight regarding this phenomenon, the von Mises stress distribution at two different increment is presented in Figure 5.35. As can be seen, after reaching certain deformation configuration, the von Mises stress started to progress at different location rather than the wrinkle fold. The progression can be tracked with the arrows included in Figure 5.35. The growth of  $\bar{\epsilon}^P$  for the critical elements was also monitored and found to be extremely small at the later stage of the displacement history. Therefore, an accordion failure mode rather than tearing at the telescoping wrinkle was observed for specimen 6.

#### 5.4 Discussion and Postulation

The double failure criteria— 'Strain Reversal Criterion' and 'Critical Plastic Strain ( $\bar{\epsilon}_c^P$ ) Limit'— have been applied to all six test specimens obtained from two different test programs. As mention before, if both of these criteria are met in any location of the pipe wall, the tearing fracture will occur at that location of the pipe wall.

Based on the results of the FE analyses demonstrated in section 5.3, it can be said that some of the critical elements located in the wrinkle fold of all the specimens had gone through the strain reversal process meeting 'Criterion-1' due to the reversed bending mechanism attributed form the loading condition. However, in only two cases, to be specific, for specimen 1 and specimen3, the equivalent plastic strain did exceed the critical strain limit ( $\bar{\epsilon}_c^P$ ), thus meeting both 'Criterion-1' and 'Criterion-2'. In those two instances, partial and/or through-thickness crack or fracture was observed at the wrinkle fold of the test specimens, thus signifying the acceptance of these 'Double Failure Criteria'. In addition to the development and application of these failure criteria, plastic strain growth along the displacement history of all the specimens was tracked for all the specimens. A comparison of these strain-displacement responses is drawn to provide better

understanding of the post-wrinkling behaviour of these specimens, emphasizing existence of different failure modes including 'tearing' and 'accordion' modes.

#### ***5.4.1 Effect of Loading Condition***

First, the strain growth of specimen 1 and specimen 3 is compared and presented in Figure 5.36, in order to identify the effect of different loading condition. The presence of shear load in case of specimen 1 (as discussed in Chapter 3) can incorporate the effect of moment gradient, whereas the end rotations applied in specimen 3 can provide more uniform distribution. Although the D/t ratio and the internal pressure condition were different for these two specimens, the effect of moment gradient is distinct as indicated in Figure 5.36. As can be seen, one of the elements of specimen 1 located at the outer surface of the wrinkle fold reached the critical strain limit ( $\bar{\epsilon}_c^p$  - X52) at a much smaller displacement (almost half) compared to that of specimen 3. It is also important to add that the end rotation for specimen 1 was much smaller than that of specimen 3 (see Table 5.3). In addition, the lower D/t ratio of specimen 1 (i.e. more stocky section) might expedite this failure mechanism. Nevertheless, the effect of moment gradient (i.e. presence of shear load) can be an important variable for this unique failure mode.

#### ***5.4.2 Effect of End Rotation***

The strain growth of specimen 2 and specimen 3 presented in Figure 5.22 can be used to analyze the effect of end rotation or curvature. As can be seen, the larger end rotations along with the presence of internal pressure for specimen 3 have increased the possibility of tearing fracture in the pipe wall.

#### ***5.4.3 Effect of D/t Ratio***

The strain growth of specimen 3 and specimen 4 is presented in Figure 5.37 to relate the influence of pipe geometry in terms of D/t ratio on the tearing behaviour

of wrinkled pipe. As can be seen from Figure 5.37, the smaller D/t ratio with larger end rotations under essentially same internal pressure condition can increase the possibility of tearing fracture initiation in the pipe wall. Similar observation can also be made by assessing Figure 5.36, where the D/t ratio was found smaller in both cases of specimen 1 and specimen 3. Therefore, the D/t ratio should be considered as an important variable for this tearing behaviour

#### ***5.4.4 Effect of Operational Condition***

A comparison of the strain growth- displacement response of specimen 4 and specimen 6 is drawn in Figure 5.38 in order to analyze the effect of operational condition in terms internal pressure to this failure mode. As discussed before and also can be seen from Figure 5.38, the presence of higher internal pressure (in case of specimen 6) may delay the strain growth along its displacement history, thus reducing the possibility of tearing fracture. However, the absence of internal pressure in the line pipe may also reduce the possibility of tearing fracture under certain loading condition, as can be seen from Figure 5.22 (in case of specimen 2). Hence, the operational condition can be a significant variable to influence this unique failure mechanism.

### **5.5 Summary**

In this chapter, a comprehensive analytical investigation was carried out to develop the failure criteria to predict the tearing fracture in the wrinkled pipe under monotonically increasing axial deformation with constant curvature. Based on the load-displacement histories obtained from these investigations, monotonic non-axisymmetric loading along with shear and/or bending deformation arising from soil displacements could generate large wrinkles in the buried energy line pipes. Eventually, fracture can trigger on sharp wrinkle folds located at the compression side of the deformed pipe under continued deformation.

The stress-strain relations obtained from all the numerical analyses performed in this research program have indicated that even under monotonic loading, significant strain reversals can occur at the sharp fold of the wrinkle. These strain reversals were identified as one of the criteria (i.e. ‘Criterion-1’) to predict the presence of this unique failure mechanism. The numerical results have also indicated that the critical equivalent plastic strain ( $\bar{\epsilon}_c^p$ ) limit, set as ‘Criterion-2’, can predict the onset of fracture in the pipe wall with reasonable accuracy. Finally, a prediction-based approach, which consists of checking of both ‘Criterion-1’ and ‘Criterion-2’ at any location of the wrinkled pipe, was successfully applied to all available the test results, demonstrating the acceptability of these criteria for predicting this unique failure mechanism. In addition, the effect of different loading and operational conditions to generate and/or expedite this unique failure mechanism is also revealed with some postulation and facts.

Table 5.1 Material Properties of Test Specimens from Coupon Tests

<b>Measured properties</b>	<b>X-52</b>	<b>X-60</b>	<b>X-65</b>
Young Modulus, E (GPa)	201.53	201	208
Poisson's Ratio, $\nu$	0.3	0.3	0.3
Static Yield Stress, $\sigma_y$ (MPa)	357	488	495
Static Ultimate Stress, $\sigma_u$ (MPa)	452	543	557
$\sigma_u/\sigma_y$	1.266	1.114	1.125
Elongation (%) (Gage Length= 200 mm)	33.8	33.4	26

Table 5.2 Cross-sectional Dimensions of Test Specimens from Coupon Tests

Test Specimen	Initial			After Fracture			$A_0/A_{fmid}$	$\epsilon_c^P$	
	$w_0$ (mm)	$t_0$ (mm)	$A_0$ (mm <sup>2</sup> )	$w_{mid}$ (mm)	$t_{mid}$ (mm)	$A_{fmid}$ (mm <sup>2</sup> )			
<b>X-65</b>	Coupon-1	39.98	8.35	333.83	32.55	3.68	119.78	1.025	<b>1.01</b>
	Coupon-2	40.00	8.36	334.40	32.53	3.94	128.17	0.959	
	Coupon-3	39.90	8.38	334.36	32.36	3.62	117.14	1.049	
<b>X-60</b>	Coupon-1	38.03	12.66	481.46	30.20	5.10	154.02	1.140	<b>1.22</b>
	Coupon-2	37.99	12.70	482.47	29.80	4.50	134.10	1.280	
	Coupon-3	37.99	12.62	479.43	29.80	4.60	137.08	1.252	
<b>X-52</b>		38.00	6.85	260.30	30.80	3.10	95.48	1.003	<b>1.00</b>

Table 5.3 Full-scale Test Parameters used in FE Simulations

Specimen Designation	Steel grade [SMYS (MPa)]	$D/t$	$L/D$	Locking Rotation, $\theta_{avg}$ (Degrees)	Internal Pressure (% of <sup>a</sup> $p_y$ )
D12P0A3.4-1	X52 [357]	48	2.3	3.4	0 <sup>b</sup>
D16P0A5-2	X60 [414]	34	3.8	5.0	0
D16P40A7-3				7.0	40
D20P40A3.5-4				3.5	40
D20P0A5-5	X65 [448]	79	3.5	5	0
D20P804-6				4	80

<sup>a</sup>Indicates that  $p_y$  = the internal pressure (in MPa) applied to the pipe such that the hoop stress reached to SMYS or  $\sigma_{ys}$ .

<sup>b</sup>For specimen 1, there was no internal pressure throughout the test. For all other specimens, an initial internal pressure (40% of  $p_y$ ) was applied.

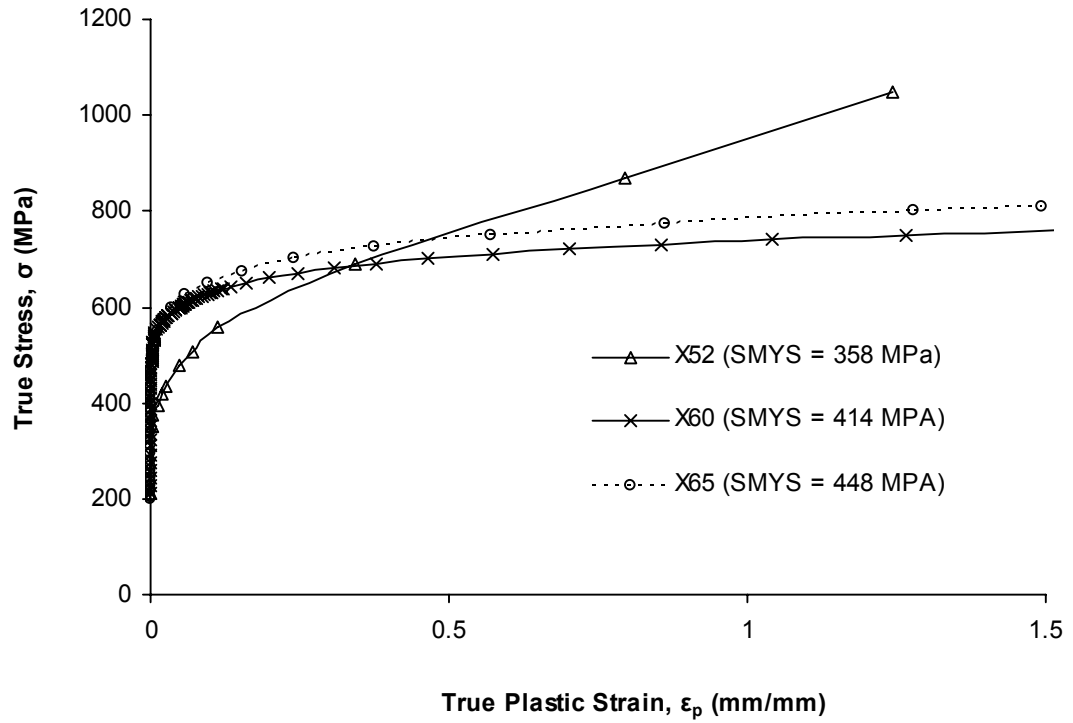


Figure 5.1 True stress-true plastic strain relationship (up to failure) all the pipe materials used in this research program

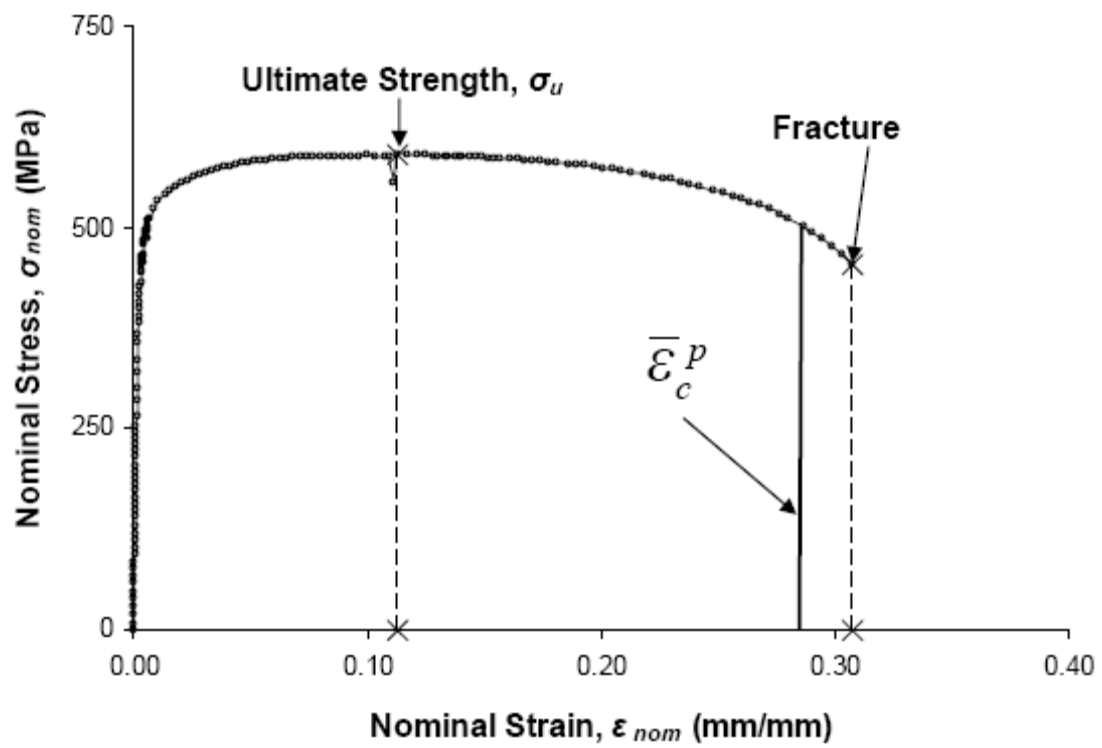


Figure 5.2 Typical engineering (nominal) stress-strain plot obtained from tension coupon test showing a schematic location of critical strain ( $\bar{\epsilon}_c^p$ )

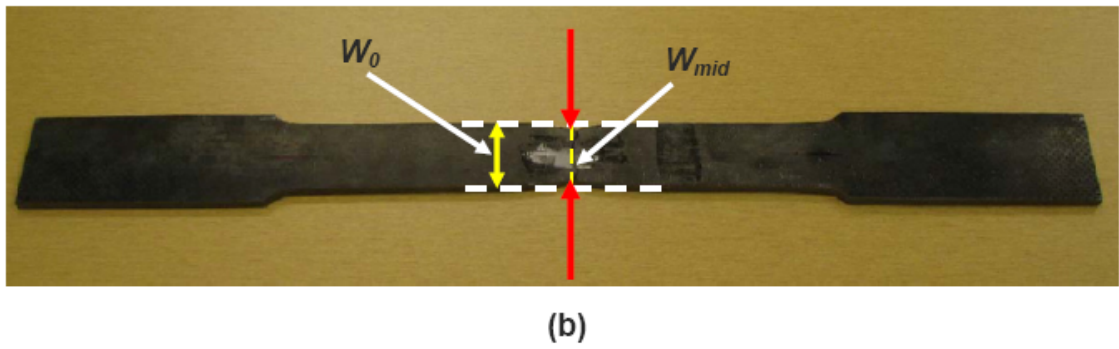
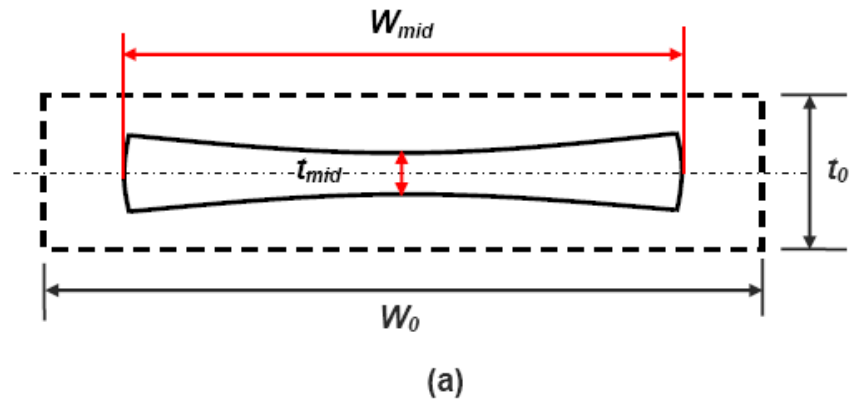


Figure 5.3 Tension coupon specimen with cross-sectional (schematic) comparison before and after test

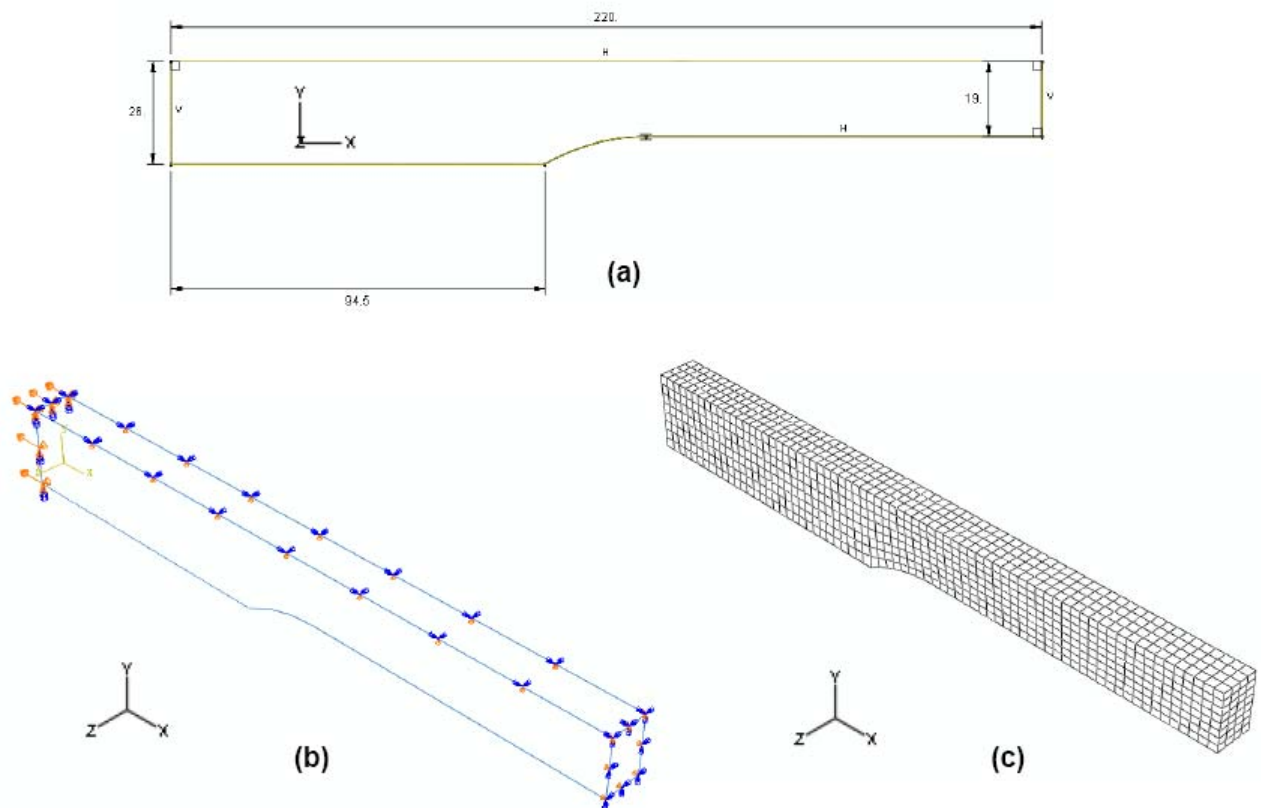


Figure 5.4 FE model of the steel tension bar: (a) a plane view with dimensions in mm; (b) loading and boundary conditions on a  $\frac{1}{4}$  FE model; (c) the FE mesh

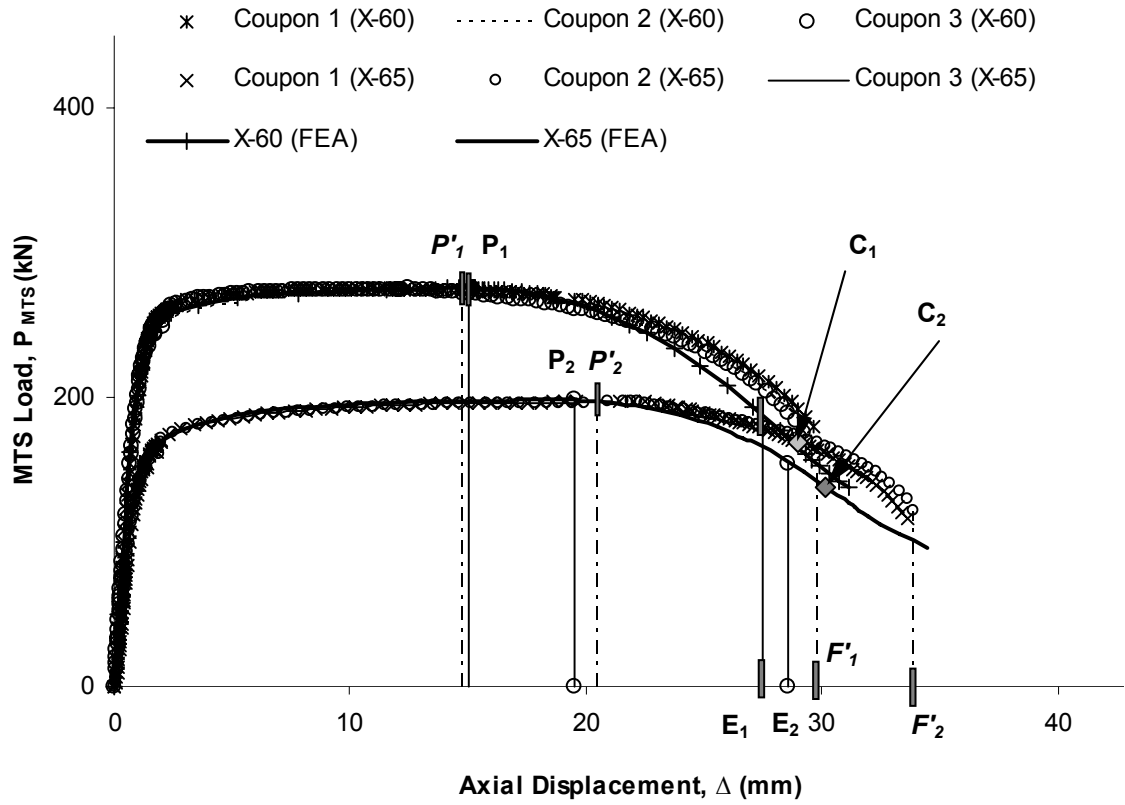


Figure 5.5 Experimentally measured and numerically computed load-displacement ( $P$ - $\Delta$ ) responses of X60 and X65 grade steel coupons

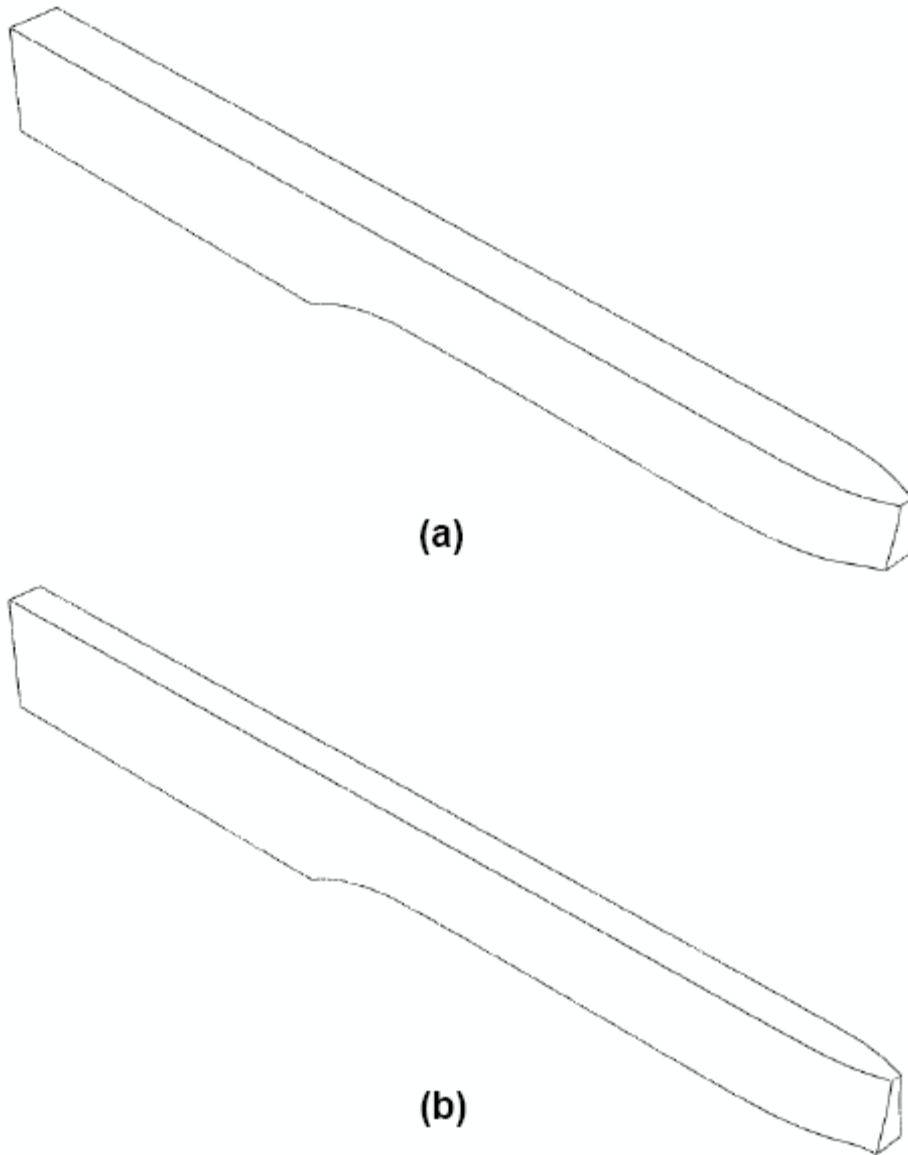
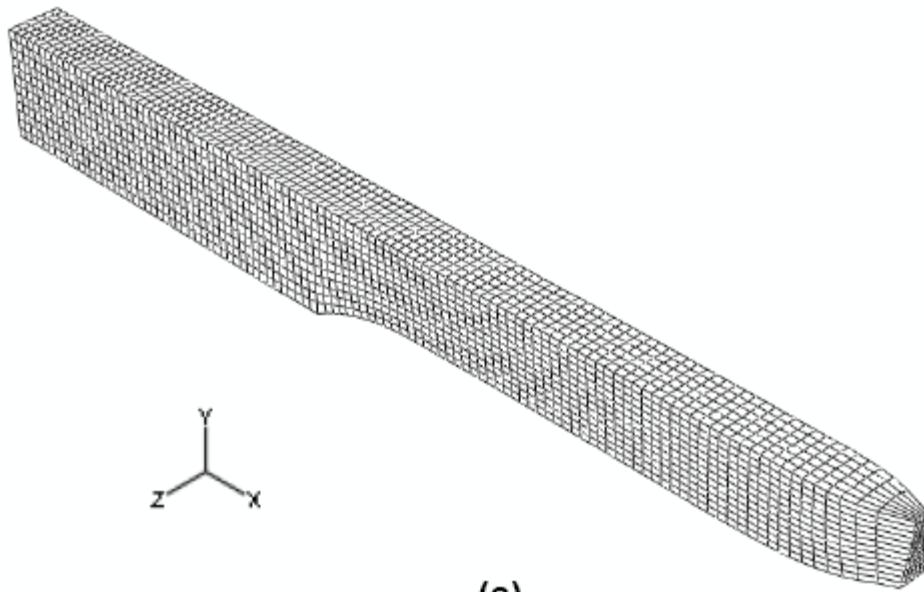
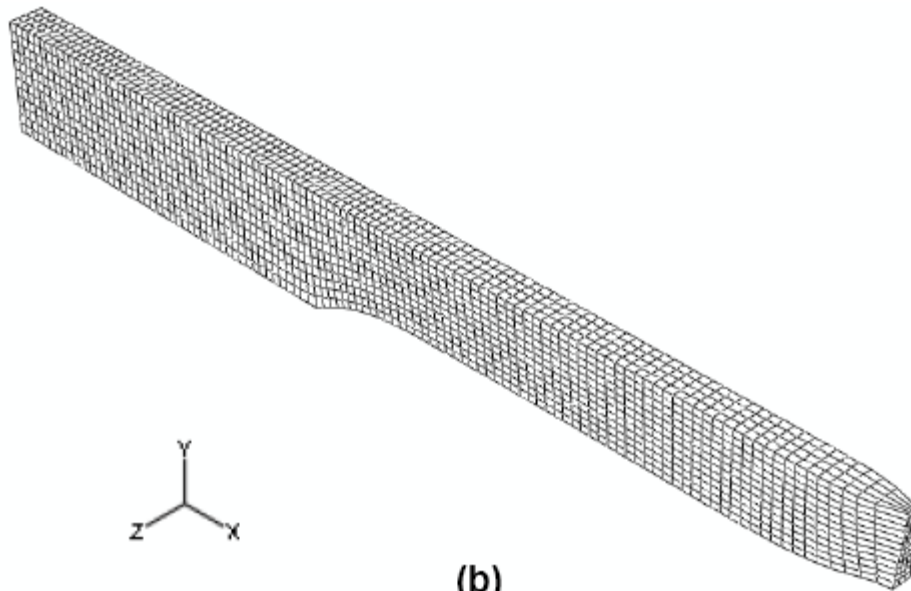


Figure 5.6 The deformed shapes of 3D FE coupons for X60 grade, and (b) X65 grade without the mesh



(a)



(b)

Figure 5.7 The deformed shapes of 3D FE coupons: (a) X60 grade, and (b) X65 grade; obtained at point  $E_1$  and  $E_2$  on P- $\Delta$  plots

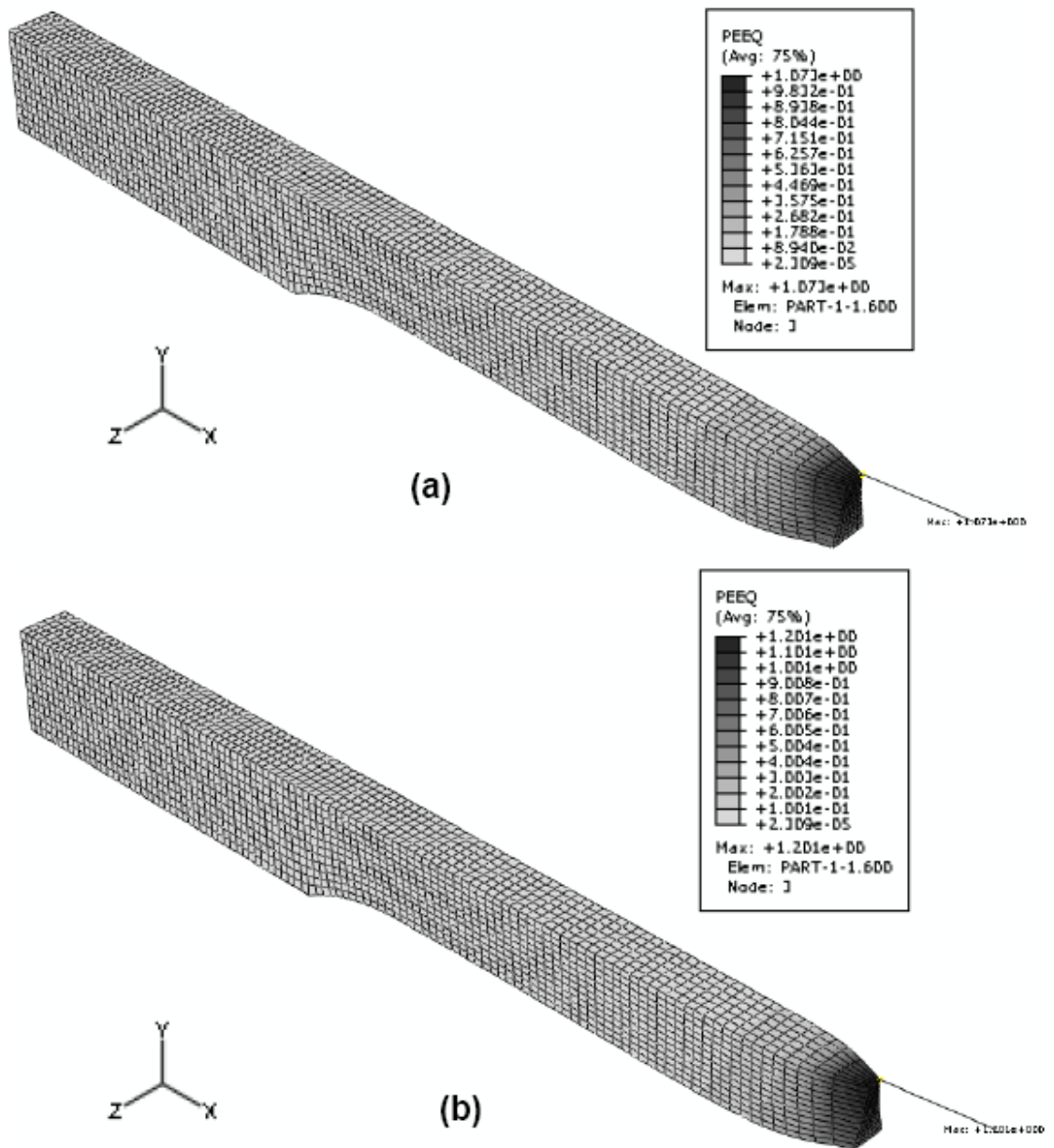


Figure 5.8 The distribution of the equivalent plastic strain (PEEQ or  $\epsilon^p$ ) at (a) point E<sub>1</sub>; and (b) point C<sub>1</sub> on P- $\Delta$  response of X60 coupon

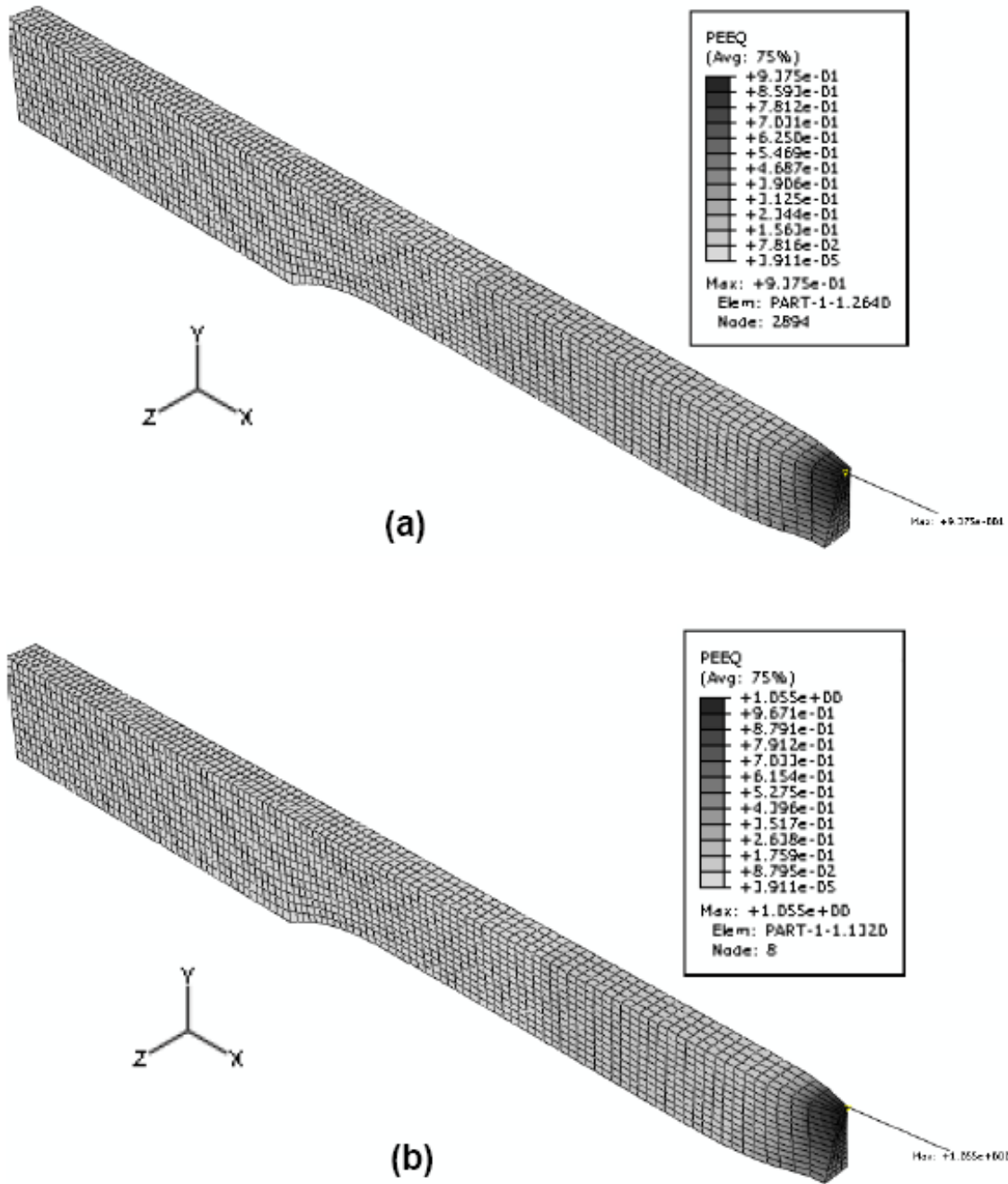


Figure 5.9 The distribution of the equivalent plastic strain (PEEQ or  $\epsilon^p$ ) at (a) point E<sub>2</sub>; and (b) point C<sub>2</sub> on P- $\Delta$  response of X65 coupon

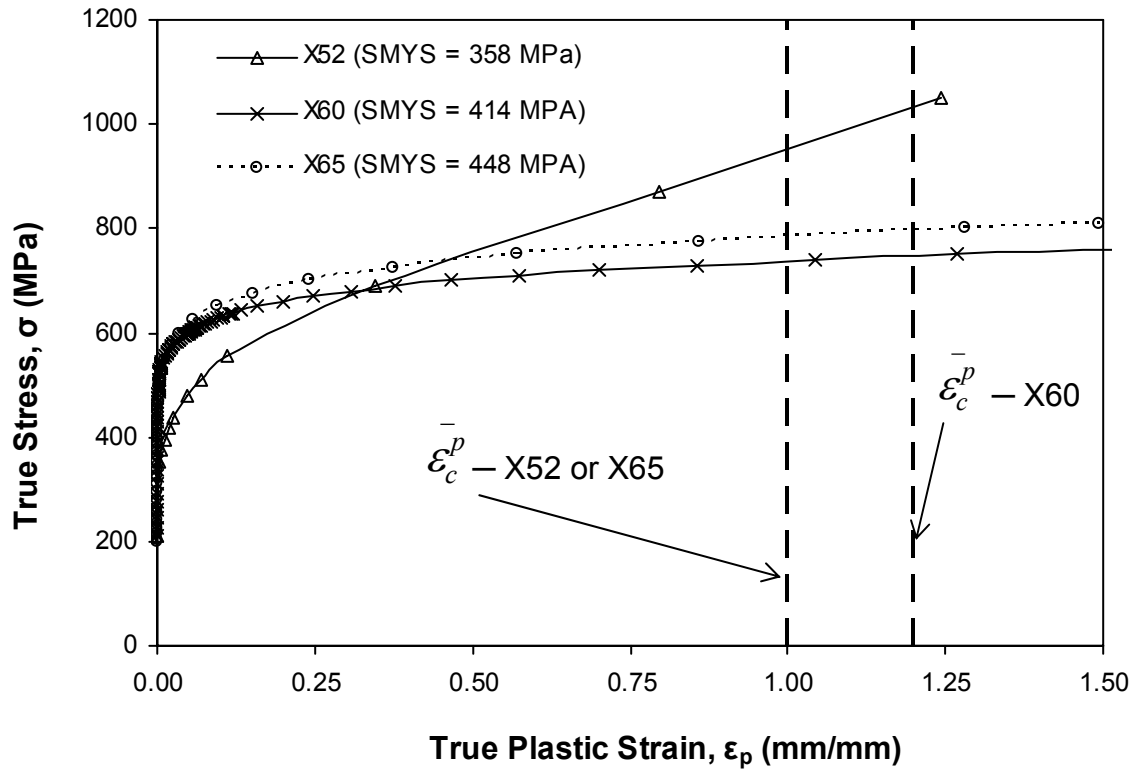


Figure 5.10 True stress-true plastic strain relationship of all the pipe materials indicating the location of the critical strain ( $\bar{\epsilon}_c^p$ ) values

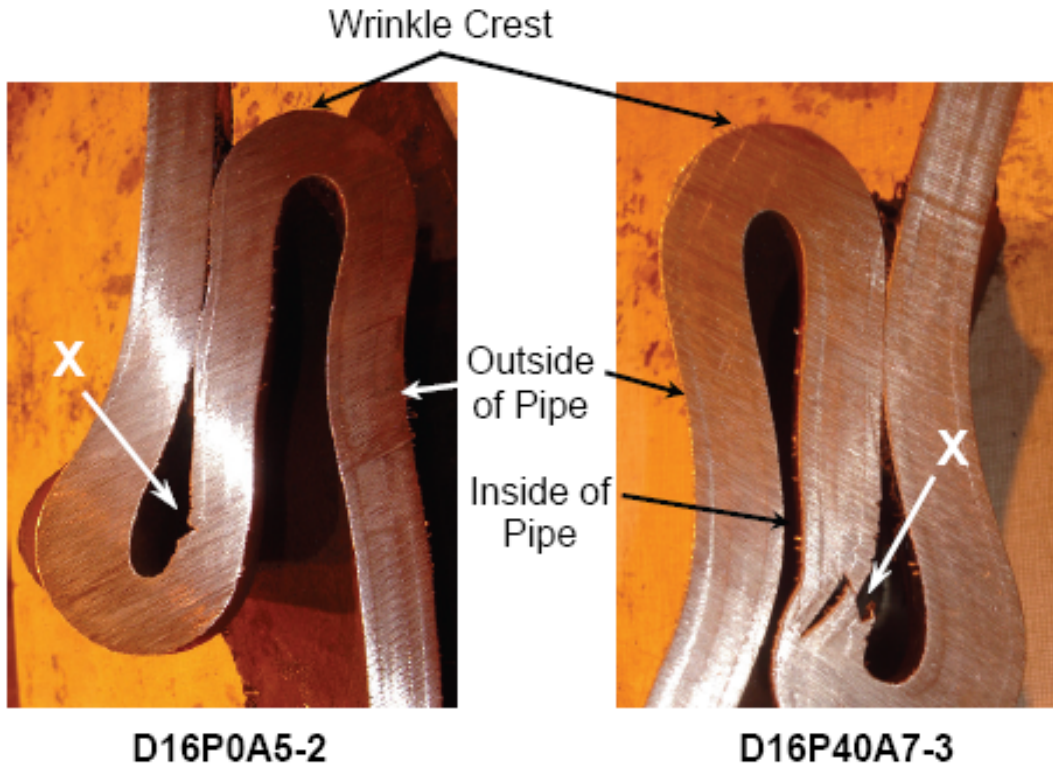


Figure 5.11 Close-up view of the cut segments from the compression side of specimen 2 (D16P0A5-2) and specimen 3 (D16P40A7-3)

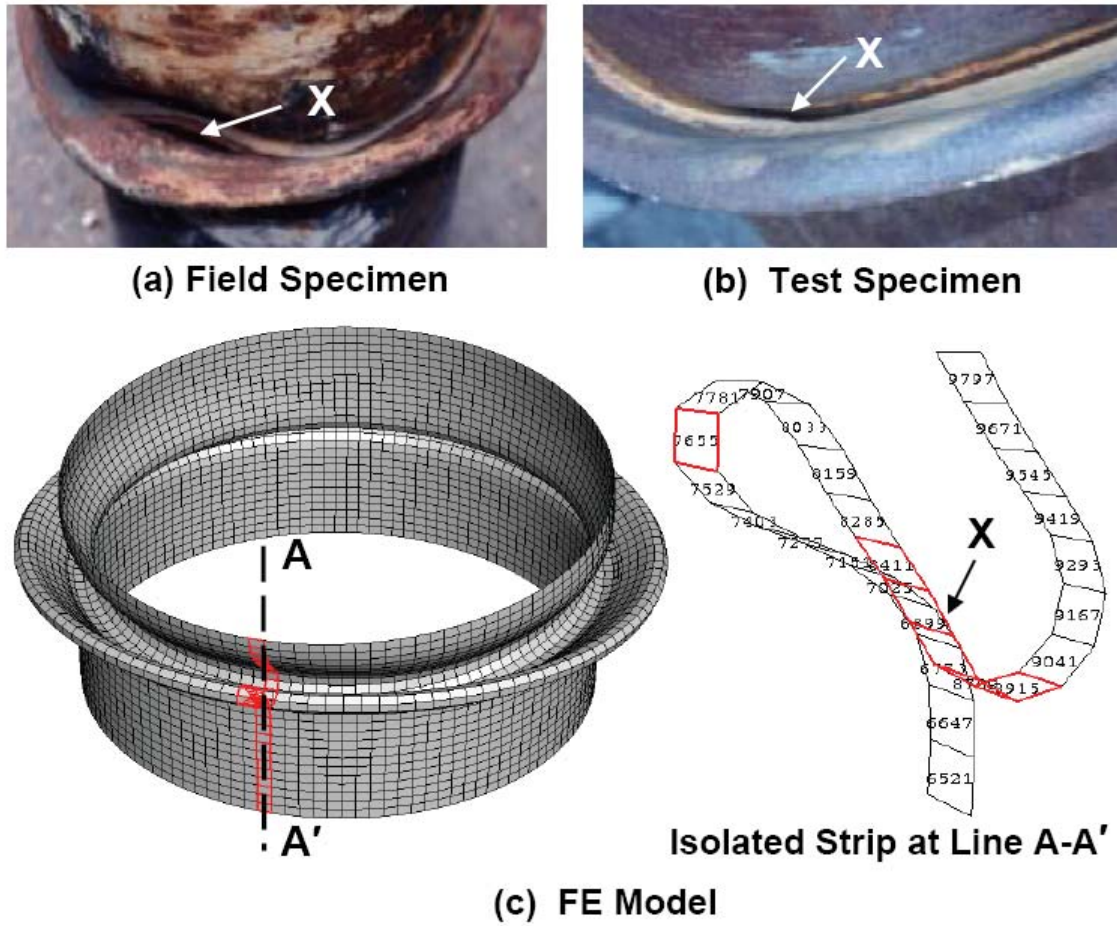
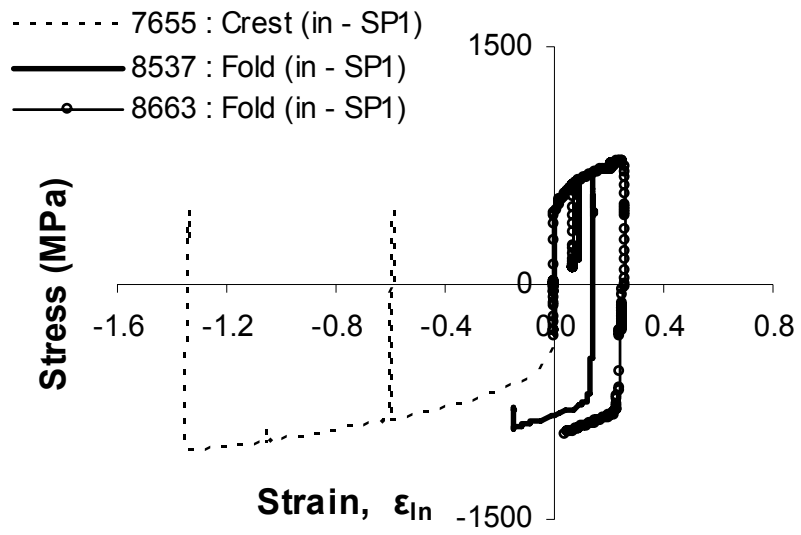
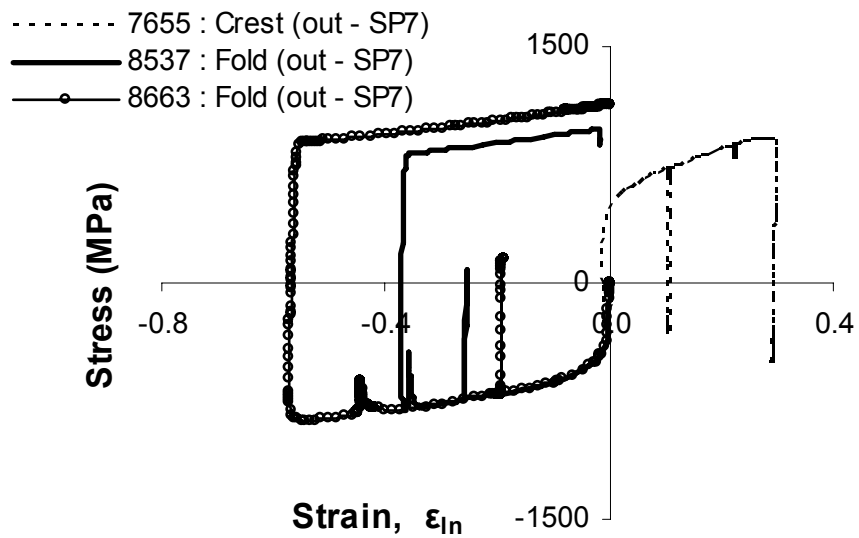


Figure 5.12 Fracture in the wrinkle fold of (a) the field (Das et al. 2002), and (b) the test specimen D12P0A3.4-1 (Das et al. 2002); and location of strain reversal in the FE (full-pipe) model (Ahmed et al. 2010)

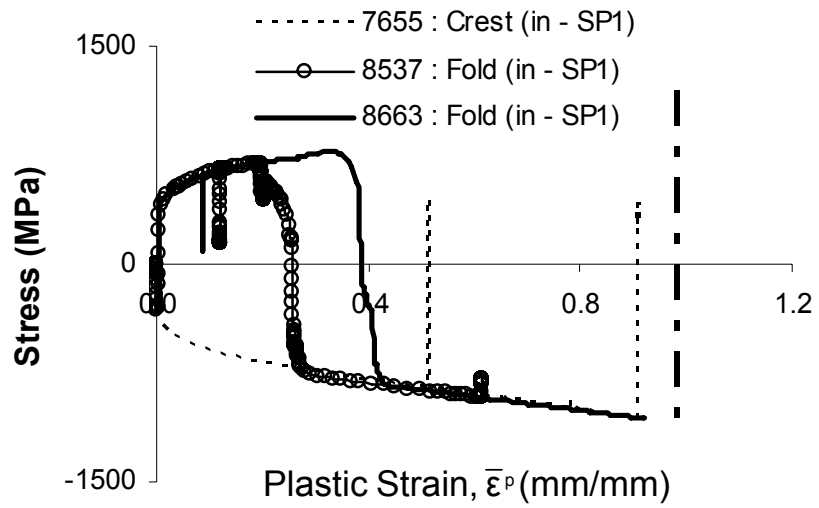


(a)

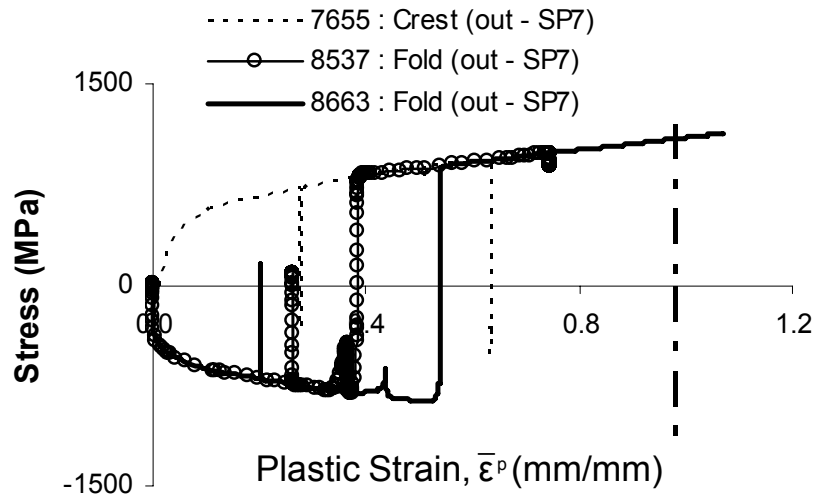


(b)

Figure 5.13 Longitudinal stress-strain relationship at some selected elements of specimen 1 (D12P0A3.4-1)



(a)



(b)

Figure 5.14 True longitudinal stress-equivalent plastic strain plots of some selected elements for specimen 1

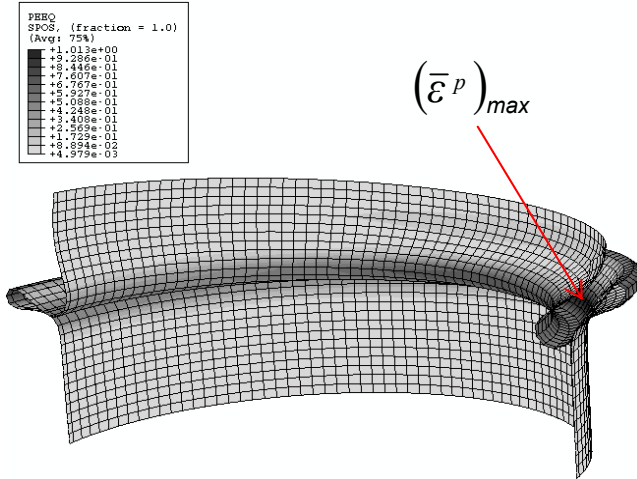
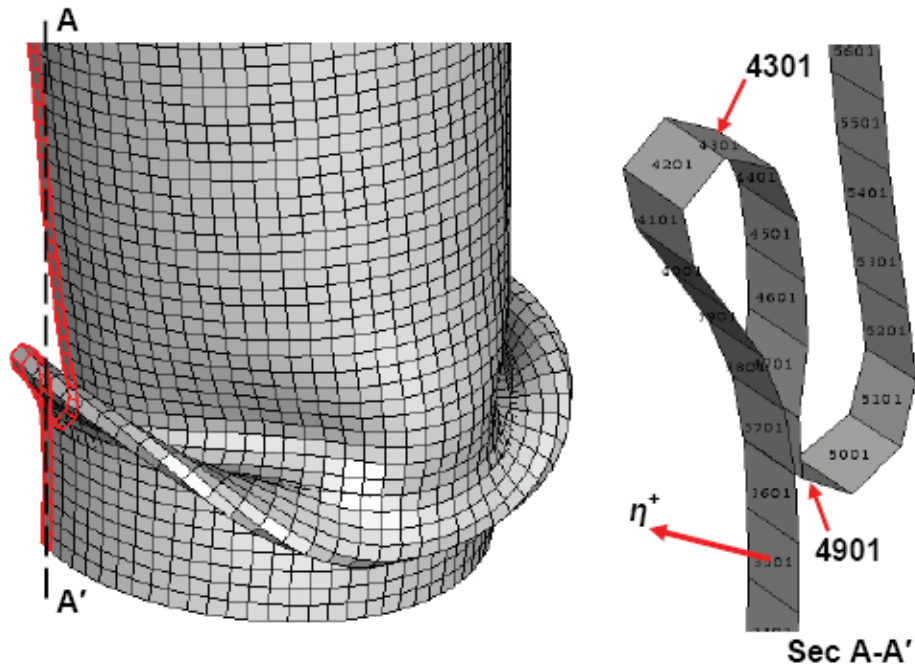
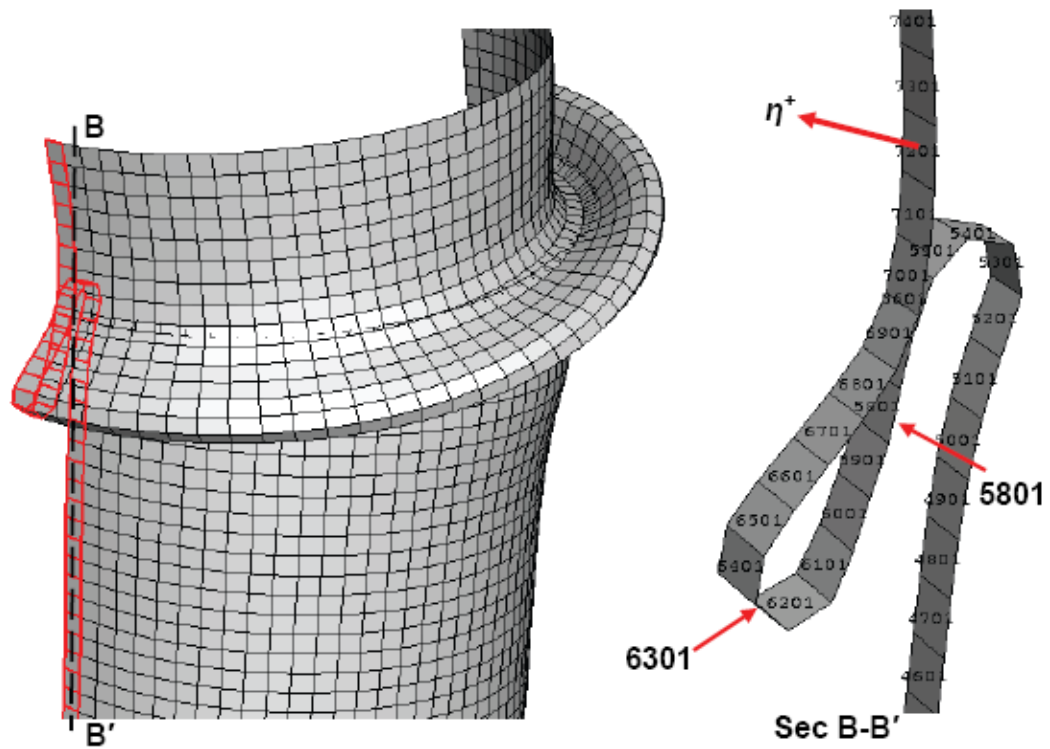


Figure 5.15 Contour plots of the equivalent plastic strain (PEEQ or  $\epsilon^p$ ) obtained from outer surface of specimen 1

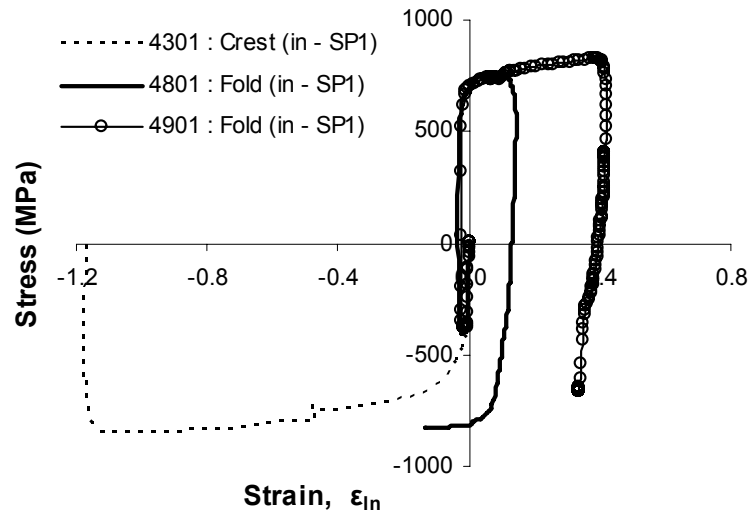


(a) Specimen 2

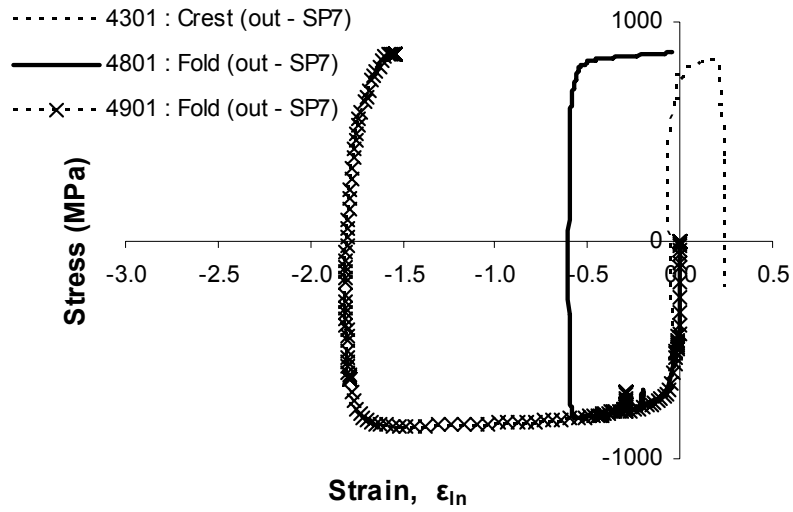


(b) Specimen 3

Figure 5.16 Close-up view of wrinkled pipe for specimen 2 and 3

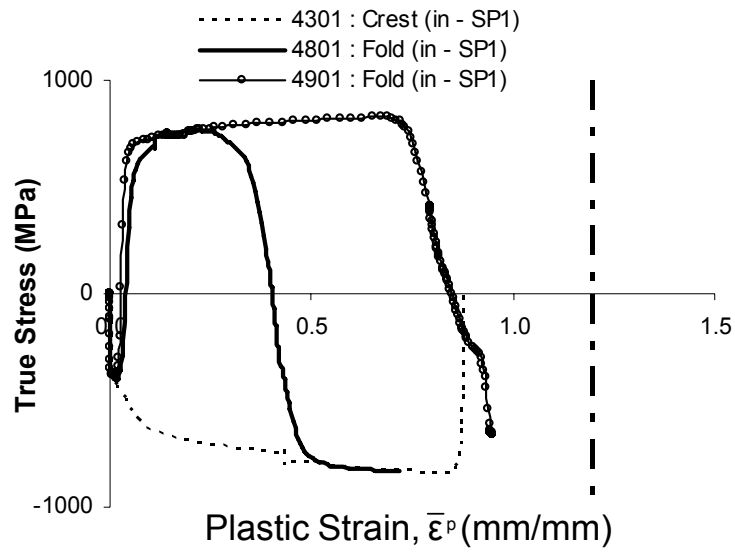


(a)

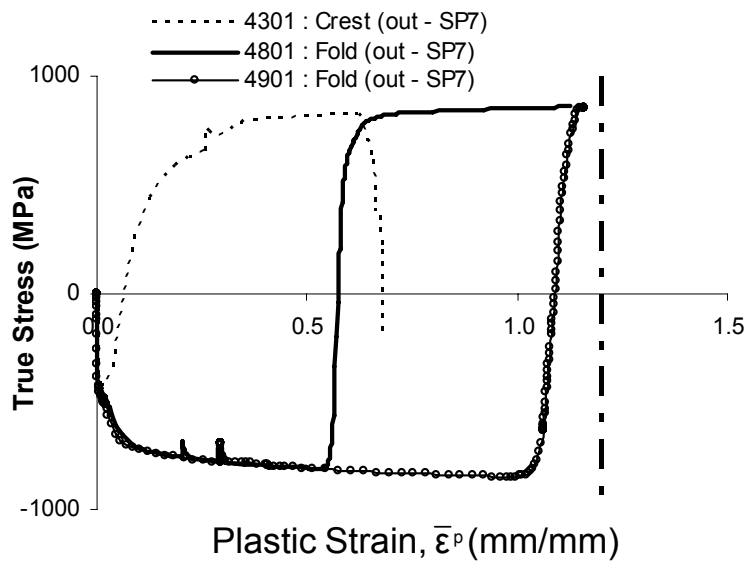


(b)

Figure 5.17 Longitudinal stress-strain relationship at some selected elements of specimen 2 (D16P0A5-2)

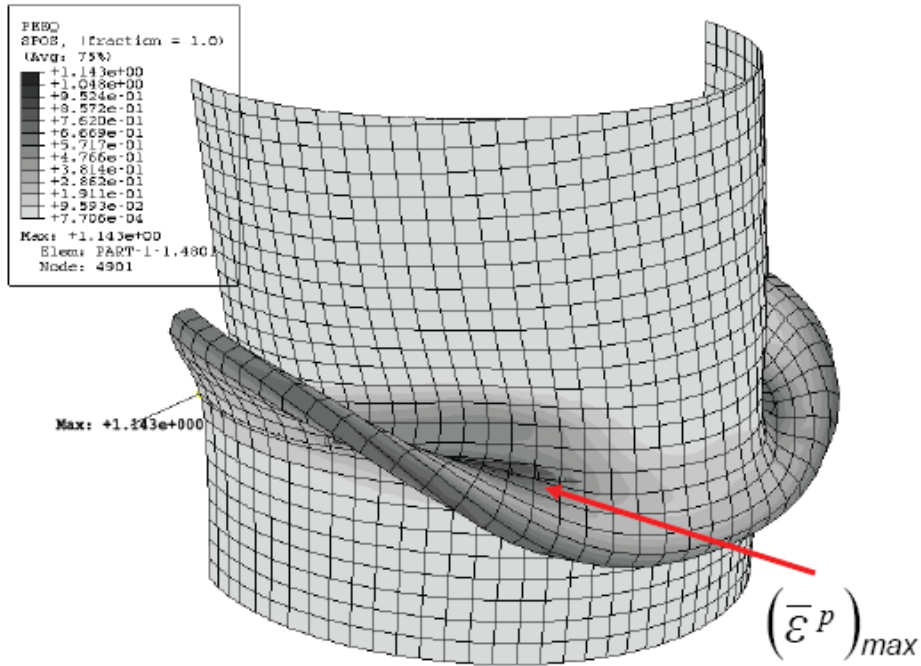


(a)

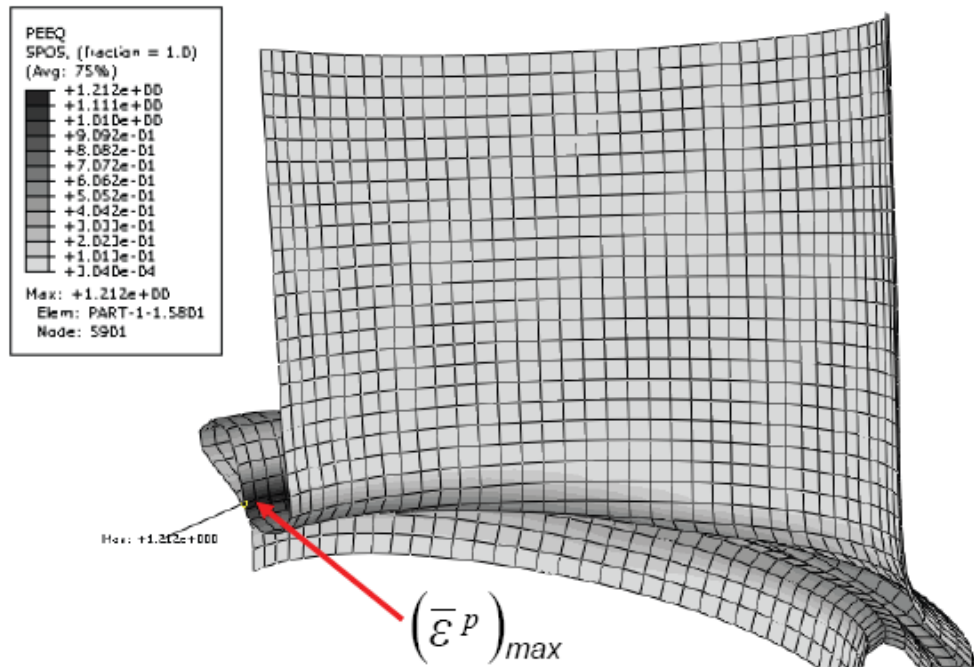


(b)

Figure 5.18 True longitudinal stress-equivalent plastic strain plots at some selected elements of specimen 2

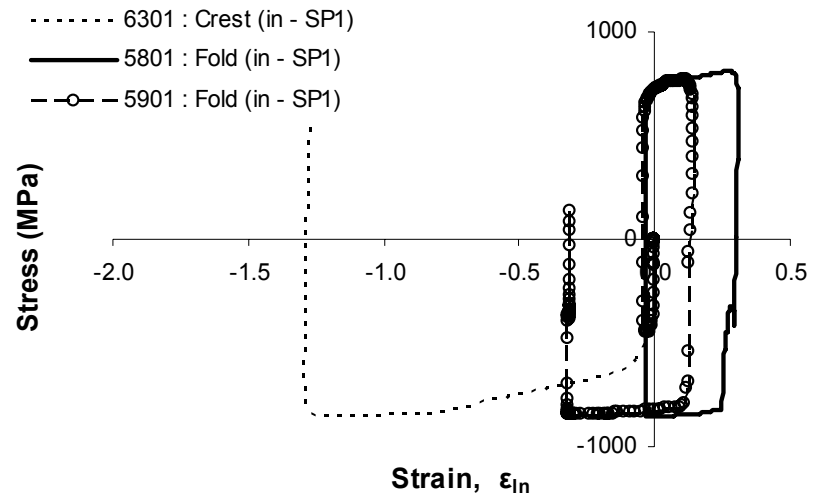


(a) D16P0A5-2

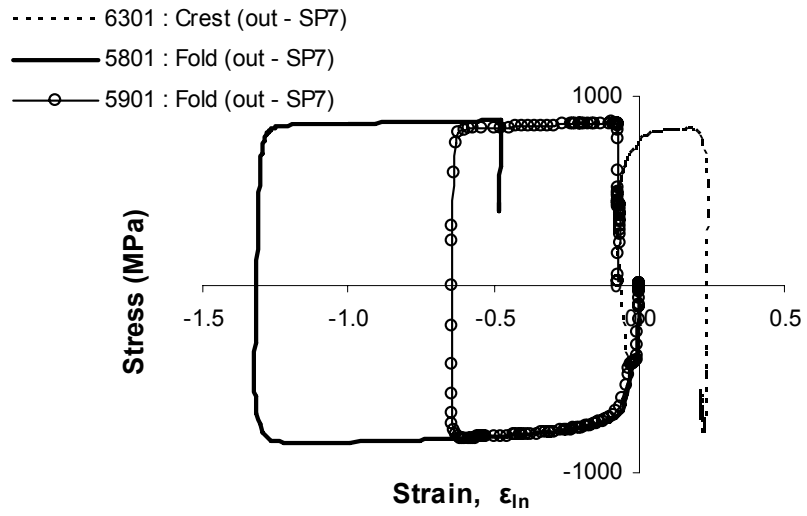


(b) D16P40A7-3

Figure 5.19 Contour plots of equivalent plastic strain (PEEQ) obtained from outer surface of specimen 2 and 3

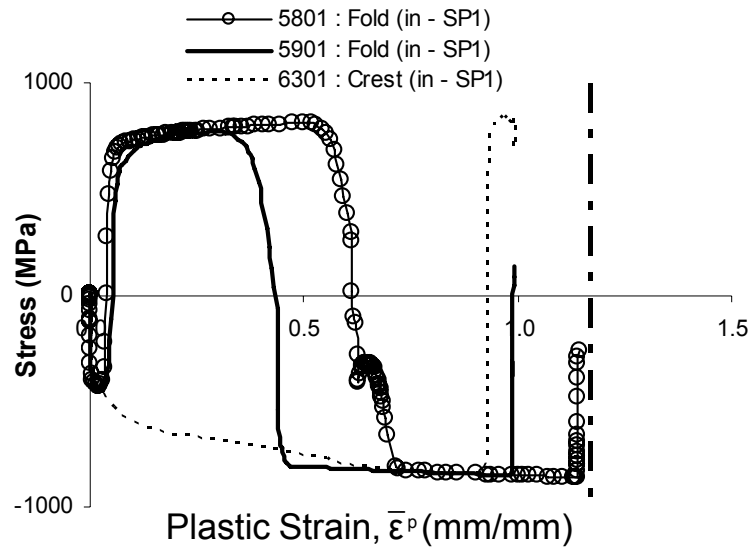


(a)

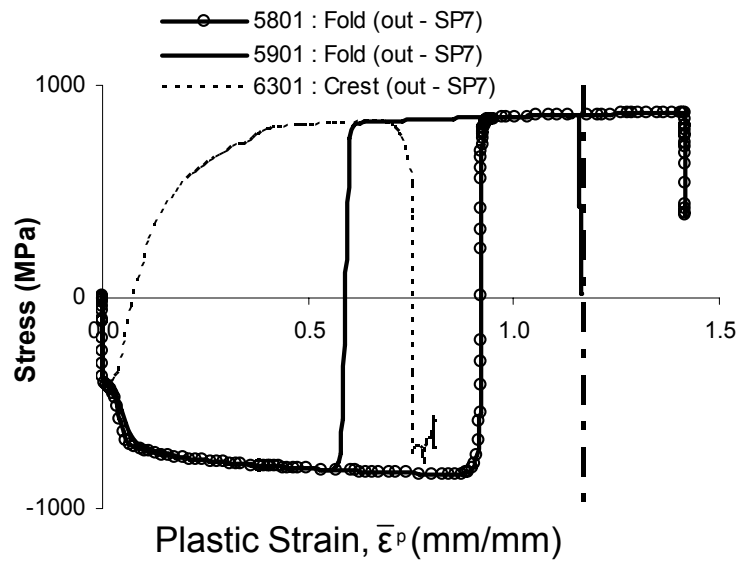


(b)

Figure 5.20 Longitudinal stress-strain relationship at some selected elements of specimen 3 (D16P40A7-3)



(a)



(b)

Figure 5.21 True longitudinal stress-equivalent plastic strain plots at some selected elements of specimen 3

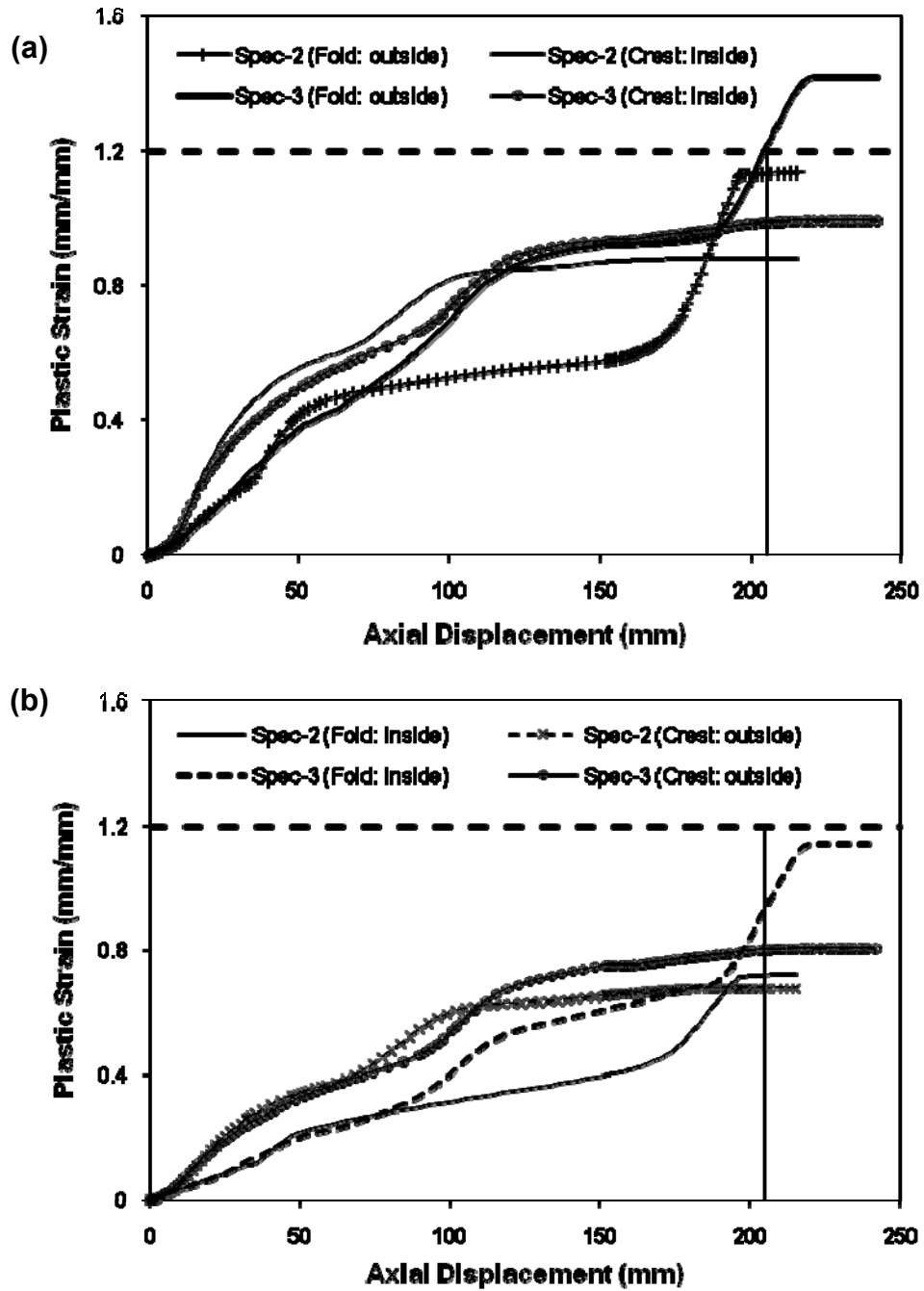


Figure 5.22 Plastic strain growth with displacement history for specimen 2 and 3

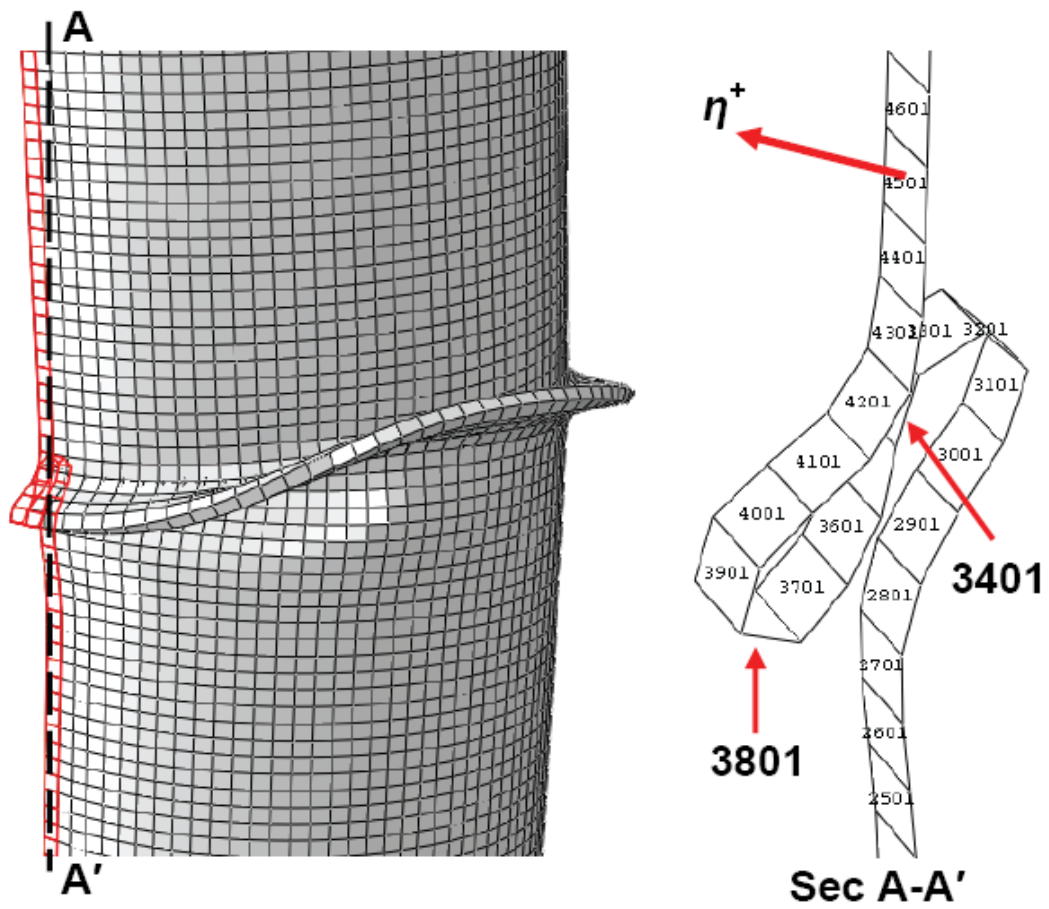
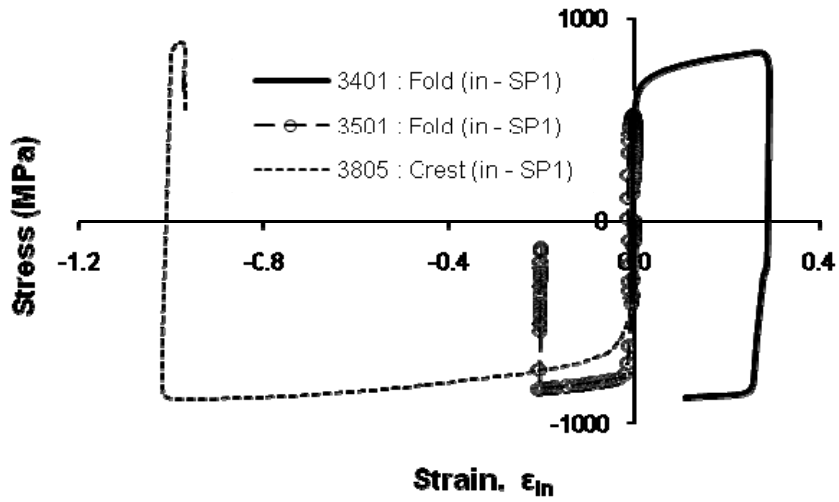
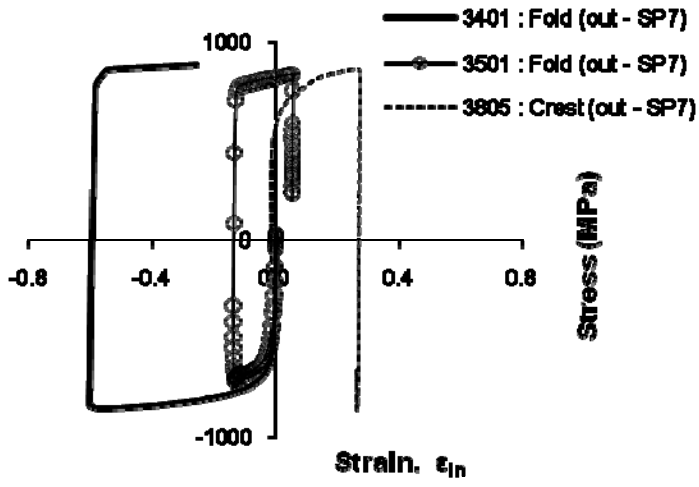


Figure 5.23 Close-up view of wrinkled pipe along with a wrinkle-strip for specimen 4

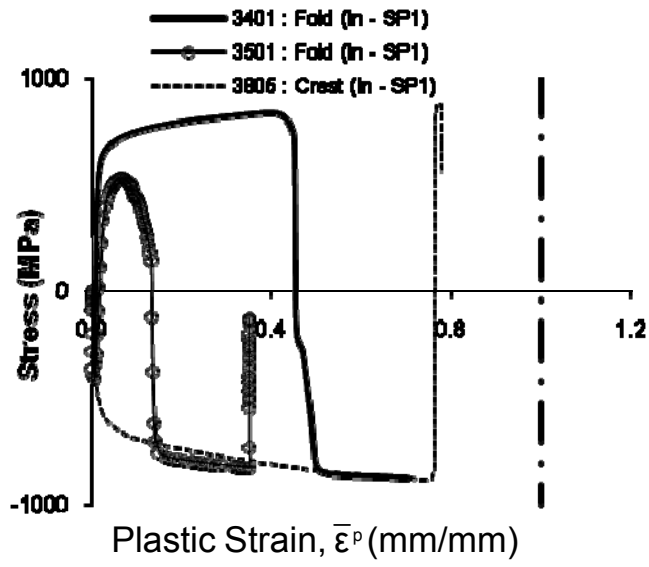


(a)

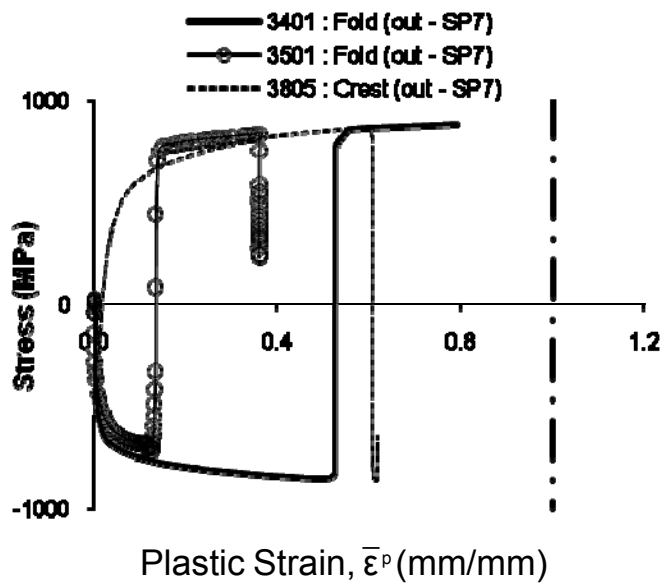


(b)

Figure 5.24 Longitudinal stress-strain relationship at some selected elements of specimen 4 (D20P40A3.5-4)



(a)



(b)

Figure 5.25 True longitudinal stress-equivalent plastic strain plots at some selected elements of specimen 4

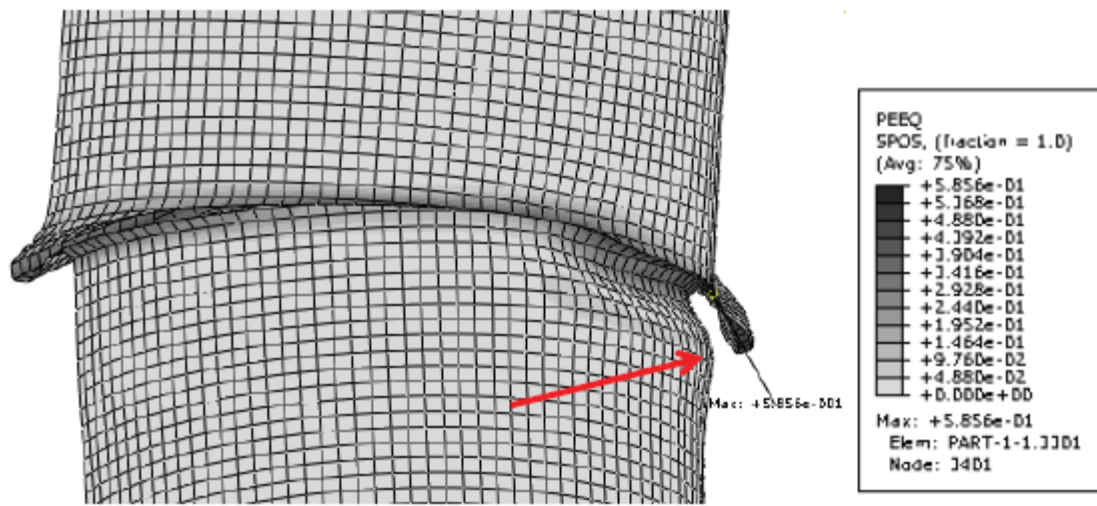


Figure 5.26 Contour plots of equivalent plastic strain (PEEQ) obtained from outer surface of specimen 4

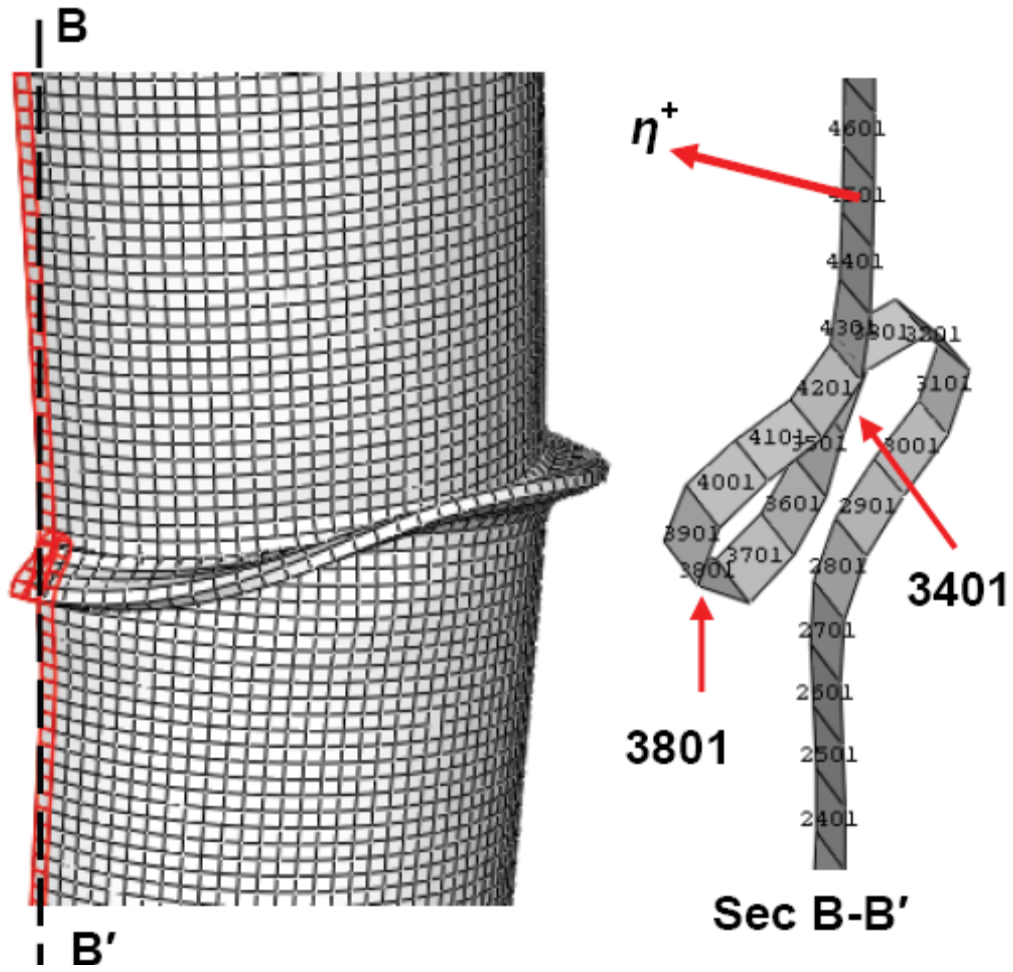


Figure 5.27 Close-up view of wrinkled pipe along with a wrinkle-strip for specimen 5

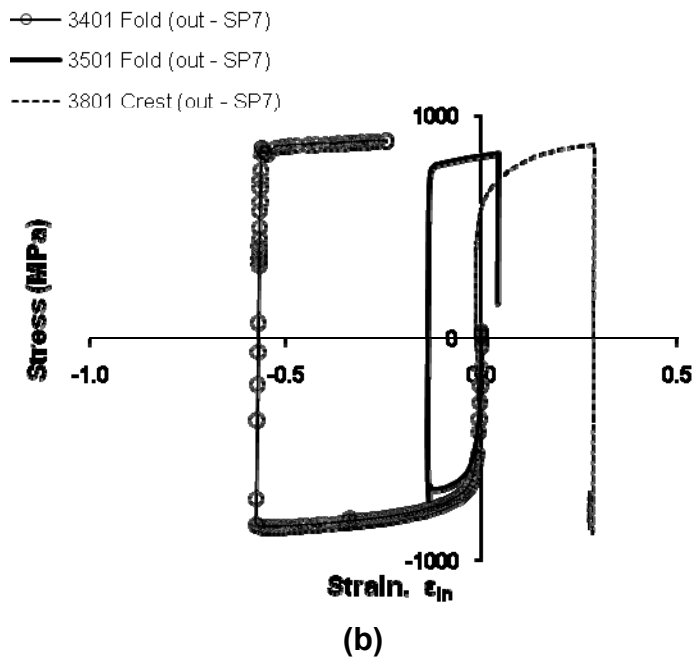
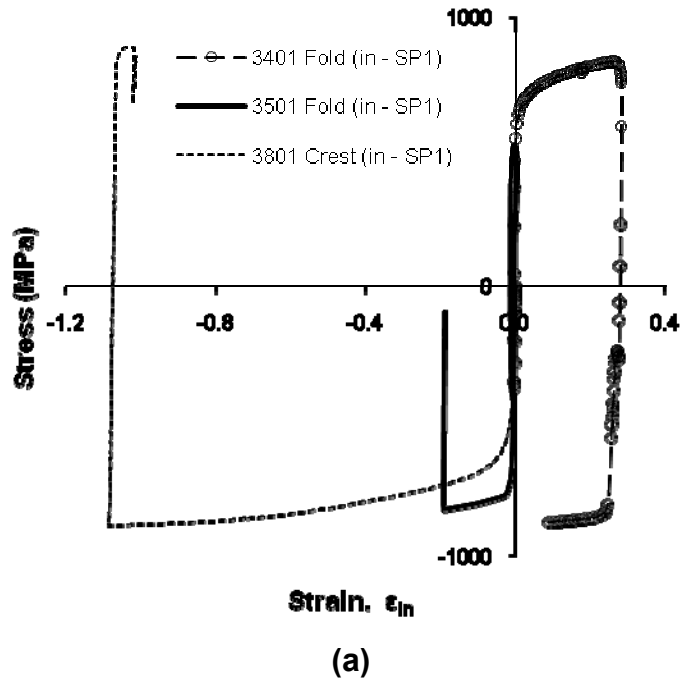
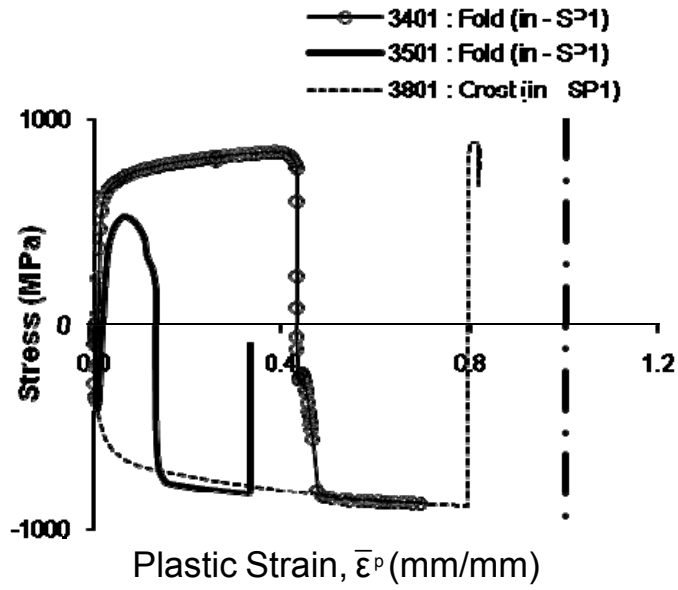
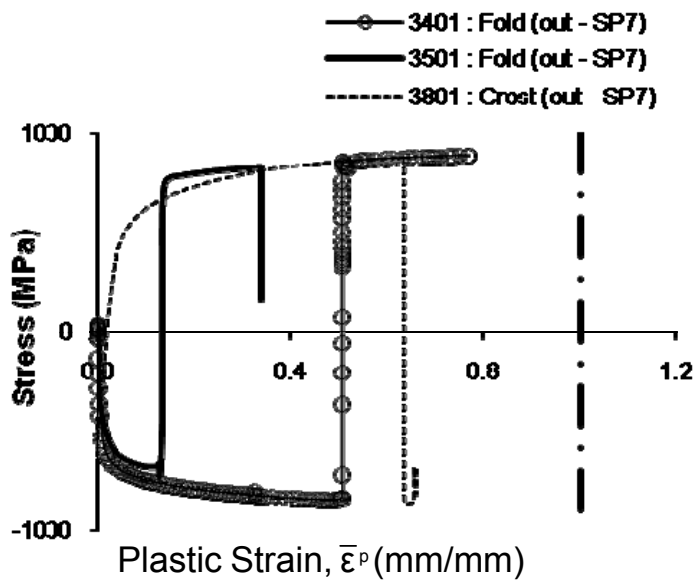


Figure 5.28 Longitudinal stress-strain relationship at some selected elements of specimen5 (D20P0A5-5)



(a)



(b)

Figure 5.29 True longitudinal stress-equivalent plastic strain plots at some selected elements of specimen 5

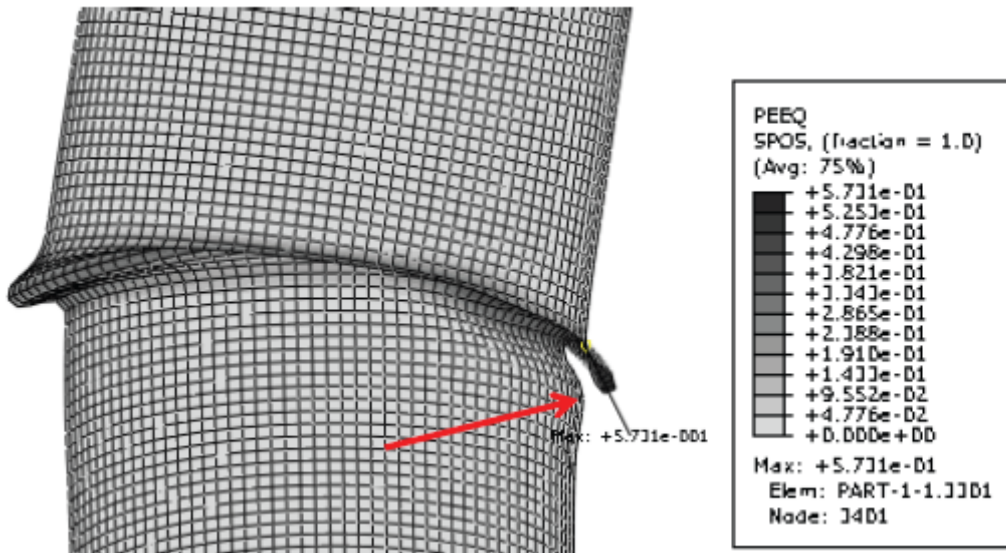


Figure 5.30 Contour plots of equivalent plastic strain (PEEQ) obtained from outer surface of specimen 5

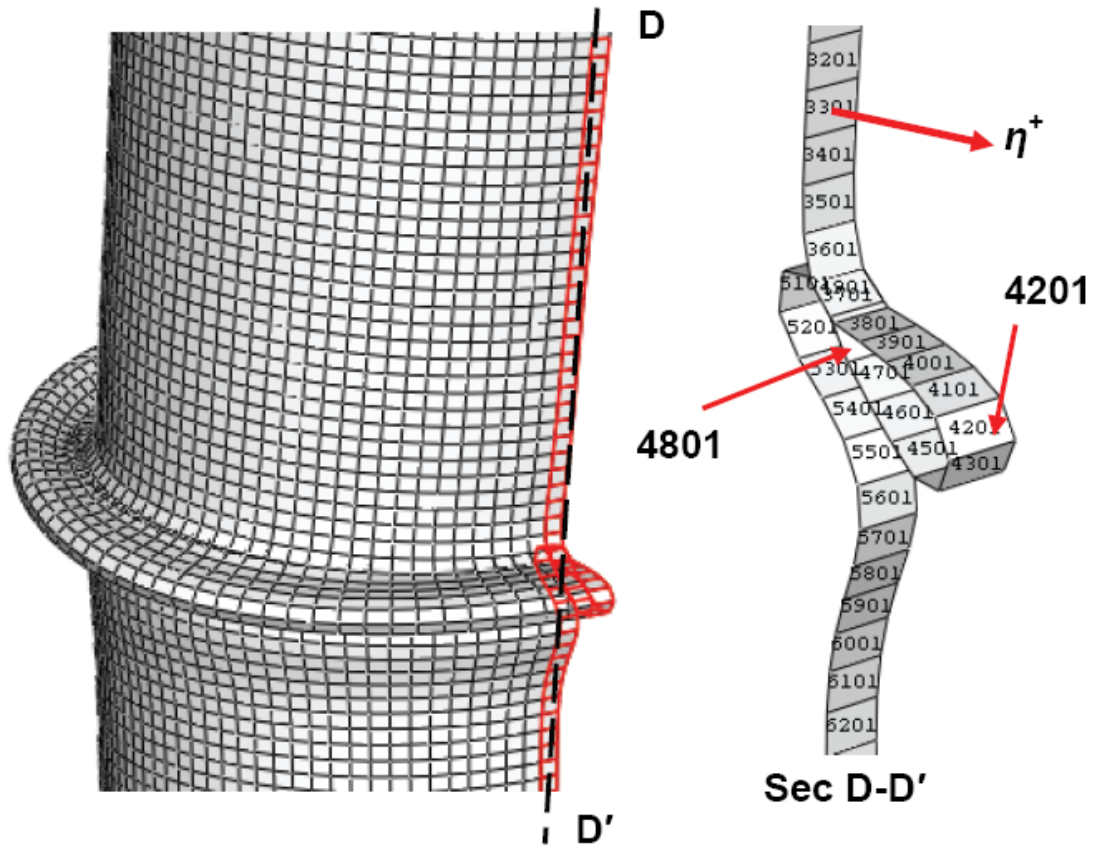
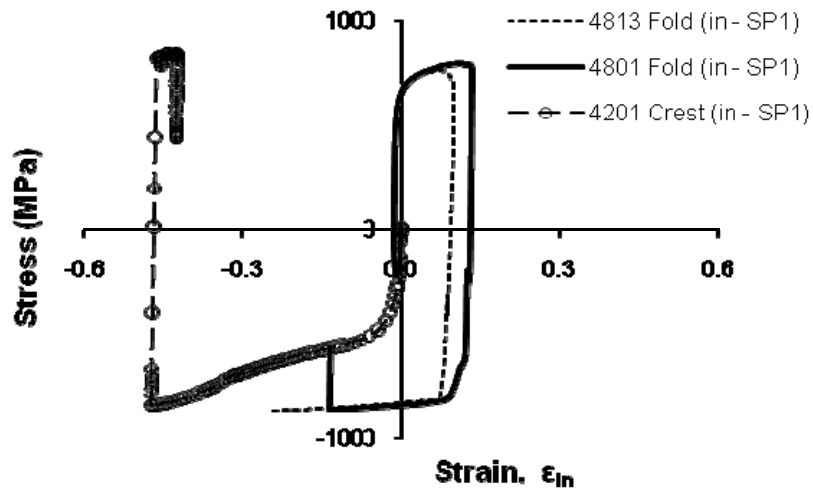
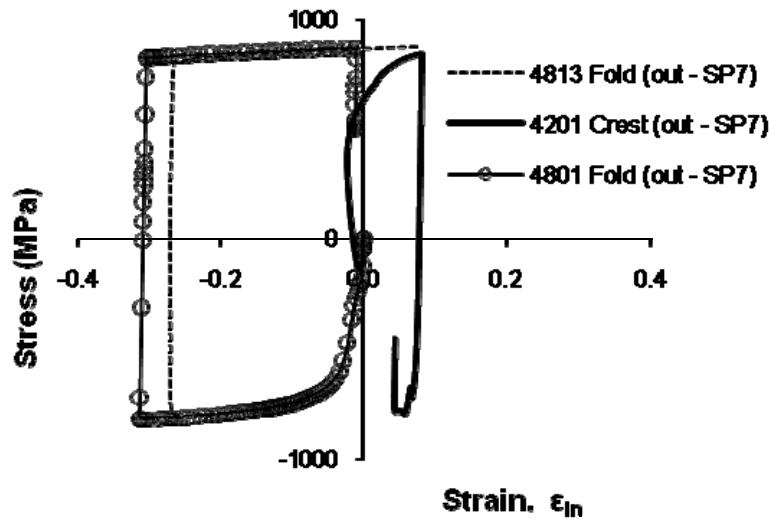


Figure 5.31 Close-up view of wrinkled pipe along with a wrinkle-strip for specimen 6

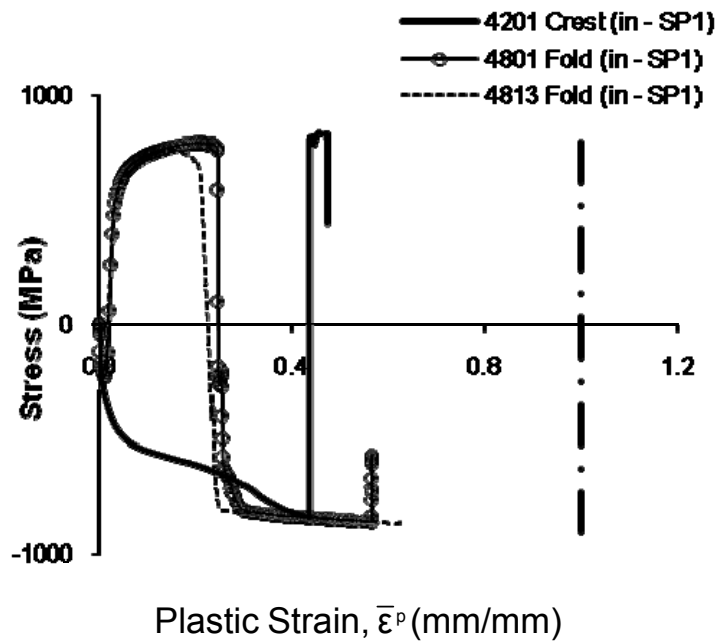


(a)

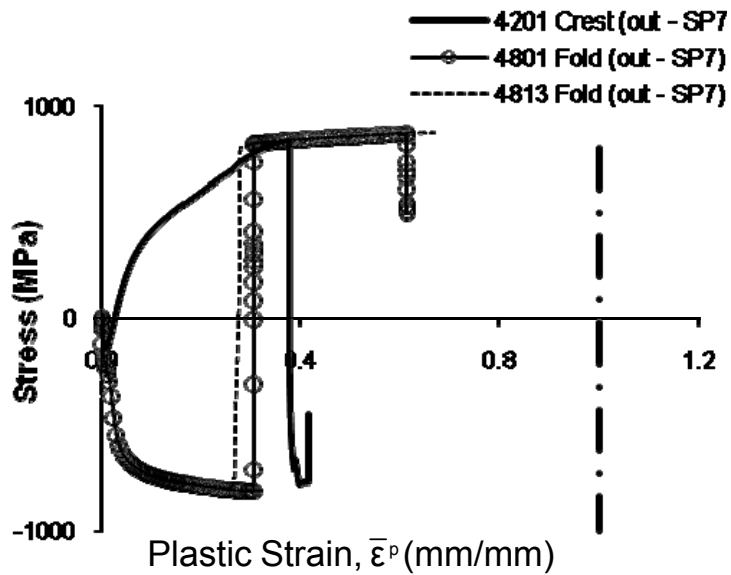


(b)

Figure 5.32 Longitudinal stress-strain relationship at some selected elements of specimen5 (D20P0A5-5)



(a)



(b)

Figure 5.33 True longitudinal stress-equivalent plastic strain plots at some selected elements of specimen 5

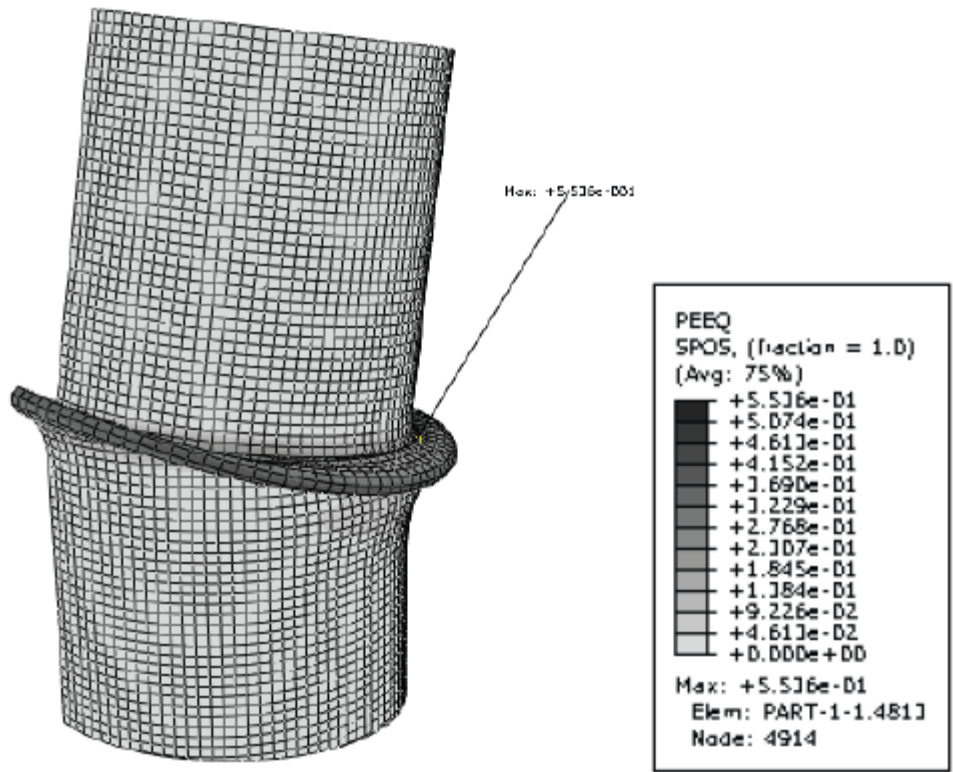


Figure 5.34 Contour plots of equivalent plastic strain (PEEQ) obtained from outer surface of specimen 6

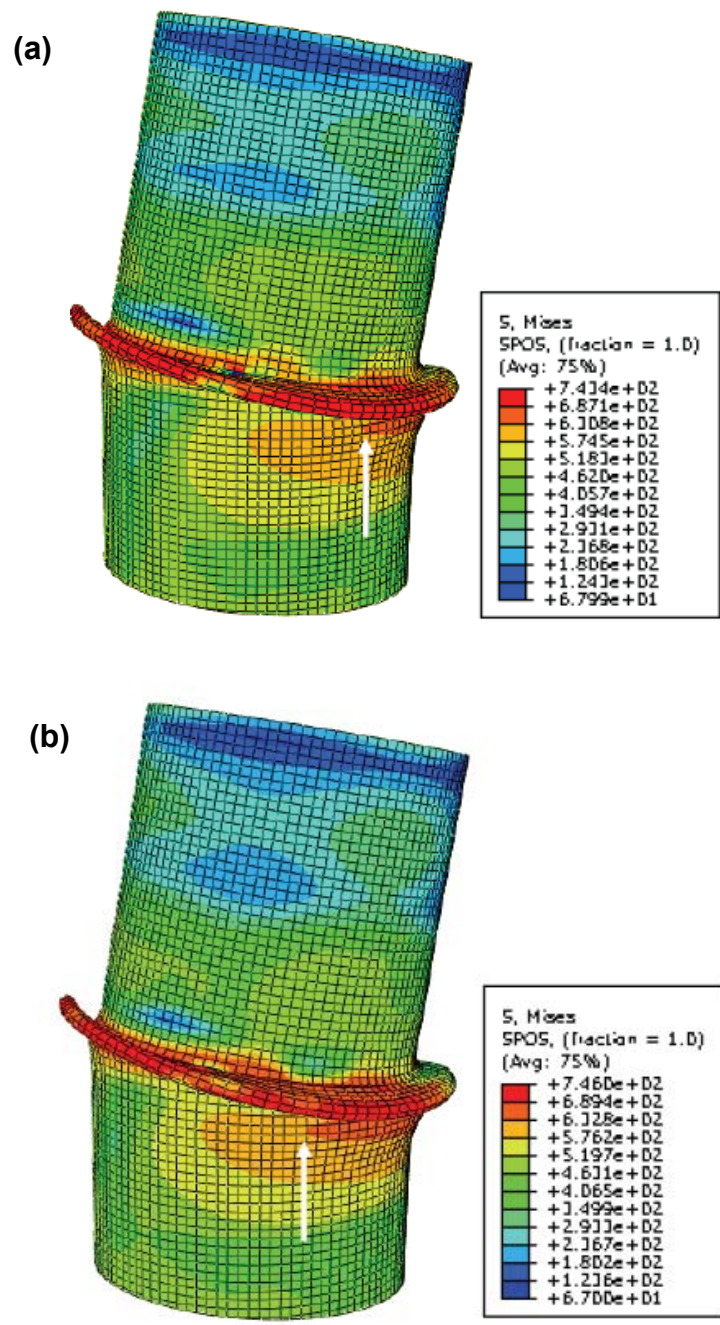


Figure 5.35 Progression of von Mises stress after few increments for specimen 6

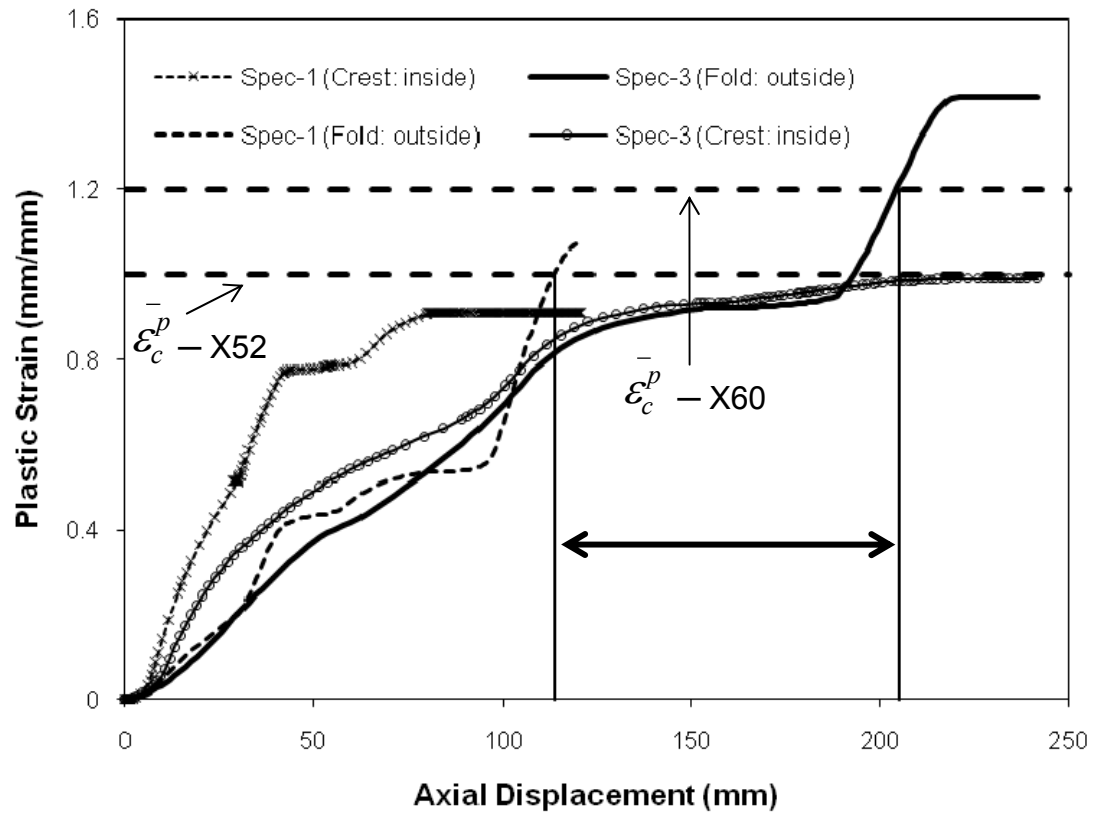


Figure 5.36 Plastic strain growth with displacement history for specimen 1 and 3

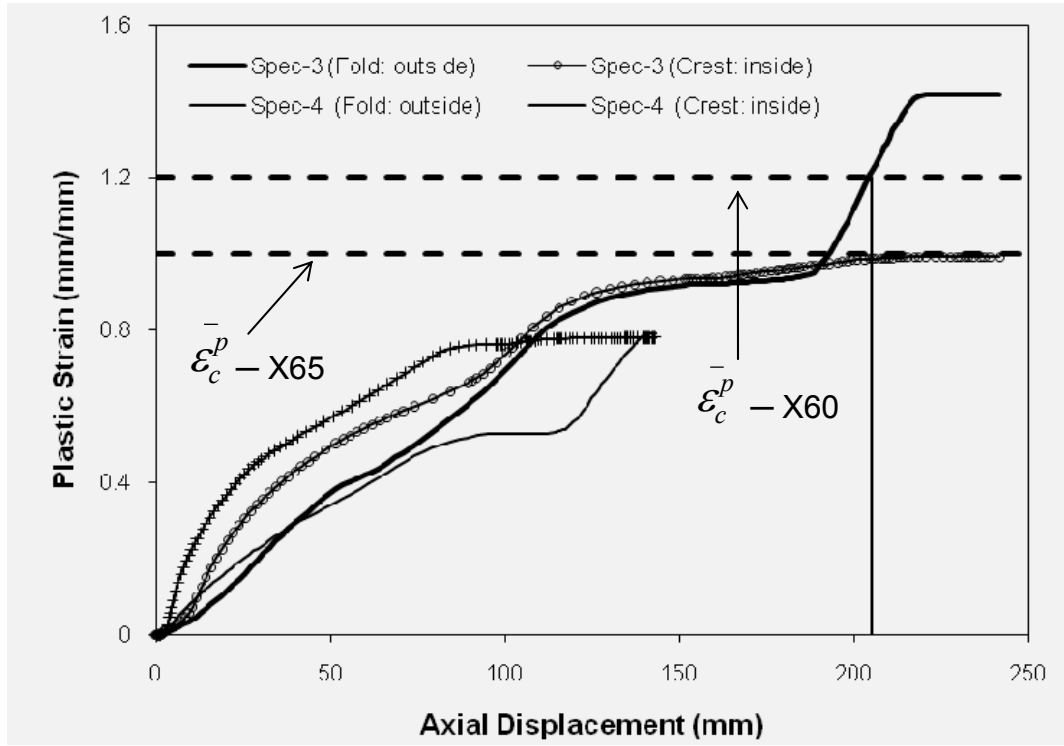


Figure 5.37 Plastic strain growth with displacement history for specimen 3 and 4

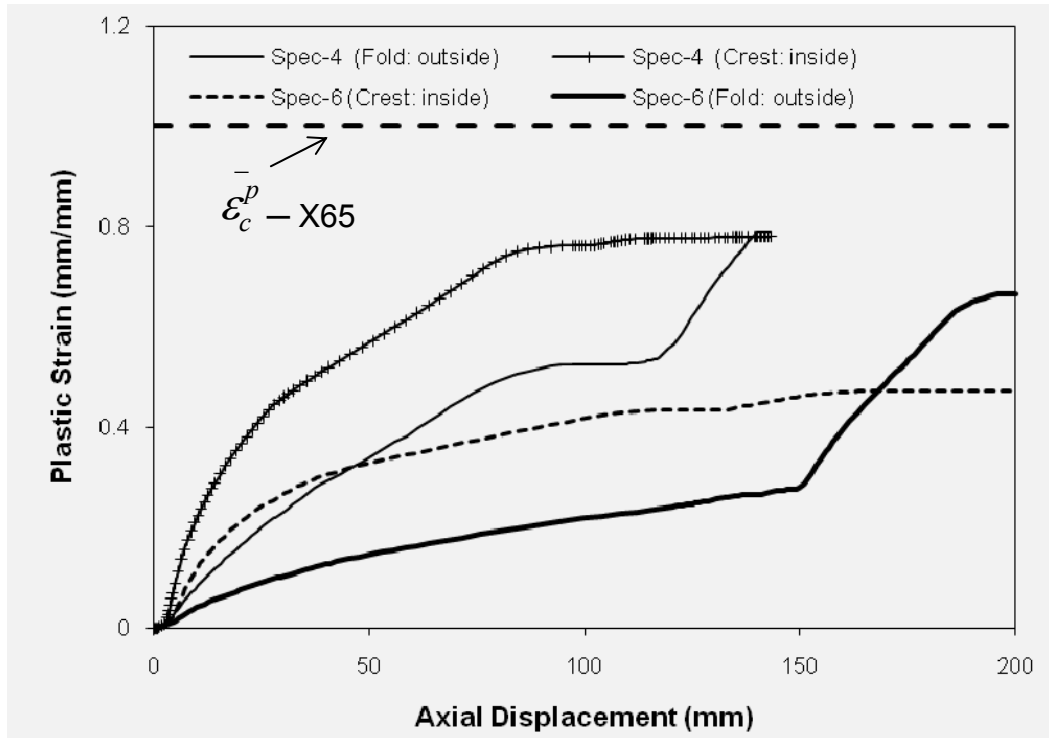


Figure 5.38 Plastic strain growth with displacement history for specimen 4 and 6

## 5.6 References

- Ahmed, A., Das, S., and Cheng, J.J.R. 2010. Numerical investigation of tearing fracture of wrinkled pipe. *Journal of Offshore Mechanics and Arctic Engineering*, 132: 011302-1.
- Ahmed, A., Aydin, M., Cheng, J.J.R., and Zhou, J. 2009. Experimental investigation of fracture in wrinkled pipelines under monotonic axial and bending deformation. *In Proceedings of the ASME 28th International Conference on Ocean, Offshore and Arctic Engineering*, Honolulu, Hawaii, USA.
- Aydin, M. 2007. Tearing fracture of energy pipelines under monotonic loading conditions. M.Sc. dissertation, University of Alberta, Edmonton, AB, Canada.
- Canadian Standards Association (CSA). 2007. Oil and gas pipeline systems. Z662-07, Canadian Standards Association, Mississauga, ON, Canada.
- Chen, W. and Han, D.J. 1988. *Plasticity for structural engineers*. Springer-Verlag, New York.
- Cheng, J.J.R., Kulak, G.L., and Khoo, H.-A. 1998. Strength of slotted tubular tension members. *Canadian Journal of Civil Engineering*, 25: 982-991.
- Das, S. 2003. Fracture of wrinkled energy pipelines. PhD in Structural Engineering, University of Alberta, Edmonton, AB, Canada.
- Das, S., Cheng, J.J.R., and Murray, D.W. 2007. Behaviour of wrinkled steel pipelines subjected to cyclic axial loadings. *Canadian Journal of Civil Engineering*, 34: 598-607.

- Das, S., Cheng, J.J.R., and Murray, D.W. 2002. Fracture in wrinkled linepipe under monotonic loading. *In* Proceedings of the 4th International Pipeline Conference, Sep 30-Oct 3 2002, Vol. B, pp. 1613-1618.
- Das, S., Cheng, J.J.R., Murray, D.W., Wilkie, S., A., and Zhou, Z.J. 2001. Wrinkle behaviour under cyclic strain reversal in NPS12 pipe. *In* 20th International Conference on Offshore Mechanics and Arctic Engineering; Polar and Arctic Pipeline Technology, Jun 3-8 2001, Vol. 4, pp. 129-138.
- Hibbitt, H.D., Karlsson, B.I., and Sorensen, P. 2006. ABAQUS version 6.6 - theory manual.
- Khoo, H.A. 2000. Ductile fracture of steel. PhD Thesis, University of Alberta, Edmonton, AB, Canada.
- Martinez-Saucedo, G., Packer, J.A., and Willibald, S. 2006. Parametric finite element study of slotted end connections to circular hollow sections. *Engineering Structures*, 28: 1956-1971.
- Murray, D.W. 1997. Local buckling, strain localization, wrinkling and postbuckling response of line pipe. *Engineering Structures*, 19: 360-371.
- Ramberg, W. and Osgood, W.R. 1943. Description of stress-strain curves by three parameters. National Advisory Committee for Aeronautics (United States Advisory Committee for Aeronautics), Washington, DC, United States.
- Yang, M.Z., Drumm, E.C., Bennett, R.M., and Mauldon, M. 1999. Measurement of earth pressures on concrete box culverts under highway embankments. *ASTM Special Technical Publication*, pp: 87-100.
- Zhang, Y. and Das, S. 2008a. Failure of X52 wrinkled pipelines subjected to monotonic axial deformation. *Journal of Pressure Vessel Technology*, 130: 021702-1.

- Zhang, Y. and Das, S. 2008b. Failure of X52 wrinkled pipeline subjected to monotonic bending deformation and internal pressure. *International Journal of Offshore and Polar Engineering*, 18: 50-55.
- Zhang, Y., Das, S., and El-Tawil, W. 2008. Numerical study on failure of X52 wrinkled pipelines subjected to bending deformation. *In* 18th 2008 International Offshore and Polar Engineering Conference, ISOPE 2008, July 06,2008 - July 11, pp. 194-198.
- Zhang, Z.L., Hauge, M., Ødegård, J., and Thaulow, C. 1999. Determining material true stress–strain curve from tensile specimens with rectangular cross-section. *International Journal of Solids and Structures*, 36: 3497-3516.
- Zhao, R., Huang, R., Khoo, H.A., and Cheng, J.J.R. 2009. Parametric finite element study on slotted rectangular and square HSS tension connections. *Journal of Constructional Steel Research*, 65: 611-621.

## 6. EFFECTS OF PARAMETERS ON TEARING FAILURE MODE

### 6.1 General

The double failure criteria — 'Strain Reversal Criterion' along with 'Critical Plastic Strain ( $\bar{\epsilon}_c^p$ ) Limit' — have been proposed in previous chapter to predict the tearing failure mechanism under monotonic loading. Based on the findings of the FE simulation of all the test specimens used in this study, the following postulation can be made.

For all specimens, the elements located in the wrinkle fold had gone through the strain reversal process meeting 'Criterion-1' due to the reversed bending mechanism attributed from the loading condition. However, depending on the presence of perfect test conditions, in only two cases, to be specific, for specimen 1 and specimen 3, the equivalent plastic strain did exceed the critical strain limit ( $\bar{\epsilon}_c^p$ ), thus meeting both 'Criterion-1' and 'Criterion-2'. In those two instances, partial and/or through-thickness crack or fracture was observed at the wrinkle fold of the test specimens, thus demonstrating the acceptance of these 'Double Failure Criteria'. In order to understand and hence, to establish the 'perfect test conditions' to generate this tearing failure, the effects of different test variables or parameters on the FE results are presented in this chapter. These variables include loading condition in terms of moment gradient (i.e. presence or absence of shear load), pipe geometry (i.e.  $D/t$  ratio), internal pressure condition, global curvature or end rotations, and pipe material property. In addition to the above parameters, it is necessary to consider the Baushinger effect (i.e. the effect of reduction of yield stress due to reversal of stress) of pipe material on the proposed failure criteria, as the pipe specimens went through a strain reversal process.

## 6.2 Simulation of Field Loading

Before studying the effect of different parameters, it is important to establish, under what field loading condition, a tearing failure can occur. According to prior research observations (Das 2003), an axisymmetric or bulging (see Figure 4.1a) wrinkle can occur under monotonic axial load or displacement due to the presence of thermal strain (due to temperature differential in northern climates) and/or soil movement along the pipe. Depending on the driving mechanism, there are two possibilities. First possibility, under continued deformation, the half-wave length of the wrinkle decreases, and eventually, the interior surfaces of the wrinkle can come into direct contact providing a different load path in the pipe wall. As the load bypasses the wrinkle, a second wrinkle may develop adjacent to the first. This process may lead to stacking of wrinkles, i.e. 'accordion' wrinkles (see Figure 4.2a) and, conceptually, there will be a rare possibility of fracture at the wrinkle location. However, recent research has shown that, under low cyclic fatigue load-deformation, fracture can occur at the crest of an axisymmetric wrinkle (see Figure 4.2b) (Das et al. 2001; Das et al. 2007a; Das et al. 2007b).

Second possibility (similar to specimen 1 in Chapter 5), subsequent or simultaneous lateral thrust generated from geo-movement, due to slope instability or other geo-hazards, on the wrinkle region along with continued axial deformation can force the initial axisymmetric wrinkle to a non-axisymmetric one, as a plastic hinge was already formed due to pipe wrinkling. This process can create an offset between two segments of the wrinkled pipe. Under continued deformation, the interior surface of the wrinkle can come in contact with each other and, at some point, one segment of the pipe slipped inside the other segment in a “telescoping” manner. During this process, a sharp fold is created in the pipe wall and, eventually, a tearing failure can occur at that location.

When differential settlements resulting from slope movements, frost heave, and thaw settlements take place, onshore or buried pipelines can often undergo large deformations because of beam bending and stretching. Curvature imposed by

differential settlements can induce large compressive longitudinal strains resulting into non-axisymmetric wrinkles on the concave side of the pipe (see Figure 4.1b). In laboratory as well as in numerical simulation, settlement-imposed curvatures are simulated by applying monotonically increasing rotations at both ends of the specimens. Depending on the magnitude of the frictional forces developing between the pipe and the soil, two extreme cases can be identified for test boundary conditions in the longitudinal direction. First scenario, keeping the pipe segment ends fully restrained due to high frictional force along the pipe, the end rotations i.e. curvature of the pipe is increased monotonically. During this process, the pipe wrinkle at the compression side will amplify significantly with the increase of the curvature (see Figure 6.1), and eventually, either the pipe can lose its axial capacity leading to a structural instability problem, or there can be a fracture in the pipe wall due to the presence of high tensile strain on the convex side of the deformed pipe (Sen 2006). It can also be added that, similar to axisymmetric wrinkle, under cyclic loading, may be extremely low cycle in nature, a fracture can trigger at the crest of a non-axisymmetric wrinkle.

Another scenario, after keeping the pipe segment ends fully restrained at certain curvature where a sizeable wrinkle was formed, the continued axial displacement due to subsequent soil movement along the pipe can force one segment of the pipe to slip inside the other segment of the pipe in a telescoping manner. At this point, two things can happen. Depending on the driving mechanism, either a sharp fold can be created at the wrinkle location (similar to specimen 3) resulting in tearing failure in the pipe wall, or the load induced from soil movement can bypass the wrinkle as wrinkle on both compression and tension side closes, and eventually, results in initiation of second wrinkle (similar to specimen 2 or specimen 6), i.e. accordion failure mode.

In summary, it can be said that there are two possible loading condition for which tearing failure can occur. First, with the presence of an initial axisymmetric wrinkle, a lateral thrust or shear load induced from geo-movement along with continued axial deformation can generate tearing failure. Second, with the

presence of an initial non-axisymmetric wrinkle due to differential settlement or discontinuous permafrost, a fully restrained pipe segment at a certain curvature along with subsequent soil movement inducing axial deformation can be a candidate of tearing fracture.

### **6.3 Effect of Loading Condition**

As described in Chapter 3, a shear load was applied to specimen 1 (with an initial bulging wrinkle and zero internal pressure) for generating the curvature. Whereas, for other specimens with or without internal pressure conditions (see Chapter 4), end rotations were applied to generate curvature. Using the concept of solid mechanics, it can be said that the presence of shear load in case of specimen 1 (as discussed in Chapter 3) can incorporate the effect of moment gradient, whereas the end rotations applied in specimen 3 can provide more uniform distribution. In order to identify the effect of this difference in terms of moment gradient, the strain growth of specimen 1 and specimen 3 is compared and presented in Figure 6.2.

Although the D/t ratio and the internal pressure condition were different for these two specimens, the effect of moment gradient is distinct as indicated by ' $\Delta_d$ ' in Figure 6.2. As can be seen, the outer surface of one of the elements at the wrinkle fold of specimen reached the critical strain limit ( $\bar{\varepsilon}_c^p$  - X52 in Figure 6.2) at a much smaller displacement (almost half) compared to that of specimen 3. It is also important to add that, although the end rotation for specimen 1 was much smaller than that of specimen 3 (see Table 5.3); due to smaller span length of specimen 1, the global curvature of both specimens was almost identical ( $\approx 160 \times 10^{-6}$  rad/mm). In addition, the higher D/t ratio as well no internal pressure condition of specimen 1 might expedite this failure mechanism. Nevertheless, the effect of moment gradient (i.e. presence of shear load) can be an important variable for this unique failure mode.

Before going to further detail, it is important to explain the logic for choosing the loading procedures of specimen 1. First, why an initial wrinkle was necessary? Second, how or why the presence of shear loads expedites the tearing failure mechanism? To address these issues, a number of FE analyses were performed using specimen 1.

As mention in Chapter 3, an initial axial load or displacement was applied to trigger a bulge type wrinkle at the mid-span of the specimen 1 before applying the shear load. To justify the importance of this step, a FE analysis was performed using a much smaller axial load ( $\approx$  quarter of  $P_{MTS}$  in Figure 3.4) compared to specimen 1 before applying the shear load at pipe mid-span. During this step, the pipe's end conditions were pinned-pinned. The shear load was increased monotonically. However, the analysis had to stop because of very slow convergence before even reaching the end rotations similar to specimen 1 (see Table 5.3). The deformed shape obtained from this analysis is presented in Figure 6.3. A severe localized dent or diamond buckling mode (typical for unpressurized condition) along with excessive cross-sectional distortion can be observed in Figure 6.3. This rationalizes the importance of generating an initial wrinkle in the form of a (pseudo) plastic hinge, which in turn, helped the pipe to rotate under shear load without having significant localized deformation.

Next, in order to explain the significance of shear load over end moments, a FE analysis was performed using a loading sequence similar to specimen 1. The only difference was applying end moments at both ends of the pipe instead of applying the shear load. The final deformed shape and the contour plot of equivalent plastic strain obtained from the outer surface of the wrinkled pipe are presented in Figure 6.4a and Figure 6.4b, respectively. A pictorial comparison can be made between the final deformed shapes obtained from analyses with shear load (see Figure 4.3c), and without shear load (see Figure 6.4a). As can be seen, the deformed configurations are almost identical. In addition, the contour plot in Figure 6.4b confirms that some of the elements at wrinkle fold reached the critical strain limit. However, by observing the plastic strain growth obtained from the outer surface

of the specimens presented in Figure 6.5, it can be said that although the strain growth trend along the displacement history found to be almost similar, the specimen under end moments reached the critical strain limit ( $\bar{\varepsilon}_c^p$ ) at higher axial displacement compared to the case with shear load (see ' $\Delta_d$ ' in Figure 6.5). Therefore, it can be said that the presence of shear load can intensify the strain growth and hence, expedite the fracture initiation process.

However, the magnitude of ' $\Delta_d$ ' in Figure 6.5 is not as significant as shown in Figure 6.2, which in turn denotes that there are contribution of other test parameters, to be specific D/t ratio and internal pressure conditions, for generating tearing fracture in specimen 1 at a much earlier displacement compared to specimen 3. Therefore, a number of FE analyses are performed to identify the effect of these parameters as well as other parameters mentioned in subsection 6.1 on different failure modes — 'tearing', or 'accordion', of wrinkled pipe. The parameters used in these analyses are tabulated in Table 6.1. In this parametric analysis, the loading condition of specimen 3 is adopted. In order to provide comparison of analytical results obtained from this parametric study, the FE results of specimen 3, including the deformed shapes, longitudinal stress-strain relations (i.e. strain-reversal process or 'Criterion-1'), and the plastic strain growth (i.e. 'Criterion-2) over displacement history, at critical locations of wrinkle fold are utilized.

#### **6.4 Effect of D/t Ratio**

The strain growth comparisons of specimen 1 and specimen 3, and specimen 3 and specimen 4, presented in Figure 5.36 and Figure 5.37, respectively, indicate the influence of pipe geometry (i.e. D/t ratio) on the tearing behaviour of wrinkled pipe. As can be seen Figure 5.37, the smaller D/t ratio with larger end rotations under essentially same internal pressure condition can increase the possibility of tearing fracture initiation in the pipe wall. Similar observation can also be made by assessing Figure 5.36, where the D/t ratio was found smaller in both cases of

specimen 1 and specimen 3. Therefore, the D/t ratio can be considered as an important parameter for this tearing behaviour.

In order to consider the effect of D/t ratio, a number of analyses were performed varying from 30 to 60, a typical range for transporting hydrocarbons. During these analyses, the other parameters, such as curvature or end rotation (i.e. locking angle), material property (X60 grade), internal pressure condition, were kept similar to that of specimen 3. The results of these analyses are summarized in rows 1 to 4 in Table 6.1. Numerical analysis results of test specimen 4 with a D/t ratio of 79 (see Table 5.1 in Chapter 5) is presented in row 5 of Table 6.1 to illustrate the effect of high D/t ratio.

The initial and final deformed shapes for different D/t ratio are presented in Figure 6.7 and Figure 6.8, respectively. As can be seen from Figure 6.7, with the increase of D/t ratio, the wrinkle amplitude increases and, the possibility of early closing of wrinkle at the compression side increases. In order to verify the above statement, the contact pressure at the interior of pipe specimens was tracked. The numerical results have shown that the self-contact at the wrinkle location was tracked at 152 mm of axial displacement for analysis 1 (i.e. D/t ratio of 34), whereas contact initiation was tracked at much earlier ( $\approx 85$  mm) for analysis 5 (i.e. D/t ratio of 79). For higher D/t ratio, this early contact can increase the possibility of wrinkle closing on the tension side as well, and thus, impart a load path to bypass the wrinkle for initiating another wrinkle in the pipe wall. After observing the final deformed shapes, it can be said that the deformation configurations closely resemble each other up to a certain value of D/t ratio (compare Figure 6.8a to Figure 6.8c). However, the presence of second wrinkle for higher D/t ratio (see Figure 6.8d) increases the possibility of ‘accordion’ of wrinkles. A close up view of wrinkled pipe with D/t ratio of 60 and 79 in Figure 6.9 also provides the evidence of accordion failure mode.

The longitudinal stress-strain relations obtained from one of the critical elements at the wrinkle fold of these analytical specimens with different D/t ratio are

presented in Figure 6.10. As can be seen, the strain-reversal phenomenon is present in all cases, and therefore, ‘Criterion-1’ has been met for all cases. In order to check ‘Criterion-2’, the equivalent plastic strain values obtained from these analyses were tracked and compared with the critical strain ( $\bar{\epsilon}_c^p$ ) limit. The plastic strain growth obtained from the outer surface of the wrinkle fold is presented in Figure 6.11. In this figure, the term ‘ $\Delta_C$ ’ represents the axial displacement at which the plastic strain reaches the critical strain limit. In other words, ‘ $\Delta_C$ ’ represents the axial displacement at which the fracture will initiate in the pipe wall. The values of ‘ $\Delta_C$ ’ obtained from different analyses are reported in Table 6.1. The terms ‘ $\Delta_{C1}$ ’, ‘ $\Delta_{C2}$ ’, and ‘ $\Delta_{C3}$ ’ in Table 6.1 represent the specimens with D/t ratio of 34, 45 and 50, respectively. As can also be observed from this figure, the onset of fracture can occur earlier with the increase of D/t ratio. However, for D/t ratio  $\geq 60$ , the strain growth was not significant enough to cross the critical strain limit. Therefore, beyond a certain D/t ratio, the possibility of tearing fracture decreases with the increase of D/t ratio, as the wrinkle deformation shown in Figure 6.9 provides a load path to generate second wrinkle in the pipe wall. Therefore, the possibility of accordion failure is more for pipes with D/t ratio  $\geq 60$ .

## 6.5 Effect of End Rotation

The strain growth comparison of specimen 2 and specimen 3 presented in Figure 5.21 indicates the effect of end rotation or curvature, although the D/t ratio as well as the internal pressure condition was different for those two specimens. As can be seen, the larger end rotations along with the presence of internal pressure for specimen 3 have increased the possibility of tearing fracture in the pipe wall. In order to consider the effect of curvature (or end rotation i.e. locking angle), a number of analyses were performed increasing the global curvature from  $75 \times 10^{-6}$  rad/mm (or  $\theta_{avg} \approx 3^\circ$ ) to  $337 \times 10^{-6}$  rad/mm (or  $\theta_{avg} \approx 17^\circ$ ). During these analyses,

the other parameters, such as D/t ratio, material property (X60 grade), and internal pressure condition, were kept similar to that of specimen 3. The results of these analyses are summarized in row 6 to row 13 in Table 6.1.

The initial and final deformed shapes under different end rotations are presented in Figure 6.12 and Figure 6.13, respectively. As can be seen from Figure 6.12, with the increase of global curvature (or end rotation), the wrinkle amplitude increases significantly, thus increasing the possibility of early closing of wrinkle at the compression side. This statement can be verified by tracking the axial displacement ( $\Delta_i$ ) values at which the contact pressure at the interior of pipe specimens was first initiated. By comparing the displacement ( $\Delta_i$ ) values presented in Table 6.1, it can be said that the self-contact initiation at the wrinkle location can happen much earlier for higher end rotations. However, for end rotations up to  $13^\circ$ , the contact initiation was tracked during the load step at which the end plates of the pipe were locked at a desired curvature values and the pipe was under continued axial deformation. Whereas, for end rotations over  $13^\circ$ , the contact initiation was tracked before locking the end plates of the pipe at the desired curvature values. Therefore, the pipe specimens with end rotation higher than  $13^\circ$  became unstable after reaching certain displacement level and the axial capacity of the pipe started to drop significantly. Therefore, the FE analyses with end rotations higher than  $13^\circ$  have been designated as structurally unstable or 'SU' in Table 6.1. The configuration of the final deformed shapes obtained with end rotations of  $7^\circ$  and  $11^\circ$ , presented in Figure 6.13a and Figure 6.13b, respectively, closely resembles each other with the presence of telescopic action. Whereas, the final deformed configuration under end rotation of  $15^\circ$ , illustrated in Figure 6.13c, represents closing of wrinkle at the compression side of the pipe without having closed on the tension side of the pipe. Eventually, the pipe specimen became unstable.

The longitudinal stress-strain relations obtained from one of the critical elements at the wrinkle fold of these analytical specimens under different end rotations are presented in Figure 6.14. As can be seen, the strain-reversal phenomenon is

present in all cases, and therefore, ‘Criterion-1’ has been met for all cases. However, it can also be observed from Figure 6.14 that with increase of global curvature or end rotation, the strain-reversal region increases, and thus, creates the possibility of higher plastic strain values. In order to check ‘Criterion-2’, the equivalent plastic strain values obtained from these analyses were tracked and compared with the critical strain ( $\bar{\epsilon}_c^p$ ) limit. The plastic strain growth obtained from the outer surface of the wrinkle fold is presented in Figure 6.15. In this figure, the term ‘ $\Delta_C$ ’ represents the axial displacement at which the plastic strain reaches the critical strain limit, and hence, indicates the onset of fracture. The values of ‘ $\Delta_C$ ’ obtained from different analyses are reported in Table 6.1. The terms ‘ $\Delta_{C1}$ ’, ‘ $\Delta_{C2}$ ’, ‘ $\Delta_{C3}$ ’ and ‘ $\Delta_{C4}$ ’ in Table 6.1 represent the specimens with end rotations of 5°, 7°, 9°, and 11°, respectively. As can also be observed from this figure, the fracture initiation can occur earlier with the increase of end rotations. However, after reaching a certain curvature and/or end rotation (e.g. 11°), the difference in ‘ $\Delta_C$ ’ values is not significant, and moreover, after reaching end rotations  $\geq 13^\circ$ , the strain growth was not significant enough to cross the critical strain limit. On the other hand, for smaller curvature and/or end rotations (e.g. 3°), the possibility of accordion failure mode increases, as indicated by initiation of second wrinkle in Figure 6.16.

In summary, for global curvature ranging from  $115 \times 10^{-6}$  rad/mm to  $290 \times 10^{-6}$  rad/mm, (i.e. for end rotation between 5° to 13° at which the endplates of the pipe specimens were kept constant), the anticipation of tearing failure mechanism increases considerably. However, for global curvature  $\leq 115 \times 10^{-6}$  rad/mm (or end rotation  $\leq 5^\circ$ ), there is a great possibility of accordion failure mode. Whereas, for global curvature  $\geq 290 \times 10^{-6}$  rad/mm (or or end rotation  $\geq 13^\circ$ ), the pipe structure can become unstable, as the pipe loses its load carrying capacity significantly.

## 6.6 Effect of Operational Condition

The comparison of strain growth of specimen 4 and specimen 6, presented in Figure 5.38, identifies the influence of operational condition (or internal pressure). Although the curvature of those two specimens was different (see Table 5.1), the presence of higher internal pressure (in case of specimen 6) may have delayed the strain growth along its displacement history (see Figure 5.38), thus reducing the possibility of tearing fracture. However, the absence of internal pressure in the line pipe may also reduce the possibility of tearing fracture under certain loading condition, as found for specimen 2 (see Chapter 5). Hence, the operation condition can be a significant variable to influence this unique failure mechanism.

In order to consider the effect of internal pressure, a number of analyses were performed by varying the internal pressure from  $0.0p_y$  (zero) to  $0.8p_y$  (high). Other parameters including pipe geometry and loading conditions were kept same as specimen 3. The test parameters of these analyses are reported in Table 6.1. The initial and final deformed shapes obtained from these analyses are presented in Figure 6.18 and Figure 6.19, respectively, for pictorial comparison. As can be seen from Figure 6.18a, under zero ( $0.0p_y$ ) internal pressure, the presence of 'diamond mode' shape with severe cross-sectional distortion is evident. Whereas, under internal pressure conditions, the presence of non-axisymmetric (due to end rotation) 'bulge mode' shape is observed (see Figure 6.18b, Figure 6.18c and Figure 6.18d). And, with the increase of the internal pressure level, the wave length of the wrinkle increases. Due to higher wave length under higher internal pressure condition (e.g.  $0.8p_y$ ), the axial displacement ( $\Delta_i$ ), at which the contact at interior surfaces of pipe wall initiated, found to be higher (see Table 6.1). This observation indicates that the higher internal pressure condition may delay the process of tearing mechanism. The final deformed shapes presented in Figure 6.19 resemble a typical deformation configuration indicating the presence of telescoping action at the compression side of the pipe. However, the initiation of 2<sup>nd</sup> wrinkle was observed for specimens with relatively higher internal pressure

(see Figure 6.20). This fact suggests that higher internal pressure condition can contribute to either ‘delayed tearing’ or ‘no tearing’ mechanism.

To provide more insights to the above comments, the stress-strain relation as well as plastic strain growth of the critical elements under different internal pressure condition were monitored and are presented in Figure 6.21 and Figure 6.22, respectively. As can be seen from Figure 6.21, the strain-reversal phenomenon is present in all cases, and therefore, ‘Criterion-1’ has been met for all cases. However, the extent of strain reversal decreases with the increase of internal pressure condition, thus increasing the possibility of ‘Accordion’ failure mode. The plastic strain growth obtained from the outer surface of the critical elements is presented in Figure 6.22 in order to check ‘Criterion-2’ i.e. critical strain ( $\bar{\epsilon}_c^p$ ) limit. In this figure, the term ‘ $\Delta_C$ ’ represents the axial displacement at which the tearing fracture can initiate in the pipe wall. Terms ‘ $\Delta_{C1}$ ’, ‘ $\Delta_{C2}$ ’, and ‘ $\Delta_{C3}$ ’ in Figure 6.22 (see Table 6.1 for values) represent the specimens with internal pressure of  $0.2p_y$ ,  $0.4p_y$ , and  $0.6p_y$ , respectively. After comparing the strain growth as well as the values of ‘ $\Delta_C$ ’, it can be said that the onset of fracture can be delayed with the increase of internal pressure, and the possibility of ‘Accordion’ failure increases for relatively higher internal pressure (e.g.  $0.8p_y$ ).

## 6.7 Effect of Material Properties

During the development and verification of the FE model (Chapter 3 and Chapter 4) and the development of the failure criteria (Chapter 5), effect of different grades of steel pipe material including X52, X60 and X65 were presented. To reduce the complexity, only X60 grade has been chosen to consider the effect of material properties. As discussed before, a material model comprising of isotropic strain hardening was used in the FE analyses. Therefore, the strain hardening exponent ( $n$ ) is considered as one of the critical parameter. On the other hand, since there is a presence of strain-reversal behaviour in the stress-strain histories

obtained from all these FE analyses, the Bauschinger effects for metals is also addressed.

### **6.7.1 Strain-hardening Exponent**

In order to consider the effect of isotropic strain hardening, a number of FE analyses were performed by varying the strain-hardening exponent ( $n$ ) from 10 to 25, a typical range suggested in pipeline standard. During these analyses, the other parameters including pipe geometry and loading sequences were kept similar to specimen 3 (see Chapter 5). The true plastic stress – strain relations for different ' $n$ ' values are illustrated in Figure 6.23. The stress – strain relation with ' $n$ ' value of 14.5 in Figure 6.23 represents the X60 grade used in the experimental program.

The stress –strain relations as well as plastic strain growth of one of the critical elements for different ' $n$ ' values are presented in Figure 6.24 and Figure 6.25, respectively. As can be seen from Figure 6.24, the strain-reversal phenomenon is present in all cases, and therefore, 'Criterion-1' has been met for all cases. However, the presence of notable strain hardening was observed for smaller values of ' $n$ ' and, whereas, the extent of strain- reversal region expands with the increase of ' $n$ ' values, thus increases the possibility of reaching critical strain limit ( $\bar{\epsilon}_c^p$ ) at a smaller axial displacement ( $\Delta_C$ ). In Figure 6.25, the terms ' $\Delta_{C1}$ ', ' $\Delta_{C2}$ ', and ' $\Delta_{C3}$ ' (see Table 6.1 for values) represent the specimens with ' $n$ ' values of 25, 20, and 10, respectively. After comparing the strain growth as well as the values of ' $\Delta_C$ ', it can be said that the fracture initiation can be delayed with the decrease of the strain hardening component, and for higher ' $n$ ' values, the difference in ' $\Delta_C$ ' is not significant.

### **6.7.2 Bauschinger Effect**

In order to address the Bauschinger effects for metals under cyclic loading, kinematic hardening in classic metal plasticity is a useful tool. Two types of

hardening models: linear kinematic hardening and nonlinear kinematic hardening/combined isotropic model, are available to consider this effect. The combined isotropic/kinematic hardening model, which provides a more accurate approximation to the stress-strain relation, has been used for the present case. The evolution laws of kinematic hardening model describe the translation of the yield surface in stress space through the back-stress tensor,  $\alpha$  as:

$$6.1) \quad f(\sigma - \alpha) = \sqrt{\frac{3}{2}(s - \alpha^{dev}) : (s - \alpha^{dev})}$$

where  $s$  is the deviatoric stress tensor and  $\alpha^{dev}$  is the deviatoric part of the back-stress tensor.

The evolution of back stress along with the yield surface of the combined isotropic-kinematic hardening model in stress space is illustrated in Figure 6.26. There are different forms of kinematic hardening. One of the most widely and successfully used kinematic evolution law is Armstrong-Fredrick non-linear kinematic hardening. In its uniaxial form, the increment of back stress,  $d\alpha$  is given as follows:

$$6.2) \quad d\alpha = c d\varepsilon^p - \gamma\alpha d\varepsilon^p$$

where  $c$  and  $\gamma$  are material constants and  $d\varepsilon^p$  is the increment in the plastic strain. Equation (2) can be integrated, taking  $\alpha$  to be 0 at  $\varepsilon^p = 0$ , to give

$$6.3) \quad \alpha = \frac{c}{\gamma}(1 - e^{-\gamma\varepsilon^p})$$

The resulting form of the back stress-strain curve, for Armstrong-Fredrick hardening is shown in Figure 6.27. As the plastic strain increases, the back-stress,  $\alpha$ , saturates to the value  $c/\gamma$ . The material model to consider the Bauschinger

effects was obtained from a cyclic test data. The material curves considering the isotropic hardening and the kinematic hardening is presented in Figure 6.28.

In order to identify the effect of kinematic hardening, the longitudinal stress-strain relation was obtained and is presented in Figure 6.29. As can be seen, there is a shift in the longitudinal strain value due to the presence of kinematic hardening. Due to that shift, the plastic strain values with combined hardening reached the critical strain limit ( $\bar{\varepsilon}_c^p$ ) at a smaller axial displacement ( $\Delta_C$ ) compared to isotropic hardening case (see Figure 6.30). However, after comparing the ' $\Delta_C$ ' values, it can be said that although there is an effect of combined hardening to predict the critical strain value at which the failure can initiate, the prediction using isotropic hardening model is reasonable.

## 6.8 Summary

In this chapter, the effect of different parameters on the different failure modes of non-axisymmetric wrinkled pipe under continued monotonic deformation are presented and summarized in Table 6.1. Based on the findings, it can be said that the effect of different loading condition in terms of presence or absence of shear load on the tearing failure mechanism is not significant. The effect of pipe geometry in terms of D/t ratio on the tearing behaviour can be considerable when the D/t ratio is relatively smaller. However, the possibility of accordion failure increases for pipes with D/t ratio  $\geq 60$ . The effect of end rotation or global curvature, which represents the initial non-axisymmetric configuration of the wrinkled pipe, can increase the possibility of fracture initiation when the global curvature lies between  $115 \times 10^{-6}$  and  $290 \times 10^{-6}$  rad/mm. However, the deformed pipe can become unstable for curvature greater than  $290 \times 10^{-6}$  rad/mm and the possibility of accordion failure mode increases for curvature lower than  $115 \times 10^{-6}$  rad/mm. The effect of internal pressure conditions was also addressed in this parametric study. For relatively lower internal pressure ( $0.2p_y$  to  $0.4p_y$ ), the most likely failure mode is tearing in the pipe wall, whereas for higher internal pressure

condition ( $0.8p_y$ ), the possible failure mode is formation of second wrinkle i.e. 'accordion' of wrinkles. However, for zero internal pressure condition, the presence of diamond buckling mode for non-axisymmetric wrinkled pipe can induce severe cross-sectional distortion, thus causing serviceability issue. The Bauschinger effects using nonlinear kinematic hardening on the failure criteria was identified. However, the numerical results obtained using the isotropic hardening is comparable and hence, seems reasonable to use isotropic hardening model to demonstrate the acceptability of the failure criteria established in this study.

Table 6.1 Summary of Parametric study

Analysis	Parameters				Crit-1	Crit-2	$\Delta_i$ (mm)	$\Delta_c$ (mm)	Failure Mode
	D/t	$\phi_{G_6}$ ( $10^{-6}$ , rad/mm)	% of $\rho_y$	n					
1	34	158	0.4	14.5	√	√	152	205	T
2	45				√	√	116	171	T
3	50				√	√	114	163	T
4	60				√	x	102		A
5 <sup>a</sup>	79	97	0.4	12	√	x	85		A
6	34	75 (3°)	0.4	14.5	√	x	169		A
7		115 (5°)			√	√	159	212	T
8		158 (7°)			√	√	152	205	T
9		205 (9°)			√	√	126	172	T
10		245 (11°)			√	√	124	170	T
11		290 (13°)			√	√	124	169	T
12		332 (15°)			√	x	124		SU
13		377 (17°)			√	x	124		SU
14	34	158	0.2	14.5	√	√	144	170	T
15			0.4		√	√	152	205	T
16			0.6		√	√	173	239	T
17			0.8		√	x	226		A
18	34	158	0.4	10	√	√	145	206	T
19				20	√	√	145	193	T
20				25	√	√	141	187	T
21 <sup>b</sup>				14.5	√	√	158	196	T

<sup>a</sup>Indicates result of specimen 4

<sup>b</sup>Indicates Bauschinger effect

Term ' $\Delta_i$ ' indicates the axial displacement at which first contact at pipe interior was tracked

Term ' $\Delta_c$ ' indicates displacement at which plastic strain has reached the critical strain limit

Term 'T' indicates initiation of 'Tearing' fracture in the pipe wall

Term 'A' indicates initiation of second wrinkle i.e. 'Accordion' failure mode

Term 'SU' indicates 'Structurally Unstable' i.e. Instability due to significant axial load drop



(a)

(b)

Figure 6.1 Wrinkled pipe under extreme curvature (Sen 2006)

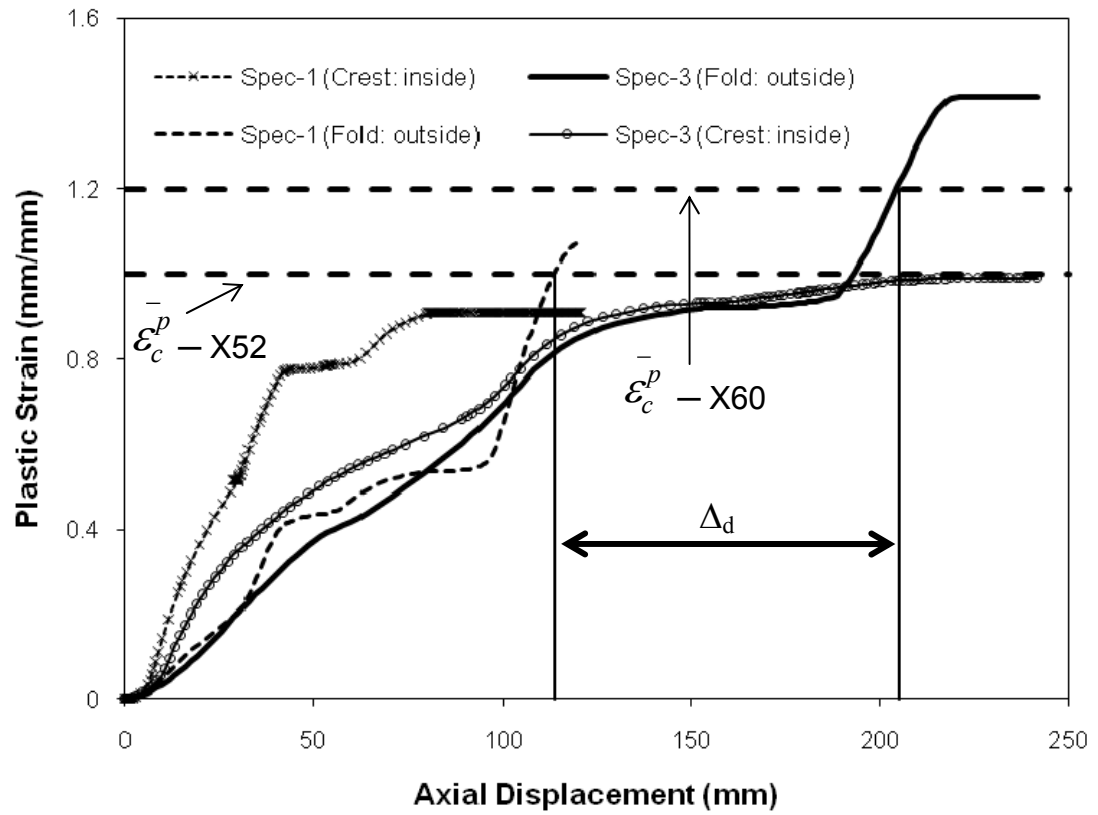


Figure 6.2 Plastic strain growth with displacement history for specimen 1 and 3

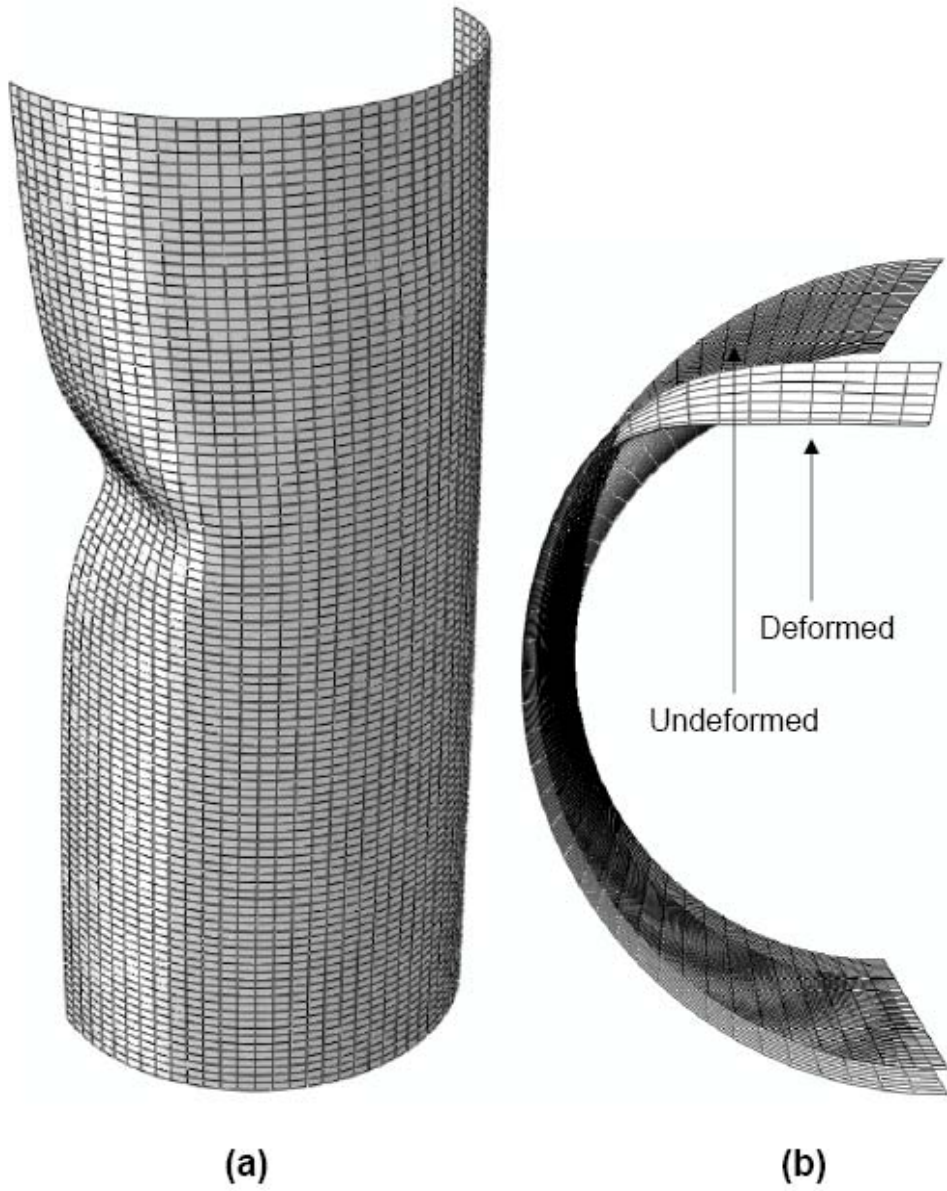


Figure 6.3 Deformed shape after applying shear load

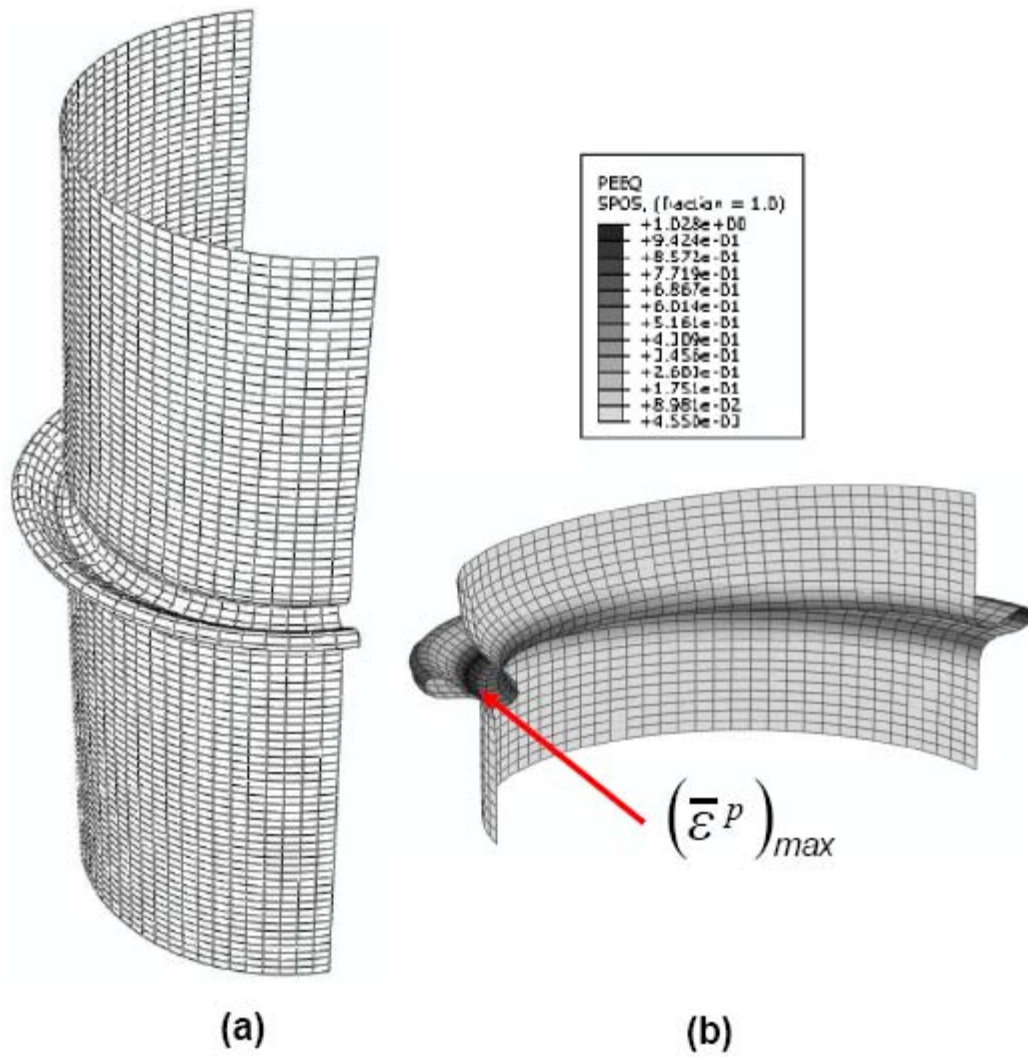


Figure 6.4 (a) Final deformed shape and (b) equivalent plastic strain contour of specimen 1 under end moments

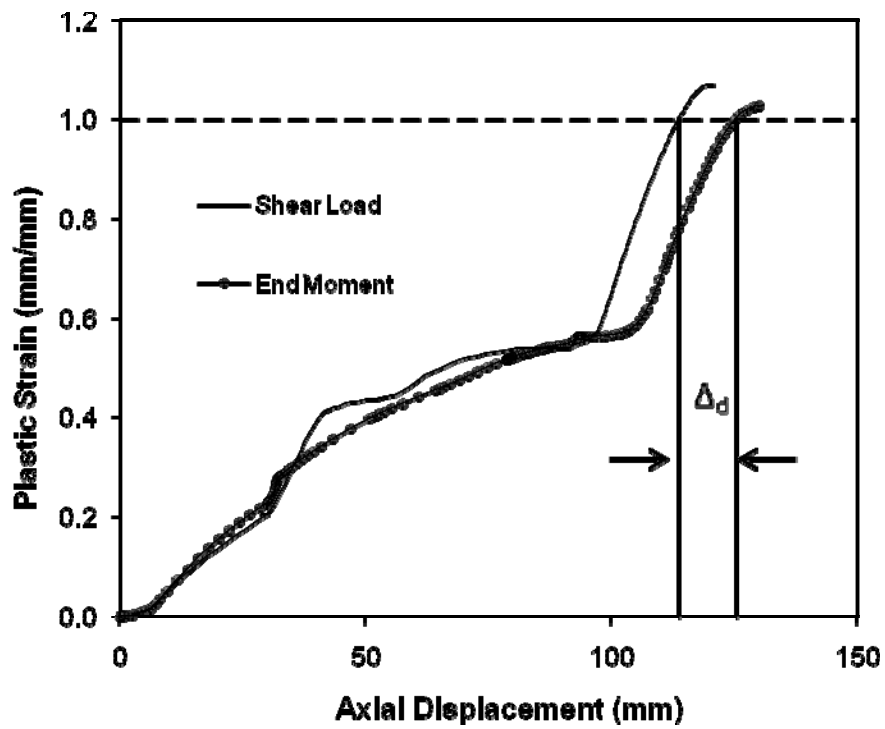


Figure 6.5 Plastic strain growth with or without shear load for specimen 1

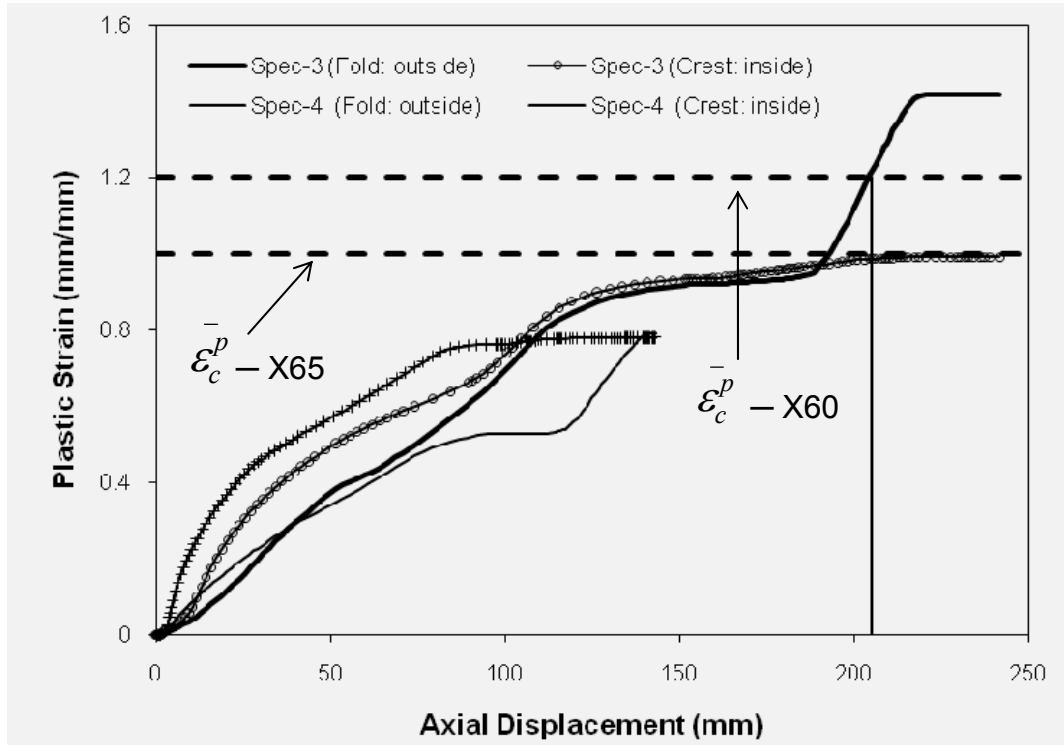


Figure 6.6 Plastic strain growth with displacement history for specimen 3 and 4

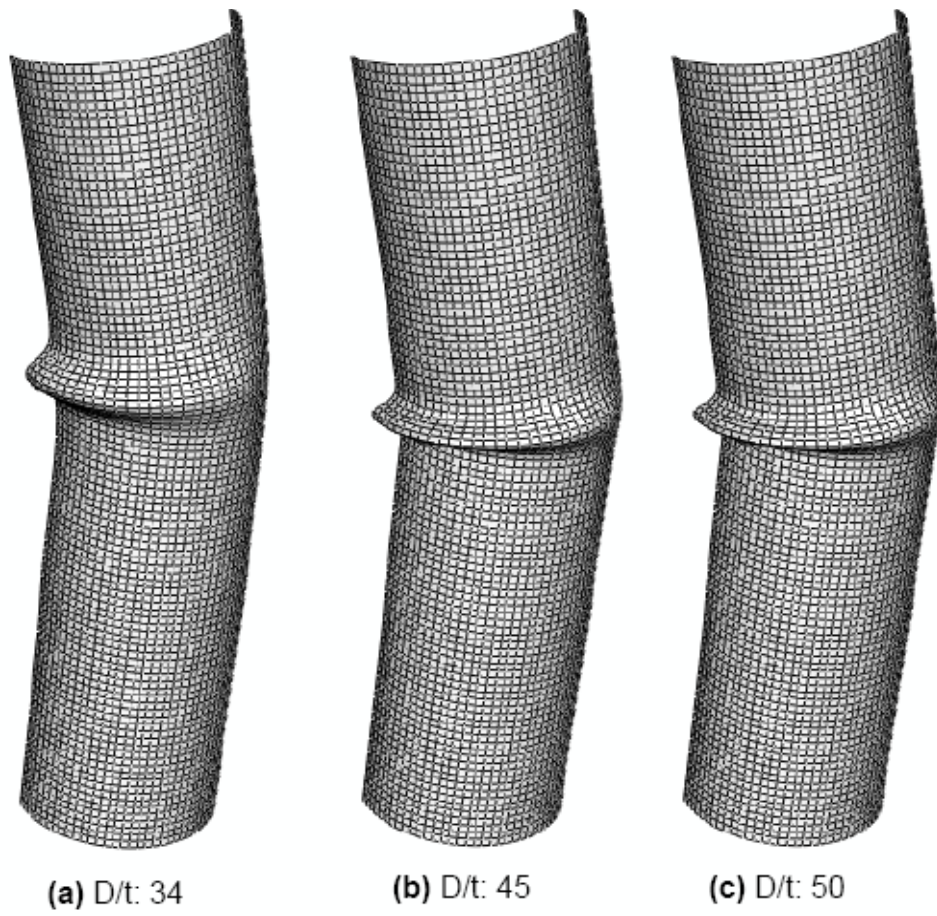


Figure 6.7 Effect of  $D/t$  ratio on initial deformed shape

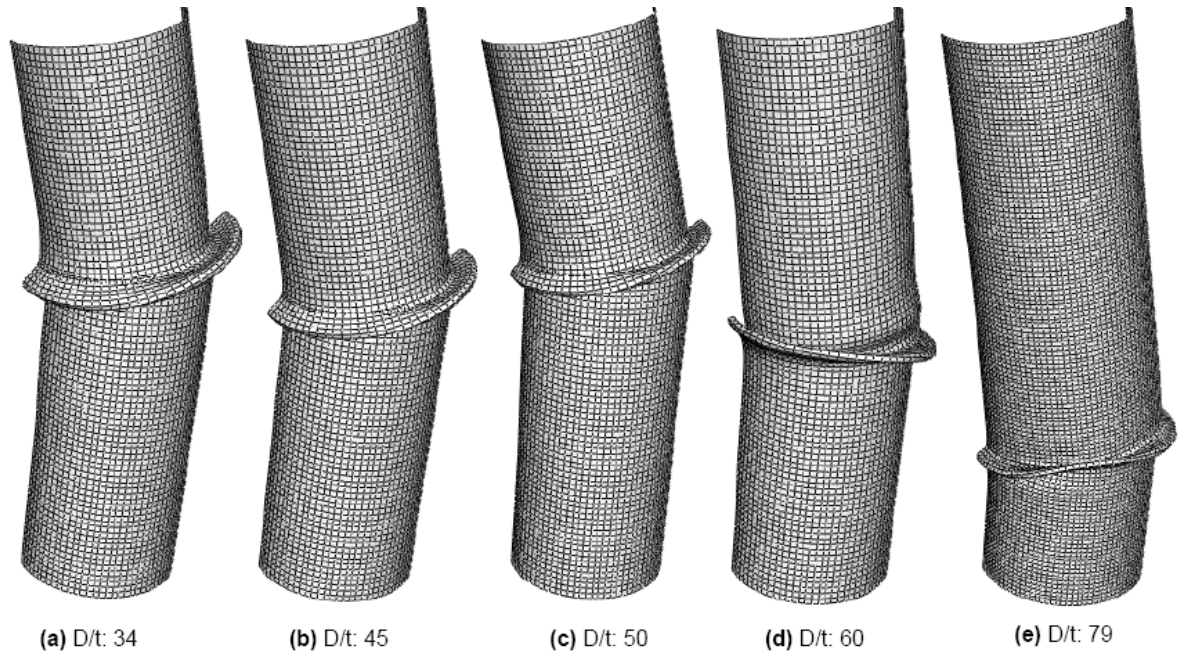


Figure 6.8 Effect of D/t ratio on final deformed shape

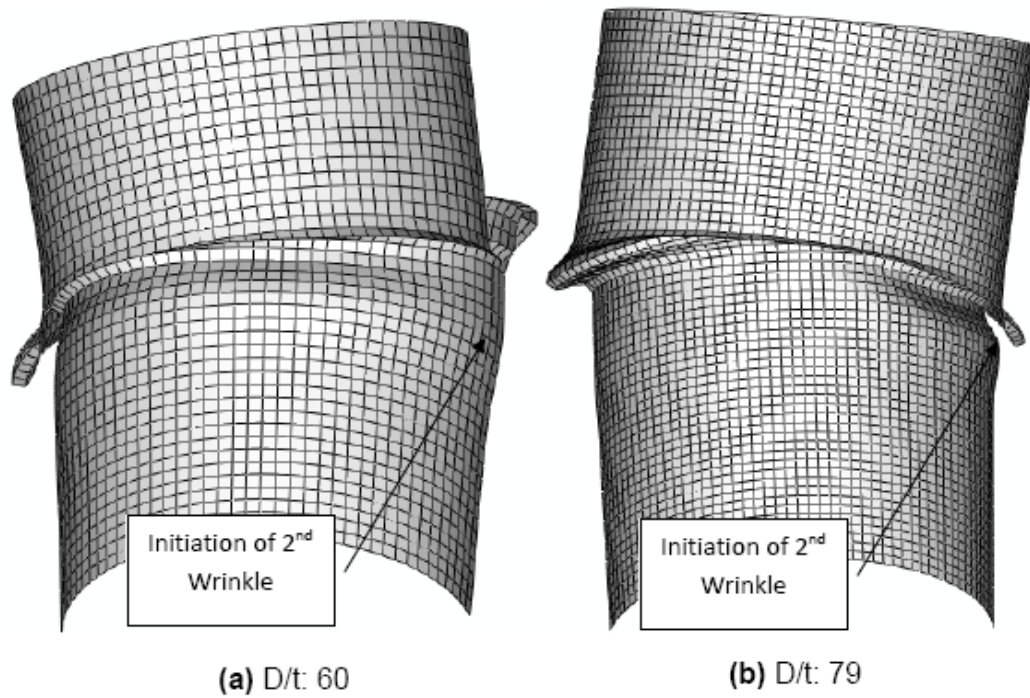


Figure 6.9 Initiation of second wrinkle for higher D/t ratio

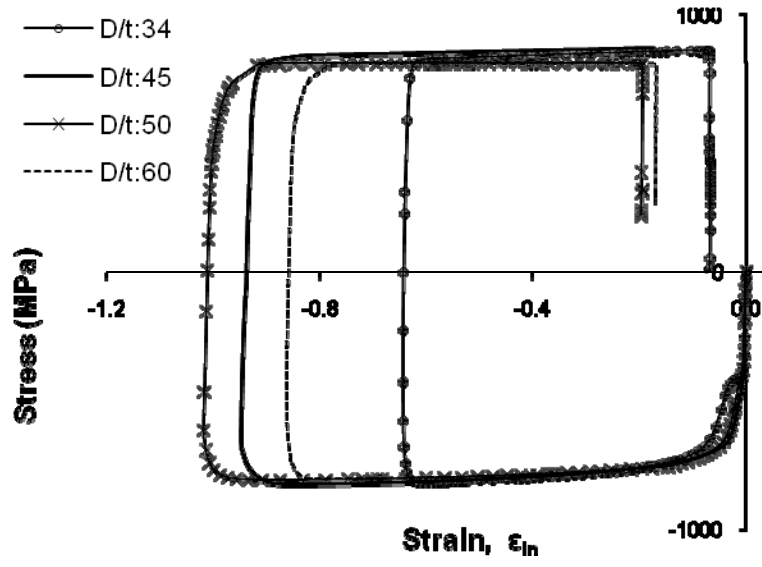


Figure 6.10 Effect of D/t ratio on longitudinal stress-strain relationship (i.e. Strain-Reversal)

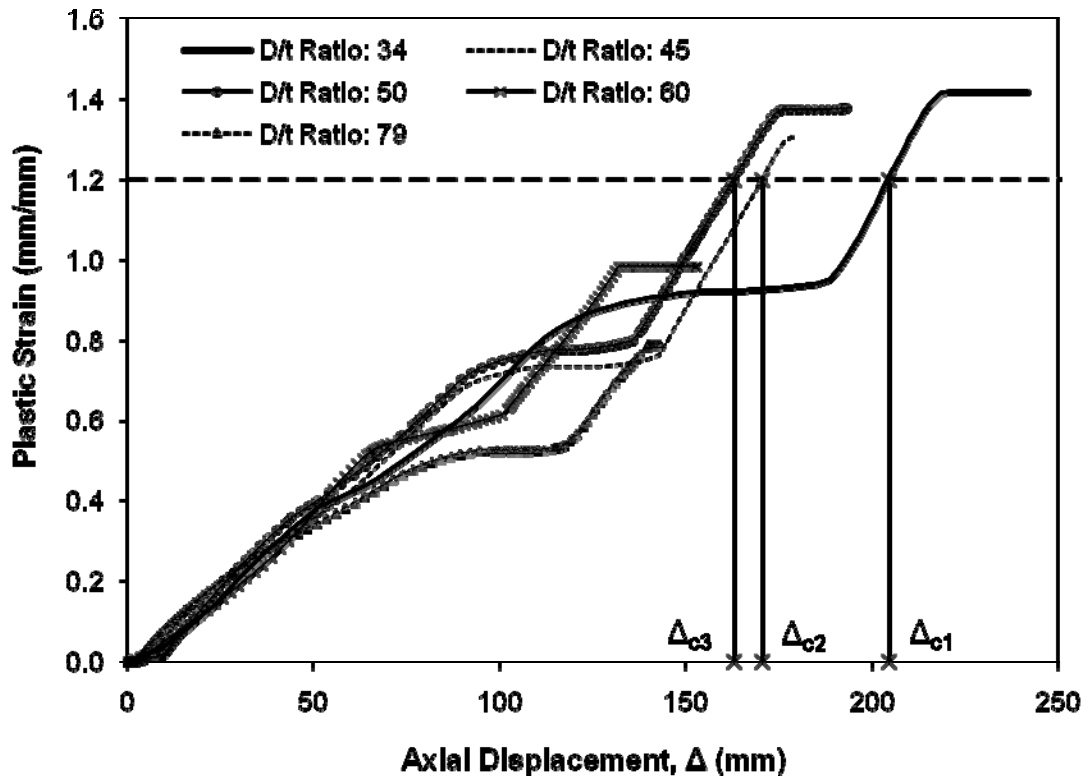


Figure 6.11 Effect of D/t ratio on plastic strain growth

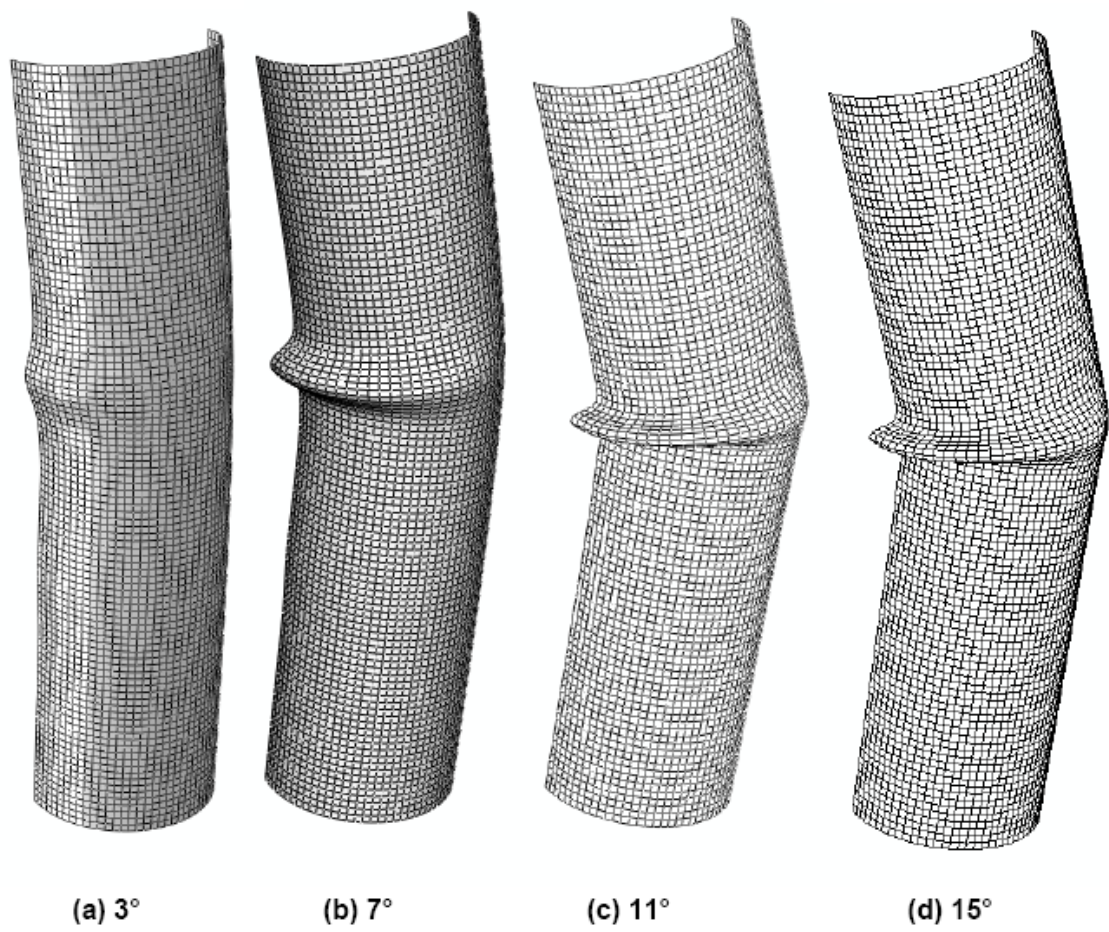


Figure 6.12 Effect of curvature on initial deformed shape

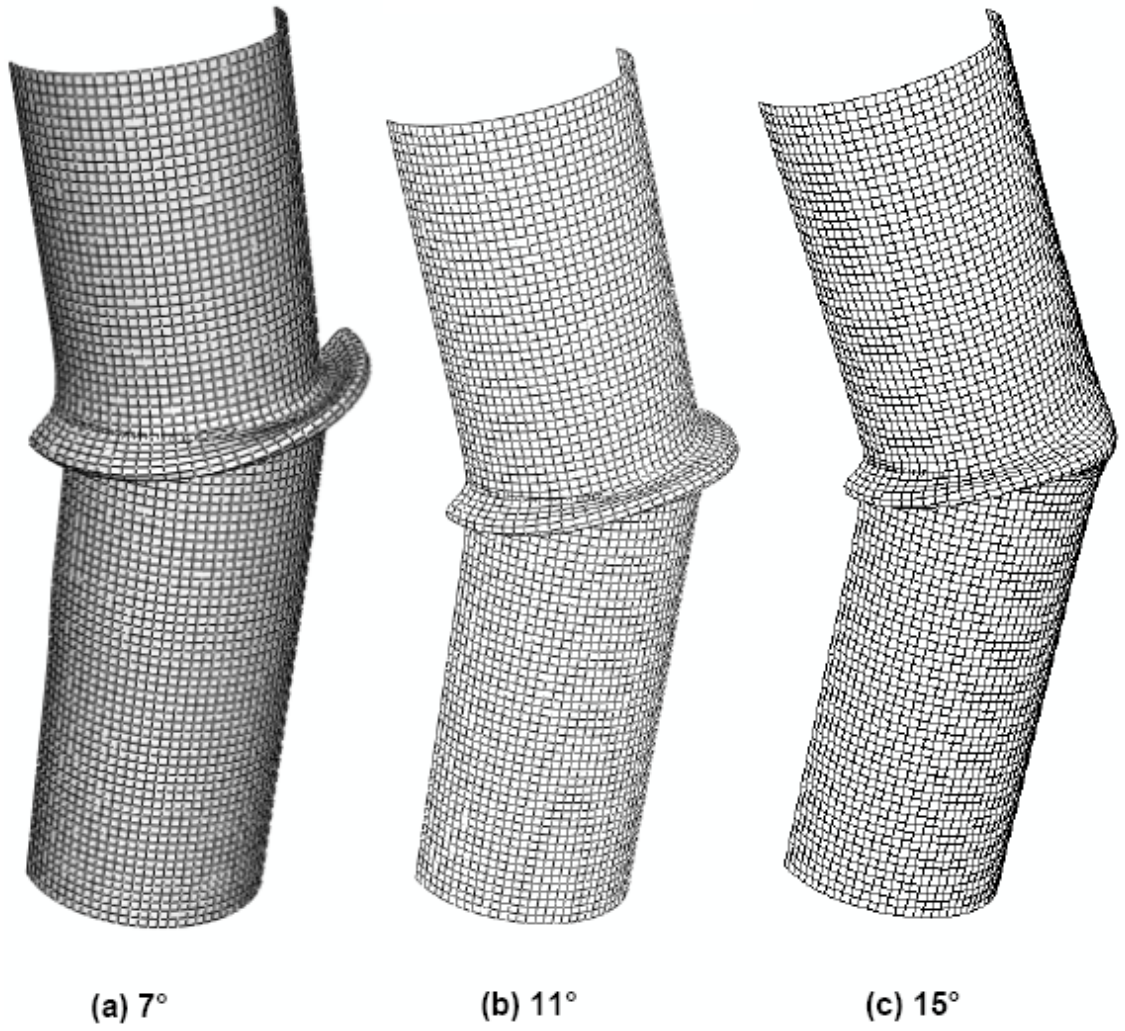


Figure 6.13 Effect of curvature on final deformed shape

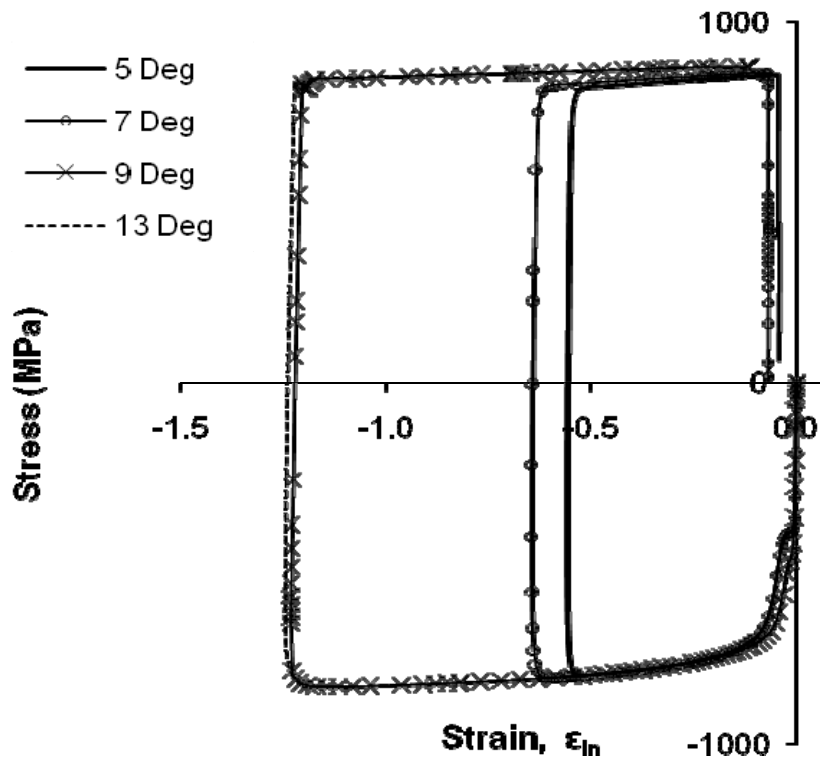


Figure 6.14 Effect of curvature on stress-strain relationship (i.e. Strain-Reversal)

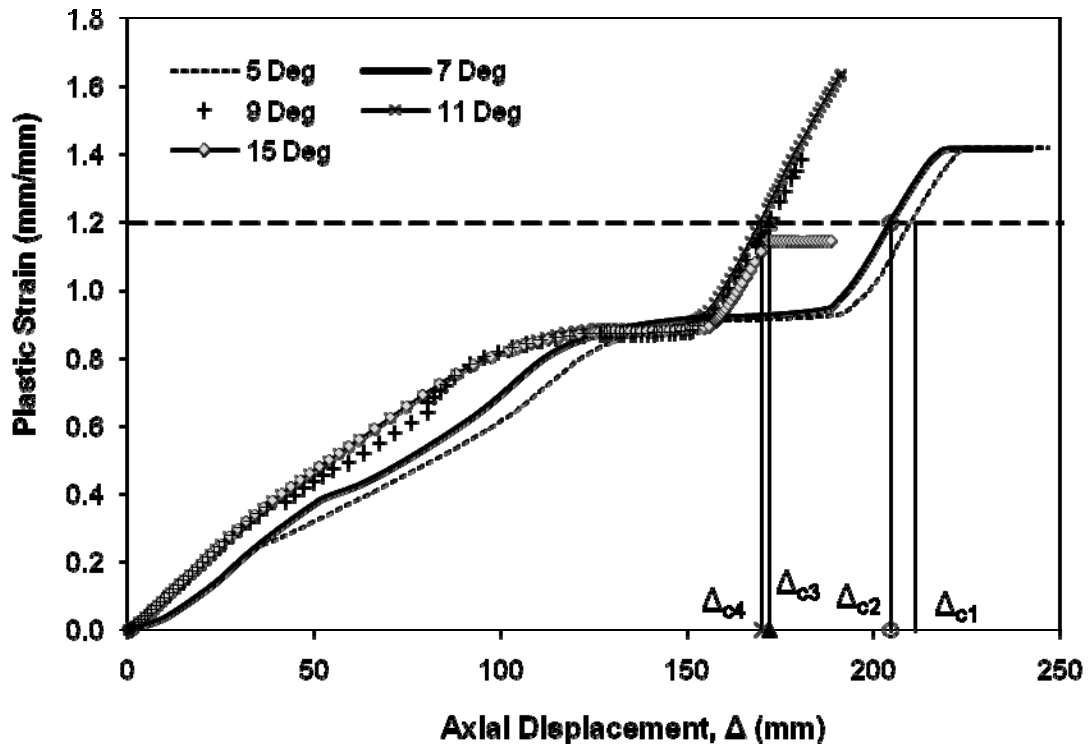


Figure 6.15 Plastic strain growth development under increasing curvature

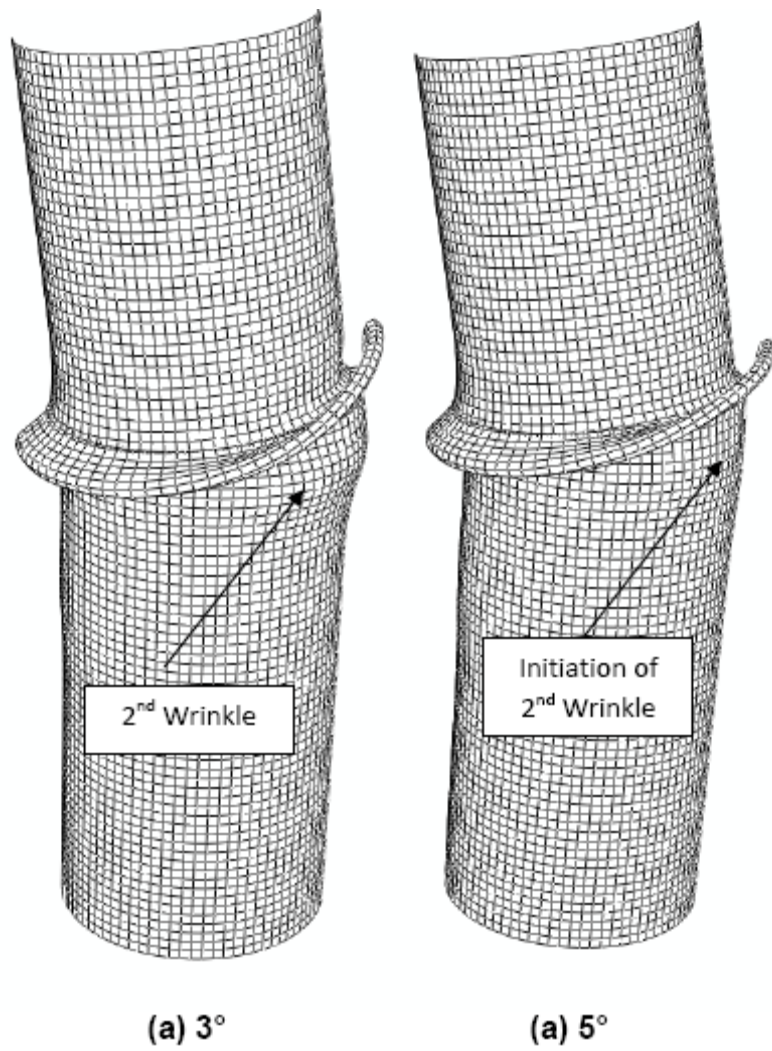


Figure 6.16 Initiation of second wrinkle under relatively smaller curvature

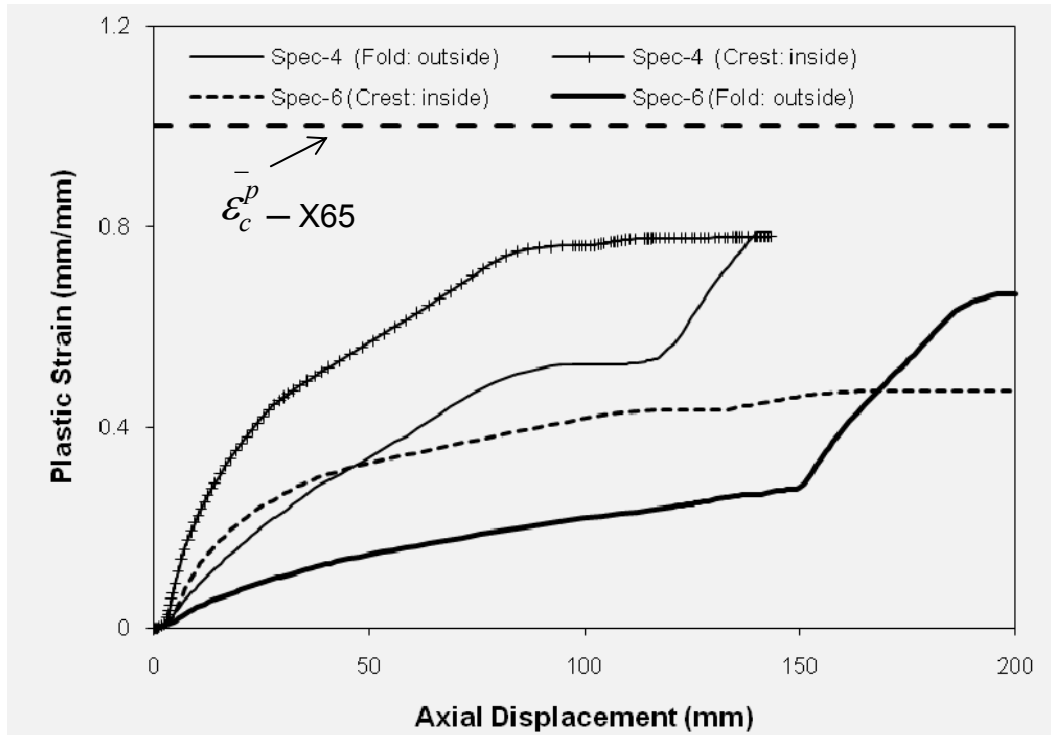


Figure 6.17 Plastic strain growth with displacement history for specimen 4 and 6

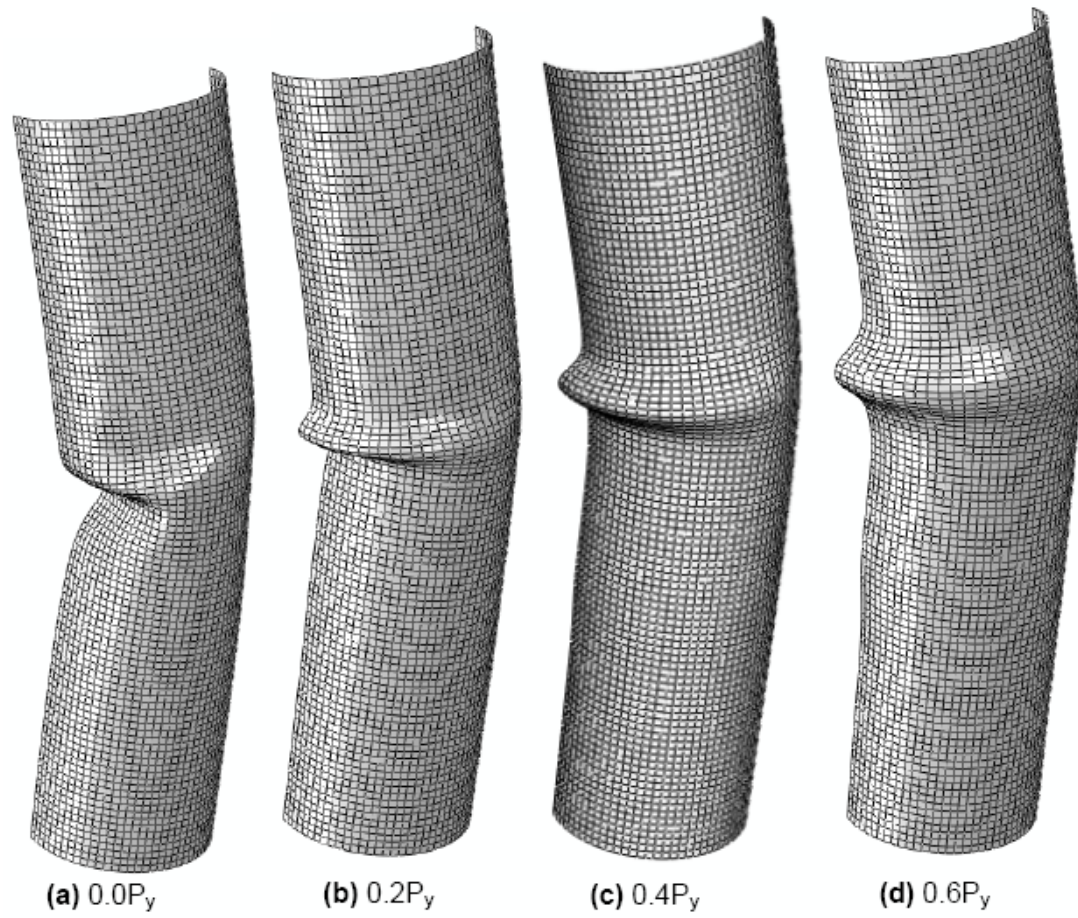


Figure 6.18 Effect of internal pressure on initial deformed shape

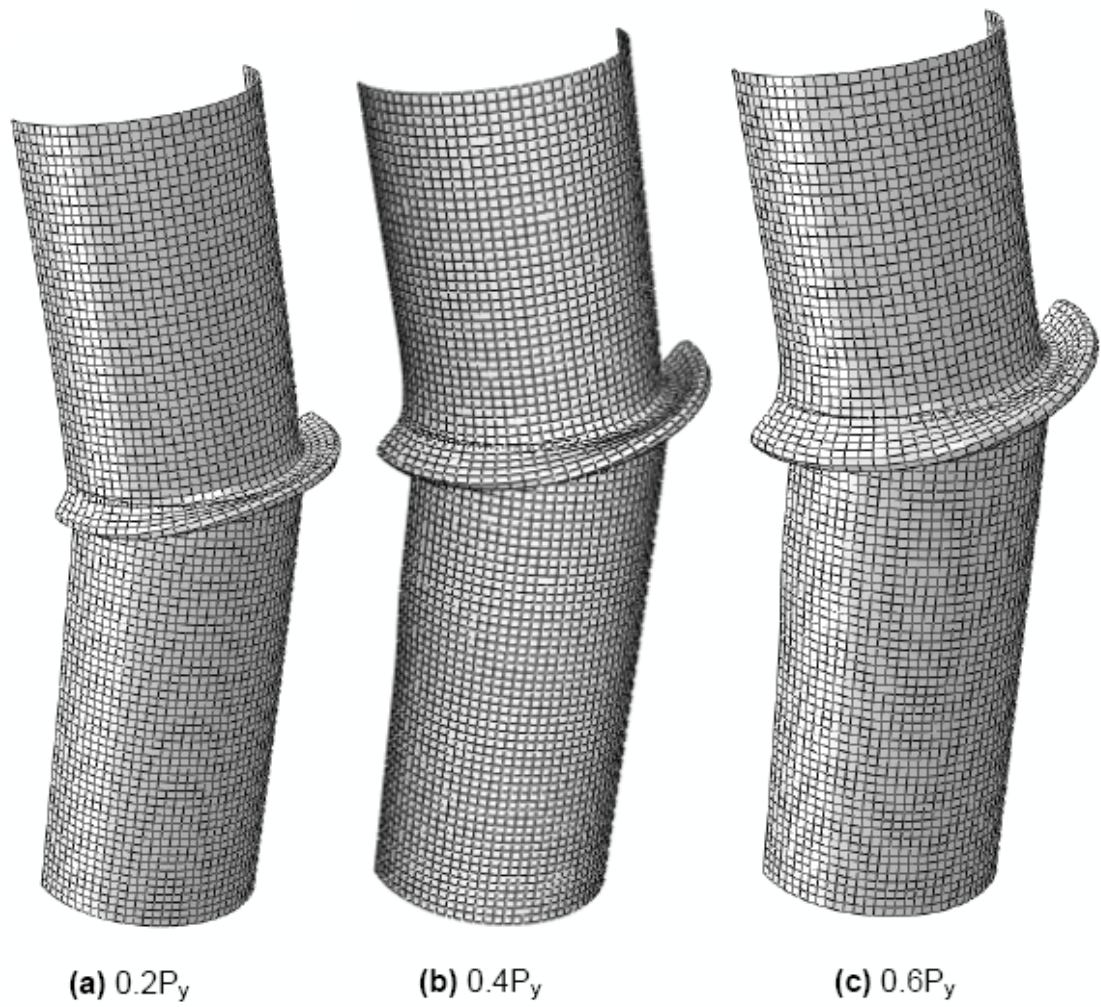


Figure 6.19 Effect of internal pressure on final deformed shape

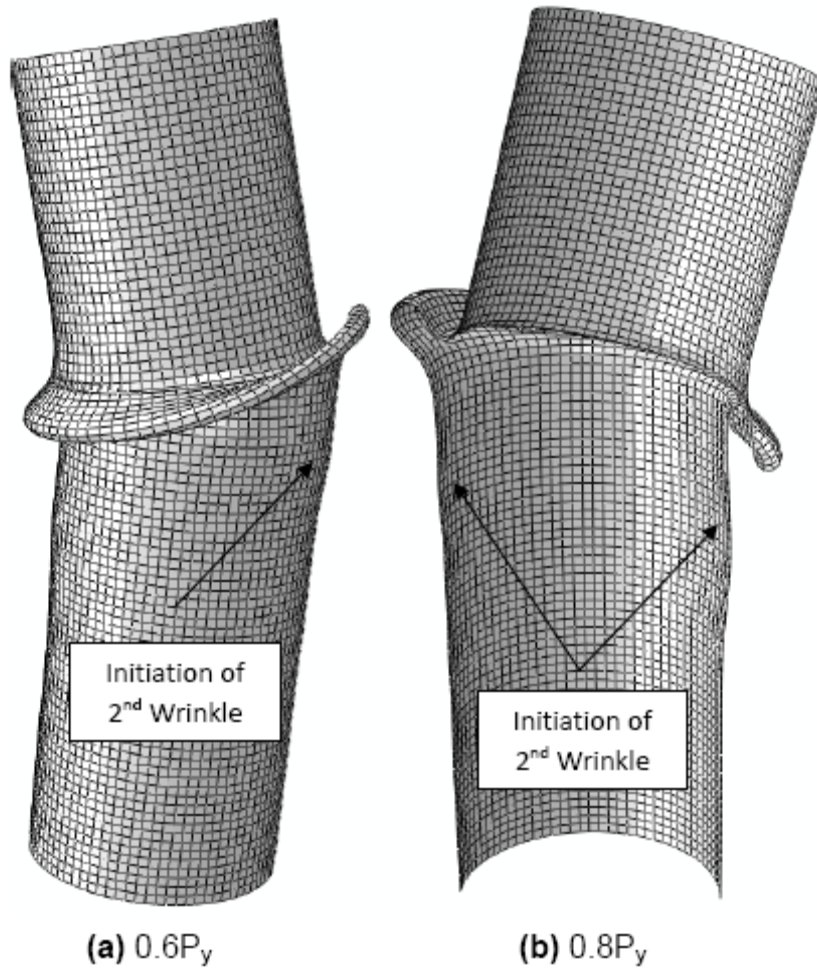


Figure 6.20 Initiation of second wrinkle under higher internal pressure condition

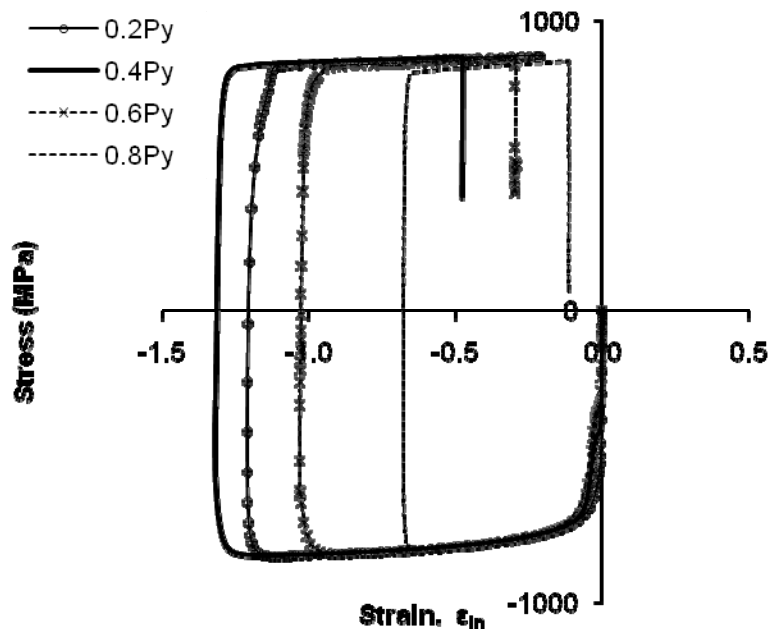


Figure 6.21 Effect of internal pressure condition on stress-strain relationship (i.e. Strain-Reversal)

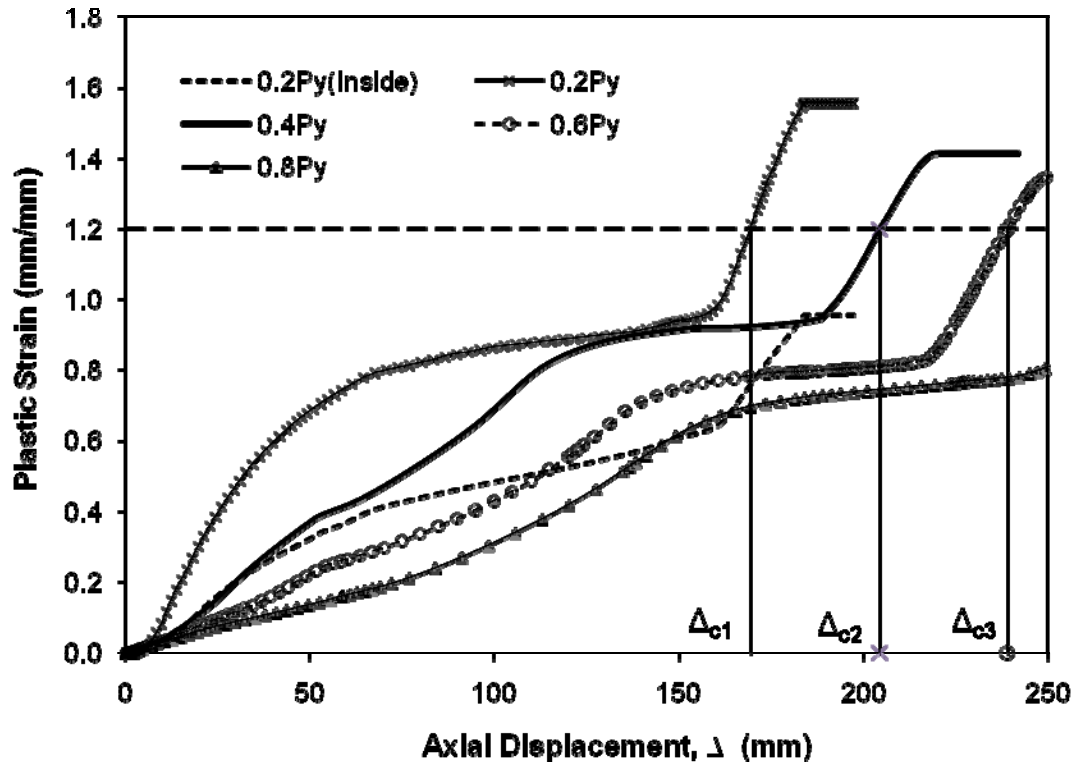


Figure 6.22 Plastic strain growth development under increasing curvature

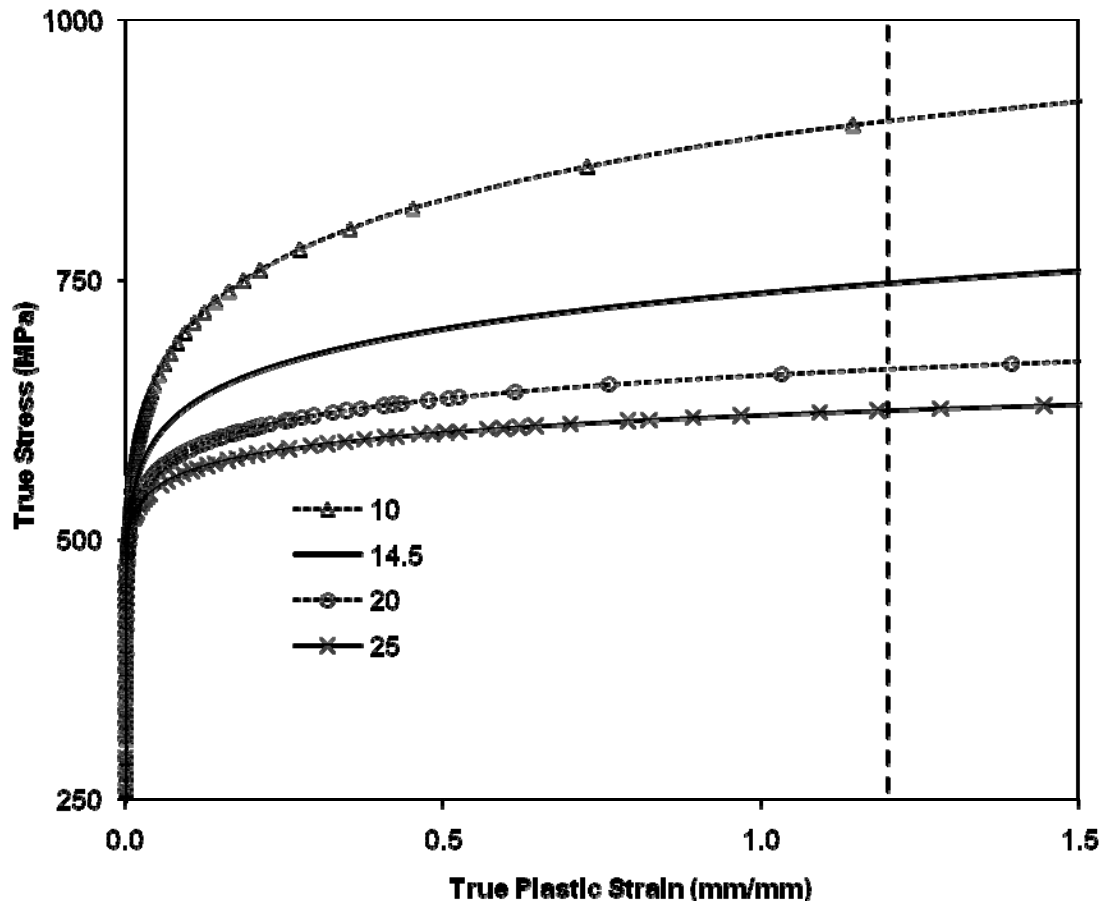


Figure 6.23 True stress-true plastic strain relations with different strain-hardening exponents (i.e. 'n' in Equation 4.13)

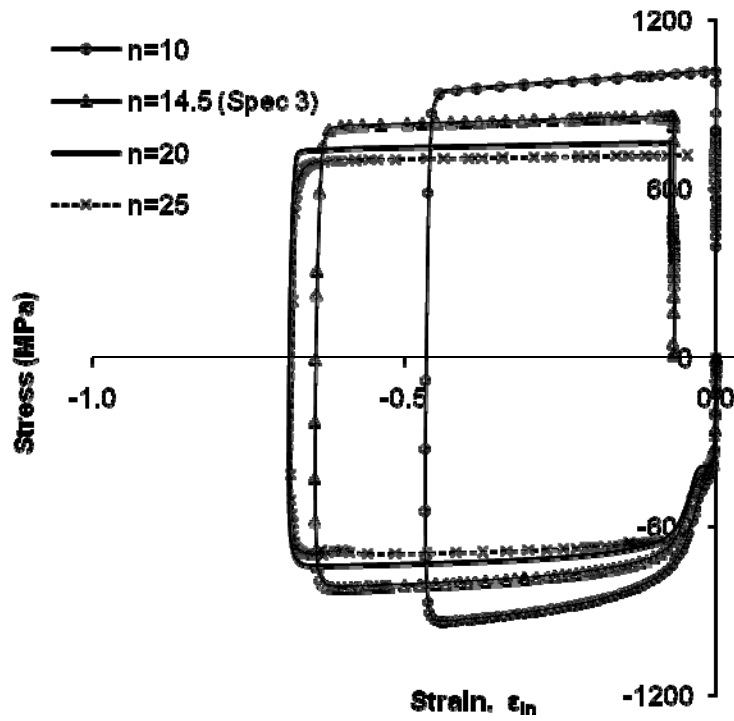


Figure 6.24 Effect of 'n' stress-strain relationship (i.e. Strain-Reversal)

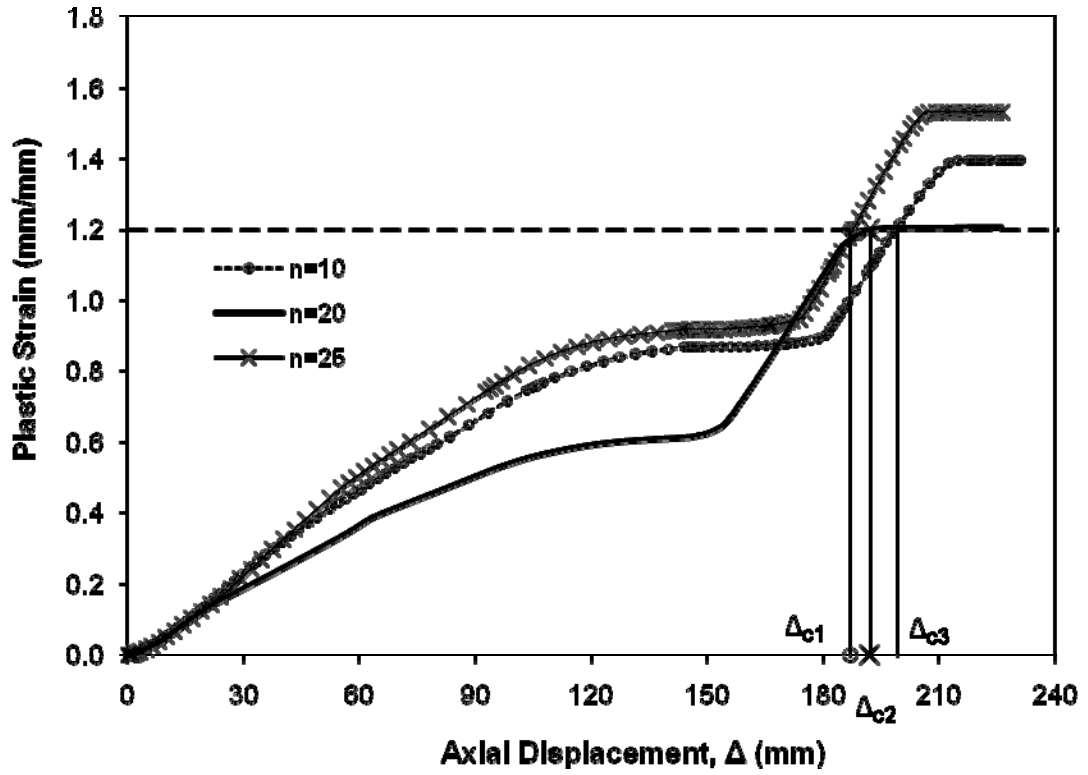


Figure 6.25 Plastic strain growth under different strain-hardening exponent

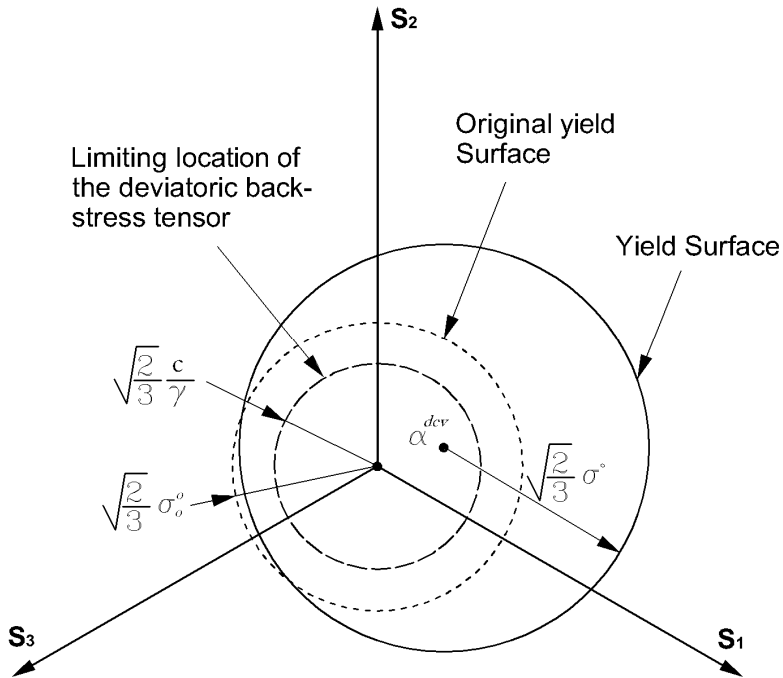


Figure 6.26 Nonlinear kinematic/Isotropic hardening illustrating evolution of yield surface in the stress space

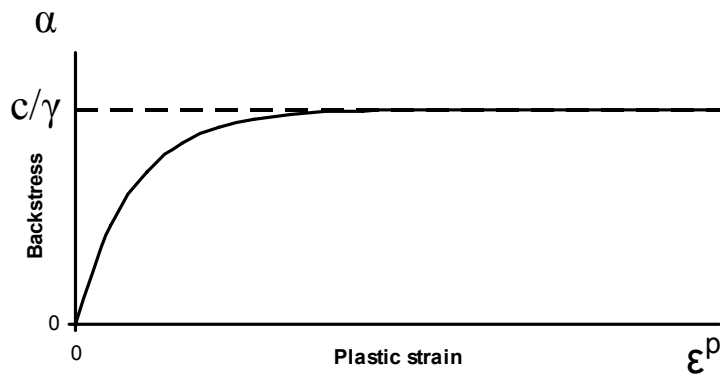


Figure 6.27 Evolution of back-stress using Armstrong-Fredrick kinematic hardening model saturating at  $c/\gamma$ .

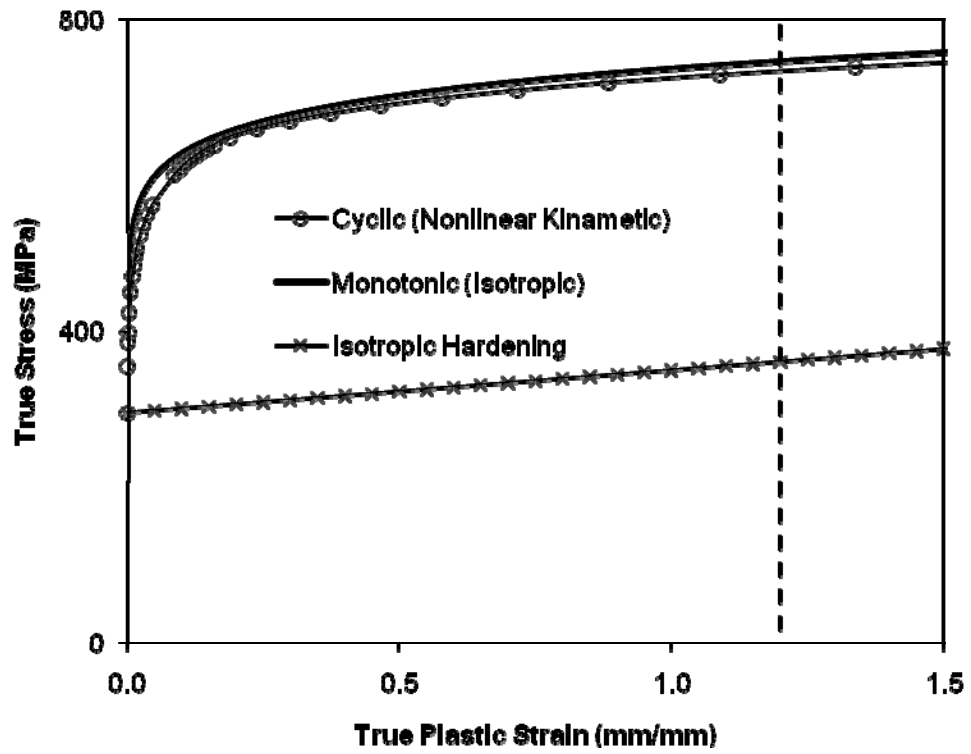


Figure 6.28 True stress-true plastic strain relations under cyclic and monotonic loading

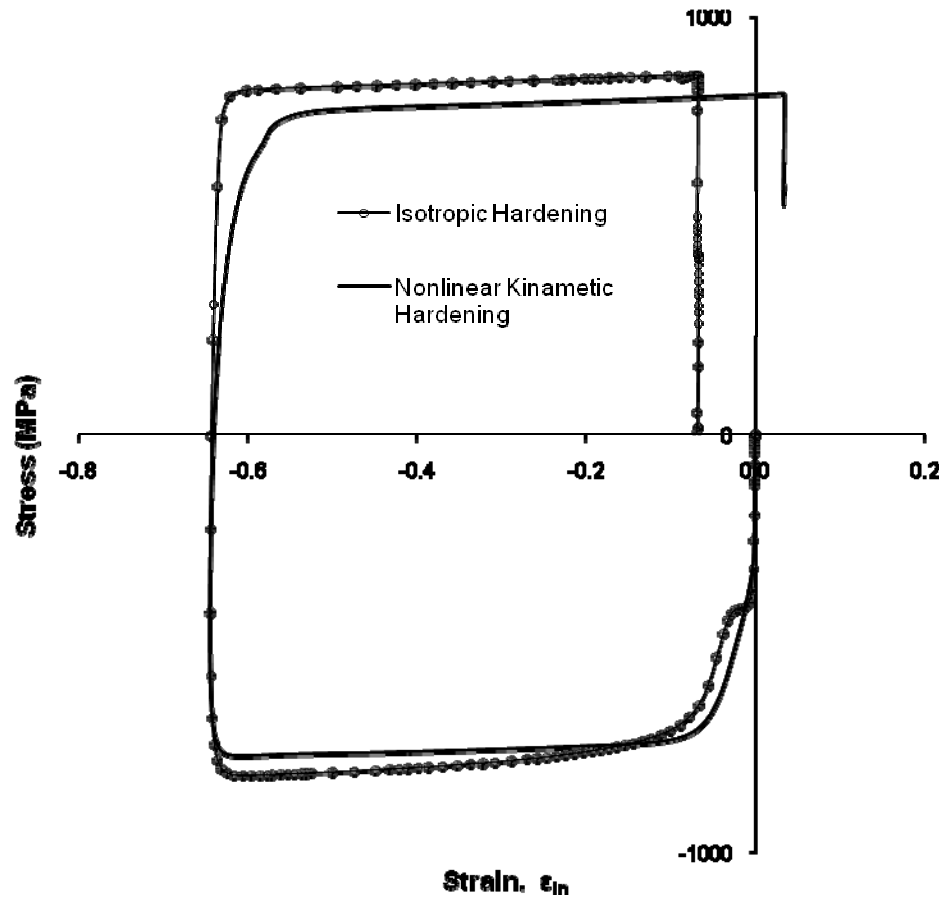


Figure 6.29 Bauschinger Effect on strain-reversal behaviour

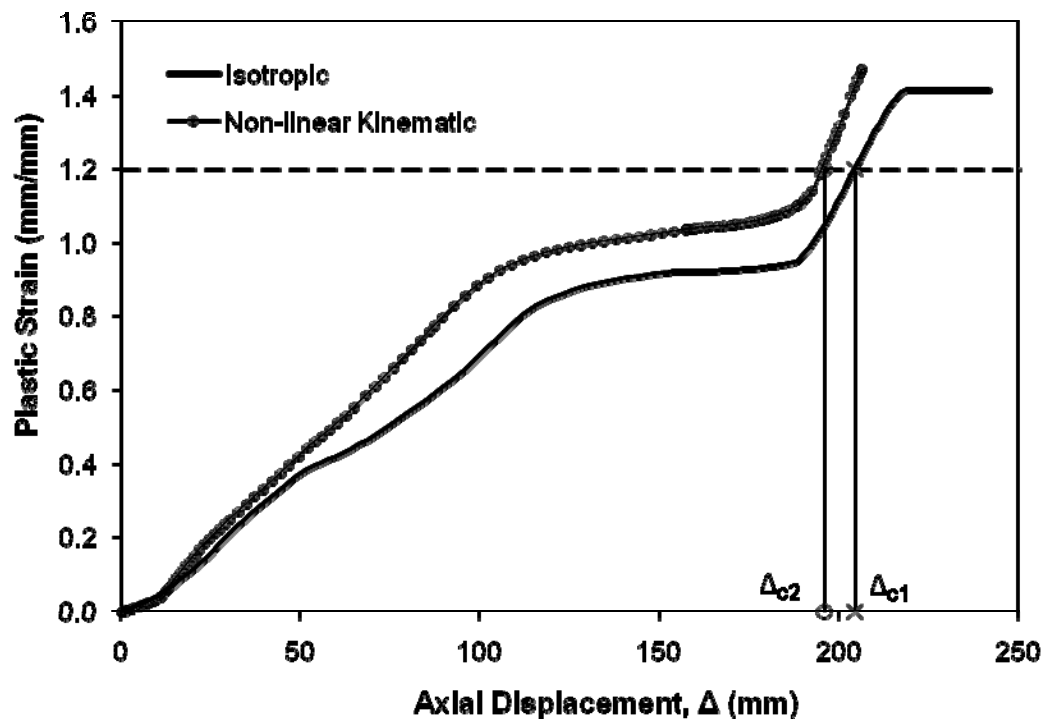


Figure 6.30 Effect of different hardening model on plastic strain growth

## 6.9 References

- Das, S. 2003. Fracture of wrinkled energy pipelines. PhD Thesis, Structural Engineering, University of Alberta, Edmonton, AB, Canada.
- Das, S., Cheng, J.J.R., and Murray, D.W. 2007a. Behaviour of wrinkled steel pipelines subjected to cyclic axial loadings. *Canadian Journal of Civil Engineering*, 34: 598-607.
- Das, S., Cheng, J.J.R., and Murray, D.W. 2007b. Prediction of fracture in wrinkled energy pipelines subjected to cyclic deformations. *International Journal of Offshore and Polar Engineering*, 17: 205-212.
- Das, S., Cheng, J.J.R., Murray, D.W., Wilkie, S.A., and Zhou, Z.J. 2001. Wrinkle behaviour under cyclic strain reversal in NPS12 pipe. *In 20th International Conference on Offshore Mechanics and Arctic Engineering; Polar and Arctic Pipeline Technology*, Jun 3-8 2001, Vol. 4, pp. 129-138.
- Sen, M., 2006. Behaviour of cold bend pipes under combined loads. Ph.D. Thesis, University of Alberta Edmonton, Alberta, Canada.

## 7. SUMMARY, CONCLUSIONS, AND RECOMMENDATIONS

This chapter summarizes the research and findings, and provides the conclusions on the work that has been done under the scope of this thesis, and recommends further work that is necessary and can be undertaken in future research.

### 7.1 Summary

Field observations of onshore pipelines, especially those buried in discontinuous permafrost, have indicated that large geotechnical movement can result in wrinkle development in the pipe wall. Prior research works have confirmed that the pipe wrinkles may not pose threat to safety and integrity of a line pipe under normal operating conditions, and these pipe lines do exhibit good ductility. However, a number of field fractures at wrinkle locations in recent years have addressed the necessity of a comprehensive research program by the pipeline research group at University of Alberta to understand the ultimate limit states of wrinkled pipes.

For the wrinkled pipe under specific load combinations, there are two ultimate (fracture) limit states: 'low cycle fatigue (LCF)' failure under cyclic load-deformation, and 'tearing' failure mode under large monotonic load-deformation. Under cyclic loading, there are two possible scenarios: (i) under axial load/deformation resulting in axisymmetric wrinkles, and (ii) under bending load/deformation resulting in non-axisymmetric wrinkles. In both cases, due to the occurrence of strain reversals in plastic range at the wrinkle crest, the fracture can trigger at the dimple of the wrinkle crest initiating from the inner surface of the pipe wall. The number of cycles required to generate this failure mode is very low in nature. A research program separate from this research program was designed to understand the LCF behaviour of wrinkled pipes. This research program was set with the intention to understand the limiting conditions related to tearing fracture at the pipe wrinkle subjected to monotonic loading, and to

develop the failure criteria capable of predicting the onset of tearing fracture in the pipe wall.

As a first step towards understanding of this failure mechanism, a proof of concept test (Das et al. 2002) was designed to simulate the tearing fracture observed in the field and the test was carried out successfully. The first phase of this research program was focused on understanding and simulating the complex behaviour observed in field and laboratory, and then, to propose a preliminary failure criterion responsible for this failure mode. In this phase, a detailed numerical investigation was carried out to verify and validate the test and field behaviour using a full-pipe finite element (FE) model. Numerical results showed that due to severe plastic bending mechanism, the presence of strain-reversal is possible at some critical location of the wrinkle fold even under monotonic load-deformation process. The occurrence of strain-reversal is defined as the preliminary/first criterion to trigger this failure mode. As a second step towards providing more rigorous insight on this unique failure mechanism, a full-scale ‘pipe wrinkling’ test program was carried out (Aydin 2007) concurrent to this research project. Six full-scale tests in two different sizes of pipes and two different grades of pipes were undertaken in this experimental program. Results of this test program have indicated that the pipe specimens did exhibit very ductile behaviour withstanding significant plastic deformation. However, several circumferential cracks at the wrinkle fold of the test specimens were observed during the experiments (Aydin 2007). In one instance, significant fractures in the pipe wall were observed at the wrinkle fold of NPS16 specimens. The occurrences of these fractures have recognized that the tearing failure can be one of the possible ultimate limit states of wrinkled pipes, and hence, provided motivation for the next phase. The second phase of this research work was to reanalyze all of the test results, and to perform numerical validation of all the tests using a half-pipe FE model developed in this study. The FE model predicted the test response with reasonable accuracy. Therefore, it seemed rational to use this numerical

model to predict true stress ( $\sigma$ ) – true plastic strain ( $\epsilon_p$ ) responses at wrinkle locations of these test specimens to develop the failure criteria.

The next phase of this research program was focused to develop the failure criteria in terms of a 'Critical Strain Limit' along with the strain reversal criterion identified in the first phase. In order to define this critical limit, the true stress ( $\sigma$ ) – true plastic strain ( $\epsilon_p$ ) relation of the pipe material beyond the initiation of necking (up to fracture) of all the tested coupons obtained from different grade full-scale pipes were established. In order to predict these  $\sigma$ - $\epsilon_p$  curves including material response in both the pre- and post-plastic localization regime, all the test behaviour of these coupons were simulated and validated using FE model. Based on the results of this phase, the critical plastic strain ( $\bar{\epsilon}_c^p$ ) is defined as an onset of fracture limit or the critical strain limit, which corresponds to a point well beyond the peak load and the initiation of necking of a tensile coupon tests, but before the complete fracture of those test coupons. The double failure criteria – 'Strain Reversal Criterion (Criterion-1)' and 'Critical Plastic Strain ( $\bar{\epsilon}_c^p$ ) Limit (Criterion-2)' proposed in this phase have been successfully applied to all test specimens used in this research program. The numerical results have indicated that the critical equivalent plastic strain ( $\bar{\epsilon}_c^p$ ) limit, set as 'Criterion-2', can predict the onset of fracture in the pipe wall with reasonable accuracy.

As the last component of this research project, a parametric study was designed and carried out to study the effects of different parameters on different failure modes of wrinkled pipe under monotonic loading. Specific emphasis was given to the tearing failure mode. The parameters included loading condition, D/t ratio, internal pressure condition, global curvature, material properties, and Baushinger effects. Results of this phase have indicated that some of the parameters can expedite the telescopic tearing action, whereas some can delay this failure mechanism, and thus lead to different failure mode, such as accordion failure mode.

## 7.2 Conclusions

Significant progress has been made in understanding the ultimate/fracture limit state, specifically tearing failure mode of wrinkled pipe subjected to monotonic loading and the potential risk of pipeline safety and integrity associated to this failure mode. A number of conclusions including a brief regarding the tearing failure mechanism can be drawn from this research program.

**Failure Mechanism:** Under sustained monotonic load/deformation process, there are two possible scenarios:

First, a load-deformation process, which includes an axial deformation process responsible for generating an axisymmetric wrinkle in order to soften the pipe, and then, followed by shear or bending deformation for transforming the axisymmetric wrinkle to a non-axisymmetric one. Eventually, under continued axial deformation, due to the influence of telescopic action, a wrinkle fold can be created. In this case, fracture is possible even without the presence of any internal pressure.

Second, a load-deformation process which involves in generating a non-axisymmetric wrinkle under the presence of axial and bending deformation. Once, a wrinkle with a sizeable amplitude is formed under the presence of sustained axial deformation at a constant curvature, a telescopic fold can be created at the wrinkle location. In this case, presence of internal pressure is critical, as under zero internal pressure condition, there can be a diamond mode shape instead of bulge shape, resulting a sever cross-sectional distortion rather than telescoping tearing.

However, in both cases, due to severe plastic bending mechanism, the occurrence of strain reversal is possible even under monotonic load-deformation process. There will be no fracture at the crest of the wrinkle, as strain-reversal phenomenon is not present at the wrinkle crest, unlike to the case of the LCF.

The following conclusions can be drawn from this research:

a) All the test specimens used in this research program have shown two specific failure modes:

(1) Presence of significant fracture in the pipe wall at the wrinkle fold (e.g. specimens D12P0A3.4-1 and D16P40A7-3 in Table 5.3), and

(2) Accordion failure model or cow-boy hat shape mode, where no fracture along with indication of second wrinkle formation was observed (e.g. specimens D20P40A3.5-4 and D20P804-6 in Table 5.3).

b) The proposed 'Double Criterion' — 'Strain Reversal' in plastic range, and 'Critical Plastic Strain Limit', have predicted the failure modes of all the test specimens with reasonable accuracy, thus demonstrating the acceptability of the proposed criteria.

c) Based on the results of the parametric study, some important conclusions can be drawn regarding the failure modes of wrinkled pipes.

1) For  $D/t$  ratio  $\geq 60$ , the possibility of tearing failure mode will be rare, whereas the possibility of accordion failure mode increases.

2) For low or moderate internal pressure condition ranging between  $0.0p_y$  to  $0.4p_y$ , the possibility of telescopic tearing at wrinkle fold increases. For higher internal pressure condition ( $0.6p_y$  to  $0.8p_y$ ), there are increasing possibilities of initiation of second wrinkle, thus reducing the chances of fracture limit state.

3) For relatively high end rotation (ranging between  $5^\circ \sim 13^\circ$ ) or initial global curvature ranging between  $115 \times 10^{-6}$  rad/mm to  $290 \times 10^{-6}$  rad/mm, the anticipation of tearing failure mechanism increases significantly. However, for relatively smaller end rotation (e.g.  $3^\circ$ ) or smaller initial global curvature (e.g.  $75 \times 10^{-6}$  rad/mm), the pipe wrinkle may have greater possibility of experiencing accordion failure mode. Whereas, for very high initial global

curvature or end rotation , the pipe structure can become unstable, as the pipe may lose its load carrying capacity significantly.

4) Effect of pipe material parameters including the exponent of isotropic strain-hardening and the Baushinger effect is evident, although the influence of these parameters is not considerable.

### **7.3 Future Research Recommendations**

This research has provided a number of significant enhancements towards the objectives of the project. Based on this research program, the following recommendations can be made in order to achieve more confidence in understanding the ultimate/fracture behaviour of pipe wrinkles:

- 1) Additional experimental works including full-scale pipe wrinkling tests are recommended to verify the range of the parameters suggested in this research responsible for the tearing failure mechanism.
- 2) A material model incorporating the effects of strain reversal through cyclic coupon/material test data can be implemented in the full-scale FE model through user's subroutine in order to improve the performance of the failure criteria proposed herein.
- 3) To study the possibility of extending the proposed failure criteria to the tensile failure of a wrinkled pipe.
- 4) To study the feasibility of extending the proposed failure criteria to predict the life of wrinkled pipe subjected to LCF loading.
- 5) This research program is limited to normal/or moderate strength of pipe material. This could be extended to high strength pipes, as pipeline industries are advocating for long distance line pipes in Canadian North and Alaska. For high strength pipes, the material anisotropy will be a significant issue to be dealt with.

- 6) Since most field pipelines under normal service and operational conditions and are far from the severe strain reversal conditions as used in this study, it is essential to extend the study to include the effectiveness of the proposed failure criteria for these loading conditions.
- 7) Field monitoring should be planned to investigate the actual loading spectra generated from operational, environmental, and geotechnical effects.

#### **7.4 References**

- Aydin, M. 2007. Tearing fracture of energy pipelines under monotonic loading conditions. M.Sc. dissertation, University of Alberta, Edmonton, AB, Canada.
- Das, S., Cheng, J.J.R., and Murray, D.W. 2002. Fracture in wrinkled line pipe under monotonic loading. *In* Proceedings of the 4th International Pipeline Conference, Sep 30-Oct 3 2002, Vol. B, pp. 1613-1618.